# Strategies Based on Peptide Antagonists

## to Improve Imaging and Treatment of Prostate Cancer and Neuroendocrine Tumors

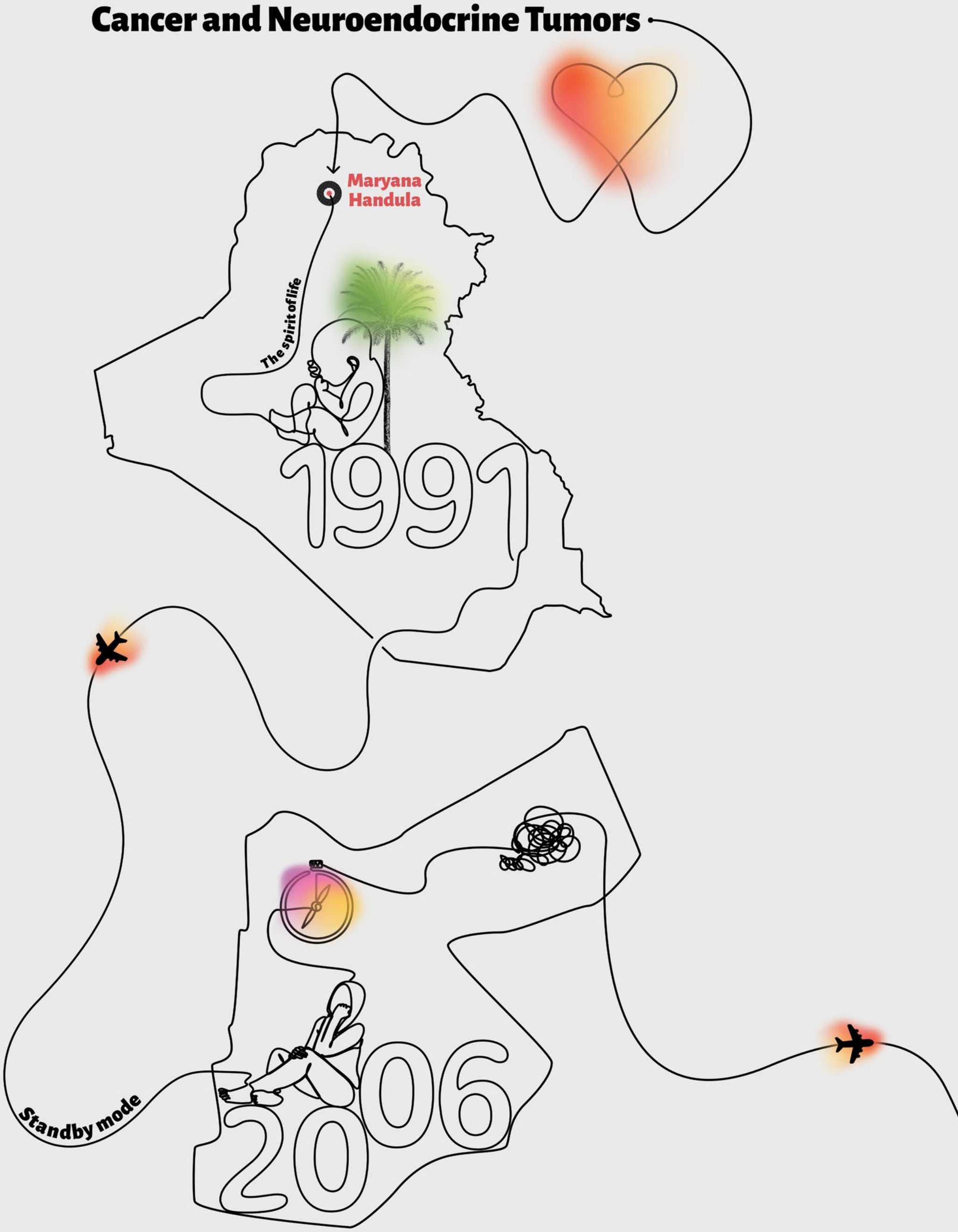

# Strategies Based on Peptide Antagonists to Improve Imaging and Treatment of Prostate Cancer and Neuroendocrine Tumors

*Maryana Handula*

Cover design: Ahmed Kadhim

Provided by thesis specialist Ridderprint, ridderprint.nl
Printing: Ridderprint
Layout and design: Jules Verkade, persoonlijkproefschrift.nl

ISBN: 978-94-6483-327-0

**Strategies Based on Peptide Antagonists to Improve Imaging and Treatment of Prostate Cancer and Neuroendocrine Tumors**

Strategieën gebaseerd op peptide antagonisten om beeldvorming en behandeling van prostaatkanker en neuro-endocriene tumoren te verbeteren

Thesis

to obtain the degree of Doctor from the
Erasmus University Rotterdam
by command of the
rector magnificus

Prof.dr. A.L. Bredenoord

and in accordance with the decision of the Doctorate Board.

The public defence shall be held on

Tuesday 17 October 2023 at 13:00

by

Maryana Handula

born in Nineveh, Iraq

Erasmus University Rotterdam

**Doctoral Committee:**

| | |
|---|---|
| **Promotor:** | Prof.dr. F.A. Verburg |
| **Other members:** | Dr. L. Mezzanotte<br>Prof.dr. A.D. Windhorst<br>Dr. K. Djanashvili |
| **Copromotors:** | Dr. Y. Seimbille<br>Dr.ir. A.G. Denkova |

**Strategies Based on Peptide Antagonists to Improve Imaging and Treatment of Prostate Cancer and Neuroendocrine Tumors**
Thesis, Erasmus University Medical Center, Rotterdam, The Netherlands

The research reported in this thesis was carried out at the department of Radiology and nuclear medicine at the Erasmus Medical Center, Rotterdam, The Netherlands.

The different projects presented in this thesis were financially supported by the Dutch Cancer Society (KWF), grant numbers YIG11671 and 12259.

## Content

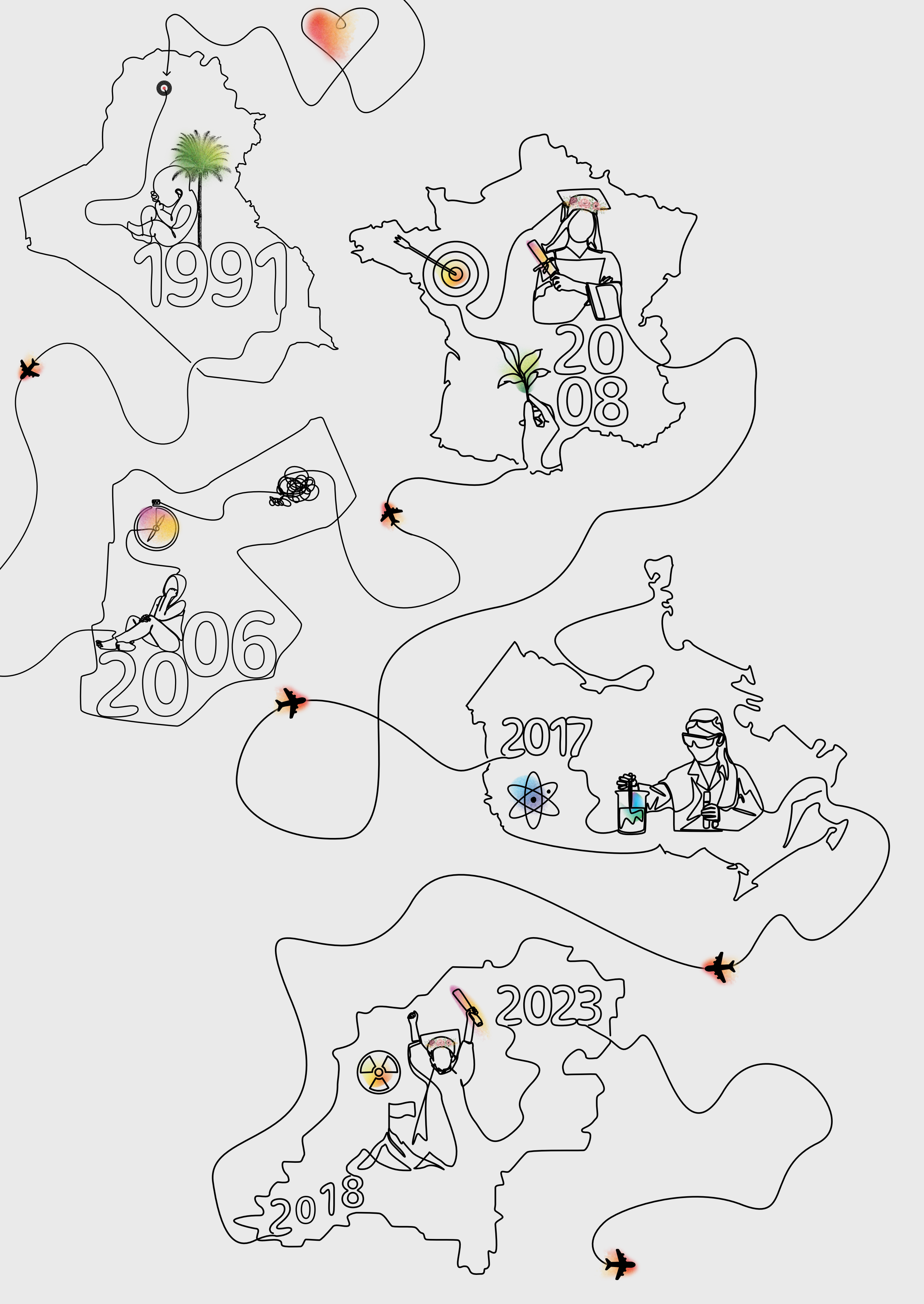

1991
2008
2006
2017
2023
2018

# CHAPTER 1

## General Introduction and Thesis Outline

## General aspects of targeted radionuclide imaging and therapy

Cancer cells are known to overexpress specific types of biomarkers, such as receptors. Targeted radionuclide imaging and therapy consists of transporting a radioactive drug specifically to the overexpressed receptor for diagnosis or treatment purposes [1]. The overexpression of the receptor by the cancer cells leads to high accumulation of the radioactive drug in the tumor. The radioactive drug is commonly known as a radiopharmaceutical. The radiopharmaceutical consists of a biovector (e.g., peptide, antibody, nanobody) possessing the ability to target the overexpressed receptor with high binding affinity. The biovector carries a radionuclide incorporated either directly into the chemical structure of the radiopharmaceutical (e.g., fluorine-18, carbon-11, iodine-131), or via complexation with a chelating agent (lutetium-177, indium-111, gallium-68, copper-64, …). The chelate is introduced into the chemical structure of the biovector directly or via a spacer that helps improving the physicochemical properties of the radiopharmaceutical (e.g., solubility, rigidity, conformation). Various chelates were used in the literature, and many of them demonstrated their preclinical and clinical relevance, such as: 2,2′,2′′,2′′′-(1,4,7,10-tetraazacyclododecane-1,4,7,10-tetrayl)tetraacetic acid (DOTA), diethylenetriaminepentaacetic acid (DTPA), 2-(4,7-biscarboxymethyl [1,4,7]triazacyclo nona-1-yl-ethyl)car-bonyl-methylamino]acetic acid (NETA), and 2,2′,2”-(1,4,7-triazacyclononane-1,4,7-triyl)triacetic acid (NOTA).

The research conducted in this thesis was based on using radiopharmaceuticals carrying a chelating agent. As such, the biovector can be radiolabeled with a radionuclide either for imaging or therapy (Table. 1). In fact, a photon-emitting radioisotope (γ) can be used for single-photon emission computed tomography (SPECT) [2]. Besides, a positron-emitting radionuclide ($\beta^+$) can be dedicated for positron emission tomography (PET), where a pair of photons (emitted at the energy of 511 keV each) is used for image acquisition [3,4]. SPECT and PET (Figure. 1) are molecular imaging methods, however, they do not provide sufficient information regarding the anatomical structure of the tumor. Therefore, they are usually combined with either computed tomography (CT) or magnetic resonance imaging (MRI) [5].

**Table 1:** Most frequently used SPECT, PET and therapeutic radioisotopes, their half-lives, type of emission, energy and commonly used chelating agents [6–10]

| Radionuclide | Half-life | Emission | Energy (keV) | Chelating agents |
|---|---|---|---|---|
| **SPECT radioisotopes** | | | | |
| $^{99m}Tc$ | 6.02 h | γ | 141 | oxo-core, dioxo-core, organohydrazino-core, tricarbonyl-core |
| $^{111}In$ | 2.80 d | γ | 171 (91%)<br>245 (94%) | DOTA, DOTA-GA, DTPA, CHX-A-DTPA |
| $^{67}Ga$ | 3.26 d | γ | 93 (39%)<br>185 (21%)<br>300 (17%)<br>394 (5%) | DOTA, DO2A, HBED-CC, NOTA, *p*-SCN-Bn-NOTA, NODA-GA |
| **PET radioisotopes** | | | | |
| $^{89}Zr$ | 78.4 h | $\beta^+$, Electron capture | 902 (22.7%) | DFO |
| $^{86}Y$ | 14.7 h | $\beta^+$ | 1221 (11.9%)<br>1545 (5.6%) | EDTA, DTPA, DOTA |
| $^{64}Cu$ | 12.7 h | $\beta^+$, Electron Capture | 660 | |
| $^{68}Ga$ | 68.1 min | $\beta^+$, Electron Capture | 1900 | DOTA, DO2A, HBED-CC, NOTA, *p*-SCN-Bn-NOTA, NODA-GA |
| **Radioisotopes for targeted radionuclide therapy** | | | | |
| $^{177}Lu$ | 6.65 d | $\beta^-$ | 134 (100%) | DOTA, DOTA-GA, DTPA, CHX-A-DTPA |
| $^{67}Cu$ | 2.58 d | $\beta^-$ | 141 (100%) | EDTA, DTPA, DOTA, TETA |
| $^{90}Y$ | 2.67 d | $\beta^-$ | 920 (100%) | DOTA, CHX-A-DTPA, 1M3B-DTPA, 1B3M-DTPA, 1B4M-DTPA |

Cancer tissue can be treated using radiopharmaceuticals carrying a therapeutic radioisotope ($\beta^-$ or α). In fact, beta emitters and alpha particles have the ability to interact with the deoxyribonucleic acid (DNA) of the cancer cell causing either DNA single-strand or DNA double-strand breaks leading to the death of the cell [11]. DNA damage can be mediated through i) direct effect that induces direct ionization to DNA, or ii) indirect effect induced by water radiolysis. However, other cell death mechanisms were reported by Pouget et al., such as the bystander effect and other off target effects that consist of generating “danger” signals from the irradiated cells to the non-irradiated cells causing their death [12].

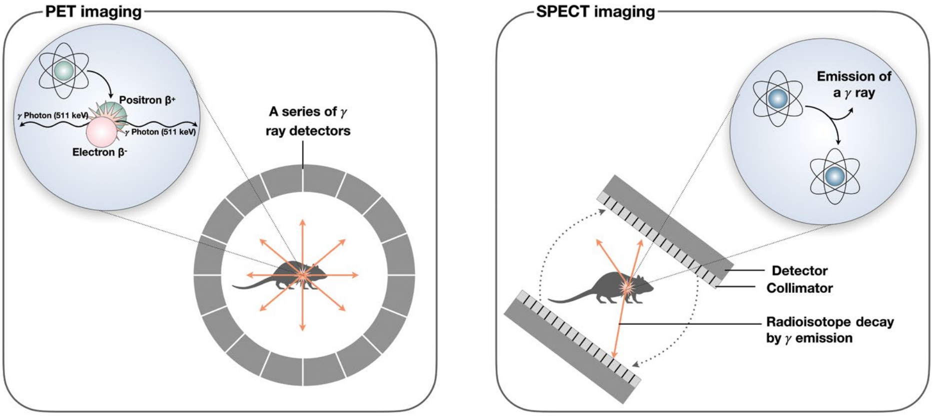


**Figure 1:** Schematic representation and principle of PET and SPECT imaging.

The radiolabeling of the same biovector with either an imaging or a therapeutic radioisotope involves the theranostic (therapeutic and diagnostic) approach. Nowadays, several theranostic relatives are routinely employed in preclinical and clinical studies, such as the radiopharmaceutical recently approved by the Food and Drug Administration (FDA), [$^{68}$Ga]Ga-DOTA-TATE for imaging and [$^{177}$Lu]Lu-DOTA-TATE for therapy of neuroendocrine tumors (NETs) [13,14]. However, in some cases, the complexation of the biovector with a different radioelement might affect its binding affinity towards the receptor (e.g., [$^{111}$In]In-DOTA-JR11 and [$^{90}$Y]Y-DOTA-JR11) [15]. Additionally, the radiolabeling of the same biovector with two different radionuclides might require different radiolabeling strategies due to the chemical nature of the radioelement. Therefore, multiple studies are aiming at the use of theranostic pairs, based on different radioisotopes of the same chemical element (e.g., iodine-124 for PET imaging and iodine-131 for therapy; scandium-44 for PET imaging and scandium-47 for therapy) [16]. Hence, the complexation of the biovector with the same radioelement will not affect its affinity towards the receptor and will require similar radiolabeling conditions.




## Prostate cancer and neuroendocrine tumors

### *Epidemiology of prostate cancer and neuroendocrine tumors*

Cancer is a major health problem and was classified by the World Health Organization (WHO) in 2019 as a second cause of mortality (after cardiovascular diseases), before the age of 70 years in 112 out of 183 countries worldwide [17]. In 2020, prostate cancer (PCa) was the second most frequent cancer and the fifth cause of death related to cancer among men worldwide [18]. PCa is the most frequently diagnosed cancer in 112 countries and represents 7.3% among all diagnosed cancers. It shows an incidence rate and a mortality of 14.1 and 6.8%, respectively [18]. Unlike PCa, the neuroendocrine tumors (NETs) are considered as a rare type of cancer with an incidence rate of 1 – 5 per 100 000 people diagnosed yearly in most European countries and United States in the past 20 years [19,20]. However, NETs are known to be asymptomatic and slow growing, therefore, an average of 52 months was reported between the first symptoms and the diagnosis, limiting treatment opportunities [21]. Furthermore, the high severity of NETs plays an important role in the quality of life of the patient. In fact, NETs can cause diarrhea, heartburn, peptic ulceration, rectal bleeding, abdominal pain, … [22]. Therefore, considering the high incidence of PCa and the severity of NETs, we proposed through the different chapters of this thesis, multiple strategies to improve diagnosis techniques for an early detection and treatment methods for an efficient therapy of those cancers.

***Frequently used techniques for diagnosis and treatment of PCa***

The high incidence of PCa involves early detection and diagnosis to prevent death or suffering of the patient. Prostate biopsy remains the main method to confirm the presence of cancer tissue, however, statistical analysis showed that this strategy mises 21 – 28% of prostate cancers. Therefore, several biomarkers were introduced to limit the false-negatives results [23]. The prostate-specific antigen (PSA) is a natural biomarker secreted by the prostate epithelial cells; and a risk of prostate cancer can be considered when an increase in the PSA levels is observed (> 4.0 ng/mL) [24]. Nevertheless, there is no clear consensus on the PSA levels to confirm the presence of cancer tissue. Men with PSA levels higher than 4.0 ng/mL might not present a risk of PCa, while others with lower PSA levels might develop PCa. Additionally, imaging techniques were involved and optimized to enhance the diagnosis performance of PCa. Among them, MRI, was found to be accurate, reproducible, and non-inferior to traditional biopsy in the detection of clinically important prostate cancers [23].

Although, active surveillance is the method of choice for many patients presenting low risk of PCa (PSA levels < 10 ng/mL), other treatment strategies for advanced disease were introduced in clinical trials. Chemotherapy is one of the methods used for treatment of PCa. Mitoxantrone, was the first chemotherapeutic agent to be approved by FDA for the treatment of metastatic PCa. However, different clinical trials showed that the drug provided a palliative effect more than improving the overall survival of patients [25]. On the other hand, further studies showed that significant overall survival was observed for patients treated with docetaxel [26]. Chemotherapy can be employed for the treatment of PCa patients, however the frequently encountered side effects can be considered as a limiting factor. In fact, due to the use of toxic agents, chemotherapy can lead to hair loss, diarrhea, loss of appetite, mouth sores, … Therefore, extensive research was conducted to identify new treatment strategies with less side effects.

Prostate-specific membrane antigen (PSMA) was identified as an overexpressed biomarker by the PCa cells, therefore; it was used as a target for the treatment of advanced PCa patients. First, [$^{177}$Lu]Lu-J591, a radiolabeled humanized monoclonal antibody, was used to target PSMA, however, side effects such as myelosuppression was reported. Later, PSMA-617 and PSMA I&T were introduced as small-molecule inhibitors of PSMA leading to better therapeutic effect and less side effects [27]. Thus, PSMA moieties can be used for radioligand imaging ([$^{68}$Ga]Ga-PSMA) and therapy ([$^{177}$Lu]Lu-PSMA) of PCa. In 2022, [$^{177}$Lu]Lu-PSMA-617 was approved by FDA for the treatment of patients with metastatic castration-resistant prostate cancer (mCRPC) who have received other treatments (e.g., chemotherapy). However, the endogenous expression of PSMA in healthy organs (e.g., salivary glands, kidneys, ...), constitutes a dose limiting factor for the use of PSMA moieties in radioligand therapy of PCa [28]. Furthermore, it was reported in the literature that the high expression of PSMA is usually related to late stages of PCa. On the other hand, the gastrin releasing peptide receptor (GRPR) was identified as another biomarker expressed in early stages of PCa. This makes the receptor an interesting target for the treatment of early stages of PCa using radionuclide therapy. However, endogenous expression of GRPR can be found in the pancreas making it of concern to some studies. Nonetheless, although the initial pancreatic uptake is high, it decreases rapidly overtime whereas the tumor retention of the radiopharmaceutical is longer [29].

Surgery is the main method of treatment for patients with localized PCa [30]. Radical prostatectomy was found to provide survival benefits and lower the risk of development of metastatic disease, consequently, patients treated with surgery presented less bone metastases. Thus, radical prostatectomy offered a curative solution for patient with localized disease and a survival benefit for those with advanced disease. However, several studies showed that PCa recurrence after curative intend can affect 30 – 50% of treated patients probably due to the positive surgical margins encountered during surgery [31]. Therefore, we proposed a strategy to help optimizing prostatectomy by a better delineation of the surgical margins to avoid disease recurrence. Besides, due to the high expression of GRPR in early stages of PCa, we based our research in developing fluorescent probes based on GRPR antagonists.



### GRPR for PCa targeting

GRPR, also known as bombesin 2 (BB2), is a seven transmembrane receptor belonging to the G protein-coupled receptor (GPCR) superfamily [32,33]. The gastrin releasing peptide (GRP) is a natural neuropeptide binding to GRPR and characterized by a peptide sequence containing 27-amino acids [32]. GRP, initially isolated from the porcine stomach, is the mammalian homologue of the amphibian 14-amino acids peptide bombesin (pyroglutamic acid-glutamine-arginine-leucine-glycine-asparagine-glutamine-tryptophan-alaninevaline-glycine-histidine-leucine-methionine-$NH_2$) [33]. GRP and bombesin share the same seven C-terminal amino acids sequence, and the peptide sequence responsible to bind to GRPR is BBN[7 – 14] (Figure. 2 A) [32,33]. GRPR is broadly distributed over the human body and can be found mainly in the central nervous system (CNS), the gastrointestinal tract and other organs. The expression of GRPR by the CNS plays an important role in the emotional responses, social interaction, memory and feeding. GRPR was widely studied and reported to be highly expressed in head and neck, lung, kidney, colon, ovarian, breast and prostate cancers [34,35]. Regarding PCa specifically, several studies showed that GRPR is expressed in 63 – 100% of PCa [36,37]. The high expression of the receptor makes it an ideal target for imaging and therapy of PCa tumors. Therefore, extensive research was carried out including the synthesis, evaluation, and optimization of several GRPR ligands [38]. Those ligands are known to be either GRPR agonists or antagonists. The agonist or antagonist character of a peptide is very often correlated to its ability to internalize or not into the cancer cell, respectively. This property is mainly dictated by the chemical modifications performed on the C-terminal of the BBN[7 – 14] peptides. However, for other peptides, there is no clear explanation reporting the identification of the chemical function responsible to induce the agonist or antagonist property to the tracer. Unlike GRPR agonists, GRPR antagonists are known to block the signaling cascade involved in the biological activity of the biomarker, mostly tumor proliferation [38].

Several preclinical and clinical studies were carried out with GRPR agonists, such as; [$^{177}$Lu]Lu-AMBA and [$^{18}$F]F-FP-MAGBBN [39,40]. GRPR antagonists, such as; [$^{177}$Lu]Lu-NeoB, [$^{111}$In]In-JMV4168, [$^{68}$Ga]Ga-SB3, [$^{68}$Ga]Ga-NOTA-P2-RM26 and [$^{111}$In]In-NOTA-P2-RM26, [$^{68}$Ga]Ga-RM2 and [$^{68}$Ga]Ga-Probomb1, were also evaluated [41–43]. Several studies showed the higher potential of GRPR antagonists over GRPR agonists when complexed to a radiometal [44,45]. However, it was demonstrated that fluorine-18 radiolabeled GRPR agonists outperformed antagonists in terms of receptor mediated accumulation in the cancer cells [40]. Nonetheless, considering the high binding affinity to GRPR and the ability of the antagonists to prevent the molecular signaling cascade, we concentrated our attention in this thesis on the GRPR antagonist, NeoB.

***Neuroendocrine tumors: staging, imaging, and therapy***

NETs represent most of the neuroendocrine neoplasms (NENs) and are characterized to be slow growing; therefore, their diagnosis is usually difficult to carry out. Gastroenteropancreatic NETs (GEP NETs) constitute 50 – 70% of all NETs [20]. GEP NETs are graded by the WHO in three main types: G1, slow evolving tumors; G2, heterogeneous group with well-differentiated aggressive tumors; and G3, characterized by poorly differentiated carcinomas with aggressive behavior and poor survival. According to the European Neuroendocrine Tumor Society and the American Joint Committee on Cancer/Union for International Cancer Control, stage 0 to IIIa correspond to non-metastatic tumors, IIIb are tumors with nodal involvement and stage IV represents the distant metastasis [46–48]. In general, NETs have tendency to metastasize to the liver and skeleton. Therefore, for an efficient therapy, it is important to evaluate the tumor staging precisely.

Diagnosis of NETs is usually carried out through multiple imaging techniques, such as MRI, CT, PET using 2-deoxy-2-[$^{18}$F]fluoro-D-glucose ([$^{18}$F]FDG) or Ga-labeled DOTA-TATE/ DOTA-TOC and metaiodobenzylguanidine (MIBG) for SPECT imaging [49,50]. The conventional imaging techniques, CT and MRI, offer precise information on the location of NETs, but they are of limited value with regard to the functionality of the disease. In fact, CT presents low sensitivity in the detection of bone metastasis and due to the small field of view of MRI, it is usually used for the evaluation of a specific body area rather than the whole-body imaging. Additionally, CT and MRI offer limited information on the detection of small nodal metastases. On the other hand, thanks to the high sensitivity and specificity of PET and SPECT imaging, those modalities offer histologic diagnosis helping to identify the stage of the disease [51]. Consequently, radionuclide imaging presents a significant advantage over the radiological imaging techniques by providing functional whole-body imaging after a single injection of radioligand [52].

Treatment of NETs is well established using radionuclide-based therapy modalities such as MIBG radiolabeled with iodine-131. In fact, it was reported that [$^{131}$I]MIBG is one of the effective drugs for the treatment of NETs. However, it also causes multiple side effects such as hematological toxicity and severe infections after treatment [53]. Furthermore, recurrence might be observed for patients in stage III and IV. This leads to the use of aggressive and more radical methods for further treatment namely high doses of chemotherapeutics, or high doses of [$^{131}$I]MIBG that might be associated with irreversible bone marrow depression. In few cases, surgery can offer the optimal treatment solution mainly to the well-differentiated gastrointestinal NETs (GI NETs) [54]. Another approach that confirmed its efficacy for the treatment of NETs is peptide receptor radionuclide therapy (PRRT) using the FDA approved radiopharmaceutical [$^{177}$Lu]Lu-DOTA-TATE [55,56]. In fact, many clinical trials reported the efficiency of PRRT for the therapy of NETs, however, resistance to the treatment and recurrence of the disease can occur. Therefore, we investigated optimized approaches to improve the therapeutic index of PRRT. In order to achieve our goal, our research was based on targeting the somatostatin receptor subtype 2 (SSTR2) highly expressed by NETs.

SSTR2 for NETs targeting

NETs are known to express five subtypes of the somatostatin receptors (SSTR 1 – 5) [57,58]. The somatostatin receptors are part of the GPCR superfamily with 7 transmembrane domains. SST receptors are naturally expressed by various organs in the human body including retina and brain [59]. The 5 subtypes of the SSTRs bind to the naturally secreted peptides somatostatin-14 (SST-14) and somatostatin-28 (SST-28). SST-14 was isolated first in 1973 from bovine hypothalamic extracts, while SST-28 was described later in 1980 [59,60]. SST-14 (Figure. 2 B) exhibits low nanomolar affinity to SSTR1 – 4, while SST-28 binds preferably to SSTR5. The binding of SST-14 and SST-28 to SSTRs results in a large biological activity such as inhibition of the gastrointestinal secretion, cell proliferation and neurotransmission [60].

SSTRs can be identified in various type of cancers, however, SSTR2 is the most prevalent. SSTR2 was associated to meningiomas, bronchopulmonary carcinoids, gliomas and in GEP NETs [61,62]. Several studies showed that SSTR2 is overexpressed in more than 80% of GEP NETs [63,64]. Since an anti-cell proliferation effect is observed when SST-14 or SST-28 are bound to SSTRs, treatment of SSTR-positive tumors with SST peptides became an interesting approach. However, both peptides are known to have very short half-life in vivo (< 3 min) limiting their potential as therapeutics [65]. Nonetheless, this motivated biochemists to develop and optimize somatostatin analogs for SSTRs-targeted therapy. Consequently, several somatostatin analogs were synthesized and evaluated; among them, the most promising agonists (octreotide, lanreotide and pasireotide) [66,67]. The somatostatin agonists are characterized by their ability to internalize upon binding to the receptor. Octreotide, displaying high affinity to SSTR2 and SSTR5, was approved by FDA for the treatment of carcinoid tumors, acromegaly, and vasoactive intestinal tumors [68,69]. Its elaborated peptide sequence (containing a sulfur bridge, a D-tryptophan and a phenylalanine incorporated on its N-terminal) made it more resistant to metabolic degradation and thus increased its bioavailability in vivo compared to the natural somatostatin [65]. Then, [$^{111}$In]In-DTPA-octreotide was approved by FDA for SPECT imaging of SSTR2-positive tumors [70]. However, radiolabeling of octreotide analogs with DTPA offered access to a limited number of radioisotopes. Therefore, extensive research was carried out to equip octreotide with a DOTA chelator. The most known octreotide analog carrying a DOTA chelator is DOTA-Tyr$^{3}$-octreotate or more commonly named DOTA-TATE.

Although, treatment of NETs with somatostatin agonists revealed positive outcomes, several researchers showed that somatostatin antagonists [71,72], such as [$^{177}$Lu]Lu-DOTA-LM3, [$^{111}$In]In-DOTA-BASS and [$^{177}$Lu]Lu-OPS201 (also known as [$^{177}$Lu]Lu-DOTA-JR11), could outperform the agonists [73–75]. The binding affinity of DOTA-JR11 to SSTR2 is weaker than the affinity of the agonist DOTA-TATE, especially when complexed to indium and gallium [15]. However, few head-to-head comparisons demonstrated that DOTA or NODAGA-JR11 were superior to DOTA-TATE [76,77]. In fact, it was reported that JR11 better detects metastases and provides a better tumor-to-background ratio compared to DOTA-TATE. This is probably due to the ability of the SSTR2 antagonist to bind to more binding sites of the receptor compared to the agonist. Furthermore, it was reported that antagonists, in general, can bind to the active and non-active conformations of the receptor unlike agonists that only bind to the active conformation of the receptor. Consequently, due to the aforementioned reasons, the research conducted in this thesis consisted of introducing novel approaches to improve the therapeutic index of the somatostatin antagonist DOTA-JR11. To achieve this goal different strategies were explored, such as improving the bioavailability of the peptide, or exploring a more efficient radionuclide therapy based on the use of more toxic radioisotopes that can induce a more efficient DNA damage (e.g., alpha emitters).

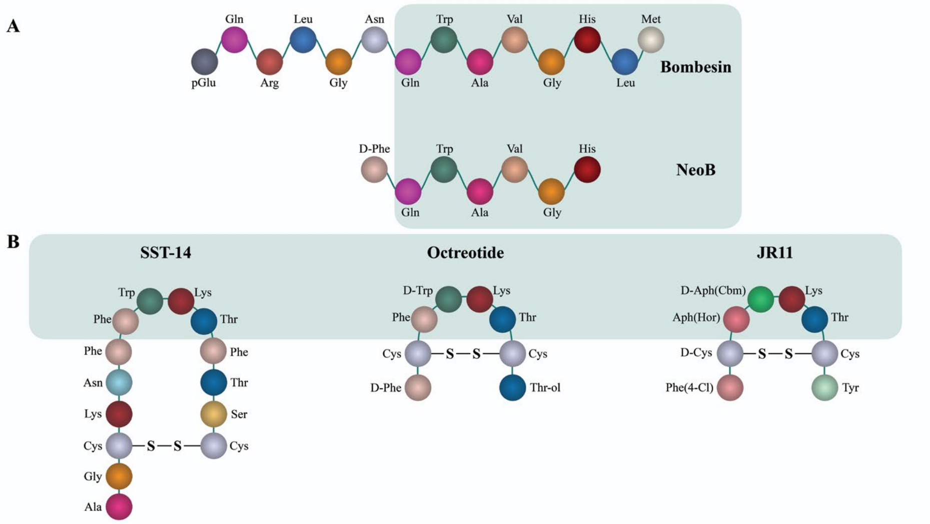


**Figure 2:** The peptide sequences of A) bombesin and NeoB and B) the somatostatin analogs SST-14, octreotide and JR11. The light green area represents the amino acids sequence responsible for binding to A) GRPR and B) SSTR2.

## New approaches in the design of radiopharmaceuticals for image guided-surgery of PCa and targeted radionuclide therapy of NETs

### *Bioorthogonal reactions*

Chemical reactions are usually performed in organic solvents and kept away from oxygen and water that might alter the efficiency of the reaction. However, over the past few years, there was a need to find selective chemical reactions occurring in a complex media, such as biological system. Thus, bioorthogonal reactions were introduced by Carolyn Bertozzi and coworkers in the beginning of the 2000 s [78,79]. This discovery was awarded a Nobel prize in chemistry in 2022, shared between Carolyn Bertozzi, Karl Barry Sharpless and Morten Meldal. The bioorthogonal reactions are based on a specific type of chemical reactions named as click reactions. The click reactions are characterized by their ability to be stereospecific, provide high yields and generate inoffensive and biochemically stable products [80,81]. Additionally, to those characteristics, a bioorthogonal reaction should be in vivo compatible (Figure. 3). The first click reaction introduced in the literature was discovered by Staudinger and Meyer in 1919 [81]. However, due to the slow reaction kinetics ($10^{-3}$ $M^{-1}$ $s^{-1}$) and sensitivity of the generated product towards oxidation, extensive research was carried out to find new click reactions with better properties. The azide-alkyne cycloaddition was first introduced by Huisgen, but the slow reaction kinetics made it incompatible for chemical reactions occurring in the biological environment. Hence, the reaction was optimized, and the copper catalyzed azide-alkyne cycloaddition (CuAAC) was introduced in 2002 by Sharpless and Meldal [82,83]. Nonetheless, due to the cytotoxicity of copper, the strain-promoted azide-alkyne cycloaddition (SPAAC) was developed and introduced by Bertozzi and coworkers in 2004 [84]. SPAAC exhibited 100-fold faster kinetics compared to the Staudinger ligation, however, it is not perfectly bioorthogonal due to the ability of the cyclooctyne ring to react with other functional groups present in the biological system. Later, the fastest bioorthogonal reaction known so far was introduced by Blackman and coworkers in 2008 [85]. The invers electron-demand Diels-Alder reaction (IEDDA), also called tetrazine ligation, is fully biorthogonal, generate a stable product, and has very fast reaction kinetics ($1 – 10^6$ $M^{-1}$ $s^{-1}$).

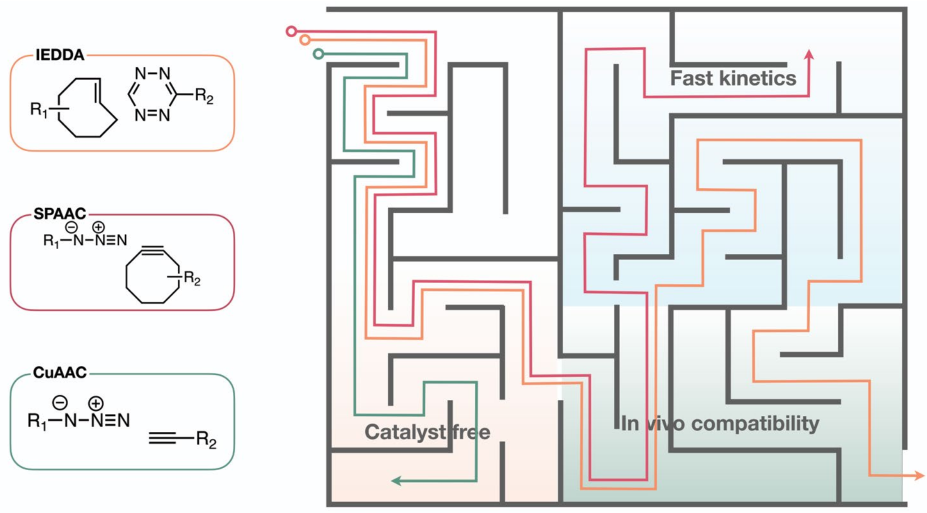


**Figure 3:** Schematic representation of the three main checkpoints (presence of a catalyst, kinetics, and in vivo compatibility) of a successful bioorthogonal reaction.

Bioorthogonal reactions showed their potential in studies aiming at following specific biological activities in vitro and in vivo [86]. However, over the past 10 years, the number of publications concerning CuAAC and SPAAC reached a plateau compared to IEDDA, where the number of accepted manuscripts is in constant increase. This is probably due to the fast kinetics of the tetrazine ligation compared to the other bioorthogonal reactions.

Bioorthogonal reactions were subject to extended research and can be applied to constitute building blocks for drug delivery (e.g., “click to release”); pretargeting applications; tracking active enzymes (activity-based protein profiling (ABPP)) and others [87–89].

Due to the importance gained by the IEDDA reaction over the past years in different domains, we report in **Chapter 2** a detailed review resuming the recent applications of the reaction. The fast kinetics and chemoselectivity of the reaction helped to establish a versatile synthesis of dual-labeled imaging probes described in **Chapters 3** and **4**. In **Chapter 5**, the chemoselectivity, orthogonality and the catalyst free character of the SPAAC played an important role in the constitution of a building block strategy.

***Dual-modality probes for image guided-surgery of PCa***

PET and SPECT coupled to either MRI or CT are the two main imaging techniques used in the field of nuclear medicine. Primary diagnosis and therapy monitoring is usually carried out using PET or SPECT radioisotopes (e.g., gallium-68, fluorine-18, indium-111, ...).

Optical imaging is usually based on the use of near infrared (NIR) fluorescent dyes (e.g., rhodamine and cyanine analogs, ProSense750, Sip650, indocyanine green (ICG) and others) [90–92]. A NIR fluorescent dye may obey to different criteria to be considered as an ideal candidate for optical imaging. The optimal probe should present an emission wavelength between 700 and 900 nm, should have a high quantum yield (~ 1.0 = 100%), must be soluble in aqueous solution, present low photobleaching, no or very low non-specific binding, a signal-to-background ratio as high as possible, should present a very low toxicity and be rapidly cleared upon administration [93].

ICG together with methylene blue (MB) are the only fluorescent probes approved by FDA. Nevertheless, cyanine dyes were largely explored and applied in different in vitro and in vivo studies [91,94]. Several other studies showed the good potential of IRDye800CW coupled to divers biovectors, in image guided surgery of PCa [95,96]. A recent review published by Liu and coworkers reports the clinical status of different fluorescent probes [97].

The aim of our study presented in **Chapters 3** and **4** was to combine radioactive and optical imaging to minimize the positive surgical margins usually encountered during the standard prostatectomy and leading to disease recurrence [98]. In fact, fluorescence-guided surgery is widely applied for real-time intraoperative imaging in the surgical field. Precise removal of the cancer tissue can be achieved by coupling a fluorescent dye to the biovector targeting the receptor overexpressed by the cancer cells. However, the optical imaging has a high spatial resolution but a low tissue penetration limiting its potential. Therefore, the high sensitivity of the radioactive imaging help to provide precise information for preoperative imaging on the localization and the depth of the cancer tissue, consequently helping to overcome the limitation of optical imaging. A recent study reported by Pogoto and coworkers report the evaluation of a GRPR targeting fluorescent biovector, bombesin-sulfo cyanine 5.5 (BBN-sCy5.5). The authors evaluated the potential of the probe, and the results showed that the fluorescent dye helped to precisely localize the malignant tissue [99]. Zhang and colleagues reported the evaluation of a bimodal probe based on PET and fluorescent imaging for prostate cancer, [$^{68}$Ga]Ga-HZ220. In fact, the GRPR antagonist, RM2 was coupled to a DOTA chelator to allow radiolabeling with the PET radioisotope gallium-68, and a IRDye 650 for the fluorescent imaging. The dual labeled probe showed lower binding affinity to GRPR compared to DOTA-RM2. Additionally, lower tumor uptake was reported for [$^{68}$Ga]Ga-HZ220 compared to [$^{68}$Ga]Ga-DOTA-RM2 (5.50 and 9.14% ID/g, respectively). However, the specificity of the probe towards the receptor was confirmed using a blocking group. Colocalization of the radioactive and the fluorescent signals was reported to demonstrate the potential of the probe for further clinical translations [100]. Besides, a first in human study of a dual-modality PET and optical imaging probe, [$^{68}$Ga]Ga-IRDye800CW-BBN, was reported by Li et al. for glioblastomas. In fact, the expression of GRPR in the CNS helped to implement this technique in image-guided surgery of brain tumors. The authors reported a correlation between the radioactive and the fluorescent uptake affirming the specificity of the probe to the receptor. Furthermore, the dual-modality probe was well tolerated and safe preoperatively and intraoperatively [95].

Due to the potential of the above-mentioned studies, in **Chapters 3** and **4**, we focused our attention on the design, synthesis and evaluation of four dual-modality imaging probes for image guided surgery of PCa. Our NeoB analogs were equipped with a DOTA chelator for radioactive imaging and a sulfo cyanine 5 (sCy5) fluorescent dye for optical imaging. In fact, sCy5 was chosen due to its small size, high absorption coefficient and acceptable quantum yield (0.27) resulting in adequate brightness.

***Building blocks for simplified and straightforward synthesis***

The building blocks strategy, also called the modular build-up approach, allows the obtention of diversely functionalized bioconjugates based on the conjugation of multiple molecules in one single step. In fact, multifunctionalized molecules can be obtained using the usual coupling strategies (e.g., amide bound). The incorporation of a lysine into the peptide sequence of different biovectors offers two attachment points that can be used to introduce two different functional groups. This strategy was applied in different studies [101–103]. However, this synthetic pathway might be complex and hampered by steric hindrances leading to low chemical yields. Furthermore, conjugation of prosthetic groups to an existing molecule via an amide bound might be challenging if multiple reactive amine or carboxylic acid groups are present. Additionally, incorporation of a chemical modification into a natural amino acid (e.g., lysine) can affect the biochemical property of the biomolecule [104]. Therefore, to overcome these limitations, the building block approach offers selective and site-specific conjugation with faster kinetics and high chemical yields. Moreover, once a building block approach is established, the same strategy can be applied to other molecules [105,106].

To construct a building block and introduce multiple functional groups into a biovector, different studies introduced the development of a multifunctional single-attachment-point (MSAP) agent. In fact, Garanger et al. reported the synthesis of bifunctional and trifunctional MSAP agents [107]. The bifunctional MSAP agent was functionalized with DTPA and NBD fluorochrome, while the trifunctional MSAP agent carried DTPA, fluorescein and a PEG linker. The authors demonstrated the utility of the bifunctional MSAP agent by its conjugation to the RGD peptide presenting high affinity to integrins. Additionally, the authors demonstrated the advantage of the trifunctional MSAP agent by reacting it with the surface of gold nanoparticles. The authors sought that MSAP agents could be commercialized for efficient and reproductible synthetic pathways. Besides, Chen and coworkers developed a MSAP agent functionalized with a DOTA chelator and sulfo cyanine 5 fluorescent dye [108]. The newly developed agent was conjugated to an acetazolamide-based small molecule and NeoB targeting the carbonic anhydrase IX (CAIX) and GRPR, respectively. The authors indicated that multifunctionalization of diverse biomolecules can be easier with a MSAP agent compared to other strategies.

Due to the promising potential of the MSAP agents in providing a straightforward and orthogonal synthesis, we introduced the design and development of a new MSAP agent in **Chapter 5**. This molecule was functionalized with a DOTA chelator and an albumin binder or a transcyclooctene (TCO) moiety. Conjugation of the MSAP agent to the biovector was established through the thiol-maleimide Michael addition.

***Albumin binding moieties for improved radionuclide therapy***

Albumin is a large protein (~ 66 kDa), highly abundant in the human serum with a concentration of 35 – 50 mg/mL [109]. The human serum albumin (HSA) is constituted of three domains, I, II and III, and each domain is divided in two subdomains A and B. Two principal sites, I and II are responsible for binding to HSA and are located in the hydrophobic subdomains IIA and IIIA [110]. HSA is mainly synthesized by the liver (~ 13.9 g/day) and has a half-life of approximately19 days [109,111]. The protein is known to bind to diverse endogenous (e.g., fatty acids, steroids ...) and exogenous (e.g., ibuprofen, warfarin ...) molecules; and it is involved in transporting ions in the blood circulation (e.g., copper, zinc, calcium ...) [109,112].

Considering the relatively long half-life of HSA and its abundance in the blood, several studies aimed to increase the blood residence of small molecules by binding to albumin. In fact, several albumin binding moieties were introduced in the literature to improve the bioavailability of bioconjugates [113]. Evans Blue is one of the interesting albumin binding moieties introduced recently. It was coupled to the somatostatin agonist TATE (EB-TATE), and the results showed that the tumor uptake was increased overtime suggesting a longer residence time in the blood circulation [114,115]. The same study reported that the SSTR2 positive tumor was completely eradicated for mice treated with 7.4 MBq of [$^{90}$Y]Y-EB-TATE [114]. Another extensively studied candidate is the 4-(4-iodophenyl)butanoic acid. This albumin binder was coupled to PSMA (HTK01169), folic acid (cm13) and TATE (Albutate) [116–119]. The results showed that the bioavailability of the bioconjugates was improved compared to the controls and longer residence in the blood circulation was clearly observed. Siwowska and coworkers revealed that the incorporation of a linker (e.g., $NH_2$-$PEG_{11}$-COOH or 7-aminoheptanoic acid) between the folic acid and the albumin binder can radically influence the biodistribution properties of the radioligand [118]. However, van Tiel *et al.* showed that the addition of an albumin binder does not always affect the biodistribution profile of a biovector positively. In fact, the dosimetry studies showed that higher absorbed dose was found in the non-targeted organs (e.g., bone marrow) limiting the application of [$^{177}$Lu]Lu-Albutate in further therapy studies [116]. On the other hand, Kuo and coworkers reported that [$^{177}$Lu]Lu-HTK01169 led to a 8.3-fold higher tumor absorbed dose compared to [$^{177}$Lu]Lu-PSMA-617. However, the same radiotracer resulted in 17.1-fold higher absorbed dose to the kidneys [119]. Therefore, the same group reported a library of albumin binding moieties based on optimized lipophilicity [120]. Replacement of the iodo substituent in the previous albumin binder ([$^{177}$Lu]Lu-HTK01169) by a chloride ([$^{177}$Lu]Lu-HTK03121) or a methoxy ([$^{177}$Lu]Lu-HTK03123) group positively impacted the biodistribution profile of the new PSMA analogs. Both radioligands showed a 12-fold higher tumor absorbed dose and a 2-fold higher tumor-to-kidney absorbed dose compared to [$^{177}$Lu]Lu-PSMA-617.

In **Chapter 6**, owing to the extensive research on substituted phenylbutanoic acid albumin binders, we have prepared and evaluated two long-acting DOTA-JR11 analogs for the treatment of NETs.

It is important to mention that other promising albumin binding moieties were recently introduced in the literature. In fact, it was shown that dansylated amino acids (e.g., dansylproline and dansylglycine) have good affinity to HSA and can be used to improve the pharmacokinetics of bioconjugates [110,121]. Additionally, a recent study showed the potential of fatty acids in the improvement of blood circulation of peptides [122].

***Targeted Alpha Therapy (TAT)***

Alpha particles were discovered in 1898 by Rutherford and were described as helium nuclei. Those particles are known to be 8000-fold larger than beta particles (electrons). Thus, when a radionuclide decays by the alpha pathway, it results in the deposit of very high energy in a limited short distance. Alpha particles have a range in tissue of 40 – 100 µm and a linear energy transfer (LET) of 100 keV/µm (Figure. 4) [123]. Due to the high energy involved in the alpha decay, several studies used alpha particles in the treatment of cancers. Although preclinical studies were reported for few decades, the first clinical trial using TAT was introduced in the literature in 1999 with the first patient treated in 1995 [124]. Later, TAT was applied to different type of cancers, such as, mCRPC, metastatic paragangliomas and NETs [125–127].

Due to the high LET of the alpha radiation, DNA double-strand breaks can be achieved with few alpha particles only [128]. Furthermore, unlike beta emission, alpha particles do not require the presence of oxygen to cause efficient DNA damage. In fact, in regular PRRT, DNA damage is caused by the generation of reactive oxygen species (ROS) produced by water radiolysis that interact with endogenous cellular components such as DNA. However, in TAT, the DNA damage is directly caused by the alpha particles. Additionally, it is well known that in solid tumor's microenvironment, hypoxic cells can be generated due to the accelerated proliferation and insufficient blood supply resulting in poor oxygenation [129]. Consequently, the presence of hypoxic cells can cause resistance towards PRRT resulting in limited therapeutic outcome. Therefore, TAT can present a better potential than PRRT in the treatment efficacy of solid tumors such as NETs.

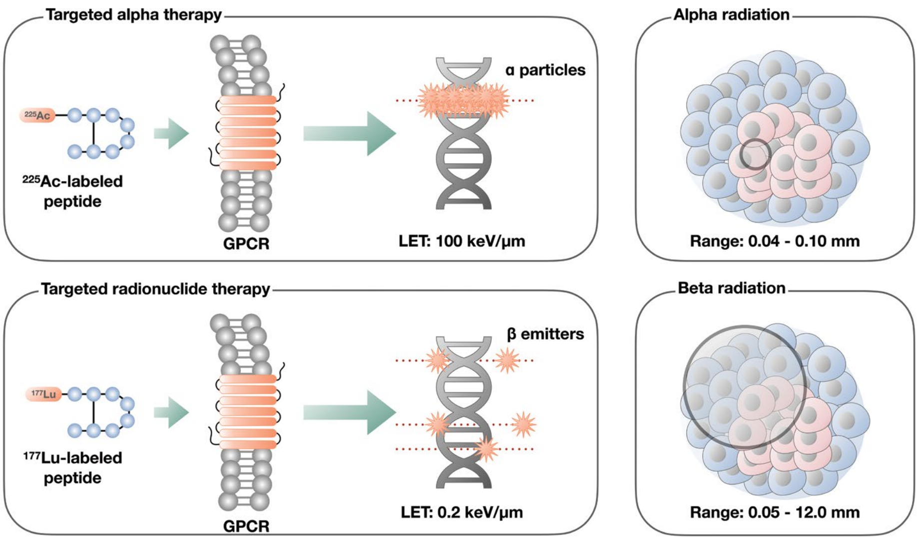


**Figure 4:** Schematic representation of targeted alpha therapy compared to targeted radionuclide therapy. Figure adapted from [130].

Many alpha emitting radioisotopes can be considered for TAT (Table. 2). However, due to either too long or too short half-life, complicated decay pathways and availability, only few candidates are frequently employed. To prove the efficacy of TAT, the potential of different alpha emitting radionuclides was evaluated. One of the promising alpha emitting radioisotopes is bismuth-213. Dekempeneer and coworkers complexed bismuth-213 to a single-domain antibody fragment ([$^{213}$Bi]Bi-DTPA-sdAbs) to target the human epidermal growth factor 2 (HER2) overexpressed in ovarian cancer. Another preclinical study reported by Chan and colleagues, [$^{213}$Bi]Bi-DOTA-TATE was used for TAT of NETs. In both studies, the authors reported an increased overall survival confirming the efficacy of TAT for the treatment of different types of cancers [127,131]. However, the short half-life of bismuth-213 ($t_{1/2}$ = 45.6 minutes) limits its applications in further therapy studies [123]. Another promising candidate that showed very promising future for TAT, especially for patients refractory to PRRT, is actinium-225. Ballal and coworkers and Yadav and colleagues used [$^{225}$Ac]Ac-DOTA-TATE in the treatment of GEP NETs and metastatic paragangliomas respectively. The authors reported the follow up of different patients that were previously treated with [$^{177}$Lu]Lu-DOTA-TATE and concluded by delineating the potential of TAT for the treatment of NETs [125,132].

Due to the promising potential reported for TAT in the treatment of NETs and the aforementioned advantages of DOTA-JR11 compared to DOTA-TATE, in **Chapter 7**, we evaluated [$^{225}$Ac]Ac-DOTA-JR11 in a preclinical model and compared the dosimetry with [$^{177}$Lu]Lu-DOTA-JR11.

**Table 2:** Frequently used alpha emitters for TAT, their daughters, half-lives, emission type, decay energy and adapted chelating agents [123,133].

| Parent radionuclide | Daughters | Half-life | Emission | Energy (MeV) | Chelating agents |
|---|---|---|---|---|---|
| $^{225}$Ac | $^{221}$Fr, $^{217}$At, $^{213}$Bi, $^{213}$Po, $^{209}$Tl, $^{209}$Pb | 9.9 d | 4 α, 3 $\beta^-$ | 5.8 | DOTA, DO3A, EDTA, DTPA, Macropa |
| $^{213}$Bi | $^{213}$Po, $^{209}$Tl, $^{209}$Pb | 45.6 min | 2 α, 3 $\beta^-$ | 5.8 | DOTA, DTPA |
| $^{212}$Pb | $^{212}$Bi, $^{212}$Po, $^{208}$Tl | 10.6 h | 2 α, 3 $\beta^-$ | 6.05 | DOTA, DTPA, TCMC, EDTA |
| $^{211}$At | $^{211}$Po, $^{207}$Bi | 7.2 h | 2 α, 2 Electron Capture | 5.9 | m-or p-$SnMe_3$-Bz, m-or p-$SnBu_3$-Bz |

## Thesis outline

Our aim in this thesis was to evaluate the potential of different chemical and radiochemical strategies intended to improve the diagnosis and therapeutic index related to the treatment of PCa and NETs. The thesis was divided in two sections. The first section consisted to evaluate the potential of multiple click reactions, and more specifically the IEDDA reaction for different applications. The second section was based on evaluating the potential of different therapeutic approaches to increase the treatment efficacy of PRRT.

The first part of the thesis aimed to investigate diverse applications of the bioorthogonal reactions. In **Chapter 2**, a detailed review on the bioorthogonal reactions and especially the IEDDA click reaction was reported. The fast kinetics of IEDDA, its bioorthogonal properties and the stability of the resulting product led us to study the potential of this reaction for different applications. In **Chapters 3** and **4**, we reported a versatile synthesis of dual-labeled imaging probes based on NeoB via the IEDDA reaction. In **Chapter 5** of the thesis, we reported the development of a MSAP agent intended for multifunctionalization of different biovetors based on a single step reaction. This approach was based on the use of different click reactions such as the SPAAC and the thiol-maleimide Michael addition.

In the second part of the thesis, we aimed to investigate the potential of different approaches to achieve a more efficient therapy of NETs. The first approach was based on the use of albumin binding moieties for enhanced bioavailability of DOTA-JR11 analogs. Thus, in **Chapter 6**, we studied the potential of two albumin binders for improved tumor uptake. On the other hand, the high incidence of treatment resistance and disease recurrence after traditional PRRT of NETs, led us to explore the benefit of TAT offered by the high LET of alpha particles compared to beta emitters. Therefore, in **Chapter 7**, [$^{225}$Ac]Ac-DOTA-JR11 was evaluated in a preclinical model. Dosimetry studies on organs of interest were conducted and a head-to-head comparison with [$^{177}$Lu]Lu-DOTA-JR11 was made.

## References


1. Weber WA, Czernin J, Anderson CJ, Badawi RD, Barthel H, Bengel F, et al. The future of nuclear medicine, molecular imaging, and theranostics. J Nucl Med 2020;61:263S–272S.
2. Patton JA, Turkington TG. SPECT/CT physical principles and attenuation correction. JNMT 2008;36:1–10.
3. Ziegler SI. Positron emission tomography: Principles, technology, and recent developments. Nucl Phys A 2005;752:679–687.
4. Berger A. Positron emission tomography. BMJ 2003;326:1449.
5. Townsend DW. Dual-modality imaging: Combining anatomy and function. J Nucl Med 2008;49:938–955.
6. Müller C, Schibli R. Single photon emission computed tomography tracer. vol. 187. 2013.
7. Pimlott SL, Sutherland A. Molecular tracers for the PET and SPECT imaging of disease. Chem Soc Rev 2011;40:149–162.
8. Wangler B, Schirrmacher R, Bartenstein P, Wangler C. Chelating Agents and their Use in Radiopharmaceutical Sciences. Mini Rev Med Chem 2011;11:968–983.
9. Ding X, Xie H, Kang YJ. The significance of copper chelators in clinical and experimental application. J Nutr Biochem 2011;22:301–310.
10. Cai Z, Anderson CJ. Chelators for copper radionuclides in positron emission tomography radiopharmaceuticals. J Label Compd Radiopharm 2014;57:224–230.
11. Marcu L, Bezak E, Allen BJ. Global comparison of targeted alpha vs targeted beta therapy for cancer: In vitro, in vivo and clinical trials. Crit Rev Oncol 2018;123:7–20.
12. Pouget JP, Georgakilas AG, Ravanat JL. Targeted and Off-Target (Bystander and Abscopal) Effects of Radiation Therapy: Redox Mechanisms and Risk/Benefit Analysis. ARS 2018;29:1447–1487.
13. Poot AJ, Lam MGEH, van Noesel MM. The Current Status and Future Potential of Theranostics to Diagnose and Treat Childhood Cancer. Front Oncol 2020;10:1–8.
14. Yordanova A, Eppard E, Kürpig S, Bundschuh RA, Schönberger S, Gonzalez-Carmona M, et al. Theranostics in nuclear medicine practice. Onco Targets Ther 2017;10:4821–4828.
15. Fani M, Nicolas GP, Wild D. Somatostatin receptor antagonists for imaging and therapy. J Nucl Med 2017;58:61S–66S.
16. Müller C, Bunka M, Haller S, Köster U, Groehn V, Bernhardt P, et al. Promising prospects for 44Sc-/47Sc-based theragnostics: Application of 47Sc for radionuclide tumor therapy in mice. J Nucl Med 2014;55:1658–1664.
17. Bray F, Laversanne M, Weiderpass E, Soerjomataram I. The ever-increasing importance of cancer as a leading cause of premature death worldwide. Cancer 2021;127:3029–3030.
18. Sung H, Ferlay J, Siegel RL, Laversanne M, Soerjomataram I, Jemal A, et al. Global Cancer Statistics 2020: GLOBOCAN Estimates of Incidence and Mortality Worldwide for 36 Cancers in 185 Countries. CA Cancer J Clin 2021;71:209–249.
19. Singh S, Granberg D, Wolin E, Warner R, Sissons M, Kolarova T, et al. Patient-reported burden of a neuroendocrine tumor (NET) diagnosis: Results from the first global survey of patients with NETs. Clin Oncol 2017;3:43–53.
20. Das S, Dasari A. Epidemiology, Incidence, and Prevalence of Neuroendocrine Neoplasms: Are There Global Differences? Curr Oncol Rep 2021;23:10–20.
21. Basuroy R, Bouvier C, Ramage JK, Sissons M, Srirajaskanthan R. Delays and routes to diagnosis of neuroendocrine tumours. BMC Cancer 2018;18:1–8.
22. Cives M, Strosberg JR. Gastroenteropancreatic Neuroendocrine Tumors. CA Cancer J Clin 2018;68:471–487.
23. Litwin MS, Tan HJ. The diagnosis and treatment of prostate cancer: A review. JAMA 2017;317:2532–2542.
24. Thompson IM, Ankerst DP. Prostate-specific antigen in the early detection of prostate cancer. CMAJ 2007;176:1853–1858.
25. Hurwitz M. Chemotherapy in Prostate Cancer. Curr Oncol Rep 2015;17:1–10.
26. Berthold DR, Pond GR, Soban F, De Wit R, Eisenberger M, Tannock IF. Docetaxel plus prednisone or mitoxantrone plus prednisone for advanced prostate cancer: Updated survival in the TAX 327 study. Clin Oncol 2008;26:242–245.

27. von Eyben FE, Roviello G, Kiljunen T, Uprimny C, Virgolini I, Kairemo K, et al. Third-line treatment and 177Lu-PSMA radioligand therapy of metastatic castration-resistant prostate cancer: a systematic review. EJNMMI 2018;45:496–508.
28. Klein Nulent TJW, Valstar MH, de Keizer B, Willems SM, Smit LA, Al-Mamgani A, et al. Physiologic distribution of PSMA-ligand in salivary glands and seromucous glands of the head and neck on PET/CT. Oral Surg Oral Med Oral Pathol Oral Radiol Endod 2018;125:478–486.
29. Lundmark F, Abouzayed A, Mitran B, Rinne SS, Varasteh Z, Larhed M, et al. Heterodimeric radiotracer targeting PSMA and GRPR for imaging of prostate cancer—optimization of the affinity towards PSMA by linker modification in murine model. Pharmaceutics 2020;12:1–15.
30. Kim EH, Bullock AD. Surgical Management for Prostate Cancer. Mo Med 2018;115:142–145.
31. Tourinho-Barbosa RR, Srougi V, Nunes-Silva I, Baghdadi M, Rembeyo G, Eiffel SS, et al. Biochemical recurrence after radical prostatectomy: What does it mean? International Braz J Urol 2018;44:14–21.
32. Roesler R, Schwartsmann G. Gastrin-releasing peptide receptors in the central nervous system: Role in brain function and as a drug target. Front Endocrinol 2012;3:1–12.
33. Lau J, Rousseau E, Zhang Z, Uribe CF, Kuo HT, Zeisler J, et al. Positron Emission Tomography Imaging of the Gastrin-Releasing Peptide Receptor with a Novel Bombesin Analogue. ACS Omega 2019;4:1470–1478.
34. Pu F, Qiao J, Xue S, Yang H, Patel A, Wei L, et al. GRPR-targeted Protein Contrast Agents for Molecular Imaging of Receptor Expression in Cancers by MRI. Sci Rep 2015;5:1–14.
35. Cornelio DB, Roesler R, Schwartsmann G. Gastrin-releasing peptide receptor as a molecular target in experimental anticancer therapy. Ann Oncol 2007;18:1457–1466.
36. Sun B, Halmos G, Schally A V., Wang X, Martinez M. Presence of receptors for bombesin/gastrin-releasing peptide and mRNA for three receptor subtypes in human prostate cancers. Prostate 2000;42:295–303.
37. Patel O, Shulkes A, Baldwin GS. Gastrin-releasing peptide and cancer. Biochim Biophys Acta - Rev Cancer 2006;1766:23–41.
38. Mansi R, Nock BA, Dalm SU, Busstra MB, van Weerden WM, Maina T. Radiolabeled bombesin analogs. Cancers (Basel) 2021;13:1–20.
39. Linder KE, Metcalfe E, Arunachalam T, Chen J, Eaton SM, Feng W, et al. In vitro and in vivo metabolism of Lu-AMBA, a GRP-receptor binding compound, and the synthesis and characterization of its metabolites. Bioconjug Chem 2009;20:1171–1178.
40. Yang M, Gao H, Zhou Y, Ma Y, Quan Q, Lang L, et al. 18 F-Labeled GRPR Agonists and Antagonists: A Comparative Study in Prostate Cancer Imaging. Theranostics 2012;1:220–229.
41. Bakker IL, Fröberg AC, Busstra MB, Verzijlbergen JF, Konijnenberg M, van Leenders GJLH, et al. GRPr antagonist 68Ga-SB3 PET/CT-imaging of primary prostate cancer in therapy-naive patients. J Nucl Med 2021;62:1517–1523.
42. Marsouvanidis PJ, Nock BA, Hajjaj B, Fehrentz JA, Brunel L, M'Kadmi C, et al. Gastrin releasing peptide receptor-directed radioligands based on a bombesin antagonist: Synthesis, 111in-labeling, and preclinical profile. J Med Chem 2013;56:2374–2384.
43. Varasteh Z, Velikyan I, Lindeberg G, Sörensen J, Larhed M, Sandström M, et al. Synthesis and characterization of a high-affinity NOTA-conjugated bombesin antagonist for GRPR-targeted tumor imaging. Bioconjug Chem 2013;24:1144–1153.
44. Lymperis E, Kaloudi A, Kanellopoulos P, Krenning EP, de Jong M, Maina T, et al. Comparative evaluation of the new GRPR-antagonist 111In-SB9 and 111In-AMBA in prostate cancer models: Implications of in vivo stability. J Label Compd Radiopharm 2019;62:646–655.
45. Cescato R, Maina T, Nock B, Nikolopoulou A, Charalambidis D, Piccand V, et al. Bombesin receptor antagonists may be preferable to agonists for tumor targeting. J Nucl Med 2008;49:318–326.
46. Deroose CM, Hindié E, Kebebew E, Goichot B, Pacak K, Taïeb D, et al. Molecular imaging of gastroenteropancreatic neuroendocrine tumors: Current status and future directions. J Nucl Med 2016;57:1949–1956.
47. Luo G, Javed A, Strosberg JR, Jin K, Zhang Y, Liu C, et al. Modified staging classification for pancreatic neuroendocrine tumors on the basis of the American Joint Committee on Cancer and European Neuroendocrine Tumor Society Systems. Clin Oncol 2017;35:274–280.

48. Klöppel G, Rindi G, Perren A, Komminoth P, Klimstra DS. The ENETS and AJCC/UICC TNM classifications of the neuroendocrine tumors of the gastrointestinal tract and the pancreas: A statement. Eur J Plant Pathol 2010;456:595–597.
49. Iravani A, Parihar AS, Akhurst T, Hicks RJ. Molecular imaging phenotyping for selecting and monitoring radioligand therapy of neuroendocrine neoplasms. Cancer Imaging 2022;22:1–20.
50. Desai H, Borges-Neto S, Wong TZ. Molecular Imaging and Therapy for Neuroendocrine Tumors. Curr Treat Options Oncol 2019;20:1–13.
51. Pollard J, McNeely P, Menda Y. Nuclear Imaging of Neuroendocrine Tumors. Surg Oncol Clin N Am 2020;29:209–221.
52. Li S, Beheshti M. The Radionuclide Molecular Imaging and Therapy of Neuroendocrine Tumors. Curr Cancer Drug Targets 2005;5:139–148.
53. Gulenchyn KY, Yao X, Asa SL, Singh S, Law C. Radionuclide Therapy in Neuroendocrine Tumours: A Systematic Review. Clin Oncol 2012;24:294–308.
54. Eto K, Yoshida N, Iwagami S, Iwatsuki M, Baba H. Surgical treatment for gastrointestinal neuroendocrine tumors. Ann Gastroenterol Surg 2020;4:652–659.
55. Kwekkeboom DJ, De Herder WW, Kam BL, Van Eijck CH, Van Essen M, Kooij PP, et al. Treatment with the radiolabeled somatostatin analog [177Lu- DOTA0,Tyr3]octreotate: Toxicity, efficacy, and survival. Clin Oncol 2008;26:2124–2130.
56. Das S, Al-Toubah T, El-Haddad G, Strosberg J. 177Lu-DOTATATE for the treatment of gastroenteropancreatic neuroendocrine tumors. Expert Rev Gastroenterol Hepatol 2019;13:1023–1031.
57. Patel YC. Somatostatin and Its Receptor Family. Front Neuroendocrinol 1999;20:157–185.
58. Kailey B, van de Bunt M, Cheley S, Johnson PR, MacDonald PE, Gloyn AL, et al. SSTR2 is the functionally dominant somatostatin receptor in human pancreatic-and-cells. Am J Physiol Endocrinol Metab 2012;303:1107–1116.
59. Ampofo E, Nalbach L, Menger MD, Laschke MW. Regulatory mechanisms of somatostatin expression. Int J Mol Sci 2020;21:1–15.
60. White BH, Whalen K, Kriksciukaite K, Alargova R, Au Yeung T, Bazinet P, et al. Discovery of an SSTR2-Targeting Maytansinoid Conjugate (PEN-221) with Potent Activity in Vitro and in Vivo. J Med Chem 2019;62:2708–2719.
61. Guenter R, Aweda T, Carmona Matos DM, Jang S, Whitt J, Cheng YQ, et al. Overexpression of somatostatin receptor type 2 in neuroendocrine tumors for improved Ga68-DOTATATE imaging and treatment. Surgery 2020;167:189–196.
62. He JH, Wang J, Yang YZ, Chen QX, Liu LL, Sun L, et al. SSTR2 is a prognostic factor and a promising therapeutic target in glioma. Am J Transl Res 2021;13:11223–11234.
63. Reubi JC, Krenning E, Lamberts SWJ, Kvols L. Somatostatin receptors in malignant tissues. J Steroid Biochem Mol Biol 1990;37:1073–1077.
64. Reubi JC, Kvols L, Krenning E, Lamberts SWJ. Distribution of somatostatin receptors in normal and tumor tissue. Metab 1990;39:78–81.
65. Cuevas-Ramos D, Fleseriu M. Somatostatin receptor ligands and resistance to treatment in pituitary adenomas. J Mol Endocrinol 2014;52:R223–R240.
66. Wolin EM. The expanding role of somatostatin analogs in the management of neuroendocrine tumors. J Gastrointest Cancer 2012;5:161–168.
67. Susini C, Buscail L. Rationale for the use of somatostatin analogs as antitumor agents. Ann Oncol 2006;17:1733–1742.
68. Lamberts SWJ, Hofland LJ. Octreotide, 40 years later. Eur J Endocrinol 2019;181:R173–R183.
69. Anthony L, Freda PU. From somatostatin to octreotide LAR: Evolution of a somatostatin analogue. Curr Med Res Opin 2009;25:2989–2999.
70. Westlin J. [111In-DTPA-D-Phe1]Octreotide scintigraphy in patients with carcinoid tumours: the predictive value for somatostatin analogue treatment. Eur J Endocrinol 1994;131:577–581.
71. Mansi R, Plas P, Vauquelin G, Fani M. Distinct in vitro binding profile of the somatostatin receptor subtype 2 antagonist [177 lu]lu-ops201 compared to the agonist [177 lu]lu-dota-tate. Pharmaceuticals 2021;14:1–12.

72. Nicolas GP, Mansi R, McDougall L, Kaufmann J, Bouterfa H, Wild D, et al. Biodistribution, pharmacokinetics, and dosimetry of 177Lu-,90Y-, and 111In-labeled somatostatin receptor antagonist OPS201 in comparison to the agonist 177Lu-DOTATATE: The mass effect. J Nucl Med 2017;58:1435–1441.
73. Baum RP, Zhang J, Schuchardt C, Müller D, Mäcke H. First-in-human study of novel SSTR antagonist 177Lu-DOTA-LM3 for peptide receptor radionuclide therapy in patients with metastatic neuroendocrine neoplasms: Dosimetry, safety and efficacy. J Nucl Med 2021;62:1571–1581.
74. Wild D, Fani M, Behe M, Brink I, Rivier JEF, Reubi JC, et al. First clinical evidence that imaging with somatostatin receptor antagonists is feasible. J Nucl Med 2011;52:1412–1417.
75. Beykan S, Dam JS, Eberlein U, Kaufmann J, Kjærgaard B, Jødal L, et al. 177Lu-OPS201 targeting somatostatin receptors: in vivo biodistribution and dosimetry in a pig model. EJNMMI Res 2016;6:1–9.
76. Rylova SN, Stoykow C, Del Pozzo L, Abiraj K, Tamma ML, Kiefer Y, et al. The somatostatin receptor 2 antagonist 64Cu-NODAGA-JR11 outperforms 64Cu-DOTA-TATE in a mouse xenograft model. PLoS One 2018;13:1–16.
77. Zhu W, Cheng Y, Wang X, Yao S, Bai C, Zhao H, et al. Head-to-head comparison of 68Ga-DOTA-JR11 and 68Ga-DOTATATE PET/CT in patients with metastatic, well-differentiated neuroendocrine tumors: A prospective study. J Nucl Med 2020;61:897–903.
78. Bertozzi CR. A decade of bioorthogonal chemistry. Acc Chem Res 2011;44:651–653.
79. Sletten EM, Bertozzi CR. Bioorthogonal chemistry: Fishing for selectivity in a sea of functionality. Angew Chem, Int Ed 2009;48:6974–6998.
80. Handula M, Chen KT, Seimbille Y. Iedda: An attractive bioorthogonal reaction for biomedical applications. Molecules 2021;26:1–20.
81. Staudinger H, Hauser E. Über neue organische Phosphorverbindungen IV Phosphinimine. Helv Chim Acta 1921;4:861–886.
82. Rostovtsev V V., Green LG, Fokin V V., Sharpless KB. A stepwise huisgen cycloaddition process: Copper(I)-catalyzed regioselective “ligation” of azides and terminal alkynes. Angew Chem, Int Ed 2002;41:2596–2599.
83. Tornøe CW, Christensen C, Meldal M. Peptidotriazoles on solid phase: [1,2,3]-Triazoles by regiospecific copper(I)-catalyzed 1,3-dipolar cycloadditions of terminal alkynes to azides. JOC 2002;67:3057–3064.
84. Agard NJ, Prescher JA, Bertozzi CR. A strain-promoted [3 + 2] azide-alkyne cycloaddition for covalent modification of biomolecules in living systems. J Am Chem Soc 2004;126:15046–15047.
85. Blackman ML, Royzen M, Fox JM. Tetrazine ligation: Fast bioconjugation based on inverse-electron-demand Diels-Alder reactivity. J Am Chem Soc 2008;130:13518–13519.
86. Kim E, Koo H. Biomedical applications of copper-free click chemistry: In vitro, in vivo, and ex vivo. Chem Sci 2019;10:7835–7851.
87. Bird RE, Lemmel SA, Yu X, Zhou QA. Bioorthogonal Chemistry and Its Applications. Bioconjug Chem 2021;32:2457–2479.
88. Meyer JP, Tully KM, Jackson J, Dilling TR, Reiner T, Lewis JS. Bioorthogonal Masking of Circulating Antibody-TCO Groups Using Tetrazine-Functionalized Dextran Polymers. Bioconjug Chem 2018;29:538–545.
89. van Onzen AHAM, Versteegen RM, Hoeben FJM, Filot IAW, Rossin R, Zhu T, et al. Bioorthogonal tetrazine carbamate cleavage by highly reactive trans-cyclooctene. J Am Chem Soc 2020;142:1–20.
90. Reja SI, Minoshima M, Hori Y, Kikuchi K. Near-infrared fluorescent probes: a next-generation tool for protein-labeling applications. Chem Sci 2021;12:3437–3447.
91. Levitus M, Ranjit S. Cyanine dyes in biophysical research: The photophysics of polymethine fluorescent dyes in biomolecular environments. Q Rev Biophys 2011;44:123–151.
92. Yuan L, Lin W, Yang Y, Chen H. Acid-Modulated Fluorescence ON/OFF Switching: Rational Design, Synthesis, Optical Properties, Theoretical Calculations, and Applications for Fluorescence Imaging in Living Animals. J Am Chem Soc 2012;134:1200–1211.
93. te Velde EA, Veerman T, Subramaniam V, Ruers T. The use of fluorescent dyes and probes in surgical oncology. EJSO 2010;36:6–15.
94. Sun C, Du W, Wang B, Dong B, Wang B. Research progress of near-infrared fluorescence probes based on indole heptamethine cyanine dyes in vivo and in vitro. BMC Chem 2020;14:1–28.
95. Li D, Zhang J, Chi C, Xiao X, Wang J, Lang L, et al. First-in-human study of PET and optical dual-modality image-guided surgery in glioblastoma using 68Ga-IRDye800CW-BBN. Theranostics 2018;8:2508–2520.

96. Lütje S, Rijpkema M, Franssen GM, Fracasso G, Helfrich W, Eek A, et al. Dual-modality image-guided surgery of prostate cancer with a radiolabeled fluorescent anti-PSMA monoclonal antibody. J Nucl Med 2014;55:995–1001.
97. Liu R, Xu Y, Xu K, Dai Z. Current trends and key considerations in the clinical translation of targeted fluorescent probes for intraoperative navigation. Aggregate 2021;2:1–23.
98. Lee S, Chen X. Dual-modality probes for in vivo molecular imaging. Mol Imaging 2009;8:87–100.
99. Pagoto A, Garello F, Marini GM, Tripepi M, Arena F, Bardini P, et al. Novel Gastrin-Releasing Peptide Receptor Targeted Near-Infrared Fluorescence Dye for Image-Guided Surgery of Prostate Cancer. Mol Imaging Biol 2020;22:85–93.
100. Zhang H, Desai P, Koike Y, Houghton J, Carlin S, Tandon N, et al. Dual-modality imaging of prostate cancer with a fluorescent and radiogallium-labeled gastrin-releasing peptide receptor antagonist. J Nucl Med 2017;58:29–35.
101. Koustoulidou S, Handula M, de Ridder C, Stuurman D, Beekman S, de Jong M, et al. Synthesis and Evaluation of Two Long-Acting SSTR2 Antagonists for Radionuclide Therapy of Neuroendocrine Tumors. Pharmaceuticals 2022;15:1–15.
102. Handula M, Verhoeven M, Chen K, Haeck J, Jong M De, Dalm SU, et al. Towards Complete Tumor Resection : Novel Dual-Modality Probes for Improved Image-Guided Surgery of GRPR-Expressing Prostate Cancer. Pharmaceutics 2022;14:1–18.
103. Zhang H, Desai P, Koike Y, Houghton J, Carlin S, Tandon N, et al. Dual-modality imaging of prostate cancer with a fluorescent and radiogallium-labeled gastrin-releasing peptide receptor antagonist. J Nucl Med 2017;58:29–35.
104. Zeglis BM, Emmetiere F, Pillarsetty N, Weissleder R, Lewis JS, Reiner T. Building blocks for the construction of bioorthogonally reactive peptides via solid-phase peptide synthesis. ChemistryOpen 2014;3:48–53.
105. Wang C, Lai Z, Xie H, Cui S. Triazenyl Alkynes as Versatile Building Blocks in Multicomponent Reactions: Diastereoselective Synthesis of β-Amino Amides. Angew Chem, Int Ed 2021;60:5147–5151.
106. Van Der Born D, Pees A, Poot AJ, Orru RVA, Windhorst AD, Vugts DJ. Fluorine-18 labelled building blocks for PET tracer synthesis. Chem Soc Rev 2017;46:4709–4773.
107. Garanger E, Aikawa E, Reynolds F, Weissleder R, Josephson L. Simplified syntheses of complex multifunctional nanomaterials. ChemComm 2008;39:4792–4794.
108. Chen KT, Nieuwenhuizen J, Handula M, Seimbille Y. A novel clickable MSAP agent for dual fluorescence/nuclear labeling of biovectors. Org Biomol Chem 2020;18:6134–6139.
109. Merlot AM, Kalinowski DS, Richardson DR. Unraveling the mysteries of serum albumin-more than just a serum protein. Front Physiol 2014;5:1–7.
110. Graciani FS, Ximenes VF. Investigation of Human Albumin-Induced Circular Dichroism in Dansylglycine. PLoS One 2013;8:1–8.
111. Liu Z, Chen X. Simple bioconjugate chemistry serves great clinical advances: Albumin as a versatile platform for diagnosis and precision therapy. Chem Soc Rev 2016;45:1432–1456.
112. Ghuman J, Zunszain PA, Petitpas I, Bhattacharya AA, Otagiri M, Curry S. Structural basis of the drug-binding specificity of human serum albumin. JMB 2005;353:38–52.
113. Zorzi A, Linciano S, Angelini A. Non-covalent albumin-binding ligands for extending the circulating half-life of small biotherapeutics. Medchemcomm 2019;10:1068–1081.
114. Tian R, Jacobson O, Niu G, Kiesewetter DO, Wang Z, Zhu G, et al. Evans blue attachment enhances somatostatin receptor subtype-2 imaging and radiotherapy. Theranostics 2018;8:735–745.
115. Lau J, Jacobson O, Niu G, Lin KS, Bénard F, Chen X. Bench to Bedside: Albumin Binders for Improved Cancer Radioligand Therapies. Bioconjug Chem 2019;30:487–502.
116. Tiel S van, Tiel S van, Maina T, Nock B, Konijnenberg M, Blois E de, et al. Albutate-1, a Novel Long-Circulating Radiotracer Targeting the Somatostatin Receptor Subtype 2. J Nucl Med Radiat Sci 2021;2:1–9.
117. Müller C, Guzik P, Siwowska K, Cohrs S, Schmid RM, Schibli R. Combining albumin-binding properties and interaction with pemetrexed to improve the tissue distribution of radiofolates. Molecules 2018;23:1–12.

118. Siwowska K, Haller S, Bortoli F, Benešová M, Groehn V, Bernhardt P, et al. Preclinical comparison of albumin-binding radiofolates: Impact of linker entities on the in vitro and in vivo properties. Mol Pharm 2017;14:523–532.
119. Kuo HT, Merkens H, Zhang Z, Uribe CF, Lau J, Zhang C, et al. Enhancing Treatment Efficacy of 177Lu-PSMA-617 with the Conjugation of an Albumin-Binding Motif: Preclinical Dosimetry and Endoradiotherapy Studies. Mol Pharm 2018;15:5183–5191.
120. Kuo HT, Lin KS, Zhang Z, Uribe CF, Merkens H, Zhang C, et al. 177Lu-labeled albumin-binder-conjugated PSMA-targeting agents with extremely high tumor uptake and enhanced tumor-to-kidney absorbed dose ratio. J Nucl Med 2021;62:521–527.
121. Bertozo L de C, Maszota-Zieleniak M, Bolean M, Ciancaglini P, Samsonov SA, Ximenes VF. Binding of fluorescent dansyl amino acids in albumin: When access to the protein cavity is more important than the strength of binding. Dyes Pigm 2021;188:1–13.
122. Zorzi A, Middendorp SJ, Wilbs J, Deyle K, Heinis C. Acylated heptapeptide binds albumin with high affinity and application as tag furnishes long-acting peptides. Nat Commun 2017;8:1–9.
123. Kim YS, Brechbiel MW. An overview of targeted alpha therapy. Physiol Behav 2012;33:573–590.
124. Sgouros G, Ballangrud ÅM, Jurcic JG, McDevitt MR, Humm JL, Erdi YE, et al. Pharmacokinetics and dosimetry of an α-particle emitter labeled antibody: 213Bi-HuM195 (anti-CD33) in patients with leukemia. J Nucl Med 1999;40:1935–1946.
125. Yadav MP, Ballal S, Sahoo RK, Bal C. Efficacy and safety of 225Ac-DOTATATE targeted alpha therapy in metastatic paragangliomas: a pilot study. EJNMMI 2022;49:1595–1606.
126. Zacherl MJ, Gildehaus FJ, Mittlmeier L, Böning G, Gosewisch A, Wenter V, et al. First Clinical Results for PSMA-Targeted α-Therapy Using 225Ac-PSMA-I&T in Advanced-mCRPC Patients. J Nucl Med 2021;62:669–674.
127. Chan HS, Konijnenberg MW, Daniels T, Nysus M, Makvandi M, de Blois E, et al. Improved safety and efficacy of 213Bi-DOTATATE-targeted alpha therapy of somatostatin receptor-expressing neuroendocrine tumors in mice pre-treated with l-lysine. EJNMMI Res 2016;6:1–11.
128. Pouget JP, Constanzo J. Revisiting the Radiobiology of Targeted Alpha Therapy. Front Med 2021;8:1–11.
129. Wulbrand C, Seidl C, Gaertner FC, Bruchertseifer F, Morgenstern A, Essler M, et al. Alpha-Particle Emitting 213Bi-Anti-EGFR Immunoconjugates Eradicate Tumor Cells Independent of Oxygenation. PLoS One 2013;8:1–9.
130. Beeler E, Gabani P, Singh O V. Implementation of nanoparticles in therapeutic radiation oncology. J Nanopart Res 2017;19:1–10.
131. Dekempeneer Y, Caveliers V, Ooms M, Maertens D, Gysemans M, Lahoutte T, et al. Therapeutic Efficacy of 213Bi-labeled sdAbs in a Preclinical Model of Ovarian Cancer. Mol Pharm 2020;17:3553–3566.
132. Ballal S, Yadav MP, Bal C, Sahoo RK, Tripathi M. Broadening horizons with 225Ac-DOTATATE targeted alpha therapy for gastroenteropancreatic neuroendocrine tumour patients stable or refractory to 177Lu-DOTATATE PRRT: first clinical experience on the efficacy and safety. EJNMMI 2020;47:934–946.
133. Nelson BJB, Andersson JD, Wuest F. Targeted alpha therapy: Progress in radionuclide production, radiochemistry and applications. Pharmaceutics 2021;13:1–28.

# PART 1

## The Multifunctionality of The Click Reaction

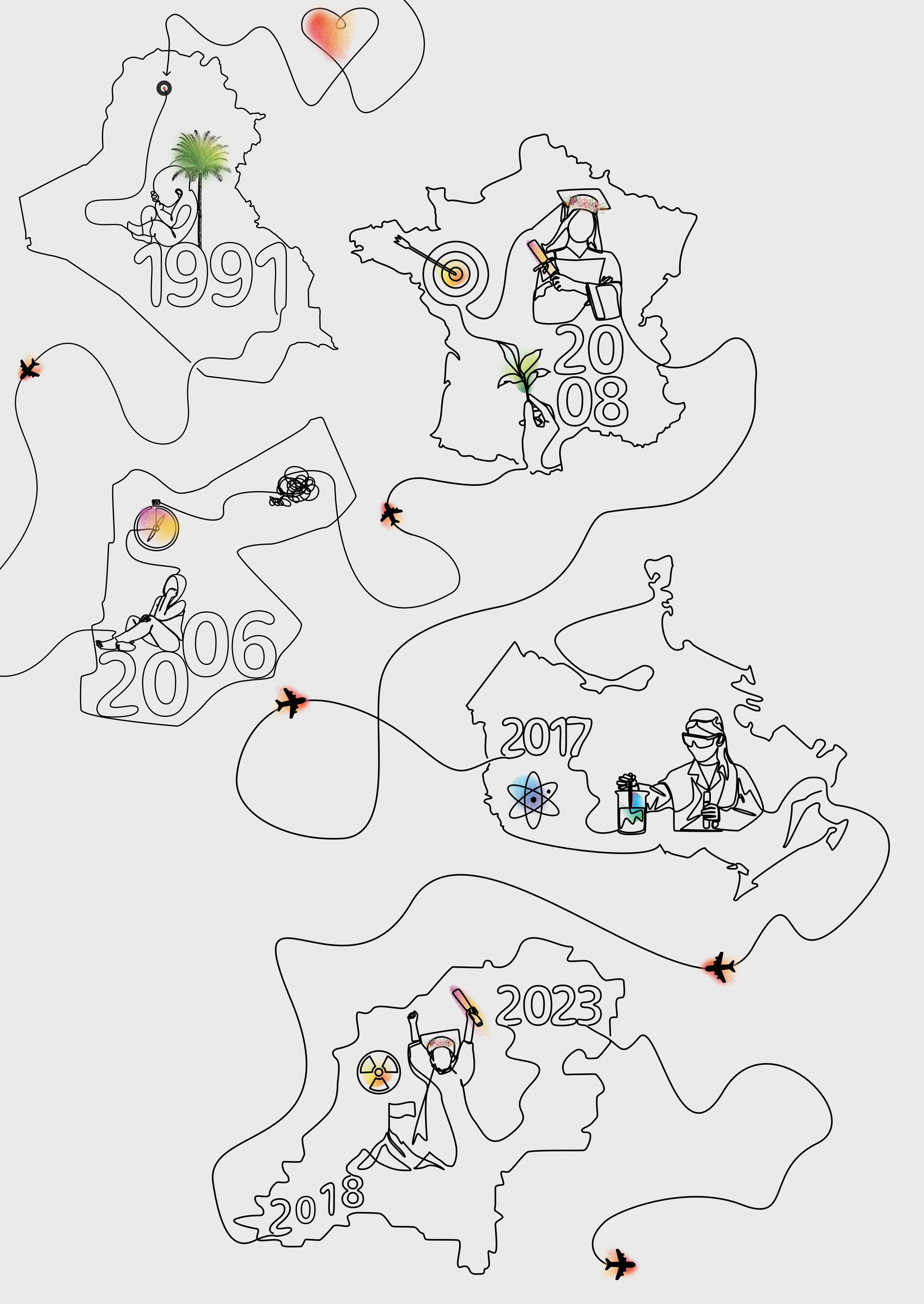
1991
2008
2006
2017
2023
2018

# CHAPTER 2

## IEDDA: An Attractive Bioorthogonal Reaction for Biomedical Applications

Maryana Handula[1], Kuo-Ting Chen[2] and Yann Seimbille[1,3]

[1] Department of Radiology and Nuclear Medicine, Erasmus MC, University Medical Center Rotterdam, Wytemaweg 80, 3015 CN Rotterdam, The Netherlands
[2] Department of Chemistry, National Dong Hwa University, Shoufeng, Hualien 974301, Taiwan
[3] Life Sciences Division, TRIUMF, 4004 Wesbrook Mall, Vancouver, BC V6T 2A3, Canada

*Molecules. 2021;26(15):4640*

**Abstract:** The pretargeting strategy has recently emerged in order to overcome the limitations of direct targeting, mainly in the field of radioimmunotherapy (RIT). This strategy is directly dependent on chemical reactions, namely bioorthogonal reactions, which have been developed for their ability to occur under physiological conditions. The Staudinger ligation, the copper catalyzed azide-alkyne cycloaddition (CuAAC) and the strain-promoted [3 + 2] azide–alkyne cycloaddition (SPAAC) were the first bioorthogonal reactions introduced in the literature. However, due to their incomplete biocompatibility and slow kinetics, the inverse-electron demand Diels-Alder (IEDDA) reaction was advanced in 2008 by Blackman et al. as an optimal bioorthogonal reaction. The IEDDA is the fastest bioorthogonal reaction known so far. Its biocompatibility and ideal kinetics are very appealing for pretargeting applications. The use of a *trans*-cyclooctene (TCO) and a tetrazine (Tz) in the reaction encouraged researchers to study them deeply. It was found that both reagents are sensitive to acidic or basic conditions. Furthermore, TCO is photosensitive and can be isomerized to its *cis*-conformation via a radical catalyzed reaction. Unfortunately, the *cis*-conformer is significantly less reactive toward tetrazine than the *trans*-conformation. Therefore, extensive research has been carried out to optimize both click reagents and to employ the IEDDA bioorthogonal reaction in biomedical applications.

**Keywords:** pretargeting; click chemistry; bioorthogonal reaction; IEDDA; tetrazine; *trans*-cyclooctene

## 1. The Emergence of the Pretargeting Approach

### *1.1. Limitations of Direct Targeting*

Radiolabeled antibodies have been used over the last decades in radioimmunodiagnosis (RID) and radioimmunotherapy (RIT) to image and treat tumors. They are attractive biovectors due to their ability to target specific antigens expressed at the surface of tumor cells. Antibodies were first labeled by covalent incorporation of radioiodine to the tyrosine residues of the antibody [1]. Then, various radiometals were conjugated to the antibody via chelators [2,3]. The biological half-life of antibodies is typically expressed in days and, therefore, long-lived radionuclides such as indium-111 ($t_{1/2}$ = 2.8 days), zirconium-89 ($t_{1/2}$ = 3.3 days) and iodine-124 ($t_{1/2}$ = 4.2 days), are required to warrant optimal accumulation of the radionuclide at the target site [1,4–6]. However, the long circulation of radiolabeled antibodies in the blood stream is a major challenge since it directly leads to unnecessary radiation exposure to healthy tissues such as the radiosensitive bone marrow [5,7]. Thus, many investigations on antibody fragments, active removal of labeled antibodies from the blood and pretargeting have been recently carried out to reduce radiotoxicity associated with radiolabeled antibodies [4,8–10].

### *1.2. Basic Principle of the Pretargeting Approach*

Pretargeting was introduced in the 1980s by Dayton D. Reardan and David Goodwin [11–13]. Many pretargeting strategies have been described in the literature, but methods based on biotin and avidin and bispecific monoclonal antibodies (mAbs) are the most common [5]. The pretargeting concept was developed to overcome the limitations encountered during direct targeting of tumors with radiolabeled antibodies [14]. It relies on four main steps (Figure 1) [7,15–17]. The first step consists of the administration of an unlabeled and modified biovector (i.e., monoclonal antibody) possessing the ability to bind an antigen or receptor and a radiolabeled small molecule. The second step is the slow accumulation of the biovector at the tumor site and its clearance from the body. The third step is the injection of the radiolabeled small molecule. Finally, the last step is based on the rapid binding of the radiolabeled small molecule to the biovector at the tumor site and its rapid clearance from the blood [10,18–21]. A clearing agent can also be employed at the end of the second step to remove the excess of biovector from the blood stream. The biovector is then transported to the liver or the spleen where it can be metabolized and eliminated from the body [14]. Several studies demonstrated that the clearing agent does not interact with the biovector already bound at the surface of the cancer cells but only with free molecules present in the blood circulation, as illustrated by SPECT/CT imaging studies [14,22–26]. Recently, Myrhammar and coworkers proposed a lactosaminated peptide nucleic acid-antibody conjugate as a potential clearing agent, whereas Cheal et al. developed a glycodendrimer-based clearing agent for pretargeting studies [27,28].

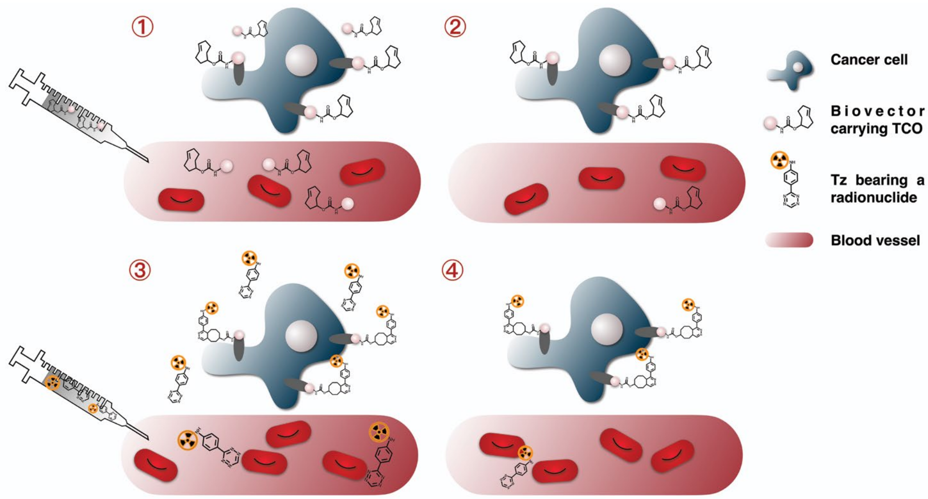


**Figure 1.** Illustration of the four basic steps of the pretargeting approach.

The main key factor of the pretargeting approach is the rapid pharmacokinetics of the radiolabeled small molecule to favor high radioactivity accumulation at the tumor sites while avoiding radiocytotoxic effects on healthy organs. However, success of the pretargeting strategy is directly dependent on the chemical reaction that allows efficient and selective binding of the radiolabeled small molecule to the biovector. Conventional bioconjugation reactions involving amine-carboxylic acid and thiol-maleimide result in undesirable conjugates in physiological conditions due to interferences with biomolecules present in the system. Hence, bioorthogonal reactions have gained a lot of attention for in vivo applications [29–33]. A bioorthogonal reaction is defined by: (1) fast reaction rate, (2) chemoselectivity, (3) no interference with the living system, (4) no toxicity and (5) stable starting materials and end-products. Moreover, the reaction has to occur in aqueous media at very low concentrations and under physiological temperature and pH [31,34,35].




## 2. Bioorthogonal Reactions

Click reactions were introduced in the early 2000s by Sharpless and coworkers [36]. According to the authors, a click reaction must be modular, stereospecific, high yielding, wide in scope and produce inoffensive products. However, the reaction should preferably be insensitive to oxygen and water and to occur in mild reaction conditions. Besides, the starting materials should be easily accessible, the products easily isolated and stable under physiological conditions. Importantly, a click reaction usually leads to a single product. To meet all these criteria, a click reaction needs to have a very high thermodynamic driving force, usually greater than 20 $Kcal.mol^{-1}$ [36]. A bioorthogonal reaction is typically a click reaction which is feasible under biologically friendly conditions

[34,35,37–39]. Most of the requirements for a bioorthogonal reaction are possessed by the azido group, and therefore it has been extensively employed as click functionality in the literature due to its stability and inertness towards other functional groups present in biological systems [31]. Furthermore, the small size of the azido group is particularly interesting because its conjugation to a biovector does not significantly impact the bioactivity of the resulting conjugate [31,40].

### *2.1. The Staudinger Ligation*

This bioorthogonal reaction was discovered by Staudinger and Meyer in 1919 (Table. 1) [41,42]. It involves the formation of an aza-ylide via coupling of a triarylphosphine and an azide. The reaction can occur in a living organism and is highly selective because both reagents are abiotic and don't react with biogenic functionalities of biomolecules. However, the main shortcoming of this reaction is the lack of stability of the aza-ylide product in water [43,44]. Therefore, Saxon and coworkers proposed stabilization of the product of the Staudinger ligation by an intramolecular cyclization. They used an electrophilic trap to capture the nucleophilic aza-ylide by adding an ester group on one of the aryl groups of the phosphine reagent at the ortho position of the phosphorus atom. The reaction led to a stable product via an amide bond formation [43]. Later on, Saxon and coworkers developed another method, dubbed the "traceless" Staudinger ligation, allowing obtention of the amide bond between the two reagents without the intervention of the triarylphosphine group [45].

The Staudinger ligation has been extensively studied in the context of in vitro and in vivo applications [46,47]. However, despite all the efforts to optimize the reaction, it still suffers from some limitations prohibiting its application to in vivo studies. In fact, oxidation of the phosphine and slow kinetics (k ~ $10^{-3}$ $M^{-1}s^{-1}$) are the main obstacles hampering successful application of the Staudinger reaction in a living system [44,48]. Consequently, further investigations in the realm of bioorthogonal chemistry have been pursued to find click reactions with better chemical properties.

### *2.2. Copper-Catalyzed [3 + 2] Azide–Alkyne Cycloaddition (CuAAC)*

The azide-alkyne cycloaddition was originally introduced by Huisgen. This classical [3 + 2] cycloaddition is characterized by relatively slow kinetic, thus it is not compatible with pretargeting in biological environments. In 2002, the copper catalyzed azide-alkyne cycloaddition (CuAAC) was described by Sharpless and Mendal [49,50]. The use of Cu(I), as a catalyst increased the second order reaction rate by seven orders of magnitude compared to the uncatalyzed reaction [37]. The kinetics of CuAAC (10 $M^{-1}$ $s^{-1}$ in presence of 20 µM of Cu(I)) are 1000-fold faster than the Staudinger ligation (Table. 1) [51]. Moreover, the CuAAC fulfills all the conditions to be classified as a click reaction. The small size of the two functional groups involved, namely azide and alkyne, enabled the incorporation of the click handles into biomolecules without disrupting their biochemical properties. Thus, CuAAC has been applied to the labeling of peptides and proteins [52]. Nevertheless, biological applications of CuAAC has been hampered by the cytotoxicity of copper, which is known to participate in the generation of reactive oxygen species (ROS) [53]. In fact, in 2009, Bertozzi et al. reported that mammalian cells could survive only one hour exposure to low concentrations of copper (lower than 500 µM) [37]. Therefore, to improve the biocompatibility of the reaction, water-soluble Cu(I) ligands were developed to stabilize the metal and prevent the release of toxic copper ions [54,55]. Another approach is to perform the [3+2] azide–alkyne cycloaddition with a strained alkyne, which avoids the need of copper catalyst.

### *2.3. Strain-Promoted [3 + 2] Azide–Alkyne Cycloaddition (SPAAC)*

The strain-promoted [3 + 2] azide–alkyne cycloaddition (SPAAC) was introduced in 2004 by Bertozzi et al. [56]. The main advantage of SPAAC in comparison to CuAAC is that the reaction occurs under physiological conditions and without a catalyst. However, the reaction kinetics ($1.2–2.4 \times 10^{-4}$ $M^{-1}$ $s^{-1}$) are slower than CuAAC and comparable to those of the Staudinger ligation [57]. Nevertheless, the slow kinetics of the reaction were improved by structural modifications of the alkyne, such as fluorination and $sp^2$-hybridization of ring atoms [57,58]. By reaching 0.1 $M^{-1}$ $s^{-1}$, Bertozzi et al. were able to accelerate by 60-fold the reaction kinetics (Table. 1) [59,60]. SPAAC has been tested in different systems including the labeling of glycol chitosan nanoparticles with copper-64 or pretargeted radioimmunotherapy (PRIT) of non-Hodgkin lymphoma [61–63]. Although SPAAC does not require toxic catalyst and exhibits kinetics 100-fold faster than the Staudinger ligation, it has been shown not to be perfectly bioorthogonal. The cyclooctyne ring can potentially react with nucleophiles present in living systems. Therefore, new type of bioorthogonal reaction offering higher kinetics and better chemoselectivity are needed.





### *2.4. Inverse Electron-demand Diels-Alder (IEDDA)*

IEDDA was introduced in 2008 by Blackman et al. as the fastest bioorthogonal reaction [66]. The reaction occurs between a diene, such as 1,2,4,5-tetrazine (Tz), and a dienophile. Contrary to the electron-demand Diels-Alder reaction, an electron-rich dienophile reacts with an electron-poor diene in IEDDA. According to the frontier molecular orbital theory (FMO), the fast reaction kinetics of IEDDA are due to the low energy gap between the highest occupied molecular orbital (HOMO) and the lowest unoccupied molecular orbital (LUMO) of the dienophile and diene, respectively [48]. The reaction can be set in organic solvents, water, as well as biological media, and does not require activation by a catalyst [66]. Moreover, reactants can be used at very low concentration for their conjugation to large biomolecules due to the high chemoselectivity of the reaction [48].

**Table 1.** Chemical characteristics of the bioorthogonal reactions covered in this review.

| Bioorthogonal Reaction | Reaction Scheme | $k$ ($M^{-1}$ $s^{-1}$) | Advantages | Drawbacks |
|---|---|---|---|---|
| **Staudinger ligation** | A: Staudinger reaction 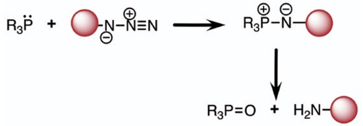 | ~ $10^{-3}$ [64] | Abiotic starting materials | Slow kinetics<br>Low stability of Aza-ylide |
| | B: Staudinger ligation 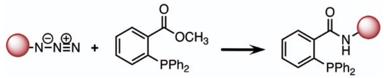 | $10^{-3}$ | Stable amide bound formation | Slow kinetics |
| | C: "Traceless" Staudinger ligation 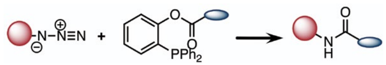 | $7.7{\times}10^{-3}$ [65] | Product obtained without the triarylphosphine group | Slow kinetics |
| **CuAAC** | 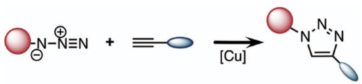 | 10 | Covalent reaction<br>Small molecules | Slow kinetics<br>Cytotoxicity caused by copper ions |
| **SPAAC** | 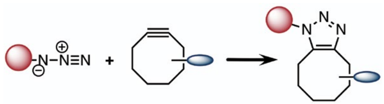 | 0.1 | Free of catalyst | Slow kinetics<br>Reactivity with thiols |
| **IEDDA** | 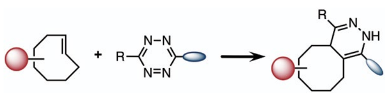 | $1–10^{6}$ | Very high second order reaction rate constant<br>Irreversible reaction<br>Fully bioorthogonal<br>Stable product | Sensitivity of TCO to acids, thiols, and copper ions<br>Sensitivity of Tz to bases |

*Trans*-cyclooctene (TCO) is the most commonly used dienophile due to its high reactivity towards diene. In fact, TCO is seven-fold more reactive than the *cis*-cyclooctene in IEDDA reaction. Tetrazines are generally employed as dienes, and the IEDDA is sometimes called tetrazine ligation [67]. The Tz and TCO pair shows very high reaction specificity, and they are not reactive toward thiols, amines and other potential nucleophiles present in the biological system. This irreversible process leads to the release of $N_2$ gas, as the only side product during the reaction [68]. The reaction between Tz and a dienophile can be monitored spectroscopically by following the disappearance of the absorption band between 510 and 550 nm [69]. This method was used by Sauer and coworkers to perform kinetic studies proving that this reaction is incredibly fast [70]. Its exceptional fast kinetics are reported between 1 and $10^6$ $M^{-1}$ $s^{-1}$. Due to all those reasons, IEDDA is so far the most efficient bioorthogonal reaction reported in the literature [71].

## 3. Dienes

Dienes are one of the two click functionalities required for the IEDDA reaction, and their stability is a key issue for in vivo pretargeting. Tetrazines (Tz) are the most commonly used dienes for IEDDA. The reactivity of Tz is influenced by the substitutions performed on the tetrazine backbone (Figure 2A) [14]. Installation of an electron-withdrawing group (i.e., aryl group) on Tz lowers the LUMO energy and leads to high reactivity. Unfortunately, the reactivity of tetrazines is inversely correlated with their stability. In 2016, Maggi et al. investigated the stability of a series of 10 tetrazines to understand the effects of different substituents on the tetrazine core (Figure 2B) [72]. In general, *C*1-monoaryl-substituted tetrazines (**2**, **4**, **8**, **9**) were found to easily decompose under biological conditions (PBS or FBS). The stability can be restored by introduction of a methyl group at the *C*4-position (**1**, **3** ,**5**). Installation of electron-donating group at either the *C*1 or both *C*1/*C*4 positions stabilized the tetrazine core but also reduced the reactivity (**6**, **7**). However, the reactivity between Tz and TCO can be enhanced by increasing the polarity of the solvent or the temperature [73]. The di-aryl substituted tetrazine, 3,6-di-(2-pyridyl)-1,2,4,5-tetrazine **10**, is the diene that exhibited the worst stability, as well as the best reactivity among all tetrazines tested. Recently, Steen et al. developed a library of 45 tetrazines and compared their lipophilicity (clog$D_{7.4}$), topological polar surface areas (TPSAs) and in vivo IEDDA reactivity [74]. A strong correlation was noticed between the tetrazine ligation efficiency and the lipophilicity of the Tz. Negative clog$D_{7.4}$ values of –3.0 or lower great improve IEDDA efficiency. However, no correlation was observed between TPSA and the click reactivity. They also reported that a very high second-order rate constant (>50,000 $M^{-1}$ $s^{-1}$) is important to achieve efficient in vivo IEDDA reaction.

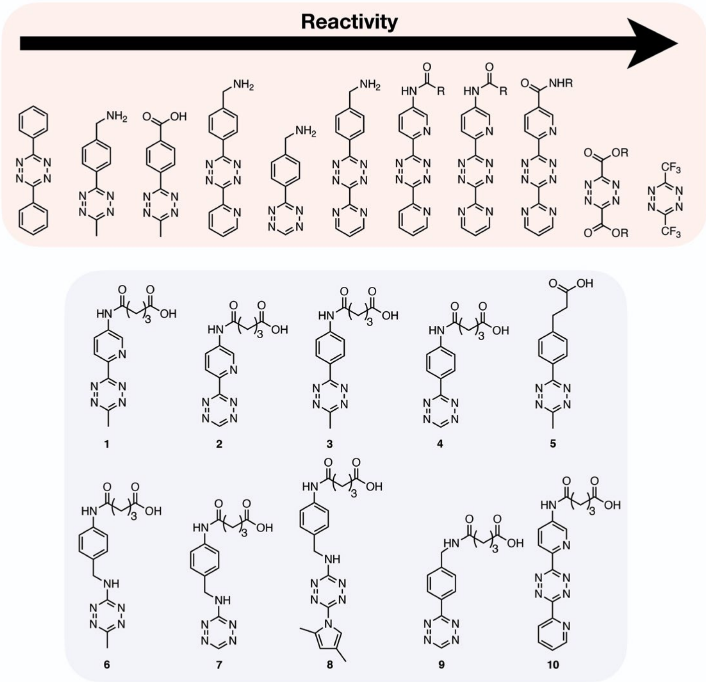


**Figure 2.** (**A**) Reactivity of different Tz-scaffolds [14] and (**B**) chemical structures of the newly synthesized tetrazine (**1**–**8**) and common tetrazines (**9**, **10**) [72].

## 4. Dienophiles

The reaction of an electron-rich dienophile and an electron-poor diene is the basis of the IEDDA reaction. Norbornene (**11**) is one of the earliest dienophiles applied for pretargeting studies (Figure 3A). Devaraj et al. demonstrated that tetrazine-substituted imaging probe specifically conjugated to a norbornene-modified HER2-antibody in the presence of live cells and serum [75]. However, the slow kinetics of this reaction ($k_2$ = 1.9 $M^{-1}s^{-1}$) prevented further applications. IEDDA kinetics are highly dependent on the reaction substrates, and therefore the activity of various dienophiles has been extensively investigated in recent years. Since the 1990s, Sauer's group and other research groups have examined the reactivity of substituted dienophiles and several principal rules have been summarized: (1) dienophiles with electron-rich substituents are favorable for fast kinetics; (2) strained dienophiles are more reactive, and (3) an increase of the steric effect hampers reactivity. Currently, the most widely used dienophile for IEDDA-based pretargeting studies is *trans*-cyclooctene (TCO). TCO is usually functionalized with a hydroxyl group at the 5-position, known as 5-hydroxy-*trans*-cyclooctene (5-OH-TCO), for further conjugation. There are two stereoisomers of 5-OH-TCO (**12** and **13**), possessing different reactivity. The axial isomer **13** was found to be more reactive than the corresponding equatorial isomer **12**.

However, despite the fast kinetics observed with these TCOs, the TCO-tag was found to be partially deactivated in vivo through isomerization to a slow-reactive *cis*-cyclooctene (CCO) [76]. Elaboration of TCO with a short linker was found to extent the half-life of the *trans*-configuration of TCO. In addition to TCO, other dienophiles with higher reactivity (**14** and **15**) [77] or better stability (**16**) [78] have been reported. Furthermore, a bifunctional dienophile (*trans,trans*-1,5-cyclooctadiene, ((*E,E*)-COD)), allowing double click reactions was reported by Leeper's group. COD is capable of undergoing a (3+2) cycloaddition with 1,3-dipoles to generate triazoline-TCOs (**17**), followed by an IEDDA reaction with tetrazine moieties [79]. The chemistry allowed less-tedious chemical modification of TCO and was exploited by Longo et al. to prepare several TCO derivatives for live-cell fluorescent imaging. However, the kinetics of **17** were too slow for an in vivo pretargeting study [80]. So far, and to the best of our knowledge, no other dienophiles than 5-OH-TCO have been successfully advanced to in vivo pretargeting studies.

5-OH-TCO was first reported in antibody-based pretargeting studies by Robillard et al. [22]. In this study, (R)-5-OH-TCO was functionalized with a benzoic acid-oligoethylene glycol hybrid linker (NHS-PEG$_{12}$-Bz-TCO, **18**) and conjugated to the anti-TAG72 antibody CC49 (Figure 3B). The resulting TCO-CC49 had a second order rate kinetic constant of 13'090 $M^{-1}s^{-1}$ in PBS buffer. It was demonstrated that TCO-CC49 was still reactive after 24 h blood circulation, thus indicating good in vivo stability. In 2016, Cook et al. introduced the activated cyclooctyne DIBO onto 5-OH-TCO (DIBO-PEG$_{12}$-TCO) for site-specific labeling of antibody. Four azido functional groups were installed on the heavy chain of the $^{ss}$huA33 antibody via a modular chemoenzymatic strategy with β-1,4-galactosidase and galactosyltransferase (Gal-T(Y289L)). Then, the azido-antibody was conjugated to DIBO-PEG$_{12}$-TCO (**19**) according to a SPAAC reaction to adapt the antibody to IEDDA-mediated pretargeting studies [18]. MALDI-TOF mass spectrometry and denaturing SDS-PAGE analyses showed that approximately 2.4 TCO groups were attached on the heavy chain of the antibody, while immunoreactivity of the conjugate was almost not influenced by the modifications (94%). Another site-specific labeling method based on reaction between cysteine and carbonylacrylic group was recently reported [81]. 5-OH-TCO was functionalized with a carbonylacrylic group (**20**) and conjugated to THIOMAB LC-V205C, a modified anti-HER2 antibody with cysteines in the light chain. LC-mass spectrometry analysis of THIOMAB LC-V205C-TCO revealed that the immunoconjugate was modified with two TCO/mAb. The reaction kinetics of THIOMAB LC-V205C-TCO were investigated by performing the click reaction with [$^{111}$In]In-DOTA-Tz. It resulted in ~92% conversion yield, but the immunoreactivity of the conjugate was not reported.

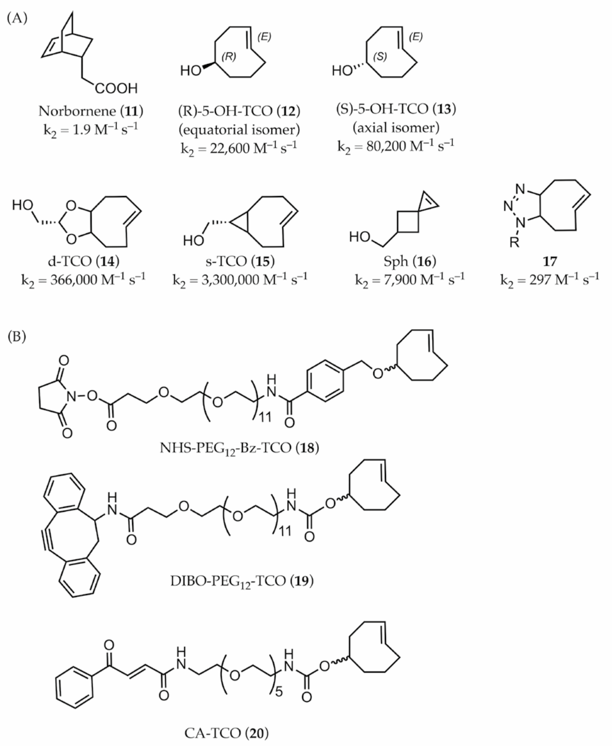

**Figure 3.** (**A**) Represented dienophiles for IEDDA reaction: **11** [75], **12–15** [77], **16** [78], **17** [80]. (**B**) Modified dienophiles for antibody-based pretargeting studies.

## 5. Applications

### *5.1. Radiolabeling of Monoclonal Antibodies (mAbs) with Short-Lived Radionuclides and Pretargeting*

Radiolabeled mAbs are widely used in preclinical and clinical positron emission tomography (PET) imaging studies due to their high selectivity for specific antigens expressed at the surface of tumor cells [82–85]. However, the long biological half-life of mAbs calls for labeling with long-lived radionuclides to warrant sufficient accumulation of radioactivity at the tumor sites. This approach is unfortunately limited by the long circulation of the radiolabeled molecule in the blood and the radiotoxicity induced to nontargeted organs [86]. To overcome this limitation, Ruivo and coworkers made use of the pretargeting method to combine the specificity of mAbs with the fast pharmacokinetics of radiolabeled small molecules. IEDDA-mediated pretargeting gave them the opportunity to perform PET imaging with mAbs and short-lived radionuclides. In 2015, Houghton et al. applied a similar strategy to improve the prognosis of pancreatic ductal adenocarcinoma (PDAC) [87]. In fact, carbohydrate antigen 19.9 (CA19.9) is highly expressed in PDAC and can be selected as molecular target for PET imaging of pancreatic cancer. However, its secretion in blood results in an increase of circulating CA19.9-targeting radiotracer and decrease in tumor uptake. Therefore, the authors proposed a pretargeting strategy based on TCO-modified monoclonal antibody targeting CA19.9 (5B1-TCO) and copper-64 labeled tetrazines ([$^{64}$Cu]Cu-NOTA-Tz and [$^{64}$Cu]Cu-NOTA-PEG$_7$-Tz). They evaluated the optimal time interval (48, 72 and 120 h) between the two injections and compared the pharmacokinetics of the two radiolabeled tetrazines. It was found that 72 h gave the best balance between blood clearance and chemical stability of TCO. Furthermore, the addition of the PEG$_7$ linker improved hydrophilicity of the $^{64}$Cu-labeled tetrazine and reduced accumulation in the gastrointestinal tract. Later, they reported a fluorine-18 labeled tetrazine (Tz-PEG$_{11}$-Al [$^{18}$F]-NOTA), which could be obtained in mild reaction conditions to avoid alkaline degradation of the tetrazine [88]. Imaging of athymic mice bearing subcutaneous CA19.9-expressing BxPC3 xenografts was performed with Tz-PEG$_{11}$-Al[$^{18}$F]-NOTA 72 h after injection of 5B1-TCO. Ex vivo biodistribution revealed increase tumor uptake overtime, which was confirmed by PET imaging data. Several other $^{18}$F-labeled tetrazines have been developed due to the attractive decay properties ($t_{1/2}$ = 109.8 min) of fluorine-18 for PET imaging [86]. Keinänen et al. described a method for the preparation of a $^{18}$F-labeled glycosylated tetrazine by oxime ligation between 5-[$^{18}$F]fluoro-5-deoxyribose and an aminooxy functionalized tetrazine [89]. Addition of the sugar moiety reduced the lipophilicity of the labeled tetrazine. In vitro stability of the radiofluorinated tetrazine in PBS buffer and mouse plasma showed no degradation in PBS over 6 h, while 90% of the compound remained intact in plasma. Ex vivo biodistribution studies revealed low level of in vivo defluorination and rapid elimination of the radiotracer via the bladder, confirming the potential of this $^{18}$F-labeled tetrazine for pretargeting purposes.





Zeglis and coworkers reported several IEDDA-mediated pretargeting studies using monoclonal antibodies functionalized with a TCO and a radiolabeled tetrazine [90–94]. They recently described an efficient radiosynthetic approach based on IEDDA to prepare actinium-225 radioimmunoconjugates [90], while previous methods presented major limitations, such as radiolytic degradation or the need of a high number of chelate per antibody (~10), which could potentially affect the radioimmunoreactivity of the conjugate. Meyer et al. reported a masking agent to neutralize the free circulating mAb-TCO before the injection of the radiolabeled tetrazine. The main objective was to increase the target-to-background ratios without affecting tumoral uptake. It was shown that the quality of the PET images was significantly improved for the mice who received the masking agent in comparison to the control animals [91]. Then, Cook and coworkers investigated the possibility to increase the number of TCO groups per antibody. They synthesized a TCO-bearing scaffold based on a disulfide-core poly(amidoamine) (PAMAM) dendrimer, which was regioselectively attached to the ${}^{ss}$huA33 antibody (${}^{ss}$huA33-DEN-TCO). Biodistribution and microPET showed that the tumor uptake after injection of [${}^{64}$Cu]Cu-SarAr-Tz was two-fold higher in mice treated with ${}^{ss}$huA33-DEN-TCO compared to the animals treated with ${}^{ss}$huA33-PEG$_{12}$-TCO [95].

In the previous studies, the dienophile was conjugated to the biovector, while the diene was radiolabeled. However, due to the long-term in vivo instability of TCO, Maggi et al. proposed attachment of the tetrazine to the antibody and radiolabeling the TCO moiety [72,76,96]. Radiofluorination of TCO was attempted to obtain [${}^{18}$F]F-TCO, but the tracer was rapidly metabolized and a nonspecific accumulation in bones via defluorination was observed. Consequently, [${}^{18}$F]F-TCO has not been successfully applied to pretargeting studies [97,98]. In 2017, Billaud et al. performed fluorine-18 labeling of a pegylated TCO for pretargeted immuno-PET imaging. Animals with HER-2 positive xenografts were first injected with a trastuzumab-tetrazine conjugate, followed by the administration 48 to 72 h later of the ${}^{18}$F-labeled TCO. The HER-2 overexpressing tumors could clearly be visualized on the PET images, proving that pretargeting immuno-PET imaging can be achieved with this fluorinated TCO analog [99]. Later, Ruivo and coworkers modified the TCO labeling method by using the 1,4,7-triazacyclononane-*N,N',N''*-triacetic acid (NOTA) chelator. TCO was radiolabeled by complexation of Al[${}^{18}$F]F by the NOTA chelator, and [${}^{18}$F]F-MICA-205 was evaluated in vivo as a probable counterpart for the IEDDA reaction with a tetrazine-modified CC49 antibody. In vivo stability studies showed that 67.7 ± 0.43% of [${}^{18}$F]F-MICA-205 remained intact 15 min after injection (p.i.) of the tracer, whereas it decreased to 51.9 ± 5.16% at 1 h p.i.. Notably, it was identified that the main radiometabolite at the later timepoint was the *cis*-isomer (Figure 4A). However, the *trans* to *cis* isomerization was not considered a major limitation because of the fast kinetics of the IEDDA reaction. Biodistribution of [${}^{18}$F]F-MICA-205 in healthy mice showed both a hepatobiliary and a renal excretion due to the hydrophobic character of the tracer. As illustrated in Figure 4B, most of the radioactivity was found in the kidneys, the liver, and the small intestine. The low uptake in bones demonstrated the in vivo stability of the radiotracer. In vivo pretargeting studies were performed in LS174T tumor-bearing mice pretreated with the anti-TAG-72 mAb CC49 or with the same antibody conjugated to a stable methyl-tetrazine. [${}^{18}$F]F-MICA-205 was injected and microPET imaging was performed 1 h after administration of the tracer (Figure 5). The tumor uptake in mice pretreated with CC49-Tz (0.67 ± 0.16% ID/g) was significantly higher than the control animals preinjected with CC49 (0.16 ± 0.08% ID/g). It clearly demonstrated that the radiolabeled TCO, [${}^{18}$F]F-MICA-205, could be applied to an in vivo pretargeting strategy.

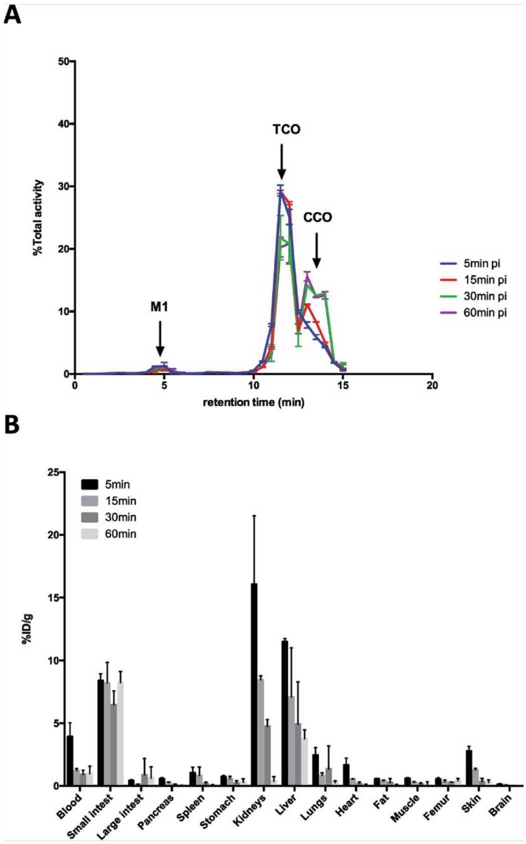


**Figure 4.** (**A**) In vivo plasma metabolites and (**B**) biodistribution of [$^{18}$F]F-MICA-205 in healthy Balb/C mice at 1 h post injection [86].

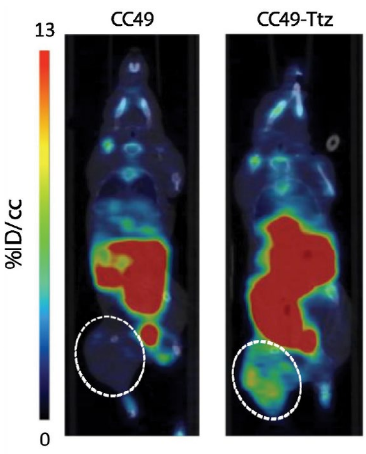


**Figure 5.** Representative microPET images of LS174T tumor-bearing mice injected with [$^{18}$F]F-MICA-205 24 h after the injection of CC49 (left) or CC49-Tz (right). Static images were acquired 1 h after administration of the [$^{18}$F]F-MICA-205. The white dashed line encircles the tumors [86].

### *5.2. Radiolabeling of Nanoparticles*

The fast kinetics and chemoselectivity of IEDDA are particularly attractive for the selective labeling of complex molecules such as nanoparticles. Recently, Goos et al. developed nanostars for multimodality molecular imaging and endoradiotherapy [100]. Nanoparticles were complexed with $Gd^{3+}$ for $T_1$-weighted magnetic resonance imaging and functionalized with a TCO group, p(TCO-AEA-co-OEGA-co-[$Gd^{3+}$]VDMD, to enable radiolabeling via IEDDA reaction. Tetrazine ligation was performed between p(TCO-AEA-co-OEGA-co-[$Gd^{3+}$]VDMD and [$^{177}$Lu]Lu-Tz-PEG$_7$-DOTA to obtain p([$^{177}$Lu]Lu-DPAEA- *co*-OEGA-*co*-[$Gd^{3+}$]VDMD. The $^{177}$Lu-labeled nanostars showed high uptake in the tumor tissue in comparison to other nanoparticles previously reported in the literature. In 2019, van Onzen and coworkers also used the selectivity of the bioorthogonal reaction between Tz and TCO to radiolabel nanoparticles, which were intrinsically fluorescent, and obtained dual-modality imaging probes (Figure 6) [101]. They incorporated a *trans*-cylooctene moiety to small molecule-based nanoparticles (SMNP) followed by the addition of a tetrazine-DOTA conjugate (Tz-DOTA) previously labeled with indium-111. The dual-modality imaging probe was obtained in over 97% radiochemical yield by reacting [$^{111}$In]In-DOTA-Tz with the cyclooctene unit (amp-TCO) in buffer for 30 min. The authors also compared this radiosynthetic strategy with two conventional labeling approaches where the DOTA chelate was directly attached to the SMNPs (amp-DOTA) or conjugated to the nanoparticles by strain-promoted azide-alkyne cycloaddition. The radiolabeling yield dropped to 45% for [$^{111}$In]In-DOTA-amp, and the radiochemical purity reached 88% after purification of the labeled nanoparticles by size exclusion chromatography. However, no reaction was observed during SPAAC with the azido-modified SMNPs (amp-azide), probably due to steric hindrances. This example clearly demonstrates the advantages of IEDDA over other techniques to radiolabel nanoparticles.

Recently, Keinänen et al. reported the development of an imaging strategy based on the IEDDA reaction and mesoporous silicon nanoparticles (PSi-NPs) [103]. Mesoporous silicon is an interesting material for targeted drug delivery in nanomedicine due to the biodegradability and nontoxicity of Psi-NPs. TCO-NPs were obtained by SPAAC reaction with TCO-PEG$_{12}$-DBCO after the conjugation of 3-azidopropylamine onto the NPs. IEDDA was carried out with [$^{18}$F]fluorodeoxyribose-tetrazine ([$^{18}$F]FDR-tetrazine). TCO-NPs were administrated intravenously to healthy mice 15 min or 24 h prior to the injection of [$^{18}$F]FDR-tetrazine. A control group was treated only with [$^{18}$F]FDR-tetrazine. PET-CT images revealed that the highest radioactive uptake was found in the spleen for the group treated with TCO-NPs 15 min prior [$^{18}$F]FDR-tetrazine administration, as typically observed for NPs. Authors reported that the click reaction between both moieties, TCO and Tz, was rapid and that 11.0 ± 1.9% ID/g was found in the spleen (vs. 2.8 ± 0.5% ID/g for the control group). However, no click reaction was observed for the group treated with TCO-NPs

24 h before the administration of the radiolabeled Tz. This might be due to the loss of reactivity of the TCO group and conversion to its unreactive *cis*-isomer, or the TCO-NPs were already completely internalized.

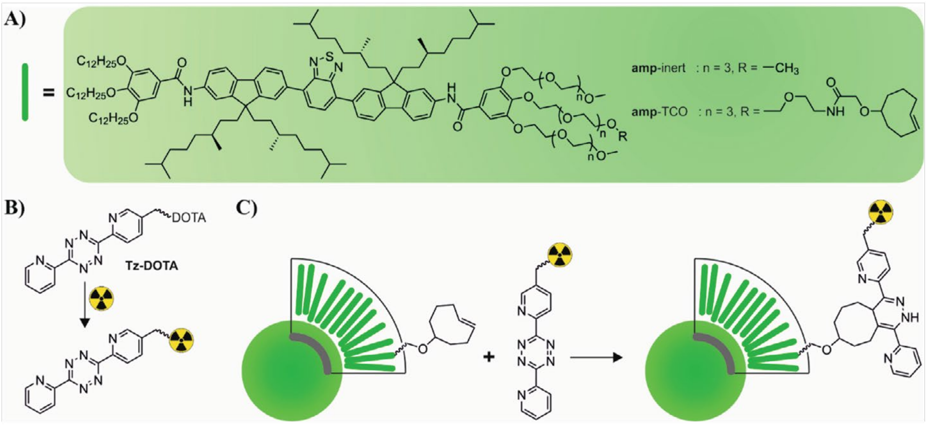


**Figure 6.** (**A**) Chemical structures of the amp-inert and amp-TCO [102], which self-assemble into SMNPs. (**B**) Two-step radiolabeling strategy by chelation of the radionuclide by Tz-DOTA followed by (**C**) conjugation of labeled Tz-DOTA to amp-TCO [101].

### *5.3. Drug to Release*

The principle of the pretargeting strategy, consisting of the injection of the targeting vector followed by the administration of an active ingredient interacting solely with the targeting vector, has not exclusively been used for the safe administration of a radioactive substance but also for the site-specific release of a drug. In 2018, Rossin et al. showed that the reaction of a tetrazine with a TCO linked to an antibody-drug conjugate (ADC) bound to a noninternalizing cancer cell receptor could lead to intracellular release of the drug while sparing the surrounding healthy tissues (Figure 7) [104]. In fact, their "click-to-release" strategy was based on previously published results showing the specific cleavage of allylic carbamates from TCO upon reaction with Tz [105,106].





As proof-of-concept, the authors selected the tumor-associated glycoprotein-72 (TAG72), as the noninternalizing receptor, and CC49 diabody conjugated to a $PEG_{24}$ linker and coupled to *trans*-cyclooctene bound to a tubulin-binding antimitotic MMAE (tc-ADC) to target TAG72. tc-ADC was compared to vc-ADC containing an enzymatically cleavable valine-citrulline linker and nb-ADC, a nonbinding anti-PSMA containing the TCO linker. To release the drug by the IEDDA reaction, a 3-methyl-6-trimethylene-tetrazine (activator) was employed. This tetrazine is known to be less reactive than the 3,6-bispyridyl-tetrazine previously reported for successful in vivo IEDDA, but it presents better releasing properties. To determine the efficiency of the "click-to-release" strategy, the click reaction was first performed in PBS buffer and in serum. Upon addition of the Tz activator, 90% of the drug was released in PBS buffer within 1 h of incubation at 37 °C, whereas in serum 80% of drug was released in 20 h. Subsequently, in vivo studies in LS174T-tumor bearing mice were carried out after the injection of the activator 48 h after the injection of tc-ADC. Biodistribution was performed at 72 or 96 h post injection of tc-ADC. MMAE release was estimated by mass spectrometry from liver and tumor homogenates as well as plasma. MMAE levels were 100-fold higher in the tumors treated by the subsequent injections of tc-ADC and the activator in comparison to the liver, the plasma or tumors treated solely with tc-ADC. Then, therapy studies were performed to compare the efficacy of tc-ADC + 3-methyl-6-trimethylene-tetrazine and vc-ADC. It was found that the click-to-release approach had a strong and durable response in OVCAR-3 xenografts without any signs of toxicity up to four months after treatment, while vc-ADC was not effective in this tumor model.

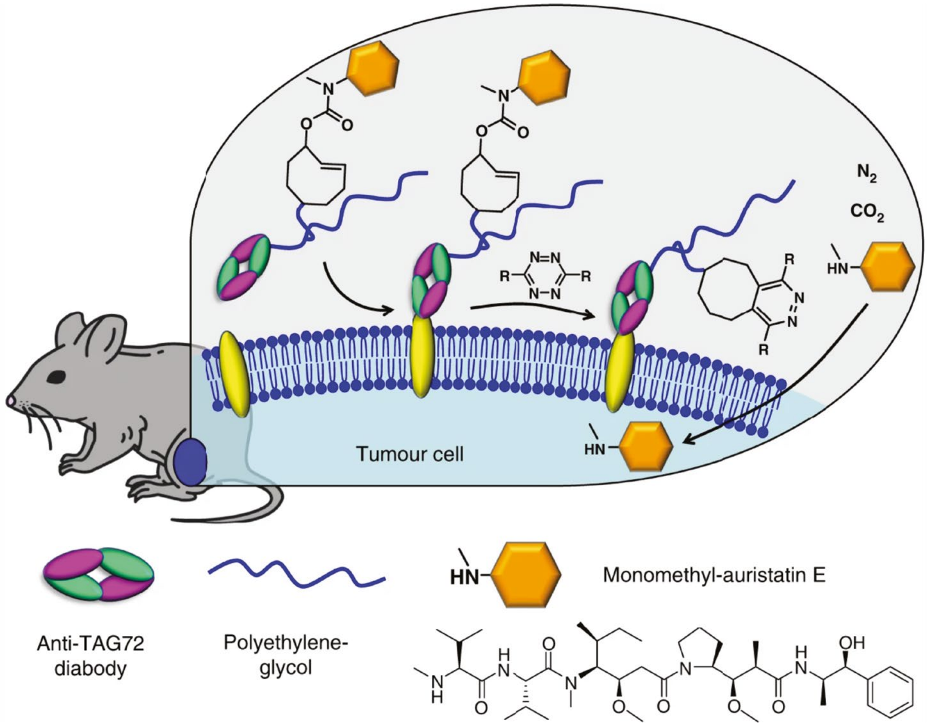


**Figure 7.** Triggered drug release using "click-to-release" chemistry in vivo: on-tumor liberation of a cell permeable drug (monomethyl auristatin E, MMAE) from a *trans*-cyclooctene-linked ADC following systemic administration of a tetrazine activator [104].

Recently, Li et al. used the same technique to investigate localized molecular imaging with tumor specificity and spatiotemporal precision [107]. In fact, fluorescence imaging showed very promising results in tumor diagnosis, but due to poor tissue penetration the results showed modest outcome. Therefore, in this study, single-walled carbon nanotubes

(SWCNTs) attached to Tz (Tz@SWCNTs) were used as delivery vehicles to increase accumulation in tumors via enhanced permeability and retention effects (EPR). For the second reagent of the IEDDA reaction, TCO was coupled to hemicyanine to yield (tHCA). tHCA is a fluorogenic near infrared probe that becomes fluorescent upon activation. The authors reported the ability of tHCA to diffuse deeply into the cancer tissue and to lead to tumor-specific imaging upon click reaction with Tz@SWCNTs. Thus, this strategy allowed deep tissue penetration via SWCNTs, and high signal-to-noise ratio by the activation of tHCA. This method enabled specific, nondestructive and real-time imaging. Then, they investigated pretargeted fluorogenic imaging in live cells, as well as in vivo. For their in vitro studies, MCF-7 cells were incubated with Tz@SWCNTs for 6 h before the addition of tHCA. The first fluorescent signal was reported after 5 min and its intensity increased over 30 min. In vivo studies were performed in CT26 tumors bearing BALB/c mice. For the group of mice intended for pretargeted imaging, mice were injected intravenously with Tz@SWCNTs and 2 h later with tHCA. The images showed a signal emerging from the tumor at 3 h post injection of tHCA. The intensity of the signal continued to increase up to 24 h after administration of tHCA. Based on their results, the authors identified a method for real-time fluorescence imaging with spatiotemporal control.

### *5.4. Activatable Fluorescence Probes*

Fluorescence imaging of live cells with caged fluorescent probes is a powerful technique to study dynamic cellular processes and events [108]. In 2010, Weissleder et al. first reported that Tz-BODIPY conjugates (e.g., tetrazine-BODIPYFL) exhibited strongly reduced fluorescence compared to their parent BODIPYs [109]. The quenching mechanism was suggested to be the result of a Förster resonance energy transfer (FRET) process between the electron-poor Tz and the fluorophore. Upon reaction with a dienophile, such as TCO, the fluorescence could be restored in the order of 15 to 20-fold. For live-cell study, the authors sequentially treated PtK2 kidney cells with taxol-TCO and tetrazine-BODIPYFL. In vitro, the IEDDA reaction was successfully demonstrated by clear visualization of the cellular tubule networks. Recently, the same authors developed another series of "superbright turn-on probes" (e.g., mTz-BODIPY, HELIOS) based on a through-bond energy transfer (TBET) process in which the Tz, acting as a quencher was attached to the fluorophore via a rigid linker [110,111]. Fluorescence increase in the order of $10^3$ to $10^4$ was observed after TCO-activation of the probes. From a mechanistic point of view, the TBET-based quenching process can be applied to any type of fluorophore, and Kele's group reported Tz-caged probes based on various fluorophores, including phenoxazine, coumarin, siliconrhodamine and rhodamine analogs [112–115]. The feasibility of applying the probes to cell-based imaging has also been demonstrated by confocal microscopy. Later, Kele et al. developed new IEDDA-activatable fluorogenic photocages based on a vinylene linked coumarinyl-Tz, which could be activated through the IEDDA reaction with a strained alkyne. Live-cell photouncaging was demonstrated by pretargeting the cells with an alkyne (TPP-BCN) followed by the addition of the fluorogenic rhodol-coumarinyl-Tz agent, resulting in fluorescence signal located in cell mitochondria [116].

### *5.5. Photodynamic Therapy*

Photodynamic therapy (PDT) is a clinically approved medical treatment that involves a photosensitizing molecule and a light source to destroy malignant cells. The treatment depends on the direct or indirect generation of cytotoxic singlet oxygen ($^1O_2$) or other ROSs (e.g., peroxide radicals, hydroxyl radicals) under exposure of the photosensitizer (PS) to light. Because the lifetime and diffusion distance of $^1O_2$ is short, specific delivery of PS at the target site is essential. Recently, Renard et al. took advantage of the IEDDA reaction to simultaneously label an EGFR-targeted VHH antibody with a complexed radionuclide ($^{111}$In-DTPA) and a PS (IRDye700DX) [117]. Micro-SPECT and near infrared fluorescence (NIFR) imaging showed that the tracer specifically accumulated in the tumor. Moreover, the dual-modality VHH exhibited dose-dependent cytotoxicity upon illumination with 60 J/cm$^2$ 690 nm light in an in vitro assay. Despite the success of targeted PDT, controllable activation of the PS is still under investigation to improve the effectiveness of PDT. Pioneer work on halogenated BODIPY-Tz by Vázquez's group demonstrated that the photosensitizer could be turned on and effectively generate $^1O_2$ through IEDDA reaction [118]. In this study, the tetrazine on the PS not only played the role of a TBET quencher but also a PS inactivator. PS activity could be restored by changing the nature of this quencher via IEDDA reaction. To validate the concept, a 5-vinyl-2′-deoxyuridine (VdU) was incorporated, as a dienophilic activator, into the DNA of HeLa cells. The cells were treated with mTz-2I-BODIPY and irradiated with a light at 525 nm for $^1O_2$ generation. The DNA-targeted PS activation proved to be successful because the product of the IEDDA reaction led to significant phototoxicity in HeLa cells. They concluded that the IEDDA-based activatable photodynamic strategies could be a useful tool for PDT. Next, Vázquez and coworkers developed a bioorthogonal turn-on peptide PS (Tz-C(2I-BODIPY)-PEPTIDE) [119]. Unlike the previous BODIPY/Tz photosensitizer, the tetrazine and BODIPY moieties were separately integrated into a cell membrane-targeted peptide. In vitro IEDDA reaction followed by proper irradiation led to significant suppression of the HeLa cell viability, showing that the new PS/quencher pair was successfully turned on by TCO treatment. Another example of IEDDA reaction-mediated activatable PS was reported by Dong et al. [120]. They used a tumor pH-responsive polymer containing a tetrazine, which formed unreactive micelles at neutral pH. However, micelles disassembled under the acidic tumor microenvironment (pH 6.5), leading to the activation of the caged PS. The authors demonstrated that the Tz-polymers were released at pH 6.5 and activated the CyPVE (a vinyl-ether-caged fluorogenic PS) through the IEDDA reaction, resulting in the photodynamic cytotoxicity of 4T1 cells. On the contrary, no cytotoxicity was observed at pH 7.4 because the Tz-micelles were stable under neutral conditions. In vivo PDT studies showed that 4T1 tumor xenografts shrunk after 12 days of treatment by the Tz micelles/CyPVE. The successful example of the IEDDA reaction in the context of the acidic tumor microenvironment may provide a general strategy for bioorthogonal prodrug activation.

## 6. Conclusions

To summarize, bioorthogonal reactions have been widely studied over the last few decades for their ability to potentially overcome the limitations in RIT. Although, several click reactions have been introduced, the IEDDA discovered in 2008 by Blackman et al., has been a game changer due to its fast kinetics, high selectivity and biocompatibility. Nowadays, most biological studies involving a bioorthogonal reaction are based on the IEDDA. However, even if some dienes and dienophiles reagents are commonly used, optimization of their chemical properties is still required. Indeed, the in vivo stability of TCO can be compromised in acidic conditions or by the presence of copper ions and nucleophiles in the biological system. Similarly, an equilibrium between reactivity and stability has to be found for the tetrazine. To overcome these limitations, various dienes and dienophiles have been synthesized to optimize the efficiency of the click reaction. For instance, norbornene derivatives or strained cyclopentene have been developed to replace TCO.

Many preclinical studies with TCO or Tz-modified antibodies have shown encouraging results. However, in vivo IEDDA applications with smaller biomolecules, such as peptides, have been barely investigated. Furthermore, implementation of such strategy into clinic is a logistic challenge, considering the number and time between the injections. Additionally, clinical deployment of IEDDA will only be effective for imaging and therapy if it remains affordable. To conclude, IEDDA is a valuable tool for biomedical research to overcome current limitations encountered with direct targeting. However, despite promising preclinical results, further optimization is likely required for the clinical translation of this novel targeting approach.

**Author Contributions:** Writing and original draft preparation, Maryana Handula; writing, review, and editing, Maryana Handula, Kuo-Ting Chen and Yann Seimbille. All authors have read and agreed to the published version of the manuscript.

**Funding:** This research was funded by the Dutch cancer society (KWF), grant number 12259.

**Conflicts of Interest:** The authors declare no conflict of interest.

## References


1. Sharkey, R.M.; Goldenberg, D.M. Advances in Radioimmunotherapy in the Age of Molecular Engineering and Pretargeting. Cancer Investig. 2006, 24, 82–97.
2. Carroll, V.; Demoin, D.; Hoffman, T.; Jurisson, S. Inorganic chemistry in nuclear imaging and radiotherapy: Current and future directions. Radiochim. Acta 2012, 100, 653–667.
3. Keire, D.A.; Jang, Y.H.; Li, L.; Dasgupta, S.; Goddard, W.A.; Shively, J.E. Chelators for radioimmunotherapy: I. NMR and ab initio calculation studies on 1,4,7,10-tetra(carboxyethyl)-1,4,7,10-tetraazacyclododecane (DO4Pr) and 1,4,7-tris(carboxymethyl)-10-(carboxyethyl)-1,4,7,10-tetraazacyclododecane (DO3A1Pr). Inorg. Chem. 2001, 40, 4310–4318.
4. Boerman, O.C.; Van Schaijk, F.G.; Oyen, W.J.G.; Corstens, F.H.M. Pretargeted radioimmunotherapy of cancer: Progress step by step. J. Nucl. Med. 2003, 44, 400–411.
5. Zeglis, B.M.; Sevak, K.K.; Reiner, T.; Mohindra, P.; Carlin, S.; Zanzonico, P.; Weissleder, R.; Lewis, J.S. A Pretargeted PET Imaging Strategy Based on Bioorthogonal Diels–Alder Click Chemistry. J. Nucl. Med. 2013, 54, 1389–1396.
6. Keinänen, O.; Fung, K.; Pourat, J.; Jallinoja, V.; Vivier, D.; Pillarsetty, N.K.; Airaksinen, A.J.; Lewis, J.S.; Zeglis, B.M.; Sarparanta, M. Pretargeting of internalizing trastuzumab and cetuximab with a 18F-tetrazine tracer in xenograft models. EJNMMI Res. 2017, 7, 95.
7. Altai, M.; Membreno, R.; Cook, B.; Tolmachev, V.; Zeglis, B.M. Pretargeted Imaging and Therapy. J. Nucl. Med. 2017, 58, 1553–1559.
8. Batra, S.K.; Jain, M.; Wittel, U.; Chauhan, S.C.; Colcher, D. Pharmacokinetics and biodistribution of genetically engineered antibodies. Curr. Opin. Biotechnol. 2002, 13, 603–608.
9. Sharkey, R.M.; Blumenthal, R.D.; Hansen, H.J.; Goldenberg, D.M. Biological considerations for radioimmunotherapy. Cancer Res. 1990, 50, 964–970.
10. Patra, M.; Zarschler, K.; Pietzsch, H.-J.; Stephan, H.; Gasser, G. New insights into the pretargeting approach to image and treat tumours. Chem. Soc. Rev. 2016, 45, 6415–6431.
11. Reardan, D.T.; Meares, C.F.; Goodwin, D.; McTigue, M.; David, G.S.; Stone, M.R.; Leung, J.P.; Bartholomew, R.M.; Frincke, J.M. Antibodies against metal chelates. Nature 1985, 316, 265–268.
12. Goodwin, D.A.; Mears, C.F.; McTigue, M.; David, G.S. Goodwin1986.Pdf. Nucl. Med. Commun. 1986, 7, 569–580.
13. Goodwin, D.; Meares, C.; Diamanti, C.; McCall, M.; Lai, C.; Torti, F.; McTigue, M.; Martin, B. Use of specific antibody for rapid clearance of circulating blood background from radiolabeled tumor imaging proteins. Eur. J. Nucl. Med. Mol. Imaging 1984, 9, 209–215.
14. Stéen, E.J.L.; Edem, P.; Norregaard, K.; Jørgensen, J.T.; Shalgunov, V.; Kjaer, A.; Herth, M.M. Pretargeting in nuclear imaging and radionuclide therapy: Improving efficacy of theranostics and nanomedicines. Biomaterials 2018, 179, 209–245.
15. Bailly, C.; Bodet-Milin, C.; Rousseau, C.; Faivre-Chauvet, A.; Kraeber-Bodéré, F.; Barbet, J. Pretargeting for imaging and therapy in oncological nuclear medicine. EJNMMI Radiopharm. Chem. 2017, 2, 6.
16. Liu, G. A Revisit to the Pretargeting Concept—A Target Conversion. Front. Pharmacol. 2018, 9, 1–14.
17. Tienken, L.; Drude, N.; Schau, I.; Winz, O.H.; Temme, A.; Weinhold, E.; Mottaghy, F.M.; Morgenroth, A. Evaluation of a Pretargeting Strategy for Molecular Imaging of the Prostate Stem Cell Antigen with a Single Chain Antibody. Sci. Rep. 2018, 8, 1–9.
18. Cook, B.E.; Adumeau, P.; Membreno, R.; Carnazza, K.E.; Brand, C.; Reiner, T.; Agnew, B.J.; Lewis, J.; Zeglis, B.M. Pretargeted PET Imaging Using a Site-Specifically Labeled Immunoconjugate. Bioconjug. Chem. 2016, 27, 1789–1795.
19. Zeglis, B.M.; Brand, C.; Abdel-Atti, D.; Carnazza, K.E.; Cook, B.E.; Carlin, S.; Reiner, T.; Lewis, J.S. Optimization of a Pretargeted Strategy for the PET Imaging of Colorectal Carcinoma via the Modulation of Radioligand Pharmacokinetics. Mol. Pharm. 2015, 12, 3575–3587.

20. Adumeau, P.; Carnazza, K.E.; Brand, C.; Carlin, S.D.; Reiner, T.; Agnew, B.J.; Lewis, J.S.; Zeglis, B.M. A Pretargeted Approach for the Multimodal PET/NIRF Imaging of Colorectal Cancer. Theranostics 2016, 6, 2267–2277.
21. Houghton, J.L.; Membreno, R.; Abdel-Atti, D.; Cunanan, K.M.; Carlin, S.; Scholz, W.W.; Zanzonico, P.B.; Lewis, J.S.; Zeglis, B.M. Establishment of the invivo efficacy of pretargeted radioimmunotherapy utilizing inverse electron demand diels-alder click chemistry. Mol. Cancer Ther. 2017, 16, 124–133.
22. Rossin, R.; Verkerk, P.R.; Van Den Bosch, S.M.; Vulders, R.C.M.; Verel, I.; Lub, J.; Robillard, M.S. In vivo chemistry for pretargeted tumor imaging in live mice. Angew. Chem. Int. Ed. 2010, 49, 3375–3378.
23. Liu, G.; Dou, S.; Chen, X.; Chen, L.; Liu, X.; Rusckowski, M.; Hnatowich, D.J. Adding a Clearing Agent to Pretargeting Does Not Lower the Tumor Accumulation of the Effector as Predicted. Cancer Biother. Radiopharm. 2010, 25, 757–762.
24. Karmani, L.; Levêque, P.; Bouzin, C.; Bol, A.; Dieu, M.; Walrand, S.; Borght, T.V.; Feron, O.; Grégoire, V.; Bonifazi, D.; et al. Biodistribution of 125I-labeled anti-endoglin antibody using SPECT/CT imaging: Impact of in vivo deiodination on tumor accumulation in mice. Nucl. Med. Biol. 2016, 43, 415–423.
25. Rossin, R.; Lappchen, T.; Bosch, S.M.V.D.; Laforest, R.; Robillard, M.S. Diels-Alder Reaction for Tumor Pretargeting: In Vivo Chemistry Can Boost Tumor Radiation Dose Compared with Directly Labeled Antibody. J. Nucl. Med. 2013, 54, 1989–1995.
26. Mirallié, E.; Saï-Maurel, C.; Faivre-Chauvet, A.; Regenet, N.; Chang, C.-H.; Goldenberg, D.M.; Chatal, J.-F.; Barbet, J.; Thedrez, P. Improved pretargeted delivery of radiolabelled hapten to human tumour xenograft in mice by avidin chase of circulating bispecific antibody. Eur. J. Nucl. Med. Mol. Imaging 2005, 32, 901–909.
27. Myrhammar, A.; Vorobyeva, A.; Westerlund, K.; Yoneoka, S.; Orlova, A.; Tsukahara, T.; Tolmachev, V.; Karlström, A.E.; Altai, M. Evaluation of an antibody-PNA conjugate as a clearing agent for antibody-based PNA-mediated radionuclide pretargeting. Sci. Rep. 2020, 10, 1–12.
28. Cheal, S.M.; Patel, M.; Yang, G.; Veach, D.; Xu, H.; Guo, H.-F.; Zanzonico, P.B.; Axworthy, D.B.; Cheung, N.-K.V.; Ouerfelli, O.; et al. An N-Acetylgalactosamino Dendron-Clearing Agent for High-Therapeutic-Index DOTA-Hapten Pretargeted Radioimmunotherapy. Bioconjug. Chem. 2020, 31, 501–506.
29. Zheng, M.; Zheng, L.; Zhang, P.; Li, J.; Zhang, Y. Development of Bioorthogonal Reactions and Their Applications in Bioconjugation. Molecules 2015, 20, 3190–3205.
30. Devaraj, N.K. The Future of Bioorthogonal Chemistry. ACS Central Sci. 2018, 4, 952–959.
31. Kenry; Liu, B. Bio-orthogonal Click Chemistry for In Vivo Bioimaging. Trends Chem. 2019, 1, 763–778.
32. Knight, J.; Cornelissen, B. Bioorthogonal chemistry: Implications for pretargeted nuclear (PET/SPECT) imaging and therapy. Am. J. Nucl. Med. Mol. Imaging 2014, 4, 96–113.
33. Porte, K.; Riberaud, M.; Châtre, R.; Audisio, D.; Papot, S.; Taran, F. Bioorthogonal Reactions in Animals. ChemBioChem 2021, 22, 100–113.
34. Sletten, E.M.; Bertozzi, C.R. Bioorthogonal Reactions. Acc. Chem. Res. 2011, 44, 666–676.
35. McKay, C.; Finn, M. Click Chemistry in Complex Mixtures: Bioorthogonal Bioconjugation. Chem. Biol. 2014, 21, 1075–1101.
36. Kolb, H.C.; Finn, M.G.; Sharpless, K.B. Click Chemistry: Diverse Chemical Function from a Few Good Reactions. Angew. Chem. Int. Ed. 2001, 40, 2004–2021.
37. Sletten, E.M.; Bertozzi, C.R. Bioorthogonal Chemistry: Fishing for Selectivity in a Sea of Functionality. Angew. Chem. Int. Ed. 2009, 48, 6974–6998.
38. Jewett, J.C.; Bertozzi, C.R. Cu-free click cycloaddition reactions in chemical biology. Chem. Soc. Rev. 2010, 39, 1272–1279.
39. Baskin, J.M.; Bertozzi, C.R. Bioorthogonal Click Chemistry: Covalent Labeling in Living Systems. QSAR Comb. Sci. 2007, 26, 1211–1219.
40. Best, M.D. Click Chemistry and Bioorthogonal Reactions: Unprecedented Selectivity in the Labeling of Biological Molecules. Biochemistry 2009, 48, 6571–6584.
41. Ariza, X.; Urpí, F.; Vilarrasa, J. A practical procedure for the preparation of carbamates from azides. Tetrahedron Lett. 1999, 40, 7515–7517.
42. Staudinger, H.; Hauser, E. Über neue organische Phosphorverbindungen IV Phosphinimine. Helv. Chim. Acta 1921, 4, 861–886.

43. Saxon, E.; Bertozzi, C.R. Cell surface engineering by a modified Staudinger reaction. Science 2000, 287, 2007–2010.
44. Van Berkel, S.S.; Van Eldijk, M.B.; Van Hest, J.C.M. Staudinger ligation as a method for bioconjugation. Angew. Chem. Int. Ed. 2011, 50, 8806–8827.
45. Saxon, E.; Armstrong, J.I.; Bertozzi, C.R. A “traceless” Staudinger ligation for the chemoselective synthesis of amide bonds. Org. Lett. 2000, 2, 2141–2143.
46. Hall, K.; Asfura, K.G.; Stabler, C. Microencapsulation of islets within alginate/poly(ethylene glycol) gels cross-linked via Staudinger ligation. Acta Biomater. 2011, 7, 614–624.
47. Vugts, D.J.; Vervoort, A.; Walsum, M.S.-V.; Visser, G.W.M.; Robillard, M.S.; Versteegen, R.; Vulders, R.; Herscheid, J.D.M.; Van Dongen, G.A.M.S. Synthesis of Phosphine and Antibody–Azide Probes forin VivoStaudinger Ligation in a Pretargeted Imaging and Therapy Approach. Bioconjug. Chem. 2011, 22, 2072–2081.
48. Oliveira, B.; Guo, Z.; Bernardes, G.J.L. Inverse electron demand Diels–Alder reactions in chemical biology. Chem. Soc. Rev. 2017, 46, 4895–4950.
49. Rostovtsev, V.V.; Green, L.G.; Fokin, V.V.; Sharpless, K.B. A stepwise huisgen cycloaddition process: Copper(I)-catalyzed regioselective “ligation” of azides and terminal alkynes. Angew. Chem. Int. Ed. 2002, 41, 2596–2599.
50. Tornøe, C.W.; Christensen, C.; Meldal, M. Peptidotriazoles on Solid Phase: [1,2,3]-Triazoles by Regiospecific Copper(I)-Catalyzed 1,3-Dipolar Cycloadditions of Terminal Alkynes to Azides. J. Org. Chem. 2002, 67, 3057–3064.
51. Kim, E.; Koo, H. Biomedical applications of copper-free click chemistry: In vitro, in vivo, and ex vivo. Chem. Sci. 2019, 10, 7835–7851.
52. Uttamapinant, C.; Sanchez, M.I.; Liu, D.S.; Yao, J.Z.; White, K.A.; Grecian, S.; Clark, S.; Gee, K.R.; Ting, A.Y.; Clarke, S. Site-specific protein labeling using PRIME and chelation-assisted click chemistry. Nat. Protoc. 2013, 8, 1620–1634.
53. Chen, X.; Wu, Y.-W. Selective chemical labeling of proteins. Org. Biomol. Chem. 2016, 14, 5417–5439.
54. Presolski, S.I.; Hong, V.; Cho, S.-H.; Finn, M. Tailored Ligand Acceleration of the Cu-Catalyzed Azide−Alkyne Cycloaddition Reaction: Practical and Mechanistic Implications. J. Am. Chem. Soc. 2010, 132, 14570–14576.
55. Soriano Del Amo, D.; Wang, W.; Jiang, H.; Besanceney, C.; Yan, A.C.; Levy, M.; Liu, Y.; Marlow, F.L.; Wu, P. Biocompatible copper(I) catalysts for in vivo imaging of glycans. J. Am. Chem. Soc. 2010, 132, 16893–16899.
56. Agard, N.J.; Prescher, J.A.; Bertozzi, C.R. A Strain-Promoted [3 + 2] Azide−Alkyne Cycloaddition for Covalent Modification of Biomolecules in Living Systems. J. Am. Chem. Soc. 2004, 126, 15046–15047.
57. Debets, M.; Van Berkel, S.S.; Dommerholt, J.; Dirks, A.J.; Rutjes, F.P.J.T.; Van Delft, F.L. Bioconjugation with Strained Alkenes and Alkynes. Acc. Chem. Res. 2011, 44, 805–815.
58. Ning, X.; Guo, J.; Wolfert, M.; Boons, G.-J. Visualizing Metabolically Labeled Glycoconjugates of Living Cells by Copper-Free and Fast Huisgen Cycloadditions. Angew. Chem. Int. Ed. 2008, 47, 2253–2255.
59. Rondon, A.; Degoul, F. Antibody Pretargeting Based on Bioorthogonal Click Chemistry for Cancer Imaging and Targeted Radionuclide Therapy. Bioconjug. Chem. 2019, 31, 159–173, doi:10.1021/acs.bioconjchem.9b00761.
60. White, B.W. Effect of temporal ordering on visual recognition. Percept. Mot. Skills 1962, 15, 75–81.
61. Bosch, S.V.D.; Rossin, R.; Verkerk, P.R.; Hoeve, W.T.; Janssen, H.; Lub, J.; Robillard, M. Evaluation of strained alkynes for Cu-free click reaction in live mice. Nucl. Med. Biol. 2013, 40, 415–423.
62. Lee, D.-E.; Na, J.H.; Lee, S.; Kang, C.M.; Kim, H.N.; Han, S.J.; Kim, H.; Choe, Y.S.; Jung, K.-H.; Lee, K.C.; et al. Facile Method To Radiolabel Glycol Chitosan Nanoparticles with 64Cu via Copper-Free Click Chemistry for MicroPET Imaging. Mol. Pharm. 2012, 10, 2190–2198.
63. Au, K.M.; Tripathy, A.; Lin, C.P.-I.; Wagner, K.; Hong, S.; Wang, A.; Park, S.I. Bespoke Pretargeted Nanoradioimmunotherapy for the Treatment of Non-Hodgkin Lymphoma. ACS Nano 2018, 12, 1544–1563.
64. Boutureira, O.; Bernardes, G.J. Advances in Chemical Protein Modification. Chem. Rev. 2015, 115, 2174–2195.
65. Soellner, M.B.; Nilsson, B.L.; Raines, R.T. Reaction Mechanism and Kinetics of the Traceless Staudinger Ligation. J. Am. Chem. Soc. 2006, 128, 8820–8828.
66. Blackman, M.L.; Royzen, M.; Fox, J.M. Tetrazine Ligation: Fast Bioconjugation Based on Inverse-Electron-Demand Diels−Alder Reactivity. J. Am. Chem. Soc. 2008, 130, 13518–13519.

67. Pagel, M. Inverse electron demand Diels-Alder (IEDDA) reactions in peptide chemistry. J. Pept. Sci. 2019, 25, e3141.
68. Jamroz, D.; Fischer-Durand, N.; Palusiak, M.; Wojtulewski, S.; Jarzyński, S.; Stępniewska, M.; Salmain, M.; Rudolf, B. Inverse electron-demand Diels-Alder (iEDDA) bioorthogonal conjugation of half-sandwich transition metallocarbonyl entities to a model protein. Appl. Organomet. Chem. 2020, 34, 1–12.
69. Devaraj, N.K.; Weissleder, R. Biomedical Applications of Tetrazine Cycloadditions. Acc. Chem. Res. 2011, 44, 816–827.
70. Sauer, J. Structure-reactivity problem in cycloaddition reactions to form heterocyclic compounds. Chemistry of heterocyclic compounds. 1995, 31, 1140–1154.
71. Mushtaq, S.; Yun, S.-J.; Jeon, J. Recent Advances in Bioorthogonal Click Chemistry for Efficient Synthesis of Radiotracers and Radiopharmaceuticals. Molecules 2019, 24, 3567.
72. Maggi, A.; Ruivo, E.; Fissers, J.; Vangestel, C.; Chatterjee, S.; Joossens, J.; Sobott, F.; Staelens, S.; Stroobants, S.; Van Der Veken, P.; et al. Development of a novel antibody–tetrazine conjugate for bioorthogonal pretargeting. Org. Biomol. Chem. 2016, 14, 7544–7551.
73. Wijnen, J.W.; Zavarise, S.; Engberts, J.B.F.N.; Charton, M. Substituent Effects on an Inverse Electron Demand Hetero Diels−Alder Reaction in Aqueous Solution and Organic Solvents: Cycloaddition of Substituted Styrenes to Di(2-pyridyl)-1,2,4,5-tetrazine. J. Org. Chem. 1996, 61, 2001–2005.
74. Stéen, J.E.L.; Jørgensen, J.T.; Christoph, D.; Battisti, U.M.; Nørregard, K.; Edem, P.E.; Bratteby, K.; Shalgunov, V.; Wilkovitsch, M.; Svatunek, D.; et al. Lipophilicity and click reactivity determine the performance of bioorthogonal tetrazine tools in pretargeted in vivo chemistry. ACS Pharmacol. Transl. Sci. 2021, 4, 824–833.
75. Devaraj, N.K.; Weissleder, R.; Hilderbrand, S.A. Tetrazine-Based Cycloadditions: Application to Pretargeted Live Cell Imaging. Bioconjug. Chem. 2008, 19, 2297–2299.
76. Rossin, R.; Bosch, S.M.V.D.; Hoeve, W.T.; Carvelli, M.; Versteegen, R.; Lub, J.; Robillard, M.S. Highly Reactive trans-Cyclooctene Tags with Improved Stability for Diels–Alder Chemistry in Living Systems. Bioconjug. Chem. 2013, 24, 1210–1217.
77. Wang, M.; Svatunek, D.; Rohlfing, K.; Liu, Y.; Wang, H.; Giglio, B.; Yuan, H.; Wu, Z.; Li, Z.; Fox, J. Conformationally Strained trans-Cyclooctene (sTCO) Enables the Rapid Construction of 18F-PET Probes via Tetrazine Ligation. Theranostics 2016, 6, 887–895.
78. Ramil, C.P.; Dong, M.; An, P.; Lewandowski, T.M.; Yu, Z.; Miller, L.J.; Lin, Q. Spirohexene-Tetrazine Ligation Enables Bioorthogonal Labeling of Class B G Protein-Coupled Receptors in Live Cells. J. Am. Chem. Soc. 2017, 139, 13376–13386.
79. Stöckmann, H.; Neves, A.A.; Day, H.A.; Stairs, S.; Brindle, K.M.; Leeper, F.J. (E,E)-1,5-Cyclooctadiene: A small and fast click-chemistry multitalent. Chem. Commun. 2011, 47, 7203–7205.
80. Longo, B.; Zanato, C.; Piras, M.; Dall'Angelo, S.; Windhorst, A.D.; Vugts, D.J.; Baldassarre, M.; Zanda, M. Design, Synthesis, Conjugation, and Reactivity of Novel trans,trans-1,5-Cyclooctadiene-Derived Bioorthogonal Linkers. Bioconjug. Chem. 2020, 31, 2201–2210.
81. Ferreira, V.F.C.; Oliveira, B.L.; D'Onofrio, A.; Farinha, C.M.; Gano, L.; Paulo, A.; Bernardes, G.J.L.; Mendes, F. In Vivo Pretargeting Based on Cysteine-Selective Antibody Modification with IEDDA Bioorthogonal Handles for Click Chemistry. Bioconjug. Chem. 2020, 32, 121–132.
82. Van Dongen, G.A.M.S.; Poot, A.J.; Vugts, D.J. PET imaging with radiolabeled antibodies and tyrosine kinase inhibitors: Immuno-PET and TKI-PET. Tumor Biol. 2012, 33, 607–615.
83. Zaroff, S.; Tan, G. Hybridoma technology: The preferred method for monoclonal antibody generation for in vivo applications. Biotechology 2019, 67, 90–92.
84. Treglia, G.; Salsano, M. PET imaging using radiolabelled antibodies: Future direction in tumor diagnosis and correlate applications. Res. Rep. Nucl. Med. 2013, 3, 9–17.
85. Bailly, C.; Cléry, P.-F.; Faivre-Chauvet, A.; Bourgeois, M.; Guérard, F.; Haddad, F.; Barbet, J.; Chérel, M.; Kraeber-Bodere, F.; Carlier, T.; et al. Immuno-PET for clinical theranostic approaches. Int. J. Mol. Sci. 2016, 18, 57.
86. Ruivo, E.; Adhikari, K.; Elvas, F.; Fissers, J.; Vangestel, C.; Staelens, S.; Stroobants, S.; Van Der Veken, P.; Wyffels, L.; Augustyns, K. Improved stability of a novel fluorine-18 labeled TCO analogue for pretargeted PET imaging. Nucl. Med. Biol. 2019, 76-77, 36–42.

87. Houghton, J.L.; Zeglis, B.M.; Abdel-Atti, D.; Sawada, R.; Scholz, W.W.; Lewis, J.S. Pretargeted Immuno-PET of Pancreatic Cancer: Overcoming Circulating Antigen and Internalized Antibody to Reduce Radiation Doses. J. Nucl. Med. 2016, 57, 453–459.
88. Meyer, J.-P.; Houghton, J.L.; Kozlowski, P.; Abdel-Atti, D.; Reiner, T.; Pillarsetty, N.V.K.; Scholz, W.W.; Zeglis, B.M.; Lewis, J.S. 18F-Based Pretargeted PET Imaging Based on Bioorthogonal Diels–Alder Click Chemistry. Bioconjug. Chem. 2016, 27, 298–301.
89. Keinänen, O.; Li, X.-G.; Chenna, N.K.; Lumen, D.; Ott, J.; Molthoff, C.F.M.; Sarparanta, M.; Helariutta, K.; Vuorinen, T.; Windhorst, A.D.; et al. A New Highly Reactive and Low Lipophilicity Fluorine-18 Labeled Tetrazine Derivative for Pretargeted PET Imaging. ACS Med. Chem. Lett. 2015, 7, 62–66.
90. Poty, S.; Membreno, R.; Glaser, J. M.; Ragupathi, A.; Scholz, W. W.; Zeglis, B. M.; Lewis, J. S. The inverse electron-demand Diels-Alder reaction as a new methodology for the synthesis of 225Ac-labelled radioimmunoconjugates. ChemComm. 2018, 54, 2599-2602.
91. Meyer, J.-P.; Tully, K.; Jackson, J.; Dilling, T.R.; Reiner, T.; Lewis, J.S. Bioorthogonal Masking of Circulating Antibody–TCO Groups Using Tetrazine-Functionalized Dextran Polymers. Bioconjug. Chem. 2018, 29, 538–545.
92. Membreno, R.; Keinänen, O.; Cook, B.E.; Tully, K.M.; Fung, K.C.; Lewis, J.S.; Zeglis, B.M. Toward the Optimization of Click-Mediated Pretargeted Radioimmunotherapy. Mol. Pharm. 2019, 16, 2259–2263.
93. Membreno, R.; Cook, B.E.; Fung, K.; Lewis, J.S.; Zeglis, B.M. Click-Mediated Pretargeted Radioimmunotherapy of Colorectal Carcinoma. Mol. Pharm. 2018, 15, 1729–1734.
94. Keinänen, O.; Brennan, J.M.; Membreno, R.; Fung, K.; Gangangari, K.; Dayts, E.J.; Williams, C.J.; Zeglis, B.M. Dual Radionuclide Theranostic Pretargeting. Mol. Pharm. 2019, 16, 4416–4421.
95. Cook, B.E.; Membreno, R.; Zeglis, B.M. Dendrimer Scaffold for the Amplification of In Vivo Pretargeting Ligations. Bioconjug. Chem. 2018, 29, 2734–2740.
96. Rahim, M.K.; Kota, R.; Haun, J.B. Enhancing Reactivity for Bioorthogonal Pretargeting by Unmasking Antibody-Conjugated trans-Cyclooctenes. Bioconjug. Chem. 2015, 26, 352–360.
97. Li, Z.; Cai, H.; Hassink, M.; Blackman, M.L.; Brown, R.C.D.; Conti, P.S.; Fox, J.M. Tetrazine–trans-cyclooctene ligation for the rapid construction of 18F labeled probes. Chem. Commun. 2010, 46, 8043–8045.
98. Wyffels, L.; Thomae, D.; Waldron, A.-M.; Fissers, J.; Dedeurwaerdere, S.; Van Der Veken, P.; Joossens, J.; Stroobants, S.; Augustyns, K.; Staelens, S. In vivo evaluation of 18F-labeled TCO for pre-targeted PET imaging in the brain. Nucl. Med. Biol. 2014, 41, 513–523.
99. Billaud, E.M.F.; Belderbos, S.; Cleeren, F.; Maes, W.; Van De Wouwer, M.; Koole, M.; Verbruggen, A.; Himmelreich, U.; Geukens, N.; Bormans, G. Pretargeted PET Imaging Using a Bioorthogonal 18F-Labeled trans-Cyclooctene in an Ovarian Carcinoma Model. Bioconjug. Chem. 2017, 28, 2915–2920.
100. Goos, J.; Cho, A.; Carter, L.M.; Dilling, T.R.; Davydova, M.; Mandleywala, K.; Puttick, S.; Gupta, A.; Price, W.S.; Quinn, J.F.; et al. Delivery of polymeric nanostars for molecular imaging and endoradiotherapy through the enhanced permeability and retention (EPR) effect. Theranostics 2020, 10, 567–584.
101. Van Onzen, A.H.A.M.; Rossin, R.; Schenning, A.P.H.J.; Nicolay, K.; Milroy, L.G.; Robillard, M.S.; Robillard, M.S.; Brunsveld, L. Tetrazine—Trans-Cyclooctene Chemistry Applied to Fabricate Self-Assembled Fluorescent and Radioactive Nanoparticles for in Vivo Dual Mode Imaging. Bioconjug. Chem. 2019, 30, 547–551.
102. Petkau-Milroy, K.K.; Kaeser, A.A.; Fischer, I.I.; Brunsveld, L.L.; Schenning, A.P.H.J. Pre- and Postfunctionalized Self-Assembled π-Conjugated Fluorescent Organic Nanoparticles for Dual Targeting. J. Am. Chem. Soc. 2011, 133, 17063–17071.
103. Keinänen, O.; Mäkilä, E.M.; Lindgren, R.; Virtanen, H.; Liljenbäck, H.; Oikonen, V.; Sarparanta, M.; Molthoff, C.; Windhorst, A.D.; Roivainen, A.; et al. Pretargeted PET Imaging of trans-Cyclooctene-Modified Porous Silicon Nanoparticles. ACS Omega 2017, 2, 62–69.
104. Rossin, R.; Versteegen, R.M.; Wu, J.; Khasanov, A.; Wessels, H.J.; Steenbergen, E.J.; Hoeve, W.T.; Janssen, H.M.; Van Onzen, A.H.A.M.; Hudson, P.J.; et al. Chemically triggered drug release from an antibody-drug conjugate leads to potent antitumour activity in mice. Nat. Commun. 2018, 9, 1–11.
105. Versteegen, R.M.; Hoeve, W.T.; Rossin, R.; de Geus, M.; Janssen, H.M.; Robillard, M.S. Click-to-Release from trans-Cyclooctenes: Mechanistic Insights and Expansion of Scope from Established Carbamate to Remarkable Ether Cleavage. Angew. Chem. Int. Ed. 2018, 57, 10494–10499.

106. Rossin, R.; Van Duijnhoven, S.M.J.; Ten Hoeve, W.; Janssen, H.M.; Kleijn, L.H.J.; Hoeben, F.J.M.; Versteegen, R.M.; Robillard, M.S. Triggered Drug Release from an Antibody-Drug Conjugate Using Fast "click-to-Release. Chemistry in Mice. Bioconjug. Chem. 2016, 27, 1697–1706.
107. Li, H.; Conde, J.; Guerreiro, A.; Bernardes, G.J.L. Tetrazine Carbon Nanotubes for Pretargeted In Vivo "Click-to-Release" Bioorthogonal Tumour Imaging. Angew. Chem. Int. Ed. 2020, 59, 16023–16032.
108. Kozma, E.; Demeter, O.; Kele, P. Bio-orthogonal Fluorescent Labelling of Biopolymers through Inverse-Electron-Demand Diels-Alder Reactions. ChemBioChem 2017, 18, 486–501.
109. Devaraj, N.K.; Hilderbrand, S.; Upadhyay, R.; Mazitschek, R.; Weissleder, R. Bioorthogonal Turn-On Probes for Imaging Small Molecules inside Living Cells. Angew. Chem. Int. Ed. 2010, 49, 2869–2872.
110. Meimetis, L.G.; Carlson, J.; Giedt, R.J.; Kohler, R.; Weissleder, R. Ultrafluorogenic Coumarin-Tetrazine Probes for Real-Time Biological Imaging. Angew. Chem. Int. Ed. 2014, 53, 7531–7534.
111. Carlson, J.; Meimetis, L.G.; Hilderbrand, S.A.; Weissleder, R. BODIPY-Tetrazine Derivatives as Superbright Bioorthogonal Turn-on Probes. Angew. Chem. Int. Ed. 2013, 52, 6917–6920.
112. Knorr, G.; Kozma, E.; Herner, A.; Lemke, E.; Kele, P. New Red-Emitting Tetrazine-Phenoxazine Fluorogenic Labels for Live-Cell Intracellular Bioorthogonal Labeling Schemes. Chem. A Eur. J. 2016, 22, 8972–8979.
113. Németh, E.; Knorr, G.; Németh, K.; Kele, P. A Bioorthogonally Applicable, Fluorogenic, Large Stokes-Shift Probe for Intracellular Super-Resolution Imaging of Proteins. Biomolecules 2020, 10, 397.
114. Kormos, A.; Kern, D.; Egyed, A.; Söveges, B.; Németh, K.; Kele, P. Microscope laser assisted photooxidative activation of bioorthogonal ClickOx probes. Chem. Commun. 2020, 56, 5425–5428.
115. Kozma, E.; Girona, G.E.; Paci, G.; Lemke, E.A.; Kele, P. Bioorthogonal double-fluorogenic siliconrhodamine probes for intracellular super-resolution microscopy. Chem. Commun. 2017, 53, 6696–6699.
116. Bojtár, M.; Németh, K.; Domahidy, F.; Knorr, G.; Verkman, A.; Kállay, M.; Kele, P. Conditionally Activatable Visible-Light Photocages. J. Am. Chem. Soc. 2020, 142, 15164–15171.
117. Renard, E.; Camps, E.C.; Canovas, C.; Kip, A.; Gotthardt, M.; Rijpkema, M.; Denat, F.; Goncalves, V.; van Lith, S. Site-Specific Dual-Labeling of a VHH with a Chelator and a Photosensitizer for Nuclear Imaging and Targeted Photodynamic Therapy of EGFR-Positive Tumors. Cancers 2021, 13, 428.
118. Linden, G.; Zhang, L.; Pieck, F.; Linne, U.; Kosenkov, D.; Tonner, R.; Vázquez, O. Conditional Singlet Oxygen Generation through a Bioorthogonal DNA-targeted Tetrazine Reaction. Angew. Chem. Int. Ed. 2019, 58, 12868–12873.
119. Linden, G.; Vázquez, O. Bioorthogonal Turn-On BODIPY-Peptide Photosensitizers for Tailored Photodynamic Therapy. Chem. A Eur. J. 2020, 26, 10014–10023.
120. Dong, Y.; Tu, Y.; Wang, K.; Xu, C.; Yuan, Y.; Wang, J. A General Strategy for Macrotheranostic Prodrug Activation: Synergy between the Acidic Tumor Microenvironment and Bioorthogonal Chemistry. Angew. Chem. Int. Ed. 2020, 59, 7168–7172.

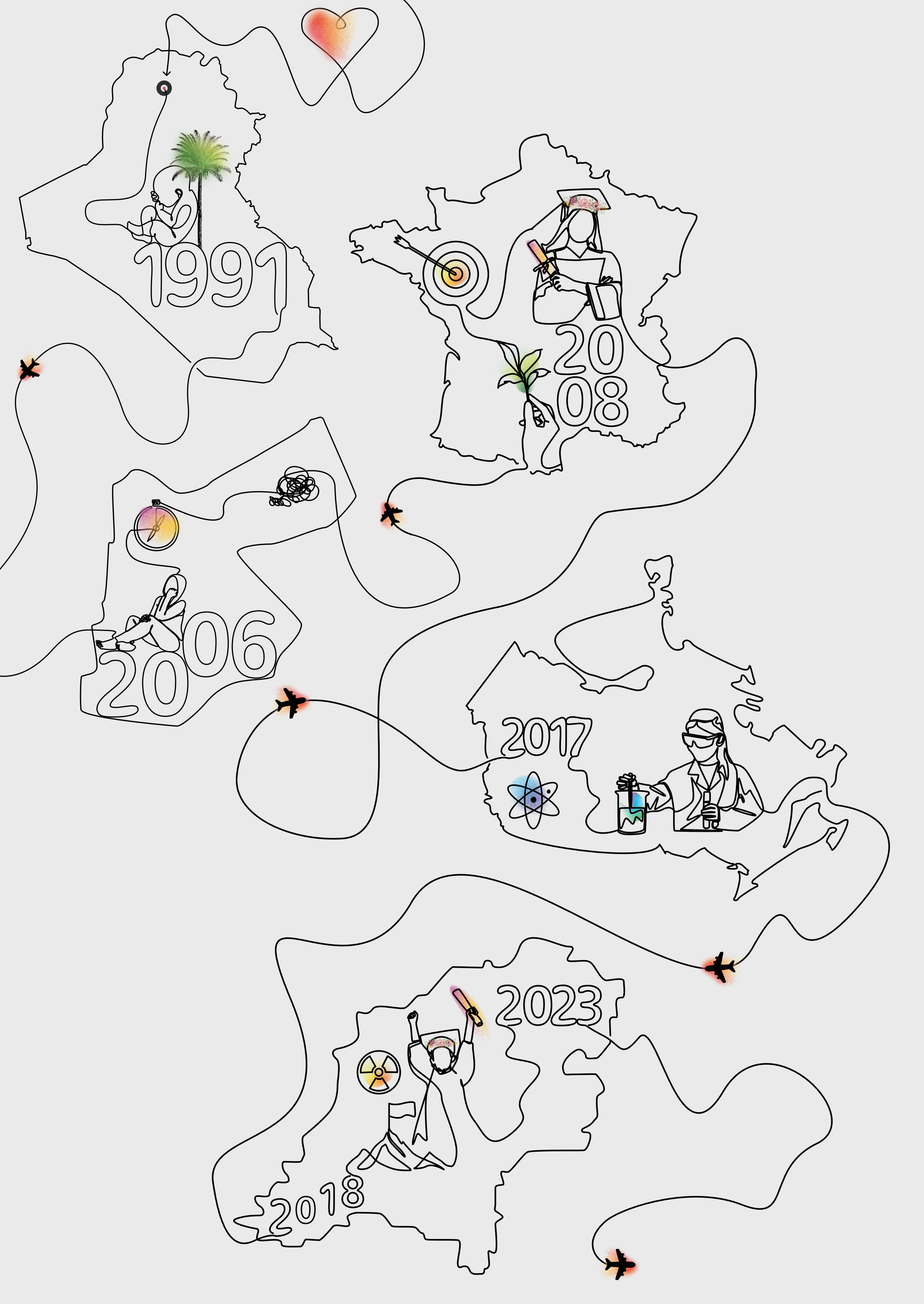
1991
2008
2006
2017
2023
2018

# CHAPTER 3

## Towards Complete Tumor Resection: Novel Dual-Modality Probes for Improved Image-Guided Surgery of GRPR-Expressing Prostate Cancer

Maryana Handula[1,†], Marjolein Verhoeven[1,†], Kuo-Ting Chen[2], Joost Haeck[3], Marion de Jong[1,‡], Simone U. Dalm[1] and Yann Seimbille[1,4]

[1] Department of Radiology and Nuclear Medicine, Erasmus MC, University Medical Center Rotterdam, 3015 GD Rotterdam, The Netherlands

[2] Department of Chemistry, National Dong Hwa University, Shoufeng, Hualien 974301, Taiwan

[3] AMIE Core Facility, Erasmus MC, University Medical Center Rotterdam, 3015 GD Rotterdam, The Netherlands

[4] Life Sciences Division, TRIUMF, Vancouver, BC V6T 2A3, Canada

[†] These authors contributed equally to the work.

[‡] This author is deceased.

*Pharmaceutics. 2022;14(1):195*

**Abstract:** Nuclear and optical dual-modality probes can be of great assistance in prostate cancer localization, providing the means for both preoperative nuclear imaging and intraoperative surgical guidance. We developed a series of probes based on the backbone of the established GRPR-targeting radiotracer NeoB. The inverse electron demand of the Diels–Alder reaction was used to integrate the sulfo-cyanine 5 dye. Indium-111 radiolabeling, stability studies and a competition binding assay were carried out. Pilot biodistribution and imaging studies were performed in PC-3 tumor-bearing mice, using the best two dual-labeled probes. The dual-modality probes were radiolabeled with a high yield (>92%), were proven to be hydrophilic and demonstrated high stability in mouse serum (>94% intact labeled ligand at 4 h). The binding affinity for the GRPR was in the nanomolar range (21.9–118.7 nM). SPECT/CT images at 2 h p.i. clearly visualized the tumor xenograft and biodistribution studies, after scanning confirmed the high tumor uptake (8.47 ± 0.46%ID/g and 6.90 ± 0.81%ID/g for probe [$^{111}$In]In-**12** and [$^{111}$In]In-**15**, respectively). Receptor specificity was illustrated with blocking studies, and co-localization of the radioactive and fluorescent signal was verified by ex vivo fluorescent imaging. Although optimal tumor-to-blood and tumor-to-kidney ratios might not yet have been reached due to the prolonged blood circulation, our probes are promising candidates for the preoperative and intraoperative visualization of GRPR-positive prostate cancer.

**Keywords:** prostate cancer; PC-3; GRPR; NeoB; dual-modality imaging; IEDDA; sCy5; pre- and intraoperative imaging

## 1. Introduction

Worldwide, prostate cancer (PCa) is the second most frequently diagnosed cancer among men, with about 1.4 million new cases in 2020 alone [1]. The surgical removal of the prostate gland, in whole or in part, combined with pelvic lymph node dissection is one of the most widely used treatment options to cure localized PCa [2]. Although successful in many cases, the recurrence rate after radical prostatectomy is still as high as 20–40% [3]. One of the indicators for an increased risk of relapse is the observation of positive surgical margins [4]. As well as the multifocal nature of many primary prostate tumors, the need to maintain physiological functions, such as potency and continence, constitutes an additional challenge for surgeons [5,6]. Such a nerve-sparing surgical approach is a complex procedure and may therefore come at the expense of complete tumor eradication [7].

To reduce recurrence and, therefore, the need for secondary treatment, new imaging techniques that provide accurate surgical guidance may offer a solution. Over the years, fluorescence-guided surgery has emerged as a powerful tool for real-time intraoperative imaging in the surgical field [8]. To enable the precise removal of cancer tissue, receptor-targeting agents coupled to a fluorescent dye can lead to improved tumor localization [8]. Fluorescent tumor-targeting tracers have a high spatial resolution but are limited by their low tissue penetration. This is where nuclear medicine can play a pivotal role, as a radioisotope can be used for non-invasive preoperative nuclear imaging that supports surgical planning, as well as for the determination of the approximate localization of deeper lesions intraoperatively, with high sensitivity [9]. The benefits of the complementary use of a radioactive and fluorescent signal for image-guided surgery have led to an increased interest in the development of nuclear and optical dual-modality probes [10,11].

In nuclear medicine, recent advances in PCa-targeting radiotracers have provided a range of promising vectors for tumor targeting. One of the aberrantly overexpressed targets in PCa is the gastrin-releasing peptide receptor (GRPR) [12,13]. Imaging studies with GRPR-targeted radiotracers have demonstrated high tumor uptake and excellent visualization of tumor lesions in cancer patients [14–17]. NeoB (formerly known as NeoBOMB1) is one such established radiotracer, with a high binding affinity for GRPR, and is favorable for in vivo pharmacokinetics [18,19]. NeoB is therefore an excellent molecule to serve as a basis for the development of a dual-modality probe.

In this study, we integrated the sulfo-cyanine 5 fluorescent (sCy5) dye into the DOTA-coupled GRPR antagonist NeoB, using the inverse electron-demand Diels–Alder reaction (IEDDA) [20,21]. A tetrazine (Tz) moiety was coupled to the fluorescent dye and a *trans*-cyclooctene (TCO) group was incorporated to the backbone of NeoB via an additional lysine residue. A linker (*p*ADA or $PEG_4$) was introduced between the binding domain and the DOTA chelator, in combination with or without a $PEG_4$ linker between the TCO group and the lysine. The methodological approach taken in this research resulted in a panel of two single- and four dual-modality probes. After the development of these compounds, we assessed the effect of the dye attachment on the stability and affinity for GRPR in vitro and the tumor-targeting capability and biodistribution in vivo. With this study, we aim to demonstrate the potential of the novel GRPR-targeting dual-modality probes for preoperative and intraoperative PCa visualization.

## 2. Materials and Methods

### *2.1. General Information*

All chemicals and solvents were obtained from commercial suppliers and used without further purification unless specified. DOTA-tris(*t*Bu)ester was purchased from Macrocyclics (Plano, TX, USA) and $^{111}InCl_3$ (370.0 MBq/mL in HCl, pH 1.5–1.9) was provided by Curium (Petten, The Netherlands). Fmoc-based solid-phase peptide synthesis (SPPS) of peptide (**1**) was conducted on a CS136 automated peptide synthesizer (C.S. Bio, Menlo Park, CA, USA). High-performance liquid chromatography (HPLC) was carried out on a Waters 2659 series system (Etten-Leur, The Netherlands) equipped with a diode array detector and a radio-detector made by Canberra (Zelik, Belgium). Low-resolution electrospray ionization (ESI) mass spectra were recorded on a TSQ Quantum UltraTM triple quadrupole mass spectrometer from Thermo Fisher Scientific (Lansingerland, The Netherlands). Nuclear magnetic resonance (NMR) spectra were recorded in $D_2O$ on a Bruker AVANCE 400 (Leiden, The Netherlands) at an ambient temperature. Chemical shifts are given as δ values in ppm, and coupling constants *J* are given in Hz. The splitting patterns are reported as s (singlet), d (doublet), t (triplet), q (quadruplet), qt (quintuplet), m (multiplet), and br (broad signal). Instant thin-layer chromatography (iTLC) plates, on silica gel impregnated glass-fiber sheets, were eluted with sodium citrate (0.1 M, pH 5). The plates were analyzed by a bSCAN radio-chromatography scanner from BrightSpec (Antwerp, Belgium), equipped with a sodium iodide detector. The radioactive samples used for the determination of Log $D_{7.4}$, in vitro assays, and in vivo uptake in tissues were counted using a Gamma counter, Wizard 2480 (Perkin Elmer, Waltham, MA, USA). Activity measurements were performed using the VDC-405 dose calibrator (Comecer, Joure, The Netherlands). The analysis of the products was performed by HPLC on an analytical column (Gemini®, Phenomenex C-18, 5 µm, 250.0 × 4.6 mm) with a gradient elution of acetonitrile (ACN) (5% to 95% in $H_2O$, containing 0.1% TFA) at a flow rate of 1 mL/min over 30 min. Purification of the peptides was performed using a semi-preparative column (Luna®, Phenomenex C-18, 5 µm, 250.0 × 10.0 mm), with a gradient elution of ACN (10% to 90% in $H_2O$) at a flow rate of 3 mL/min over 30 min.

### *2.2. Chemistry and Radiochemistry*

2.2.1. Synthesis of fQWAVGH (**1**)

fQWAVGH (**1**) was synthesized using an $N^{\alpha}$-Fmoc solid-phase peptide synthesis strategy. The conjugation of the Fmoc-protected (**1**) sequence (D-Phe-Gln(Trt)-Trp(Boc)-Ala-Val-Gly-His(Trt)) to the 2-chlorotrityl chloride resin was carried out in dimethylformamide (DMF) with 2-(1*H*-benzotriazol-1-yl)-1,1,3,3-tetramethyluronium hexafluorophosphate (HBTU) (3.9 equiv.), Oxyma Pure (4 equiv.) and *N*,*N*-diisopropylethylamine (DIPEA) (8 equiv.) for 1 h. Fmoc deprotection was accomplished by treatment of the resin with a 20% solution of piperidine in DMF. Amide formation and Fmoc deprotection were monitored using the Kaiser test. Double couplings were performed when the reaction was not complete. The peptide synthesis was initiated by loading Fmoc-His(Trt)-OH (0.5 mmol, 1 equiv.) onto the 2-chlorotrityl chloride resin (2 g, average loading capacity: 1.6 mmol/g). The resin was shaken for 90 min at room temperature (rt). Then, the resin was capped using dichloromethane/methanol/*N*,*N*-diisopropylethylamine (DCM/MeOH/DIPEA) (20 mL, *v*:*v*:*v* = 80:15:5) for 15 min at rt. Subsequent Fmoc deprotection and coupling with Fmoc-Gly-OH (4 equiv.), Fmoc-Val-OH (4 equiv.), Fmoc-Ala-OH (4 equiv.), Fmoc-Trp(Boc)-OH (4 equiv.), Fmoc-Gln(Trt)-OH (4 equiv.) and Fmoc-D-Phe-OH (4 equiv.) were achieved following the same protocol described above.

2.2.2. TCO-*p*ADA-fQWAVGH-NHCH$[CH_2CH(CH_3)_2]_2$ (**4a**)

Once the peptide sequence was completed, the Boc-NH-*p*ADA-OH linker was coupled to the peptide (Scheme 1). Coupling of the linker was carried out by the treatment of **1** with Boc-NH-*p*ADA-OH (2 equiv.), a mixture of HBTU/Oxyma Pure (3.9 and 4 equiv., respectively) and DIPEA (8 equiv.). The beads were shaken for 2 h at rt, then they were washed thrice with DMF. Subsequently, the peptide **2a** was cleaved from the resin using a cleavage cocktail of 1,1,1,3,3,3-hexafluoro-2-propanol/dichloromethane (HFIP/DCM) (2 mL, *v*:*v* = 20:80). The beads were mixed for 1 h at rt and washed twice with the cleavage cocktail, then the liquid phase was collected in a round-bottomed flask. The solvent was removed using a rotary evaporator. The resulting peptide was precipitated using cold diethyl ether and collected by centrifugation. After cleavage, the coupling of 4-amino-2,6-dimethylheptane (2.5 equiv.) on the C-terminus was performed using benzotriazole-1-yl-oxy-tris-pyrrolidino-phosphonium hexafluorophosphate (PyBOP) (2.5 equiv.) and DIPEA (5 equiv.) in DMF. The reaction mixture was stirred for 1 h at rt, the solvent was removed under a vacuum and the product was collected by precipitation in cold diethyl ether. Global deprotection of the peptide was performed by treatment of the peptide with trifluoroacetic acid/water/triisopropyl silane (TFA/$H_2O$/TIS) (2 mL, *v*:*v*:*v* = 95:2.5:2.5) for 1 h at rt. Later, the TFA was removed using a gentle air stream, and the resulting crude product **3a** was washed with cold diethyl ether and collected by centrifugation. The **3a** was purified with a Sep-Pak C18 35 cc Vac cartridge (10 g) (Waters, Etten-Leur, The

Netherlands). The column was pre-conditioned with methanol (100 mL) and $H_2O$ (200 mL). The peptide was subsequently loaded onto the column and washed with water (200 mL) until the pH of the eluate became neutral. Then, **3a** was eluted using a mixture of $H_2O$/ACN (*v*:*v* = 1:1, 4 × 20 mL), followed by two fractions of 20 mL ACN. The fractions containing the product were combined and lyophilized for further experiments. The final product **4a** was prepared by adding *trans*-cyclooctene-*N*-hydroxysuccinimide ester (TCO-NHS ester, 3 equiv.), triethylamine (10 equiv.) and $H_2O$/ACN (2 mL, *v*:*v* = 1:1). The reaction was stirred for 3 h at rt. The crude compound was purified by the semi-preparative HPLC to provide **4a** as a white solid (8.6 mg, 2.0% yield). Analytical HPLC retention time of **4a**: $t_R$ = 18.5 min. Purity > 95%. ESI-MS: *m*/*z*, calculated: 1340.73, found: 1341.00 $[M + H]^+$.

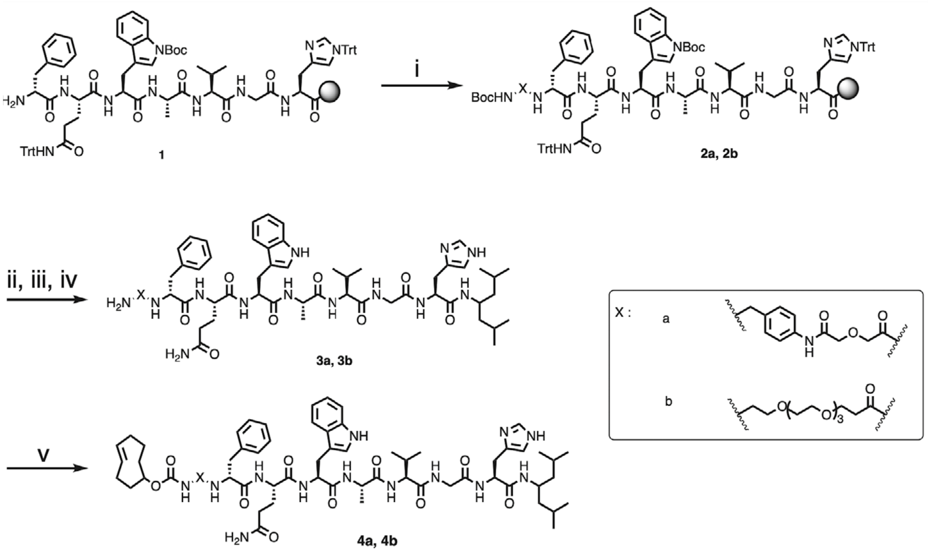

**Scheme 1.** Synthesis of **4a** and **4b**. Reagents and conditions: (**i**) linker a or b, HBTU/Oxyma Pure, DIPEA, 2 h, rt; (**ii**) HFIP/DCM, 1 h, rt; (**iii**) PyBOP, DIPEA, 4-amino-2,6-dimethylheptane, DMF, 1 h, rt; (**iv**) TFA/$H_2O$/TIS, 1 h, rt; (**v**) TCO-NHS, $Et_3N$, $H_2O$/ACN, 1 h, rt.



2.2.3. TCO-PEG$_4$-fQWAVGH-NHCH[$CH_2CH(CH_3)_2]_2$ (**4b**)

**Compound 4b** was synthesized according to the protocol previously described for **4a**, with Boc-NH-PEG$_3$-COOH (PEG$_4$) as a linker (Scheme 1). The crude product was purified by semi-preparative HPLC to yield **4b** as a white solid (11.7 mg, 2.7% yield). Analytical HPLC retention time of **4b**: $t_R$ = 18.4 min. Purity > 95%. ESI-MS: *m*/*z*, calculated: 1367.79 [M], found: 1368.79 $[M + H]^+$ and 707.46 $[M + 2Na]^{2+}$.

2.2.4. DOTA-L(TCO)-*p*ADA-fQWAVGH-NHCH[$CH_2CH(CH_3)_2]_2$ (**9a**)

The first steps of the synthesis were performed from intermediate **1**, as described in the protocol above. The linker was protected with a Fmoc group instead of a Boc protecting group on the N-terminal position. Deprotection of Fmoc was carried out using 20% piperidine in DMF. The coupling of Fmoc-L-Lys(Boc)-OH was achieved with 4 equivalents of amino acid, HBTU/Oxyma Pure (3.9 and 4 equiv., respectively) and DIPEA (8 equiv.). The beads were shaken for 1 h at rt. After coupling, the beads were washed with DMF (3 × 1 mL), and Fmoc deprotection was performed as reported above. The coupling of 1,4,7,10-tetraazacyclododecane-1,4,7,10-tetraacetic acid tris tert-butyl ester (DOTA-tris(*t*Bu) ester, 3 equiv.) was realized in the presence of PyBOP (3 equiv.), DIPEA (6 equiv.) and DMF (3 mL) (Scheme 2). The reagents and the resin were mixed for 2 h at rt. The beads were washed with DMF (3 × 1 mL), followed by the cleavage of the peptide from the solid support, the coupling of 4-amino-2, 6-dimethylheptane on histidine, global deprotection, C18 Sep-Pak purification and conjugation of the TCO-NHS ester, as described above. Compound **9a** was purified by semi-preparative HPLC to give a white solid (28.2 mg, 1.2% yield). Analytical HPLC retention time of **9a**: $t_R$ = 14.5 min. Purity > 98%. ESI-MS: *m*/*z*, calculated: 1855.00 [M], found: 928.51 $[M + 2H]^{2+}$.

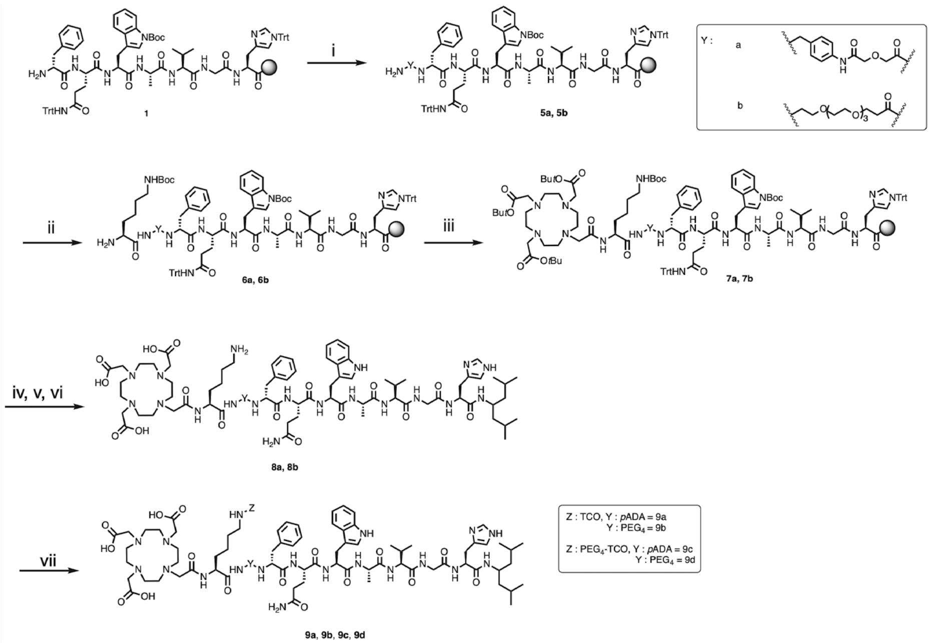


**Scheme 2.** Synthesis of **9a**, **9b**, **9c** and **9d**. Reagents and conditions: (**i**) linker a or b, HBTU/Oxyma Pure, DIPEA, 2 h, rt, and 20% piperidine in DMF; (**ii**) Fmoc-L-Lys(Boc)-OH, HBTU/Oxyma Pure, DIPEA, 1 h, rt, and 20% piperidine in DMF; (**iii**) DOTA-tris(*t*Bu) ester, PyBOP, DIPEA, 2 h, rt; (**iv**) HFIP/DCM, 1 h, rt; (**v**) PyBOP, DIPEA, 4-amino-2, 6-dimethylheptane, DMF, 1 h; rt; (**vi**) TFA/$H_2O$/TIS, 1 h, rt; (**vii**) TCO-NHS ester or TCO-PEG$_4$ NHS ester, $Et_3N$, $H_2O$/ACN, 1 h, rt.

### 2.2.5. DOTA-L(TCO)-PEG$_4$-fQWAVGH-NHCH[CH$_2$CH(CH$_3$)$_2$]$_2$ (**9b**)

After the conjugation of TCO, the crude product was purified by semi-preparative HPLC to obtain **9b** as a white solid (14.7 mg, 0.6% yield). Analytical HPLC retention time of **9b**:

$t_R$ = 15.5 min. Purity > 95%. ESI-MS: *m/z*, calculated: 1882.06 [M], found: 1883.13 $[M + H]^+$, 941.88 $[M + 2H]^{2+}$, 952.87 $[M + Na + H]^{2+}$ and 963.93 $[M + 2Na]^{2+}$.

2.2.6. DOTA-L($PEG_4$-TCO)-*p*ADA-fQWAVGH-NHCH$[CH_2CH(CH_3)_2]_2$ (**9c**)

TCO-$PEG_4$ NHS ester was coupled to **8a** to give **9c**, following the same protocol described above (Scheme 2). Compound **9c** was purified by semi-preparative HPLC and was obtained as a white solid (17.2 mg, 0.7% yield). Analytical HPLC retention time of **9c**: $t_R$ = 15.6 min. Purity > 94%. ESI-MS: *m/z*, calculated: 2102.15 [M], found: 1051.91 $[M + 2H]^{2+}$.

2.2.7. DOTA-L($PEG_4$-TCO)-$PEG_4$-fQWAVGH-NHCH$[CH_2CH(CH_3)_2]_2$ (**9d**)

The TCO-$PEG_4$ NHS ester was coupled to **8b** and purification by semi-preparative HPLC provided **9d** as a white solid (18.6 mg, 0.7% yield) (Scheme 2). Analytical HPLC retention time of **9d**: $t_R$ = 14.7 min. Purity > 97%. ESI-MS: *m/z*, calculated: 2129.20 [M], found: 1065.63 $[M + 2H]^{2+}$.

2.2.8. Tetrazine-Sulfo Cyanine 5 (**Tz-sCy5**)

The synthesis of Tz-Cy5 was performed, following the protocol described by Sasmal and coworkers [22]. The characteristics of the compound are provided in the Supplementary Materials.

2.2.9. Synthesis of **10**

Compound **10** was prepared by reacting **4a** (2.01 mg, 1.49 µmol) and **Tz-sCy5** (1.33 mg, 1.1 equiv.). Both starting materials were dissolved in $H_2O$/ACN (*v*:*v* = 1:1) and incubated at 37 °C for 10 min in an Eppendorf tube protected from light. The reaction mixture was purified by the semi-preparative HPLC to give **10** as a blue solid (2 mg, 63% Yield). Analytical HPLC retention time: $t_R$ = 16.0 min. Purity > 92%. ESI-MS: *m/z*, calculated: 2124.00 [M], found: 1062.63 $[M + H]^+$.

2.2.10. Synthesis of **11**

Compound **11** was synthesized by following the experimental method reported above for **10**. Reaction of **4b** (2.5 mg, 1.80 µmol) and **Tz-sCy5** (1.6 mg, 1.1 equiv.) provided **11**, after purification and lyophilization, as a blue solid (1.8 mg, 46% yield). Analytical HPLC retention time: $t_R$ = 15.9 min. Purity > 91%. ESI-MS: *m/z*, calculated: 2151.06 [M], found: 2153.88 $[M + H]^+$ and 1077.04 $[M + 2H]^{2+}$.

2.2.11. Synthesis of **12**

Compound **12** was synthesized by following the experimental method reported above for **10**. Reaction of **9c** (4.3 mg, 2.04 µmol) and **Tz-sCy5** (1.8 mg, 1.1 equiv.) provided **12**, after purification and lyophilization, as a blue solid (1.33 mg, 23% yield). Analytical HPLC retention time: $t_R$ = 15.2 min. Purity > 90%. ESI-MS: *m/z*, calculated: 2885.42 [M], found: 1442.92 $[M + 2H]^{2+}$ and 969.63 $[M + Na + H]^{2+}$.

2.2.12. Synthesis of **13**

Compound **13** was synthesized by following the experimental method reported above for **10**. Reaction of **9d** (3 mg, 1.41 µmol) and **Tz-sCy5** (1.26 mg, 1.1 equiv.) provided **13**, after purification and lyophilization, as a blue solid (1.21 mg, 29% yield). Analytical HPLC retention time: $t_R$ = 14.7 min. Purity > 96%. ESI-MS: *m/z*, calculated: 2912.48 [M], found: 1456.22 $[M + 2H]^{2+}$ and 971.21 $[M + 3H]^{3+}$.

2.2.13. Synthesis of **14**

Compound **14** was synthesized by following the experimental method reported above for **10**. The reaction of **9a** (3 mg, 1.60 µmol) and **Tz-sCy5** (1.44 mg, 1.1 equiv.) provided **14**, after purification and lyophilization, as a blue solid (3.35 mg, 79% yield). Analytical HPLC retention time: $t_R$ = 13.9 min. Purity > 95%. ESI-MS: *m/z*, calculated: 2638.28 [M], found: 1319.49 $[M + 2H]^{2+}$ and 880.08 $[M + 3H]^{3+}$.

2.2.14. Synthesis of **15**

Compound **15** was synthesized by following the experimental method reported above for **10**. Reaction of **9b** (2.88 mg, 1.53 µmol) and **Tz-sCy5 (**1.37 mg, 1.1 equiv.) provided **15**, after purification and lyophilization, as a blue solid (1.89 mg, 46% yield). Analytical HPLC retention time: $t_R$ = 14.7 min. Purity > 97%. ESI-MS: *m/z*, calculated: 2665.34 [M], found: 1332.81 $[M + 2H]^{2+}$ and 888.54 $[M + 3H]^{3+}$.

### ***2.3. Radiolabeling of 12, 13, 14 and 15 with $^{111}$In***

All $^{111}$In-labeled conjugates were prepared by adding 100 MBq of $^{111}InCl_3$ (62.2 µL) to a solution of 1 nmol of peptide (**12**, **13**, **14** or **15**), ascorbic acid/gentisic acid (Gz/Asc) (10 µL, 50 mM), sodium acetate (1 µL, 2.5 M, pH 8) and $H_2O$ (60.8 µL). The final mixture, with a pH of 4.5, was incubated for 20 min at 90 °C. The reaction was monitored by instant thin-layer chromatography (iTLC) on silica gel impregnated glass-fiber sheets and with a solution of sodium citrate (0.1 M, pH 5) as an eluent. The reaction mixture was left to cool down for 5 min and diethylenetriaminepentaacetic acid (DTPA) (5 µL) was added to complex free $^{111}$In. Then, the radiochemical yield of the $^{111}$In-labeled peptides was determined using radio-HPLC.

### ***2.4. Determination of the Distribution Coefficients (LogD$_{7.4}$)***

Distribution coefficients (LogD$_{7.4}$) for the $^{111}$In-labeled compounds were determined by a shake-flask method. The experiments were performed in triplicate for each radioligand. A sample containing the radioligand (0.5–2.0 MBq) was dissolved in 1 mL solution of phosphate-buffered saline (0.01 M, pH 7.4) and *n*-octanol (*v*:*v* = 1:1). The vials were vortexed vigorously and then centrifuged at 10,000 rpm for 3 min, for phase separation. Samples (10 µL) of each phase were taken out and analyzed using a gamma counter. $\text{LogD}_{7.4}$ values were calculated, using the following equation: $\text{LogD}_{7.4}$ = log [(counts in *n*-octanol phase)/(counts in PBS phase)].

***2.5. Stability Studies in PBS and Mouse Serum***

Stability in PBS was determined by incubating 20 µL of the labeled compounds (~11 MBq) in PBS (80 µL) at 37 °C. Radiochemical purity was determined by iTLC at 30 min, 1 h, 2 h and 4 h. Stability in the serum was carried out by adding 70 µL of the labeled compound (~35 MBq) to 330 µL of mouse serum (Merck, Haarlerbergweg, The Netherlands). The mixture was incubated at 37 °C. At different time points (30 min, 1 h, 2 h and 4 h), an aliquot of the mixture (50 µL) was added to 50 µL ACN. The vial was vortexed and centrifuged at 10,000 rpm for 20 min and the supernatant was analyzed by iTLC.

***2.6. Cell Culture and Competition Binding Assay***

GRPR-positive human-derived prostate adenocarcinoma epithelial PC-3 cells (ATCC, Manassas, VA, USA) were cultured in Ham's F-12K (Kaighn's) Medium (Gibco, Paisley, UK) supplemented with 10% fetal bovine serum, penicillin (100 units/mL) and streptomycin (100 µg/mL). Cells were routinely passaged and grown in tissue culture flasks at 37 °C in a humidified atmosphere with 5% $CO_2$.

The affinity of all six probes for GRPR was determined using a competition binding assay. PC-3 cells were seeded in 12-well plates ($2.5 \times 10^5$ cells/well) one day prior to the experiment. The next day, cells were washed with warm Dulbecco's phosphate-buffered saline (PBS) (Gibco). Subsequently, cells were incubated for 1 h at 37 °C with 0.5 mL incubation medium (Ham's F-12K, 20 mM HEPES, 1% BSA, pH 7.4) containing $10^{-9}$ M [$^{111}$In]In-NeoB, in the presence or absence of increasing concentrations ($10^{-12}$ to $10^{-6}$ M) of one of the six unlabeled probes or NeoB (positive control). After incubation, the medium was removed and cells were washed twice with cold PBS. To determine the amount of activity that was taken up by the cells, cells were lysed using 1 M NaOH for > 20 min at rt, then collected and measured in a γ-counter. To determine the amount of radioactivity added per well, samples of the incubation medium containing $10^{-9}$ M [$^{111}$In]In-NeoB were also measured. The results are expressed as the percentage of added dose (%AD) and were normalized to the uptake of [$^{111}$In]In-NeoB (in the absence of cold compound). Data represent the mean ± standard deviation (SD) of triplicate wells.

### 2.7. Animal Model

Seven-week-old male Balb/c nu/nu-specific and opportunistic pathogen-free (SOPF) mice (Janvier Labs, Le Genest-Saint-Isle, France) were housed in individually ventilated cages, with 4 mice per cage. Upon arrival, mice were acclimated for 1 week, with access to food and water ad libitum. Mice were subcutaneously inoculated on the right shoulder with PC-3 cells ($5 \times 10^6$ cells suspended in 100 µL of 1/3 Matrigel (Corning Inc., Corning, NY, USA) and 2/3 Hank's balanced salt solution (Gibco). PC-3 xenografts were allowed to grow for 3 weeks. Tumor sizes were 391 ± 173 $mm^3$ at the start of the studies. All animal experiments were approved by the Animal Welfare Committee of the Erasmus MC and were conducted in agreement with institutional guidelines (license number: AVD101002017867, 28 September 2017).

### 2.8. In Vivo SPECT/CT Imaging Studies

Mice ($n$ = 3 per probe) were intravenously injected in the tail vein with 200 µL of Kolliphor® HS 15 (Merck, Haarlerbergweg, The Netherlands) in PBS (0.06 mg/mL) containing [$^{111}$In]In-**12** (13.40 ± 0.76 MBq, ~670 pmol) or [$^{111}$In]In-**15** (17.50 ± 1.78 MBq, ~875 pmol). To determine the receptor specificity of the probes, one additional animal was injected with [$^{111}$In]In-**12** (9.78 MBq, 489 pmol) or [$^{111}$In]In-**15** (10.17 MBq, 509 pmol), plus an excess of unlabeled NeoB (150 nmol). Two hours post-injection (p.i.), mice were imaged in a prone position on a heated bed under 2% isoflurane/$O_2$ anesthesia, in a dedicated small-animal PET/SPECT/CT scanner (VECTor$^5$CT scanner, MILabs B.V., Utrecht, The Netherlands) with a high sensitivity pinhole collimator (XXUHS-M, 3.0 mm pinhole diameter). Whole-body SPECT images (transaxial field of view (FOV) 54 mm) were acquired over 30 min using a spiral scan in normal scan mode, in list-mode acquisition. This was followed by a whole-body CT scan within 5 min, with the following imaging settings: full angle scan, angle step 0.75 degrees, normal scan mode, 50 kV tube voltage, 0.21 mA tube current, 500 µm aluminum filter. Reconstruction of the SPECT images was performed using the similarity-regulated OSEM method and MLEM method (MILabs Rec 11.00 software, MILabs B.V., Houten, The Netherlands) performing 9 and 128 iterations, respectively, at 0.8 $mm^3$ resolution, using 173 keV ± 10% and 247 keV ± 10% energy windows for indium-111. Two adjacent background windows per photo peak were used for triple-energy window scatter and crosstalk correction. Reconstructed volumes of SPECT scans were post-filtered with an isotropic 3-dimensional Gaussian filter of 1 mm full width, at half-maximum. The CT and registered, attenuation-corrected SPECT images were analyzed using PMOD (PMOD 3.9, Zurich, Switzerland) and quantification was performed by placing volumes of interest (VOIs) around the tumors and kidneys. An Eppendorf tube filled with a solution of indium-111 of a known activity was measured to determine the calibration factor. The total activity measured in the VOI was divided by the volume of all VOI pixel values and multiplied by the calibration factor to obtain the percentage of injected activity per volume unit (%IA/mL).

### *2.9. Ex Vivo Biodistribution Studies and Optical Imaging*

To determine the biodistribution of the compounds after imaging (~3 h p.i.), blood was collected via cardiac puncture under isoflurane/$O_2$ anesthesia, after which the mice were sacrificed. The tumor and organs of interest (prostate, pancreas, spleen, liver, GI tract (stomach, small intestine, cecum, large intestine), kidneys, lungs, heart, muscle, bone, and brain) were excised, washed in PBS and blotted dry. The stomach, intestines and cecum were emptied of their contents. The tumor was cut in half; one half was fresh-frozen for further analysis and the other half was collected for ex vivo optical imaging and radioactivity measurements. After imaging, the blood, tumor, and relevant organs were weighed and measured in a γ-counter. To determine the total injected radioactivity per animal, samples of the injected solutions were measured as well. The percentage of injected dose per gram (%ID/g) was determined for each tissue sample and corrected for both the injected volume and %ID present at the injection site (the tail). Because the low weight of the prostate limited accurate organ weight measurements, the average prostate weight of all animals was used.

Before gamma counter measurements, the tumor half, pancreas, kidneys, lungs, small intestine, large intestine, liver, muscle, and bone were placed in two petri dishes and ex vivo optical imaging was performed with the IVIS Spectrum system (Perkin Elmer, Waltham, MA, USA) using the following settings for all measurements: FOV 12.6 cm, medium binning, f2, 0.5 s exposure with an excitation/emission filter of 640 nm/680 nm. Living Image version 4.5.2 software (Perkin Elmer) was used to perform data analysis by drawing a region of interest around the organ/tissue to quantify the radiant efficiency {(photons/second/$cm^2$/steradian)/(μW/$cm^2$)}.

### *2.10. Statistical Analysis*

Statistical analysis was performed using GraphPad Prism version 5.01 (GraphPad Software Inc., San Diego, CA, USA). The half-maximal inhibitory concentration ($IC_{50}$) values were estimated by the log (inhibitor) vs. the normalized response fitting routine. To compare the uptake values of the two probes studied in vivo, an unpaired *t*-test was used with the significance levels set at 5%. The results are represented as mean ± standard deviation (SD).

## 3. Results

### *3.1. Chemistry and Radiochemistry*

Synthesis of the NeoB analogs was performed following solid-phase peptide synthesis (SPPS) protocols, using a standard Fmoc strategy. Coupling of the commercially available amino acids and linkers containing a Fmoc or a Boc protecting group was carried out with conventional coupling reagents, HBTU and Oxyma Pure (Scheme 1). Cleavage of the peptides from the solid support was achieved via treatment with a solution containing HFIP and DCM. Briefly, 4-Amino-2, 6-dimethylheptane was coupled on the C-terminal histidine by using PyBOP under basic conditions. Subsequent removal of the protecting groups from the compounds was achieved using a cocktail of TFA/$H_2O$/TIS. Next, the peptides were purified by a C18 Sep-Pak cartridge, using $H_2O$/ACN. Finally, compounds **4a** and **4b** were obtained in 2.0 and 2.7% yields, respectively, after coupling of the TCO-NHS ester under basic conditions and the purification of the products by semi-preparative HPLC.

Synthesis of the compounds **9a**, **9b**, **9c** and **9d** (Scheme 2) was achieved following a similar synthetic approach. Briefly, the Fmoc-protected linkers (*p*ADA and $PEG_4$) were successfully coupled to the peptide sequence, followed by the removal of the Fmoc-protecting group with piperidine. The subsequent coupling of the lysine residue and DOTA chelator provided intermediates **7a** and **7b**. Cleavage of the peptides from the solid support, the coupling of 4-amino-2, 6-dimethylheptane on histidine, deprotection of the remaining protecting groups, and purification of the crude compounds by a C18 Sep-Pak cartridge afforded compounds **8a** and **8b**. The final peptides were obtained by coupling TCO-NHS ester or TCO-$PEG_4$ NHS ester to the free amine on the side chain of the lysine residue. Compounds **9a**, **9b**, **9c** and **9d** were purified by semi-preparative HPLC and obtained in 1.2, 0.6, 0.7 and 0.7% yields, respectively.

**Tz-sCy5** was obtained in 63% yield in a one-step synthesis under basic conditions [22]. With the six final NeoB analogs and **Tz-sCy5** in hand, we prepared two mono- and four dual-modality probes (Figure 1) via an IEDDA click reaction. The reaction was performed under mild conditions at 37 °C. The final compounds **10**, **11**, **12**, **13**, **14** and **15** were obtained in 63, 46, 23, 29, 79 and 46% yields, respectively, after semi-preparative HPLC purification.

Labeling of the final dual-modality probes was performed with $^{111}InCl_3$ using a mixture of sodium acetate and Gz/Asc as scavengers to prevent radiolysis. The labeling efficiency was monitored by iTLC and radio HPLC (Table 1). The [$^{111}$In]In-**12**, [$^{111}$In]In-**13**, [$^{111}$In]In-**14** and [$^{111}$In]In-**15** were obtained in 97, 97, 92 and 96% yields, respectively.

All our probes exhibited a negative $LogD_{7.4}$ value, proving their hydrophilicity. Stability studies in PBS showed that the percentage of intact labeled ligand considerably decreased over time, specifically for [$^{111}$In]In-**14** (74.2% intact labeled ligand at 30 min, vs. 33.7% at 4 h) and [$^{111}$In]In-**15** (83.1% intact labeled ligand at 30 min, vs. 57.1% at 4 h). However, all radiopeptides demonstrated high stability in mouse serum (> 94% intact labeled ligand at 4 h) (Table 1).

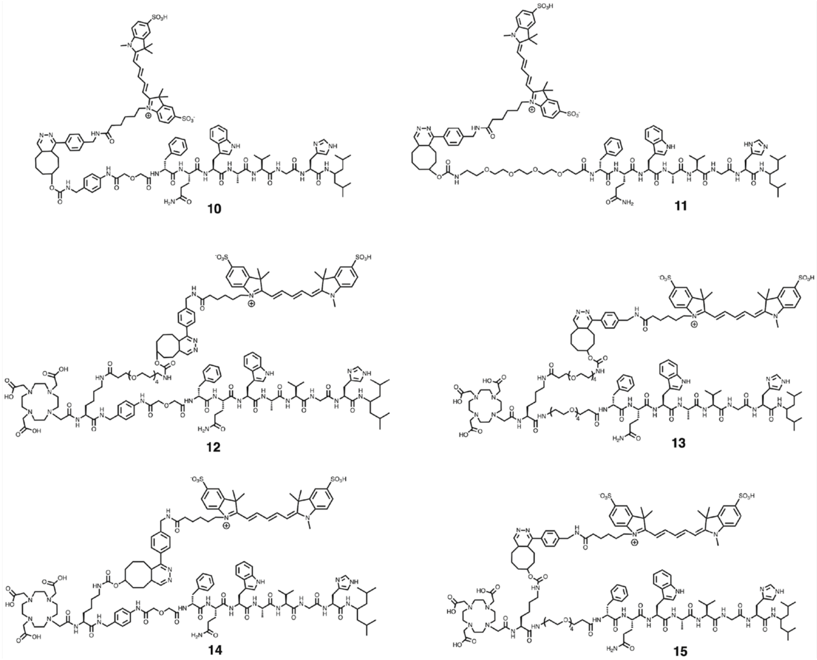


**Figure 1.** The chemical structures of the two mono-, **10** and **11**, and four dual-, **12**, **13**, **14** and **15** modality probes obtained via the IEDDA click reaction.

### *3.2. Binding Affinity Assays*

[$^{111}$In]In-NeoB was displaced from the GRPR binding site in PC-3 cells by the newly synthesized NeoB analogs. The results presented in Table 2 indicate that the binding affinity of the probes is 4.5 to 24.6-fold (21.9–118.7 nM) lower than the binding affinity of the parent peptide NeoB (4.8 nM) (Figure S1). The two dual-modality probes with the highest binding affinity (i.e., **12** and **15**) were selected for pilot in vivo pharmacokinetic characterization.

**Table 2.** $IC_{50}$ values of the dual-modality probes, compared to the native NeoB peptide.

| Compound | IC50 (nM) | Ratio Compound/NeoB |
|---|---|---|
| NeoB | 4.8 | |
| **10** | 62.3 | 12.9 |
| **11** | 21.9 | 4.5 |
| **12** | 44.1 | 9.1 |
| **13** | 88.0 | 18.2 |
| **14** | 118.7 | 24.6 |
| **15** | 53.9 | 11.2 |

**Table 1.** RCY, Log$D_{7.4}$ and stability in PBS and mouse serum of [$^{111}$In]In-**12**–**15**.

| | | | Stability in PBS (%) [a] ($n$ = 1) | | | | Stability in Mouse Serum (%) [a] ($n$ = 1) | | | | | |
|---|---|---|---|---|---|---|---|---|---|---|---|---|
| **Compound** | **RCY (%)** | **$R_f$** | **30 min** | **1 h** | **2 h** | **4 h** | **30 min** | **1 h** | **2 h** | **4 h** | **Protein-Bound Fraction at 4 h (%)** | **Log $D_{7.4}$ ($n$ = 3)** |
| [$^{111}$In]In-**12** | 97 | 0.04 | 85.8 | 80.1 | 75.0 | 73.1 | 96.3 | 96.4 | 96.5 | 96.5 | 7.0 | −1.66 ± 0.01 |
| [$^{111}$In]In-**13** | 97 | 0.06 | 87.4 | 87.5 | 86.2 | 84.4 | 98.1 | 97.9 | 97.6 | 97.3 | 5.6 | −1.80 ± 0.01 |
| [$^{111}$In]In-**14** | 92 | 0.07 | 74.2 | 48.5 | 30.9 | 33.7 | 94.6 | 94.1 | 94.0 | 94.1 | 7.1 | −1.52 ± 0.1 |
| [$^{111}$In]In-**15** | 96 | 0.06 | 83.0 | 71.8 | 67.0 | 57.1 | 96.9 | 96.7 | 96.9 | 97.1 | 6.5 | −1.75 ± 0.09 |

[a] Results are expressed as a percentage (%) of intact labeled ligand after incubation at 37 °C.

### *3.3. In Vivo SPECT/CT Imaging*

SPECT/CT imaging of PC-3-xenografted mice 2 h after the administration of [$^{111}$In]In-**12** or [$^{111}$In]In-**15** demonstrated clear visualization of the tumor xenografts (Figure 2A). The uptake was GRPR-specific, since reduced tumor uptake was observed when the GRPR was blocked using an excess of unlabeled NeoB. As expected, uptake was observed in the kidneys and bladder as a result of the renal excretion of the probe and in the abdominal region, where GRPR-positive organs, such as the pancreas, are located. Quantification of the radioactivity in tissues of interest showed a similar uptake pattern for [$^{111}$In]In-**12** and [$^{111}$In]In-**15** in both the tumor and kidneys (Figure 2B), resulting in comparable tumor-to-kidney ratios (0.47 ± 0.05 for [$^{111}$In]In-**12** and 0.49 ± 0.05 for [$^{111}$In]In-**15**).

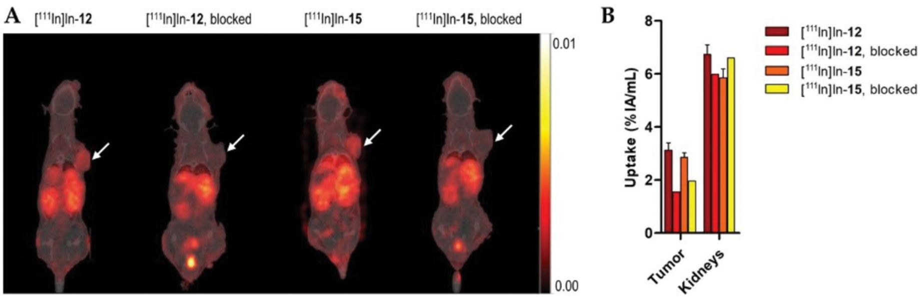


**Figure 2.** SPECT/CT imaging of [$^{111}$In]In-**12** and [$^{111}$In]In-**15** in PC-3-xenograft Balb/c nu/nu mice, 2 h p.i. (**A**) SPECT/CT images: overlay of a CT slice and the corresponding SPECT slice, on which the tumor cross-section is distinctly visible. The tumor is located on the right shoulder (white arrow). For the non-blocked groups, one representative image is shown. (**B**) Radioactivity uptake in tumor and kidney volumes of interest, determined from SPECT images, is expressed as a percentage of injected activity per mL (%IA/mL). The values for the unblocked groups are recorded as mean ± SD ($n$ = 3).

### *3.4. Biodistribution Studies*

The results of the ex vivo biodistribution of [$^{111}$In]In-**12** and [$^{111}$In]In-**15** in PC-3-xenograft Balb/c nu/nu mice after SPECT/CT scanning are depicted in Figure 3 and Table S1. In agreement with the in vivo measurements, high radioactivity uptake was observed in the tumor with both probes (8.47 ± 0.46%ID/g and 6.90 ± 0.81%ID/g for probe [$^{111}$In]In-**12** and [$^{111}$In]In-**15**, respectively). In addition, the probes highly accumulated in the GRPR-expressing pancreas (16.55 ± 1.41%ID/g for [$^{111}$In]In-**12**; 9.72 ± 1.63%ID/g for [$^{111}$In]In-**15**). Both probes have similar tumor-to-muscle ratios, but the higher pancreas uptake of probe [$^{111}$In]In-**12** resulted in a significantly lower tumor-to-pancreas ratio ($p$ = 0.0131). In low-level GRPR-expressing organs, such as the GI tract and the prostate gland, moderate uptake was observed. Co-injection with an excess of unlabeled NeoB resulted in a strongly decreased uptake level of the probes in the GRPR-positive tumor and organs, indicating receptor specificity.

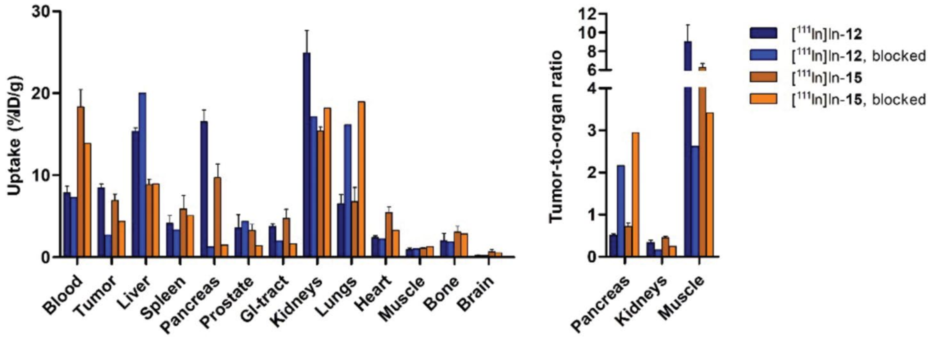


**Figure 3.** Ex vivo biodistribution (left) and tumor-to-organ ratios (right) of [$^{111}$In]In-**12** and [$^{111}$In]In-**15** in PC-3-xenograft Balb/c nu/nu mice after SPECT/CT scanning. Mice were injected intravenously with 1 nmol of [$^{111}$In]In-**12** or [$^{111}$In]In-**15,** alone or in combination with 150 nmol of non-labeled NeoB (blocked). Radioactivity uptake in tissues was calculated as a percentage of the injected dose per gram of tissue (%ID/g). Data for the unblocked group are presented as an average value ± SD (*n* = 3).

At the time of sacrifice, [$^{111}$In]In-**12** and [$^{111}$In]In-**15** were not completely cleared from the blood (7.83 ± 0.84%ID/g for [$^{111}$In]In-**12**; 18.32 ± 2.12%ID/g for [$^{111}$In]In-**15**). Probes were mainly eliminated via renal clearance; kidney uptake was 24.88 ± 2.78%ID/g for [$^{111}$In]In-**12** and 15.38 ± 0.50%ID/g for [$^{111}$In]In-**15**. The higher kidney uptake for probe [$^{111}$In]In-**12** resulted in a lower tumor-to-kidney ratio for [$^{111}$In]In-**12** ($p$ = 0.0409). Furthermore, a relatively high radioactivity uptake was seen in the lungs (6.51 ± 1.15%ID/g for [$^{111}$In]In-**12**; 6.77 ± 1.73%ID/g for [$^{111}$In]In-**15**). This uptake was not GRPR-specific since a 2–3-fold higher uptake in this organ was also observed in animals that were co-injected with an excess of unlabeled NeoB (16.14%ID/g and 18.95%ID/g for [$^{111}$In]In-**12** and [$^{111}$In]In-**15**, respectively). Next to the lungs, unexpected high radioactivity levels were noticed in the liver (15.35 ± 0.43%ID/g for [$^{111}$In]In-**12**; 8.87 ± 0.65%ID/g for [$^{111}$In]In-**15**).

### *3.5. Ex Vivo Optical Imaging*

A subset of organs and the tumor were also imaged by ex vivo fluorescence imaging, to confirm the localization of the dye (Figure 4). Here, the results showed that the fluorescence intensities of the organs generally followed the same trend as the radioactivity uptake. As can be deduced from Figure 4, high signal levels were measured in the tumor ([4.31 ± 1.03 and 4.66 ± 1.35] x $10^8$ p/sec/cm$^2$/sr per µW/cm$^2$ for [$^{111}$In]In-**12** and [$^{111}$In]In-**15** respectively), GRPR-positive pancreas ([6.32 ± 0.50 and 5.12 ± 1.93] x $10^8$ p/sec/cm$^2$/sr per µW/cm$^2$ for [$^{111}$In]In-**12** and [$^{111}$In]In-**15,** respectively) and kidneys ([9.41 ± 0.92 and 7.80 ± 0.92] x $10^8$ p/sec/cm$^2$/sr per µW/cm$^2$ for [$^{111}$In]In-**12** and [$^{111}$In]In-**15,** respectively) (Table S2). The intensities of bone and muscle are low, but muscle fluorescence is slightly higher for [$^{111}$In]In-**15** than for [$^{111}$In]In-**12** ($p$ = 0.0456).

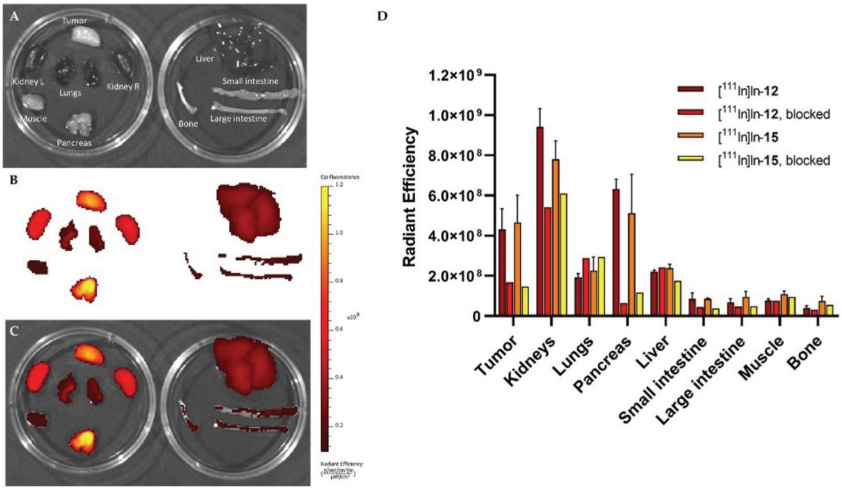


**Figure 4.** Ex vivo fluorescence imaging of a subset of organs. A representative example of (**A**) a photograph (organ tags in white), (**B**) a fluorescence image, and (**C**) their overlay, obtained with IVIS imaging of [$^{111}$In]In-**15** in PC-3-xenografted Balb/c nu/nu mice after dissection. The scale bar shows the fluorescent signal intensities in radiant efficiency {(p/sec/cm$^2$/sr)/(μW/cm$^2$)}. (**D**) Quantified ex vivo radiant efficiencies of [$^{111}$In]In-**12** and [$^{111}$In]In-**15** uptake in tumor and organs (non-blocked ($n$ = 3); blocked ($n$ = 1)). Values for the unblocked group are presented as an average value ± SD.

## 4. Discussion

Image-guided surgery of PCa can greatly aid surgeons to resect tumor tissues completely. Extensive research has been carried out on probes targeting the prostate-specific membrane antigen (PSMA), but it has been suggested that GRPR-targeted imaging probes may be of great value for PSMA-negative tumor lesions [23]. Moreover, the overexpression of GRPR typically occurs at an early stage of the disease, while PSMA is often associated with late-stage disease. Considering that image-guided surgery is particularly suitable for primary tumors, dual-modality probes targeting GRPR would be very attractive. NeoB exhibits a very high GRPR affinity and was introduced in the literature as a very promising peptide for GRPR-mediated radionuclide imaging and therapy [18,24]. Therefore, the chemical design of the dual-labeled probes is based on the amino acid sequence of the parent peptide NeoB. We herein described the synthesis of the new library of NeoB analogs with two linkers, the *p*ADA and PEG$_4$ linkers. Those two linkers provide different physicochemical properties to the peptides, such as hydrophilicity, rigidity and spacing. In the chemical structure of compounds **4a** and **4b**, the original DOTA chelator was replaced by a TCO moiety, in order to preserve a chemical structure closer to that of the parent peptide. To add a TCO moiety to the original NeoB, a lysine residue was introduced between the peptide sequence and the DOTA chelator. This method has already been used by Li et al. and Zhang et al. for the insertion of a fluorescent dye into peptides [25,26]. Purification of the peptides by a C18 Sep-Pak cartridge before the coupling of TCO was implemented to remove the excess of TFA remaining from the removal of the protecting groups in the previous step. In fact, La-Venia and coworkers demonstrated that TCO is sensitive to acidic conditions and results in its change of conformation from TCO to CCO, the latter being less reactive toward Tz [27]. The final dual-labeled probes, containing a DOTA chelator and a fluorescent dye, were obtained via an IEDDA click reaction between the TCO coupled to the peptides and Tz coupled to the fluorescent dye, sCy5. The IEDDA reaction was chosen because of its fast kinetics, irreversibility, and stability of the generated product. The sCy5 dye was employed due to its strong fluorescence intensity and extinction coefficient, and excellent brightness [28,29]. Fluorescent dyes can show instability in aqueous solutions and a low pH. However, IEDDA provides the opportunity to synthesize the dual-labeled probes after obtaining the radiolabeled peptides containing the TCO moiety, preventing such instability from occurring. Another advantage of the click reaction is that it offers the possibility of synthesizing a large library of compounds in a single step.

The radiolabeling of the dual-labeled probes with $^{111}InCl_3$ was successfully achieved with high RCYs. The negative $LogD_{7.4}$ values were obtained for all the radiolabeled peptides. Compared to their radiolabeled NeoB analog, [$^{68}$Ga]Ga-NeoB ($LogD_{7.4}$ = −0.88 ± 0.02) [30], the introduction of the fluorescent dye to the peptides increased their hydrophilicity; therefore, negative $LogD_{7.4}$ values were obtained for all the radiolabeled peptides. All radiolabeled compounds were stable in mouse serum, demonstrating their inertness toward peptidase digestion. However, the dual-labeled probes turned out to be less stable in PBS, demonstrating their sensitivity toward radiolysis [31].

The replacement of the DOTA chelator by a TCO moiety in compound **10** impaired the binding affinity of the peptide toward the receptor, probably due to a change in the conformation of the molecule. However, the introduction of a $PEG_4$ linker instead of a *p*ADA linker did not substantially hamper the binding affinity of **11** toward GRPR, probably due to the flexibility offered by the linker. The introduction of two linkers in the four dual-labeled probes, **12**, **13**, **14** and **15,** induced changes in the conformation of the molecules, leading to a lower affinity of the compounds toward GRPR in comparison to the parent peptide, NeoB.

The results of the pilot in vivo study showed that probes [$^{111}$In]In-**12** and [$^{111}$In]In-**15** also possess good in vivo binding properties, depicted by a high tumor accumulation and a clear delineation of the xenograft on the SPECT scans. When compared to previous studies with NeoB [18,24], the fluorescent dye component of the probes noticeably influences the in vivo pharmacokinetic profile. The dual-modality probes have a prolonged blood circulation time, as high levels of radioactivity in the blood were observed at ~3 h post-injection. Hence, it could conceivably be hypothesized that the optimal tumor uptake and tumor-to-background levels may not have been reached in the current study. The observed uptake levels in the excretory organs (i.e., the liver and kidneys), compared to the biodistribution profile of the parent peptide NeoB, can also be attributed to the longer blood circulation time. Further work is needed to see if this can be improved, for example, by performing biodistribution and imaging studies at later time points.

The elevated radioactivity levels observed in the liver might be indicative of both renal and hepatobiliary routes of elimination. The elimination through hepatobiliary excretion was unexpected because this is unusual for probes with a non-lipophilic character [32]. However, TCO-Tz conjugates have a tendency to accumulate in hepatobiliary organs [33,34]. Furthermore, the involvement of this excretion pathway can possibly be attributed to aggregate formation due to increased "stickiness" (i.e., cohesive forces) of the dual-modality probes. This process could also be the cause of the unexpected uptake in the lungs, as the presence of aggregates in this organ can lead to capillary blockages, especially when high peptide amounts are injected, as was the case for the blocked animals [35]. Additional studies are needed that focus on mass optimization and practical and chemical implementations to reduce stickiness.

For a high image contrast on the preoperative scan and good visual inspection of the surgical field intraoperatively, it is crucial to have a high tumor-to-background ratio. As a rule of thumb, a ratio of 2 is reported in the literature [9]. In our study, the tumor-to-muscle ratios of the probes were found to be 9.04 ± 1.74 and 6.27 ± 0.44 for probe [$^{111}$In]In-**12** and [$^{111}$In]In-**15**, respectively. However, the tumor-to-blood ratio was not favorable. In addition, sufficient washout from the bladder (and thus, indirectly, the kidneys**)** is especially important in the image-guided surgery of PCa, because it is close to the surgical site [36]. A later imaging time point will most likely lead to reduced background signals in the blood and excretory organs.

To our knowledge, this is the second study, next to the investigations by Zhang et al. [26], about the in vivo evaluation of GRPR-targeted optical and nuclear dual-modality probes for PCa. The tumor uptake at ~2 h reported in our study (8.47 ± 0.46%ID/g and 6.90 ± 0.81%ID/g for probe [$^{111}$In]In-**12** and [$^{111}$In]In-**15**, respectively) was higher than the value that Zhang et al. obtained at ~1 h (5.50 ± 1.03%ID/g) for their GRPR-directed dual-modality probe, based on the RM2 backbone. However, they conducted a biodistribution study following a PET scan 1 h after injection. At this time point, their nuclear scan did benefit from a low background, due to a higher tumor-to-blood ratio compared to our designed probes, again arguing for optimization of the imaging time point in the future.

Further increasing the signal specificity is important for accurate intraoperative delineation of the target region and, more specifically, to distinguish between normal and tumor tissue

[37]. Here, the specificity of our probes for the GRPR as a tumor target was demonstrated by a pilot blocking study using a single animal. Co-injection of an excess of unlabeled NeoB led to a strongly decreased uptake in the tumor and the GRPR-expressing organs, such as the pancreas [38]. A reduction in activity levels in non-GRPR-expressing organs, such as the kidneys, on blocking might be due to a lower amount of activity injected in those animals. Despite the use of kolliphor as a surfactant in the solvent for the injections, this measure was not enough to compensate for the cohesive and adhesive properties of NeoB and the probes [18].

Another important finding was that the ex vivo fluorescence imaging confirmed the co-localization of the fluorescent and radioactive signal. This nicely illustrates the benefit of using a dual-modality probe with the same pharmacokinetics for 2 different purposes: pre- and intraoperative guidance. It is difficult to compare our measurements to previous studies with fluorescent agents targeting the GRPR because there is a potential for bias from the injected mass [39–43]. The injected amount can influence uptake, especially when receptor saturation levels are not yet reached. Nuclear imaging techniques have a slightly higher sensitivity than optical imaging. This means that in general, nmol amounts must be administered to allow fluorescence detection, while pmol amounts are often sufficient for nuclear detection. A further study with more focus on the optimal mass and specific labeling activity for both modalities is therefore suggested.

Since our study accommodated a pilot in vivo evaluation, future work should include a late-uptake analysis for all probes with a larger sample size for the blocked groups. Our study is supported by quantitative data obtained using various methods. Due to the image resolution and the fact that regions were drawn manually, the uptake values that were quantified by volume and count measurements from the SPECT/CT scans are less accurate than those obtained from the ex vivo biodistribution study. However, the ratios between organs calculated using both methods correlate well. Quantification of ex vivo optical data suffers from light attenuation. The differences between the organs relative to each other are therefore smaller overall, as is the difference between the two probes. The differences are therefore more evident from the radioactivity uptake levels measured in the ex vivo biodistribution study.

This study demonstrated the successful development and initial characterization of four promising dual-modality probes for the preoperative imaging and image-guided surgery of GRPR-positive PCa. Despite its exploratory nature, this study provides valuable insights into the influence of the incorporation of the sCy5 dye into the radiotracer NeoB on its binding affinity and pharmacokinetic properties. Although uptake was seen in the liver, lungs and pancreas, their location is not near the prostate and will therefore not interfere with the image-guided surgery. The prolonged blood circulation and high renal uptake require further evaluation of the optimal timing for imaging. Moreover, further in vivo preclinical evaluation with all four dual-modality probes will be performed to select the best probe for clinical translation. Overall, this study reinforces the idea that multimodal probes have very interesting properties to advance the field of image-guided surgery.

**Supplementary Materials:** The following supporting information can be downloaded at: https: //www.mdpi.com/article/10.3390/pharmaceutics14010195/s1. Synthesis of **Tz-Cy5.,** Supplemental Figure 1: Inhibition of [$^{111}$In]In-NeoB binding to PC-3 cells with probes **10, 11, 12, 13, 14, 15** and NeoB (as positive control)., Table S1: Biodistribution of [$^{111}$In]In-**12** and [$^{111}$In]In-**15** in PC-3 xenograft Balb/c nu/nu mice after SPECT/CT scanning., Table S2: Fluorescent signal of [$^{111}$In]In-**12** and [$^{111}$In]In-**15** in organ/tissue samples after dissection.

**Author Contributions**: Conceptualization, Y. S. and S. U. D.; methodology, Y. S.; software, M. H., M. V. and J. H.; validation, M. H. and M. V.; formal analysis, K.-T. C.; investigation, Y. S.; resources, Y. S. and M. d. J.; data curation, M. H. and M. V.; writing—original draft preparation, M. H. and M. V.; writing—review and editing, M. H., M. V., K.-T. C., S. U. D. and Y. S.; visualization, Y. S.; supervision, S. U. D. and Y. S.; project administration, Y. S.; funding acquisition, S. U. D. and Y. S..

**Funding:** This research was funded by the Dutch cancer society (KWF), grant numbers YIG11671 and 12259.

**Institutional Review Board Statement:** The study was conducted according to the guidelines of the Declaration of Helsinki and approved by the Animal Welfare Committee of the Erasmus MC and were conducted in agreement with institutional guidelines (license number: AVD101002017867, 28 September 2017).





**Informed Consent Statement:** Not applicable.

**Data Availability Statement:** Data can be requested by contacting the corresponding author.

**Acknowledgments:** The authors are grateful to the Dutch cancer society (KWF) for the financial support and the department of Radiology and Nuclear Medicine at the Erasmus MC for the technical assistance. This work was supported through the use of imaging equipment provided by the Applied Molecular Imaging Erasmus MC facility.

**Conflicts of Interest:** The authors declare no conflict of interest.

## References


1. Sung, H.; Ferlay, J.; Siegel, R.L.; Laversanne, M.; Soerjomataram, I.; Jemal, A. Global Cancer Statistics 2020: GLOBOCAN Es-timates of Incidence and Mortality Worldwide for 36 Cancers in 185 Countries. CA Cancer J. Clin. 2021, 71, 209–249.
2. Mottet, N.; van den Bergh, R.C.N.; Briers, E.; van den Broeck, T.; Cumberbatch, M.G.; De Santis, M.; Fanti, S.; Fossati, N.; Gandaglia, G.; Gillessen, S.; et al. EAU-EANM-ESTRO-ESUR-SIOG Guidelines on Prostate Cancer—2020 Update. Part 1: Screening, Diagnosis, and Local Treatment with Curative Intent. Eur. Urol. 2021, 79, 243–262.
3. Tourinho-Barbosa, R.; Srougi, V.; Nunes-Silva, I.; Baghdadi, M.; Rembeyo, G.; Eiffel, S.S.; Barret, E.; Rozet, F.; Galiano, M.; Cathelineau, X.; et al. Biochemical recurrence after radical prostatectomy: What does it mean? Int. Braz. J. Urol. 2018, 44, 14–21.
4. Zhang, L.; Wu, B.; Zha, Z.; Zhao, H.; Yuan, J.; Jiang, Y.; Yang, W. Surgical margin status and its impact on prostate cancer prognosis after radical prostatectomy: A meta-analysis. World J. Urol. 2018, 36, 1803–1815.
5. Andreoiu, M.; Cheng, L. Multifocal prostate cancer: Biologic, prognostic, and therapeutic implications. Hum. Pathol. 2010, 41, 781–793.
6. Saranchuk, J.W.; Kattan, M.W.; Elkin, E.; Touijer, A.K.; Scardino, P.T.; Eastham, J.A. Achieving Optimal Outcomes After Radical Prostatectomy. J. Clin. Oncol. 2005, 23, 4146–4151.
7. Soeterik, T.F.W.; van Melick, H.H.E.; Dijksman, L.M.; Stomps, S.; Witjes, J.A.; van Basten, J.P.A. Nerve Sparing during Robot-Assisted Radical Prostatectomy Increases the Risk of Ipsilateral Positive Surgical Margins. J. Urol. 2020, 204, 91–95.
8. Hernot, S.; van Manen, L.; Debie, P.; Mieog, J.S.D.; Vahrmeijer, A.L. Latest developments in molecular tracers for fluorescence image-guided cancer surgery. Lancet Oncol. 2019, 20, e354–e367.
9. Van Leeuwen, F.W.; Schottelius, M.; Brouwer, O.R.; Vidal-Sicart, S.; Achilefu, S.; Klode, J.; Wester, H.-J.; Buckle, T. Trending: Radioactive and Fluorescent Bimodal/Hybrid Tracers as Multiplexing Solutions for Surgical Guidance. J. Nucl. Med. 2019, 61, 13–19.
10. Jennings, L.E.; Long, N.J. 'Two is better than one'—Probes for dual-modalitymolecular imaging. Chem. Comm. 2009, 3511–3524.
11. Lee, S.; Chen, X. Dual-Modality Probes for in Vivo Molecular Imaging. Mol. Imaging 2009, 8, 87–100.
12. Ananias, H.J.; Heuvel, M.C.V.D.; Helfrich, W.; de Jong, I.J. Expression of the gastrin-releasing peptide receptor, the prostate stem cell antigen and the prostate-specific membrane antigen in lymph node and bone metastases of prostate cancer. Prostate 2009, 69, 1101–1108.
13. Beer, M.; Montani, M.; Gerhardt, J.; Wild, P.J.; Hany, T.F.; Hermanns, T.; Müntener, M.; Kristiansen, G. Profiling gastrin-releasing peptide receptor in prostate tissues: Clinical implications and molecular correlates. Prostate 2011, 72, 318–325.
14. Bakker, I.L.; Fröberg, A.C.; Busstra, M.B.; Verzijlbergen, J.F.; Konijnenberg, M.; van Leenders, G.J.L.H.; Schoots, I.G.; de Blois, E.; van Weerden, W.M.; Dalm, S.U.; et al. GRPr Antagonist 68Ga-SB3 PET/CT Imaging of Primary Prostate Cancer in Therapy-Naïve Patients. J. Nucl. Med. 2021, 62, 1517–1523.
15. Zhang, J.; Niu, G.; Fan, X.; Lang, L.; Hou, G.; Chen, L.; Wu, H.; Zhu, Z.; Li, F.; Chen, X. PET Using a GRPR Antagonist 68Ga-RM26 in Healthy Volunteers and Prostate Cancer Patients. J. Nucl. Med. 2018, 59, 922–928.
16. Gruber, L.; Jiménez-Franco, L.D.; Decristoforo, C.; Uprimny, C.; Glatting, G.; Hohenberger, P.; Schoenberg, S.O.; Reindl, W.; Orlandi, F.; Mariani, M.; et al. MITIGATE-NeoBOMB1, a Phase I/IIa Study to Evaluate Safety, Pharmacokinetics, and Preliminary Imaging of 68Ga-NeoBOMB1, a Gastrin-Releasing Peptide Receptor Antagonist, in GIST Patients. J. Nucl. Med. 2020, 61, 1749–1755.
17. Touijer, K.A.; Michaud, L.; Alvarez, H.A.V.; Gopalan, A.; Kossatz, S.; Gonen, M.; Beattie, B.; Sandler, I.; Lyaschenko, S.; Eastham, J.A.; et al. Prospective Study of the Radiolabeled GRPR Antagonist BAY86-7548 for Positron Emission Tomography/Computed Tomography Imaging of Newly Diagnosed Prostate Cancer. Eur. Urol. Oncol. 2019, 2, 166–173.

18. Dalm, S.U.; Bakker, I.L.; De Blois, E.; Doeswijk, G.N.; Konijnenberg, M.W.; Orlandi, F.; Barbato, D.; Tedesco, M.; Maina, T.; Nock, B.A.; et al. 68Ga/177Lu-NeoBOMB1, a novel radio-labeled GRPR antagonist for theranostic use in oncology. J. Nucl. Med. 2017, 58, 293–299.
19. Nock, B.A.; Kaloudi, A.; Lymperis, E.; Giarika, A.; Kulkarni, H.R.; Klette, I.; Singh, A.; Krenning, E.P.; De Jong, M.; Maina-Nock, T.; et al. Theranostic Perspectives in Prostate Cancer with the Gastrin-Releasing Peptide Receptor Antagonist NeoBOMB1: Preclinical and First Clinical Results. J. Nucl. Med. 2016, 58, 75–80.
20. Handula, M.; Chen, K.-T.; Seimbille, Y. IEDDA: An Attractive Bioorthogonal Reaction for Biomedical Applications. Molecules 2021, 26, 4640.
21. Pagel, M. Inverse electron demand Diels-Alder (IEDDA) reactions in peptide chemistry. J. Pept. Sci. 2019, 25, e3141.
22. Sasmal, R.; Das Saha, N.; Pahwa, M.; Rao, S.; Joshi, D.; Inamdar, M.S.; Sheeba, V.; Agasti, S.S. Synthetic Host–Guest Assembly in Cells and Tissues: Fast, Stable, and Selective Bioorthogonal Imaging via Molecular Recognition. Anal. Chem. 2018, 90, 11305–11314.
23. Iagaru, A. Will GRPR Compete with PSMA as a Target in Prostate Cancer? J. Nucl. Med. 2017, 58, 1883–1884.
24. Kaloudi, A.; Lymperis, E.; Giarika, A.; Dalm, S.; Orlandi, F.; Barbato, D.; Tedesco, M.; Maina, T.; De Jong, M.; Nock, B.A. NeoBOMB1, a GRPR-Antagonist for Breast Cancer Theragnostics: First Results of a Preclinical Study with [67Ga]NeoBOMB1 in T-47D Cells and Tumor-Bearing Mice. Molecules 2017, 22, 1950.
25. Li, D.; Zhang, J.; Chi, C.; Xiao, X.; Wang, J.; Lang, L.; Ali, I.; Niu, G.; Zhang, L.; Tian, J.; et al. First-in-human study of PET and optical dual-modality image-guided surgery in glioblastoma using 68Ga-IRDye800CW-BBN. Theranostics 2018, 8, 2508–2520.
26. Zhang, H.; Desai, P.; Koike, Y.; Houghton, J.; Carlin, S.D.; Tandon, N.; Touijer, K.; Weber, W.A. Dual-Modality Imaging of Prostate Cancer with a Fluorescent and Radiogallium-Labeled Gastrin-Releasing Peptide Receptor Antagonist. J. Nucl. Med. 2017, 58, 29–35.
27. La–Venia, A.; Dzijak, R.; Rampmaier, R.; Vrabel, M. An Optimized Protocol for the Synthesis of Peptides Containing trans -Cyclooctene and Bicyclononyne Dienophiles as Useful Multifunctional Bioorthogonal Probes. Chem. A Eur. J. 2021, 27, 13632–13641.
28. Zettlitz, K.A.; Waldmann, C.M.; Tsai, W.-T.K.; Tavaré, R.; Collins, J.; Murphy, J.; Wu, A. A Dual-Modality Linker Enables Site-Specific Conjugation of Antibody Fragments for 18F-Immuno-PET and Fluorescence Imaging. J. Nucl. Med. 2019, 60, 1467–1473.
29. Yi, X.; Wang, F.; Qin, W.; Yang, X.; Yuan, J. Near-infrared fluorescent probes in cancer imaging and therapy: An emerging field. Int. J. Nanomed. 2014, 9, 1347–65.
30. Lau, J.; Rousseau, E.; Zhang, Z.; Uribe, C.F.; Kuo, H.-T.; Zeisler, J.; Zhang, C.; Kwon, D.; Lin, K.-S.; Bénard, F. Positron Emission Tomography Imaging of the Gastrin-Releasing Peptide Receptor with a Novel Bombesin Analogue. ACS Omega 2019, 4, 1470–1478.
31. Hernandez, R.; Heskamp, S.; Rijpkema, M.; Bos, D.L.; Goldenberg, D.M.; McBride, W.J.; Morgenstern, A.; Bruchertseifer, F.; Cai, W.; Boerman, O.C. Preventing Radiobleaching of Cyanine Fluorophores Enhances Stability of Nuclear/NIRF Multimodality Imaging Agents. Theranostics 2017, 7, 1–8.
32. Remmer, H. The role of the liver in drug metabolism. Am. J. Med. 1970, 49, 617–629.
33. Ruivo, E.; Adhikari, K.; Elvas, F.; Fissers, J.; Vangestel, C.; Staelens, S.; Stroobants, S.; Van der Veken, P.; Wyffels, L.; Augustyns, K. Improved stability of a novel fluorine-18 labeled TCO analogue for pretargeted PET imaging. Nucl. Med. Biol. 2019, 76-77, 36–42.
34. García, M.F.; Gallazzi, F.; Junqueira, M.D.S.; Fernández, M.; Camacho, X.; Mororó, J.D.S.; Faria, D.; de Godoi Carneiro, C.; Couto, M.; Carrión, F.; et al. Synthesis of hydrophilic HYN-IC-[1,2,4,5]tetrazine conjugates and their use in antibody pretargeting with 99mTc. Org. Biomol. Chem. 2018, 16, 5275–5285.
35. Hunt, A.; Frier, M.; Johnson, R.; Berezenko, S.; Perkins, A. Preparation of Tc-99m-macroaggregated albumin from recombinant human albumin for lung perfusion imaging. Eur. J. Pharm. Biopharm. 2006, 62, 26–31.
36. Van Leeuwen, F.W.B.; Van Der Poel, H.G. Surgical guidance in prostate cancer: “From molecule to man” translations. Clin. Cancer Res. 2016, 22, 1304–1306.
37. Koch, M.; Ntziachristos, V. Advancing Surgical Vision with Fluorescence Imaging. Annu. Rev. Med. 2016, 67, 153–164.

38. Xiao, D.; Wang, J.; Hampton, L.L.; Weber, H. The human gastrin-releasing peptide receptor gene structure, its tissue expression and promoter. Gene 2001, 264, 95–103.
39. Xu, H.; Bandari. R.P.; Lee, L.E.; Li, R.; Yu, P.; Smith, C.J.; Ma, L. Design, Synthesis, and in Vitro and in Vivo Evaluation of High Affinity and Specificity Near-Infrared Fluorescent Bombesin Antagonists for Tumor Imaging. J. Med. Chem. 2018, 61, 7657–7670.
40. Pagoto, A.; Garello, F.; Marini, G.M.; Tripepi, M.; Arena, F.; Bardini, P.; Stefania, R.; Lanzardo, S.; Valbusa, G.; Porpiglia, F.; et al. Novel Gastrin-Releasing Peptide Receptor Targeted Near-Infrared Fluorescence Dye for Image-Guided Surgery of Prostate Cancer. Mol. Imaging Biol. 2020, 22, 85–93.
41. Shrivastava, A.; Ding, H.; Kothandaraman, S.; Wang, S.-H.; Gong, L.; Williams, M.; Milum, K.; Zhang, S.; Tweedle, M.F. A high-affinity near-infrared fluorescent probe to target bombesin receptors. Mol. Imaging Biol. 2014, 16, 661–9.
42. Cai, Q.-Y.; Yu, P.; Besch-Williford, C.; Smith, C.J.; Sieckman, G.L.; Hoffman, T.J.; Ma, L. Near-infrared fluorescence imaging of gastrin releasing peptide receptor targeting in prostate cancer lymph node metastases. Prostate 2012, 73, 842–854.
43. Chen, H.; Wan, S.; Zhu, F.; Wang, C.; Cui, S.; Du, C.; Ma, Y.; Gu, Y. A fast tumor-targeting near-infrared fluorescent probe based on bombesin analog for in vivo tumor imaging. Contrast Media Mol. Imaging 2014, 9, 122–134.

## Supplemental Information

### Tetrazine-Sulfo Cyanine 5 (Tz-sCy5)

**Tz-sCy5** was obtained as a blue solid (13.11 mg, 63% yield). Analytical HPLC retention time: $t_R$ = 15.20 min. Purity > 94%. ESI-MS: m/z, calculated: 811.28 [M], found: 834.01 $[M+Na]^+$. $^1H$ NMR (400 MHz, $D_2O$): δ 10.00 (s, 1H), 7.84 (d, 2H, *J* = 7.7 Hz), 7.56-7.72 (m, 5H), 6.97-7.13 (m, 4H), 6.08 (t, 1H, *J* = 11.4 Hz), 5.83 (d, 1H, *J* = 13.2 Hz), 5.73 (d, 1H, *J* = 12.2 Hz), 4.20 (s, 2H), 3.77 (s, 1H), 3.63 (qt, 2H, *J* = 13.6, 6.7 Hz) 3.24 (s, 2H), 3.12 (q, 2H, *J* = 7.5 Hz), 2.17 (br, 1H), 1.52 (br, 2H), 1.29 (s, 3H) 1.27 (s,6H), 1.25 (s, 6H).

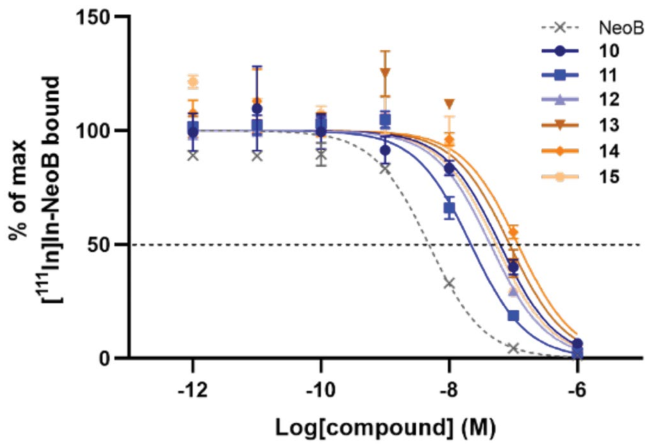


**Supplemental Figure 1.** Inhibition of [$^{111}$In]In-NeoB binding to PC-3 cells with probes **10**, **11**, **12**, **13**, **14**, **15** and NeoB (as positive control). The dotted black line at 50% crosses the curves at the $IC_{50}$ values. Data are presented as the average value of three wells.

**Supplemental Table 1.** Biodistribution of [$^{111}$In]In-**12** and [$^{111}$In]In-**15** in PC-3 xenograft Balb/c nu/nu mice after SPECT/CT scanning. The uptake values are expressed as percentage injected dose per gram tissue (%ID/g).

| | **[$^{111}$In]In-12** | | **[$^{111}$In]In-15** | |
|---|---|---|---|---|
| **Organ/tissue** | **Non-blocked (n=3)** | **Blocked (n=1)** | **Non-blocked (n=3)** | **Blocked (n=1)** |
| Blood | 7.83 ± 0.84 | 7.31 | 18.32 ± 2.12 | 13.87 |
| Tumor | 8.47 ± 0.46 | 2.72 | 6.90 ± 0.81 | 4.39 |
| Pancreas | 16.55 ± 1.41 | 1.26 | 9.72 ± 1.63 | 1.49 |
| Prostate | 3.56 ± 1.62 | 4.36 | 3.27 ± 0.74 | 1.42 |
| Liver | 15.35 ± 0.43 | 20.04 | 8.87 ± 0.65 | 8.93 |
| Spleen | 4.11 ± 0.94 | 3.32 | 5.86 ± 1.70 | 5.05 |
| Stomach | 3.22 ± 0.54 | 3.12 | 4.40 ± 1.04 | 3.48 |
| Small intestine | 4.40 ± 2.45 | 1.45 | 3.79 ± 0.69 | 1.97 |
| Cecum | 3.73 ± 0.40 | 2.35 | 5.21 ± 1.94 | 2.31 |
| Large intestine | 3.88 ± 0.40 | 2.06 | 5.60 ± 1.44 | 2.35 |
| Kidneys | 24.88 ± 2.78 | 17.11 | 15.38 ± 0.50 | 18.19 |
| Lungs | 6.51 ± 1.15 | 16.14 | 6.77 ± 1.73 | 18.95 |
| Heart | 2.39 ± 0.23 | 2.24 | 5.43 ± 0.69 | 3.27 |
| Muscle | 0.96 ± 0.16 | 1.04 | 1.10 ± 0.09 | 1.28 |
| Bone | 2.03 ± 0.89 | 1.87 | 3.05 ± 0.74 | 2.82 |
| Brain | 0.20 ± 0.03 | 0.20 | 0.67 ± 0.28 | 0.51 |
| Tumor-to-organ ratios | | | | |
| Tumor-to-blood | 1.09 ± 0.15 | 0.37 | 0.38 ± 0.04 | 0.32 |
| Tumor-to-pancreas | 0.51 ± 0.03 | 2.16 | 0.72 ± 0.08 | 2.95 |
| Tumor-to-prostate | 2.86 ± 1.58 | 0.62 | 2.16 ± 0.46 | 3.09 |
| Tumor-to-liver | 0.55 ± 0.04 | 0.14 | 0.78 ± 0.04 | 0.49 |
| Tumor-to-kidney | 0.34 ± 0.05 | 0.16 | 0.45 ± 0.04 | 0.24 |
| Tumor-to-muscle | 9.04 ± 1.74 | 2.62 | 6.27 ± 0.44 | 3.42 |

**Supplemental Table 2.** Fluorescent signal of [$^{111}$In]In-**12** and [$^{111}$In]In-**15** in organ/tissue samples after dissection. The signal is expressed as average radiant efficiency in $10^8$ p/sec/cm$^2$/sr per µW/cm$^2$.

| | **[$^{111}$In]In-12** | | **[$^{111}$In]In-15** | |
|---|---|---|---|---|
| **Organ/tissue** | **Non-blocked (n=3)** | **Blocked (n=1)** | **Non-blocked (n=3)** | **Blocked (n=1)** |
| Tumor | 4.31 ± 1.03 | 1.67 | 4.66 ± 1.35 | 1.47 |
| Pancreas | 6.32 ± 0.50 | 0.66 | 5.12 ± 1.93 | 1.17 |
| Liver | 2.20 ± 0.09 | 2.42 | 2.38 ± 0.21 | 1.75 |
| Small intestine | 0.85 ± 0.30 | 0.44 | 0.85 ± 0.04 | 0.38 |
| Large intestine | 0.68 ± 0.19 | 0.47 | 0.94 ± 0.28 | 0.49 |
| Kidneys | 9.41 ± 0.92 | 5.42 | 7.80 ± 0.92 | 6.09 |
| Lungs | 1.93 ± 0.18 | 2.88 | 2.25 ± 0.70 | 2.93 |
| Muscle | 0.78 ± 0.08 | 0.76 | 1.08 ± 0.16 | 0.96 |
| Bone | 0.40 ± 0.11 | 0.32 | 0.74 ± 0.24 | 0.55 |
| Tumor-to-organ ratios | | | | |
| Tumor-to-pancreas | 0.69 ± 0.22 | 2.54 | 0.95 ± 0.18 | 1.25 |
| Tumor-to-liver | 1.96 ± 0.47 | 0.69 | 1.96 ± 0.57 | 0.84 |
| Tumor-to-kidney | 0.47 ± 0.16 | 0.31 | 0.59 ± 0.14 | 0.24 |
| Tumor-to-muscle | 5.69 ± 1.94 | 2.21 | 4.50 ± 1.87 | 1.54 |

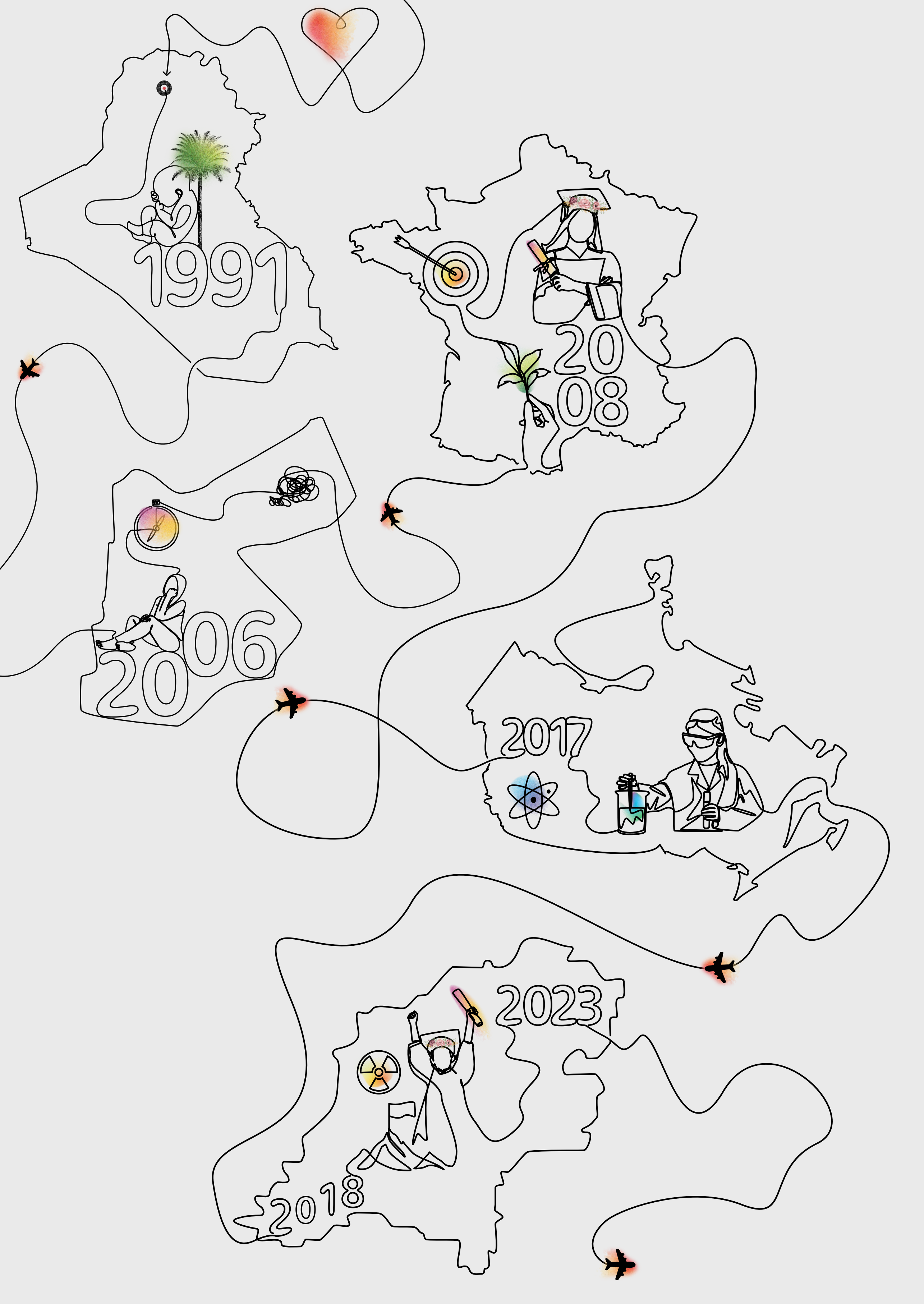
1991
2008
2006
2017
2023
2018

# CHAPTER 4

## Pre- and Intraoperative Visualization of GRPR-Expressing Solid Tumors: Preclinical Profiling of Novel Dual-Modality Probes for Nuclear and Fluorescence Imaging


Marjolein Verhoeven [1], Maryana Handula [1], Lilian van den Brink [1], Corrina M. A. de Ridder [2], Debra C. Stuurman [1], Yann Seimbille [1,3] and Simone U. Dalm [1]

[1] Department of Radiology and Nuclear Medicine, Erasmus Medical Center, University Medical Center Rotterdam, 3015 GD Rotterdam, The Netherlands

[2] Department of Experimental Urology, Erasmus Medical Center, University Medical Center Rotterdam, 3015 GD Rotterdam, The Netherlands

[3] Life Sciences Division, TRIUMF, Vancouver, BC V6T 2A3, Canada



*Cancers. 2023;15(7):2161*

**Simple Summary:** Image-guided surgery is a technique that can help the surgeon detect and remove tumors more precisely. Using a tumor-targeting agent with both a radioactive and a fluorescent label allows us to combine the benefits of two imaging modalities; preoperative nuclear imaging for tumor localization and intraoperative fluorescence imaging for precise and real-time visualization of tumor tissue during surgery. The gastrin-releasing peptide receptor (GRPR) is a promising target for this application because of its overexpression in several solid tumors, e.g., prostate and breast cancers. In this study, a full preclinical characterization of four previously developed GRPR-targeting dual-modality probes is presented, including the characterization of the biodistribution profile, selection of the optimal probe and a proof-of-concept for image-guided surgery. This project is the first comprehensive investigation of the effect of linker modifications and administered dose on the in vivo behavior of GRPR-targeting dual-modality probes, and provides a basis for clinical translation.

**Abstract:** Image-guided surgery using a gastrin-releasing peptide receptor (GRPR)-targeting dual-modality probe could improve the accuracy of the resection of various solid tumors. The aim of this study was to further characterize our four previously developed GRPR-targeting dual-modality probes that vary in linker structures and were labeled with indium-111 and sulfo-cyanine 5. Cell uptake studies with GRPR-positive PC-3 cells and GRPR-negative NCI-H69 cells confirmed receptor specificity. Imaging and biodistribution studies at 4 and 24 h with 20 MBq/1 nmol [$^{111}$In]In-**12**-**15** were performed in nude mice bearing a PC-3 and NCI-H69 xenograft, and showed that the probe with only a *p*ADA linker in the backbone had the highest tumor-to-organ ratios (T/O) at 24 h after injection (T/O > 5 for, e.g., prostate, muscle and blood). For this probe, a dose optimization study with three doses (0.75, 1.25 and 1.75 nmol; 20 MBq) revealed that the maximum image contrast was achieved with the lowest dose. Subsequently, the probe was successfully used for tumor excision in a simulated image-guided surgery setting. Moreover, it demonstrated binding to tissue sections of human prostate, breast and gastro-intestinal stromal tumors. In summary, our findings demonstrate that the developed dual-modality probe has the potential to aid in the complete surgical removal of GRPR-positive tumors.

**Keywords:** gastrin-releasing peptide receptor (GRPR); image-guided surgery; dual-modality probe; NeoB; optical imaging; SPECT imaging; multi-modality imaging

## 1. Introduction

Among cancer types, solid cancers have the highest incidence, with breast, lung and prostate cancer accounting for nearly a third of all newly diagnosed cases in 2020 [1]. Surgery is the most common treatment for these cancers, and complete tumor resection is fundamental to its success. However, one of the greatest challenges for surgeons is to identify tumor boundaries intraoperatively. For prostate cancer, for example, the percentage of resected specimens with cancer cells present at the resection border is, on average, as high as 21.03% [2]. These positive surgical margins have been associated with an increased risk of tumor recurrence and a consequent increased administration of adjuvant treatments [3–5]. Hence, there is an important need to improve the accuracy of tumor resection.

One strategy that has been proposed to aid tumor identification and delineation is image-guided surgery [6]. A breakthrough in this field is the recent FDA approval of the first tumor-targeting agent for fluorescence-guided surgery, commercially called CYTALUX. The intraoperative use of CYTALUX revealed additional lesions in 27% of ovarian cancer patients that would otherwise have been missed, clearly illustrating the benefit of image-guided surgery [7]. However, fluorescence imaging is unfortunately limited by penetration depth, and, therefore, the combined use of nuclear and optical imaging modalities has been proposed as a strategy to further improve surgical navigation. This dual-modality concept is based on both preoperative and intraoperative illumination of cancerous tissue. Nuclear imaging has proved to be a highly sensitive technique for preoperatively detecting cancer, and the radioisotope can additionally be used to locate deeper lesions intraoperatively [8]. Complementary to this, intraoperative optical imaging can improve the surgical view of tumor boundaries in real time. Accordingly, dual-modality nuclear/fluorescent imaging probes would potentially possess the excellent sensitivity and high penetration depth of nuclear imaging and the high, but shallow, resolution and real-time visualization capability of fluorescence imaging in a single agent [9].

The gastrin-releasing peptide receptor (GRPR) is considered an attractive target for molecular imaging, as it is overexpressed in several high-incidence solid tumors, such as prostate, breast, lung and colon cancer [10]. For this reason, multiple GRPR-targeting radiopharmaceuticals and fluorescent agents have been developed and successfully evaluated in preclinical and/or initial clinical studies [11–15]. Among them is the potent DOTA-coupled peptide NeoB (formerly called NeoBOMB1), which has shown good tumor-targeting ability and favorable pharmacokinetics in vivo [16,17]. Due to these promising characteristics, we functionalized NeoB with the sulfo-cyanine 5 (sCy5) far-red fluorescent dye to facilitate its bimodal use. In our previously published work, we described the synthesis of four novel dual-modality probes based on the NeoB backbone and with different linker structures. These probes presented with a good GRPR binding affinity in vitro, and for two of the dual-modality probes, we showed promising tumor uptake in a pilot preclinical biodistribution and imaging study [18].

In the present study, we further characterized the four developed GRPR-targeting dual-modality probes. First, we determined the biodistribution profile of all four probes at two time points and selected the dual-modality probe and time point that resulted in optimal tumor-to-background ratios (TBR). Second, the relationship between dose and TBR was investigated for both imaging techniques to achieve maximal imaging contrast. Lastly, we mimicked image-guided tumor resection in a small proof-of-concept study and performed an ex vivo binding study on a wide range of solid cancers to illustrate the translational utility of our selected dual-modality probe. Ultimately, we aim to improve surgical efficacy for patients with GRPR-expressing solid tumors and thereby reduce the likelihood of tumor recurrence.

## 2. Methods

### *2.1. Chemistry and Radiolabeling*

The synthesis and radiolabeling of the dual-modality probes was reported previously [18]. A total of four probes were generated by introducing a linker (p-aminomethylanilinediglycolic acid (*p*ADA) or $PEG_4$) and lysine between the binding domain of NeoB and DOTA chelator, in combination with or without a PEG4 linker coupling the lysine and trans-cyclooctene (TCO) moiety (Figure 1). A short overview of the methodology can be found in the Supplementary Materials.

The radiolabeling of the four dual-modality probes with [$^{111}$In]$InCl_3$ (Curium, Petten, The Netherlands) was performed in water containing Kolliphor® HS 15 (Merck, Amsterdam, The Netherlands) (0.5 mg/mL) in the presence of sodium acetate, gentisic and ascorbic acid, which acted as radiolysis quenchers [19]. The radiolabeling mixture was incubated at 90 °C for 20 min. Then, diethylenetriaminepentaacetic acid was added to complex free radionuclide. The radiochemical yield (>95%) and radiochemical purity (>95%) of the radiopeptides were determined using instant thin-layer chromatography and radio high-performance liquid chromatography, respectively. The radiolabeled dual-modality probes were prepared with a molar activity of 20 MBq/nmol for all in vitro experiments.

### *2.2. Cell Culture*

The GRPR-positive human-derived prostate adenocarcinoma epithelial PC-3 cells (ATCC, Manassas, VA, USA) and the GRPR-negative human small-cell lung carcinoma NCI-H69 cells (ECACC, Salisbury, UK) were cultured in F-12K Nutrient mix (Gibco, Paisley, UK) and RPMI medium 1640 + GlutaMAX-I (Gibco), respectively. Both media were supplemented with 10% fetal bovine serum (FBS; Gibco), penicillin (100 units/mL; Sigma-Aldrich, Darmstadt, Germany) and streptomycin (100 µg/mL; Sigma-Aldrich). Cell lines were routinely passaged and grown at 37 °C in a humidified atmosphere with 5% $CO_2$.

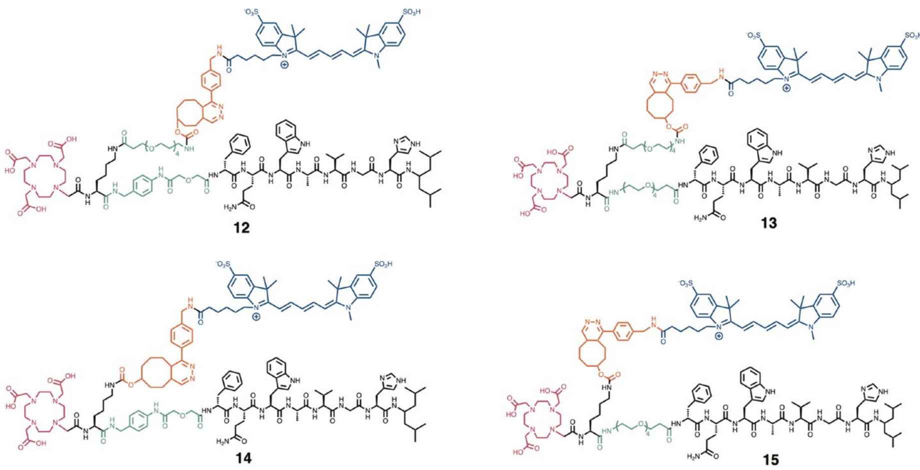

**Figure 1.** Chemical structures of the four dual-modality probes **12**-**15**. In black, the peptide sequence responsible for binding to the GRPR, and the lysine residue. In green, the $PEG_4$ and *p*ADA linkers. In red, the DOTA chelator. In orange, the inverse electron demand Diels-Alder click reaction, and in blue, the sulfo-cyanine 5 fluorescent dye.

### *2.3. In Vitro Cell Uptake Assay*

A cell uptake assay was performed to determine the receptor specificity of [$^{111}$In]In-**12**-**15**.

PC-3 cells were seeded in 12-well plates (2.5 × $10^5$ cells/well) one day prior to the experiment. The next day, cells were washed with Dulbecco's phosphate-buffered saline (PBS; Gibco) and incubated with 0.5 mL of Kolliphor® HS 15 in PBS (0.06 mg/mL) containing $10^{-9}$ M [$^{111}$In]In-NeoB (positive control) or [$^{111}$In]In-**12**-**15** in the presence or absence of $10^{-6}$ M unlabeled NeoB for 1 h at 37 °C. After incubation, the medium was removed, and cells were washed twice with cold (4 °C) PBS. The cells were then exposed to 50 mM glycine (pH 2.8) for 10 min at RT to determine the membrane-bound fraction and lysed using 1M NaOH for >20 min at RT to collect the internalized fractions.

On the day of the experiment, 1 × $10^6$ NCI-H69 cells were incubated with 1.0 mL of the incubation solutions described above. After incubation, the cells were pelleted twice through centrifugation (5 min, 0.5 g, 4 °C) and washed in between with cold (4 °C) PBS.

The collected PC-3 cell fractions (membrane-bound and internalized fractions separately) and NCI-H69 cell pellets (total binding) were measured in a γ-counter (Perkin Elmer, Waltham, MA, USA) to determine the radioactivity uptake. To calculate the amount of radioactivity added to the cells, samples of the incubation solutions were also measured. The results of the uptake assays are expressed as the percentage of added activity (%AA). Data represent the mean ± standard deviation (SD) of triplicate wells.

### *2.4. Animal Model and Experimental Design In Vivo Studies*

All animal experiments were approved by the animal welfare committee of the Erasmus MC and were conducted in agreement with the institutional guidelines. In vivo studies were performed to determine (1) the biodistribution profile of [$^{111}$In]In-**12**-**15** and to select the most suitable probe and optimal time point for imaging, (2) to determine the ideal dose of the probe selected based on (1) and (3) to determine the clinical potential of the selected probe in a proof-of-concept simulated image-guided surgery setting.

Five- to eight-week-old male Balb/c nu/nu-specific and opportunistic pathogen-free mice (Janvier Labs, Le Genest-Saint-Isle, France) were used for the biodistribution ($n$ = 3/4 mice per condition) and dose optimization studies ($n$ = 4 mice per dose), and six-week-old male NMRI-Foxn1 nu/nu mice (Janvier Labs) were used for the proof-of-concept study ($n$ = 2). Upon arrival, mice were housed in individually ventilated cages (2–4 mice per cage) with ad libitum access to water and food, and left to acclimate for one week. Animals were subcutaneously inoculated on the right shoulder with PC-3 cells ($5 \times 10^6$ cells suspended in 200 µL of 1/3 Matrigel (Corning Inc., Corning, NY, USA) and 2/3 Hanks' balanced salt solution (HBSS; Gibco)). For the biodistribution and proof-of-concept studies, in addition to the PC-3 xenografts, mice were xenografted with NCI-H69 cells on the left shoulder ($5 \times 10^6$ cells suspended in 200 µL of 1/3 Matrigel and 2/3 HBSS). PC-3 and NCI-H69 xenografts were allowed to grow for 3 and 2.5 weeks, respectively. At the start of the experiment, the tumor sizes were 401 ± 84 mm$^3$ and 282 ± 102 mm$^3$ for PC-3 and NCI-H69 xenografts, respectively, for the biodistribution study and 378 ± 168 mm$^3$ for PC-3 xenografts for the dose optimization study. The tumor sizes were 163 and 409 mm$^3$ for PC-3 xenografts and 1066 and 697 mm$^3$ for NCI-H69 xenografts for animal 1 and 2, respectively, in the proof-of-concept study.



### *2.5. Administration of [$^{111}$In]In-12-15*

The biodistribution profile of [$^{111}$In]In-**12**-**15** was studied after the administration of approximately 20 MBq/1 nmol. For the dose optimization study, three different doses of [$^{111}$In]In-**14** were administered: 0.75, 1.25 or 1.75 nmol (20 MBq per administered dose). The simulated image-guided surgery was performed after the injection of 20 MBq/0.75 nmol [$^{111}$In]In-**14**. The injected solutions were prepared in PBS containing Kolliphor® HS 15 (0.06 mg/mL). All mice were intravenously injected via the tail vein with a total volume of 200 µL.

### *2.6. In Vivo SPECT/CT/OI for the Biodistribution and Dose Optimization Studies*

For the biodistribution study, each dual-modality probe was evaluated at 4 and 24 h post injection (p.i.). In the dose optimization study, each administered dose was studied at 24 h p.i. Whole-body single-photon emission computerized tomography (SPECT)/computed tomography (CT) and optical imaging (OI) were executed for one mouse per group under isoflurane/$O_2$ anesthesia using the VECTor$^5$/OI-CT small animal scanner (MILabs B.V., Utrecht, The Netherlands). SPECT imaging was performed over 30 min in list mode using the XXUHS-M collimator with a 3.0 mm pinhole diameter. Corresponding CT scans were obtained within 5 min with the following settings: full angle scan, 50 kV tube voltage, 0.21 mA tube current, 500 µm aluminum filter. Lastly, optical imaging was performed with a 624 nm excitation and 692 nm emission filter with 4 × 4 binning for 400 ms or 600 ms in the biodistribution and dose optimization study, respectively.

SPECT images were reconstructed utilizing the similarity-regulated OSEM algorithm (MILabs Rec 12.00 software) with a voxel size of 0.8 mm$^3$, 128 subsets, 9 iterations and photo peak energy windows of 171 keV ± 20% and 246 keV ± 20% for indium-111. Two adjacent background windows per photo peak were used for triple-energy window scatter and crosstalk correction. A post-reconstruction Gaussian filter of 1 mm FWHM was applied to both the SPECT and OI images. The CT was reconstructed at 200 µm$^3$ and analyzed together with the registered attenuation-corrected SPECT images using PMOD (PMOD 3.9, Zurich, Switzerland). OI images were processed in MILabs OI Post Processing software v2.3.5.

### *2.7. Ex Vivo Biodistribution and Optical Imaging*

Ex vivo biodistributions were performed to determine the radioactivity and fluorescent tumor and organ uptake of [$^{111}$In]In-**12**-**15** at 4 and/or 24 h p.i. Blood was collected via a retro-orbital puncture under isoflurane/$O_2$ anesthesia, after which mice were euthanized via cervical dislocation. The tumors and organs of interest (adrenal glands, bone, cecum, colon, heart, kidneys, liver, lungs, muscle, pancreas, prostate, small intestine, spleen, stomach and tail) were excised, washed in PBS and dried. The stomach, cecum and intestines were cleared of their contents. The PC-3 and NCI-H69 tumors were cut in half and one half of each tumor was snap-frozen in liquid nitrogen for further ex vivo analysis. The other half of the tumors, together with the bone, kidneys, liver, lungs, muscle, pancreas, small intestine, spleen and stomach were placed in small Petri dishes, and ex vivo optical imaging was performed using the IVIS Spectrum system (Perkin-Elmer) with the following settings: FOV 12.6 cm, medium binning, f-stop 2, 0.5–0.75 s exposure with an excitation/emission filter of 640 nm/680 nm. The fluorescent signal was quantified by drawing a region of interest around the organ/tissue using Living Image version 4.5.2 or 4.7.3 software (Perkin Elmer) and expressed as radiant efficiency [(photons/second/cm$^2$/steradian)/(µW/cm$^2$)].

After imaging, all tissues and organs were weighed and measured in a γ-counter. To calculate the total radioactivity injected per animal, aliquots of the injected solutions were measured as well. For the adrenal glands and prostate, the average weight of all animals was used because of the low weight of these organs. The percentage injected activity per gram (%IA/g) was determined for each organ and corrected for the %IA present at the injection site (tail).

***2.8. Ex Vivo Analysis of Xenografts***

Fresh frozen xenograft samples were sectioned (10 µm thick) using the CryoStar NX70 cryostat (Thermo Scientific, Waltham, MA, USA) and mounted on glass slides. On consecutive sections, we performed autoradiography to localize the radioactive signal within the samples, a fluorescent scan to localize the fluorescent signal within the samples and hematoxylin-eosin (H&E) staining following standard protocol for histological evaluation. The radioactive slides were covered with copper tape on the back and imaged using the Beaquant system (Ai4r, Nantes, France). The fluorescent slides were scanned using the Odyssey flatbed scanner system (Li-Cor, Lincoln, NE, USA) applying a 700 nm laser. High-resolution images of the H&E-stained sections were acquired using the NanoZoomer digital slide scanner (Hamamatsu Photonics, Shizuoka, Japan).

***2.9. In Vitro Dead/Alive Cell Binding Assay***

A dead/alive cell binding assay was performed to illustrate that dead cell binding was mediated by the sCy5 dye. PC-3 cells were seeded in 24-wells plate ($1.25 \times 10^5$ cells/well) one day prior to the experiment. The next day, cells were washed with PBS and then either kept alive or killed with 50 µL 70% EtOH solution. Dead and alive cells were incubated with 0.5 mL of $10^{-9}$ M [$^{111}$In]In-**14** or [$^{111}$In]In-NeoB (control) with or without $10^{-6}$ M unlabeled NeoB in PBS containing Kolliphor® HS 15 (0.06 mg/mL) for 1 h at 37 °C. Empty wells were included as well to determine the non-specific binding of the probe. After three gentle washes with PBS, the plates were placed on super-resolution phosphor screens for 24 h and read using the Cyclone Plus system (Perkin Elmer).





***2.10. In Vivo Proof-of-Concept Image-Guided Surgery***

SPECT/CT images were acquired at 24 h p.i. while mice ($n$ = 2) were under isoflurane/$O_2$ anesthesia as described above. After imaging, the mice were sacrificed via cervical dislocation and the PC-3 tumor was removed post-mortem under fluorescent guidance. Fluorescent scans were performed before, during and after tumor excision using the IVIS Spectrum system (Perkin Elmer) with the following settings: FOV 18.6 cm, medium binning, f-stop 2. An image sequence was acquired using a 605 nm excitation filter and emission filters from 660 to 700 nm in 20 nm increments, and a 640 nm excitation filter and emission filters from 680 to 740 nm in 20 nm increments (exposure time: 3–20 s). Images were processed using Living Image software, version 4.7.3. Spectral unmixing was performed to remove tissue autofluorescence.

### 2.11. Ex Vivo Autoradiography on Human Cancer Specimens

An in vitro autoradiography study on human cancer specimens was performed to illustrate the tumor-targeting capacity of **14** for various GRPR-expressing malignancies. This study adhered to the Code of Conduct of the Dutch Federation of Medical Scientific Societies. Fresh frozen human breast cancer, prostate cancer and gastro-intestinal stromal tumor (GIST) specimens ($n$ = 5 per cancer type) were obtained from the Erasmus MC tissue bank. Specimens were sectioned at 10 µm thickness and subsequently mounted on glass slides. Tissue sectioning exposed intracellular proteins to which sCy5 could potentially bind. Therefore, tissue sections were incubated with 100 µL of $10^{-9}$ M [$^{111}$In]In-NeoB in the absence and presence of $10^{-5}$ M **14** in PBS containing Kolliphor® HS 15 (0.06 mg/mL) for 1 h at RT instead of the other way around. This allowed the focus to only be on the tumor-targeting capacity of **14**. Following incubation, each slide was drained off and washed twice in cold (4 °C) wash buffer containing BSA (167 mM Tris-HCl, 5 mM $MgCl_2$, 0.25% BSA), then once in cold wash buffer without BSA and, finally, briefly in cold demi-water. Dried slides were covered with copper tape on the back and imaged with the Beaquant system to localize the radioactive signal within the sample. Adjacent tissue sections were used for H&E staining following standard protocol and imaged using the NanoZoomer digital slide scanner (Hamamatsu Photonics). Tumor regions were manually drawn by experienced pathologists.

### 2.12. Statistics

All statistical analyses were carried out using GraphPad Prism software, version 9 (GraphPad Software Inc., San Diego, CA, USA). A $p$ value below 0.05 was considered statistically significant. To confirm receptor specificity, an independent $t$-test was performed for each probe separately to compare total binding to non-specific binding. Regarding the animal studies, significant outliers were detected with Grubbs' test and excluded from the data set. Tissue and organ uptake of the four dual-modality probes and of the three tested doses were compared by performing a two-way analysis of variance with a Tukey test to correct for multiple comparisons. All data are represented as mean ± standard deviation (SD).

## 3. Results

### 3.1. In Vitro Characterization

In our previous publication, we showed that the binding affinity of the dual-modality probes was in the nanomolar range ($IC_{50}$: 44.1–118.7 nM) [18]. To further characterize **12**-**15** in vitro, an internalization assay was performed. The dual-modality probes presented lower total binding and less receptor-antagonistic properties than the established GRPR-targeting radioligand NeoB; the membrane-bound fraction of [$^{111}$In]In-**12**-**15** was lower than that of [$^{111}$In]In-NeoB (mean of 47.7–61.0% versus 88.0% for [$^{111}$In]In-**12**-**15** and [$^{111}$In]In-NeoB, respectively). In addition, the receptor specificity of **12**-**15** was demonstrated, as an excess of unlabeled NeoB successfully blocked the uptake of [$^{111}$In]In-**12**-**15** in GRPR-positive PC-3 cells ($p < 0.05$) (Figure S1A). An uptake assay using GRPR-negative NCI-H69 cells showed no specific binding for all probes, proving the suitability of using an NCI-H69 xenograft as the negative control for subsequent in vivo studies (Figure S1B).

### *3.2. In Vivo Comparison of the Biodistribution Profiles*

The first in vivo study examined the impact of linker structures on the biological behavior of the dual-modality probes. Figure 2 depicts the biodistribution of [$^{111}$In]In-**12**-**15** in PC-3 and NCI-H69 tumor-bearing mice at 4 and 24 h p.i.

In spite of their different chemical structures, radioactivity uptake in the PC-3 tumor was similar for all dual-modality probes at the early time point (3.03 ± 1.08%IA/g for [$^{111}$In]In-**12**, 3.16 ± 0.91%IA/g for [$^{111}$In]In-**13**, 2.96 ± 0.78%IA/g for [$^{111}$In]In-**14** and 3.31 ± 0.37%IA/g for [$^{111}$In]In-**15**) (Figure 2A, Table S1). Interestingly, [$^{111}$In]In-**12** and [$^{111}$In]In-**14** showed better tumor retention properties, as tumor uptake was maintained at 24 h p.i. (Figure 2C, Table S2). This contributed to more favorable tumor-to-organ ratios (T/O) for [$^{111}$In]In-**12** and [$^{111}$In]In-**14** compared to [$^{111}$In]In-**13** and [$^{111}$In]In-**15** at the late time point, with a T/O for blood of >10, for the prostate of >5 and for muscle of >12 ($p < 0.05$) (Figure 2B&D). In addition to a faster tumor washout, [$^{111}$In]In-**13** and [$^{111}$In]In-**15** also demonstrated prolonged blood circulation, as the blood uptake at 4 h p.i. was higher than for [$^{111}$In]In-**12** and [$^{111}$In]In-**14** ($p < 0.01$), and was still elevated for [$^{111}$In]In-**15** at 24 h p.i.

High radioactivity uptake levels were also observed in the GRPR-expressing pancreas and the organs responsible for excretion, i.e., the liver and the kidneys. The pancreatic uptake of [$^{111}$In]In-**12** and [$^{111}$In]In-**14** was significantly higher than [$^{111}$In]In-**13** at both time points. Regarding excretion, [$^{111}$In]In-**13** showed significantly less hepatic excretion than the other dual-modality probes at 4 h p.i. ($p < 0.05$). At the late time point, this was the case for both [$^{111}$In]In-**13** and [$^{111}$In]In-**15** ($p < 0.01$). Excretion also largely occurred via the kidneys with [$^{111}$In]In-**12** and [$^{111}$In]In-**13** showing higher kidney uptake than [$^{111}$In]In-**14** at 4 h p.i. ($p < 0.01$). At 24 p.i., kidney uptake was still higher for [$^{111}$In]In-**12** than for all other dual-modality probes ($p < 0.0001$).

In Figure 2E, the distribution of the fluorescent signal in a subset of organs is visualized. This distribution largely corresponds with the distribution of the radioactive signal. Semi-quantitative measurements of the fluorescent intensity verified the highest uptake in the PC-3 tumor, pancreas and kidneys at both time points (Figure S2, Tables S3 and S4). Although, again, a high initial uptake was detected in the pancreas, it also showed a relative rapid washout compared to the PC-3 tumor; a 2.0- vs. 10.9-fold for [$^{111}$In]In-**12**, a 3.7- vs. 5.8-fold for [$^{111}$In]In-**13**, a 2.0- vs. 9.7-fold for [$^{111}$In]In-**14** and a 2.2- vs. 6.0-fold lower uptake for [$^{111}$In]In-**15** in the tumor and pancreas, respectively, measured at 24 vs. 4 h p.i. The longer blood circulation of [$^{111}$In]In-**13** and [$^{111}$In]In-**15** was reflected by a higher signal in background tissues, such as the NCI-H69 tumor and muscle. However, co-localization of the fluorescent and radioactive signal was not observed for the liver, which can be at least partially explained by signal attenuation due to the size of this organ. In addition, the differences between the dual-modality probes were less pronounced for, e.g., the PC-3 tumor at 24 h p.i., which is probably due to the limited sensitivity of this quantification method.

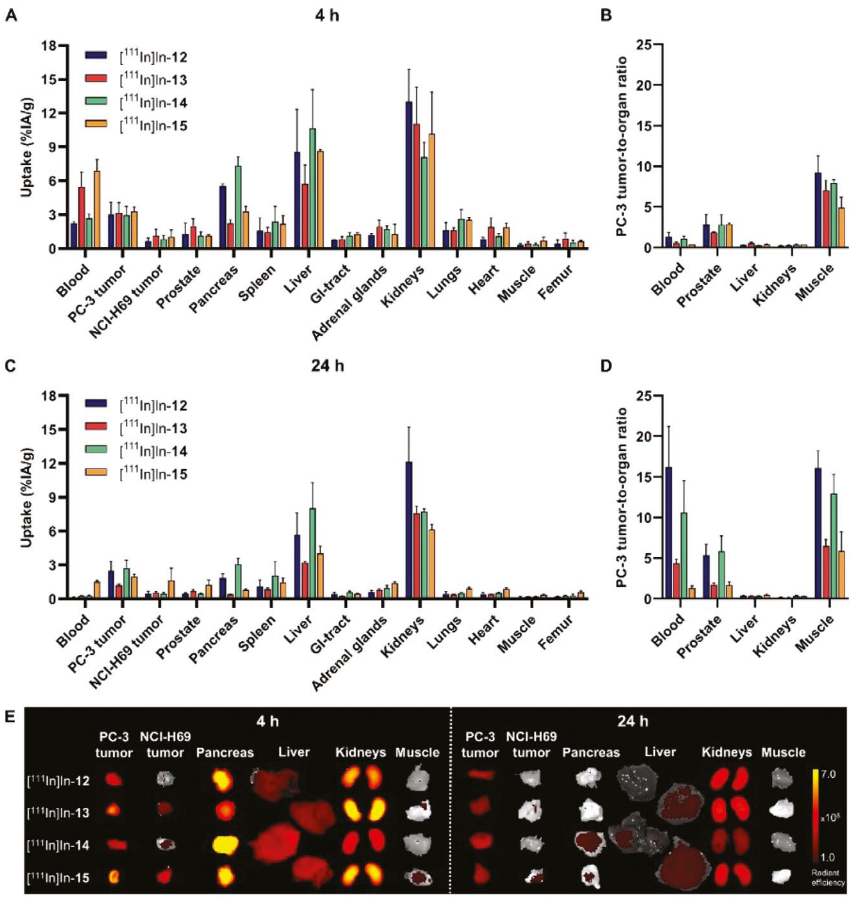


**Figure 2.** *Ex vivo* biodistribution of [$^{111}$In]In-**12-15** (20 MBq/1 nmol) in mice bearing GRPR-positive PC-3 and GRPR-negative NCI-H69 xenografts. Radioactivity uptake values are expressed as percentage injected activity per gram of tissue (%IA/g) and as PC-3 tumor-to-organ ratios at 4 h (A, B) and 24 h (C, D) post injection and represent the mean ± standard deviation ($n$ = 3/4). *Ex vivo* merged photograph and fluorescence images of a subset of dissected tissues and organs (E) are shown for one representative mouse per group. The fluorescent signal is displayed as average radiant efficiency in p/sec/cm$^2$/sr per µW/cm$^2$.

Regarding the imaging time point, imaging at 24 h led to improved tumor contrast due to the clearance from normal organs. Figure 3 shows that PC-3 xenografts, unlike NCI-H69 xenografts, could be clearly delineated in both nuclear and optical images at 24 h p.i. (provided that the tumor was located in the field of view). Target specificity was demonstrated by the low signal detected in the GRPR-negative tumor. The signal in the abdominal regions in the coronal SPECT/CT images reflects the excretion of the probes, and the signal in the cardiac region in the axial SPECT/CT image and the increased background signal in the optical image of [$^{111}$In]In-**15** again highlight the prolonged blood circulation of this probe.

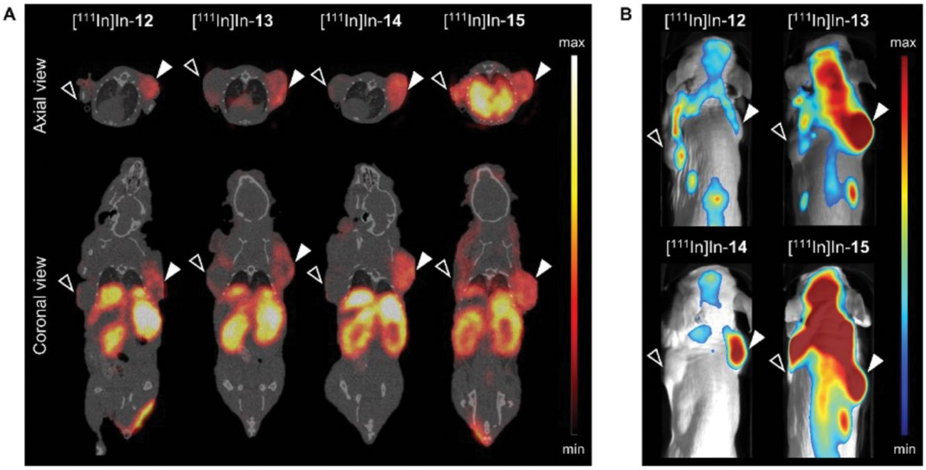


**Figure 3.** In vivo SPECT/CT (A) and optical (B) images of GRPR-positive PC-3 (▲; right shoulder) and GRPR-negative NCI-H69 (Δ; left shoulder) tumor bearing mice at 24 h post injection of [$^{111}$In]In-**12-15** (20 MBq/1 nmol). SPECT/CT images represent an overlay of a CT slice and the corresponding SPECT slice on which the tumor cross-sections are clearly visible. The arrow heads point at the location of the tumor.

Together, these results show that the use of dual-modality probes with a *p*ADA linker in their backbone leads to a higher T/O favorable for good tumor delineation in an image-guided surgery application. Although the biodistribution profiles of [$^{111}$In]In-**12** and [$^{111}$In]In-**14** were largely similar, [$^{111}$In]In-**14** presented lower kidney uptake than [$^{111}$In]In-**12** at both time points. Therefore, [$^{111}$In]In-**14** was selected for further evaluations.

### *3.3. Dose Optimization*

The purpose of the next in vivo study was to study the effect of the injected dose on T/O to select the ideal dose to achieve maximum image contrast with both imaging modalities. Figure 4 presents the evaluation of three different doses, i.e., 0.75 nmol, 1.25 nmol and 1.75 nmol, of [$^{111}$In]In-**14** in PC-3 xenografted mice at 24 h p.i.

With respect to nuclear imaging, no clear differences were observed in the SPECT/CT images (Figure S3), but a slightly lower radioactivity uptake in the tumor with increasing dose was recognized (2.74 ± 0.18%IA/g, 2.35 ± 0.40%IA/g and 2.09 ± 0.30%IA/g for 0.75, 1.25 and 1.75 nmol, respectively) (Figure 4A, Table S5). However, significant changes were noted in the route of excretion. The injection of a higher dose resulted in reduced kidney uptake (8.90 ± 0.91%IA/g, 7.05 ± 1.40%IA/g and 5.55 ± 0.24%IA/g for 0.75, 1.25 and 1.75 nmol, respectively) ($p < 0.001$). In contrast, a significantly higher radioactivity uptake in the liver and spleen was observed with an increasing dose. This indicates that hepatic clearance plays a greater role than renal clearance in the excretion of [$^{111}$In]In-**14** when higher doses are administered. The increased hepatic excretion translated into a 20.5-fold lower tumor-to-liver ratio for 1.75 vs. 0.75 nmol ($p < 0.0001$) (Figure 4B).

Regarding optical imaging, the fluorescence images showed a strong increase in the fluorescent signal in the tumor upon application of an increasing dose (Figure 4E). The quantification of this signal revealed a 1.7-fold increase for 1.75 vs. 0.75 nmol ($p < 0.0001$) (Figure 4C, Table S6). However, the fluorescent signal in most background organs also increased, e.g., 2.0-, 2.2- and 1.9-fold higher signal in the liver, kidneys and muscle, respectively, when a dose of 1.75 vs. 0.75 nmol was administered. Together, this resulted in similar T/O for all doses (Figure 4D). Based on this and the better tumor-to-liver ratios of the radioactive signal distribution following the injection of a lower dose, 0.75 nmol was identified as the ideal dose.

Since the radioactive and fluorescent signal distribution in the tumor showed an opposite trend with respect to dose, an ex vivo analysis of PC-3 xenografts was performed to localize the respective signals within the tumor. From the data in Figure 4F, it is apparent that the radioactive and fluorescent signal are heterogeneously distributed throughout the tumor. H&E staining revealed that the radioactive signal is mostly restricted to viable regions, while the fluorescent signal is not restricted and strongest in non-viable regions, i.e., the necrotic core of the tumor. The binding of [$^{111}$In]In-**14** to dead cells was confirmed by an in vitro cell binding experiment (Figure S4). The fact that the binding of [$^{111}$In]In-**14** to dead PC-3 cells, unlike living cells, could not be blocked by an excess of unlabeled NeoB illustrates that the dead cell binding is not mediated by the GRPR binding domain.

### *3.4. Translational Applicability*

In order to assess the applicability of [$^{111}$In]In-**14** for image-guided tumor resection, image-guided surgery was mimicked on PC-3 and H69 xenografted mice (Figure 5). The GRPR-positive tumor could be clearly localized via a preoperative SPECT/CT evaluation at 24 h p.i. Post-mortem IVIS imaging allowed the location of the incision to be accurately determined and the tumor tissue to be distinguished and monitored during the operative procedure through fluorescent guidance.

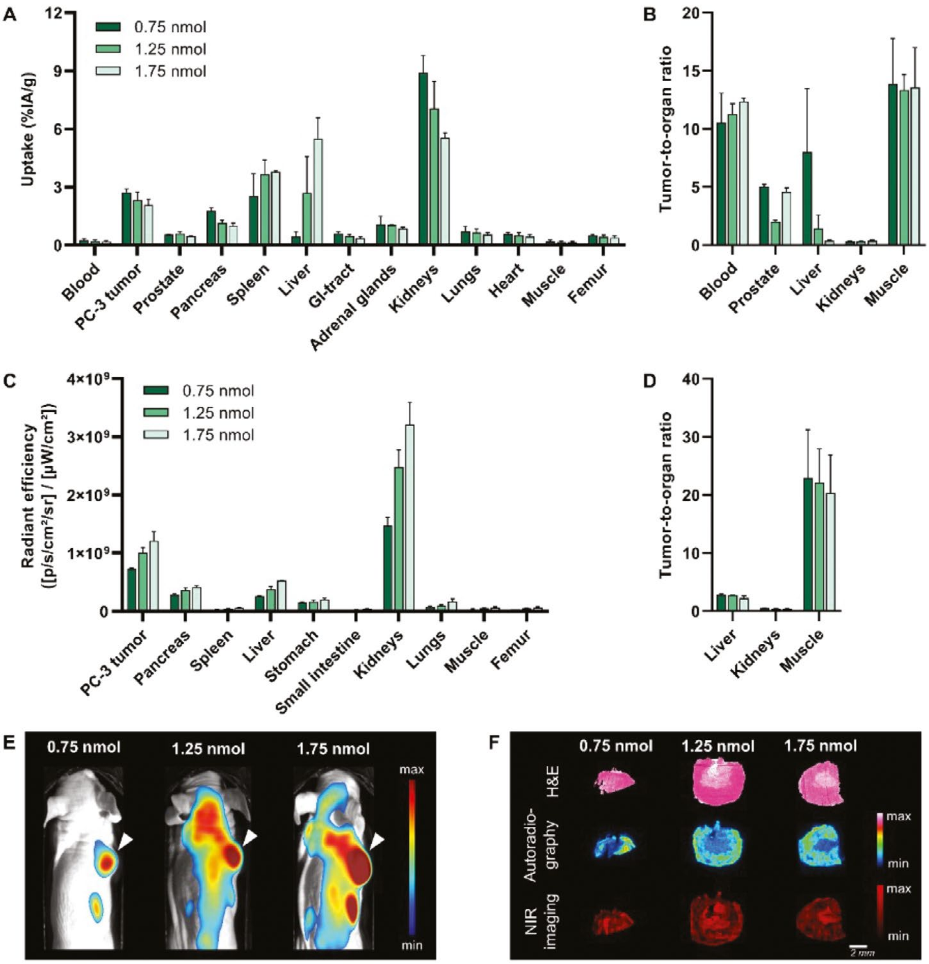


Figure 4. Evaluation of 0.75 nmol, 1.25 nmol and 1.75 nmol [$^{111}$In]In-**14** (20 MBq per administered dose) in PC-3 xenografted mice at 24 h post injection. Ex vivo biodistribution presented as radioactivity uptake (expressed as percentage injected activity per gram of tissue (%IA/g)) (**A**) and the corresponding tumor-to-organ ratios (**B**). Quantification of ex vivo fluorescence imaging of a selection of dissected organs and tissues expressed as average radiant efficiency in p/sec/cm$^2$/sr per µW/cm$^2$ (**C**) and corresponding tumor-to-organ ratios (**D**). Data are presented as mean ± standard deviation ($n$ = 4). In vivo whole-body optical imaging displayed as merged photographs and fluorescence images (**E**). The arrow head points at the location of the PC-3 tumor. Ex vivo PC-3 xenograft analysis of one representative mouse per group demonstrating the histology (top row), radioactive signal distribution (middle row) and fluorescent signal localization (bottom row) (**F**).

An ex vivo binding study was performed on a wide range of solid cancer specimens (i.e., breast cancer, prostate cancer and GIST) to demonstrate the broad applicability of [$^{111}$In]In-**14**. Figure 6 shows that an excess of the dual-modality probe can successfully block the [$^{111}$In]In-NeoB signal in all three cancer types studied, illustrating its potential to bind to various human GRPR-positive cancerous tissues.


**Figure 5.** Proof-of-concept image-guided surgery on PC-3 (▲; right shoulder) and NCI-H69 (Δ; left shoulder) tumor-bearing mice at 24 h post injection 20 MBq/0.75 nmol [$^{111}$In]In-**14**. Shown are a preoperative SPECT/CT scan (**left panel**), post-mortem merged photograph and fluorescence images obtained prior to, during and after PC-3 tumor resection (**middle panel**), plus a final image to check the surgical margins with a more sensitive scale (**right panel**). The fluorescent signal is displayed as average radiant efficiency in p/sec/cm²/sr per µW/cm². For the SPECT/CT scan, a maximum intensity projection is shown in combination with an axial SPECT/CT image representing an overlay of a CT slice and the corresponding SPECT slice on which the tumor cross-sections are clearly visible. The arrow heads point to the location of the tumor.

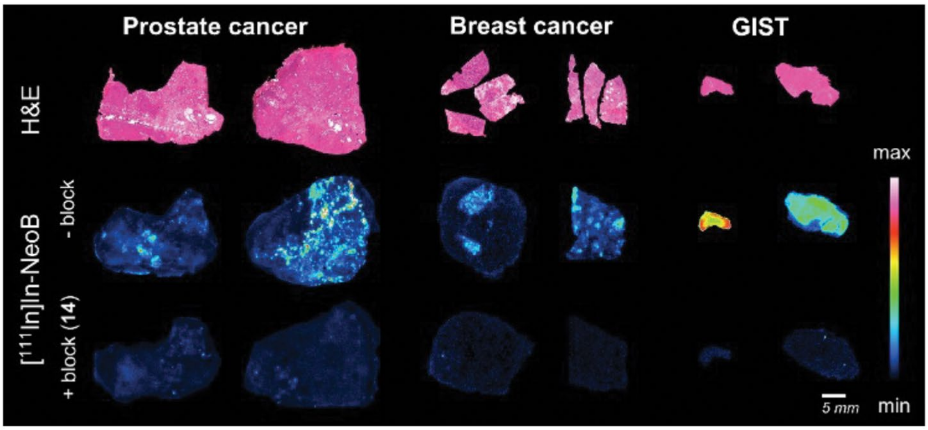


**Figure 6.** Hematoxylin-eosin staining (**top row**) and ex vivo autoradiography of human prostate cancer, breast cancer and gastro-intestinal stromal tumor (GIST) sections from six representative patients demonstrating binding of [$^{111}$In]In-NeoB in the absence (- block; **middle row**) or presence (+ block (**14**); **bottom row**) of an excess of **14**. Tumor regions were circled in black by experienced pathologists.

## 4. Discussion

Surgery is the gold standard treatment for several solid tumors. Complete tumor resection is related to favorable outcomes, but it can be challenging for the surgeon to delineate tumors intraoperatively solely by visual and tactile guidance. To increase surgical precision, guidance by fluorescence imaging has been proposed to aid in the differentiation of tumor tissue from adjacent non-cancerous tissue [20]. The use of dual-labeled analogs containing both a radioisotope and fluorescent dye can combine the strengths of two modalities; tumor localization by nuclear imaging and real-time visualization by fluorescence imaging. The field of image-guided surgery can build on the success of targeted radioligands, where a common strategy is to add a fluorescent dye to an established radioligand. In a previous publication, we described the development of four dual-modality probes based on the potent radioligand NeoB that targets the GRPR and using two different linkers, i.e., the *p*ADA and $PEG_4$ linker [18]. In this study, we focused on characterizing the biological behavior of the four developed GRPR-targeting dual-modality probes, optimizing the dose of the most promising probe and determining its translational applicability.

As a result of the relatively small size of radioligands, the conjugation of a fluorescent dye and linker can greatly influence their biological behavior [21]. We observed that the receptor-specific properties of NeoB were preserved within the developed probes, most likely because the binding domain was unchanged. However, the strong antagonistic properties of NeoB were not retained as the intracellular fraction of the probes was increased by ~35%. We assume that this effect is probably due to the incorporation of the dye rather than the differences in linker structures. The observed increase in cell internalization after dye conjugation has also been reported for the radioligands RM2 and PSMA-11 [22,23]. Moreover, since the use of GRPR antagonists has been shown to lead to higher levels of tumor accumulation, the more agonistic properties of the developed dual-modality probes could partly explain the observed decrease in total binding [24].



The incorporation of the fluorescent dye also largely determines the in vivo biodistribution. From comparing the biodistribution profile of the probes with that of the radiolabeled parent peptide NeoB at similar doses [25], it is apparent that the probes have prolonged blood circulation. The prolonged circulation time, and thus delayed clearance, results in higher kidney uptake at both time points. Moreover, the injection of the probes led to higher levels of liver accumulation. This biodistribution profile is in line with our preliminary data on [$^{111}$In]In-**12** and [$^{111}$In]In-**15** and with the findings of Zhang et al., who characterized a GRPR-targeting dual-modality probe that was based on the radioligand RM2 [18,22]. The observed increase in liver uptake can at least partly be attributed to metabolism of the dye in this organ [26]. Accordingly, a loss of fluorescent signal may be the consequence of the degradation of the dye [27]. This might also be the reason for the discrepancy when it comes to the co-localization of the fluorescent and radioactive signal in the liver. The observed impact of the dye on the biological behavior of probes has previously been reported for other peptide-based dual-modality probes [28–30]. As different fluorescent dyes have different chemical properties, further research into the use of other dyes could potentially lead to optimization of the biodistribution profile. Taken together, these findings underline the need for preclinical evaluations when radiolabeled peptides are repurposed for image-guided surgery applications.

The in vivo data also demonstrated that the linker contributed to the biodistribution of the probes. This is in agreement with the findings of Shrivastava et al. [31], who illustrated that fluorescent GRPR-targeting peptides are highly sensitive to linker adaptations. The two linkers evaluated in our study were the *p*ADA linker, which is part of the original NeoB structure, and $PEG_4$. $PEG_4$ provides more spacing than *p*ADA and was selected to potentially limit steric hindrance from the fluorescent label. The dual-modality probes [$^{111}$In]In-**12** and [$^{111}$In]In-**14**, both with a *p*ADA linker in their backbone, presented with better tumor retention properties. This suggests that the more rigid *p*ADA linker is an integral part of NeoB and partly responsible for the good tumor-targeting properties of this radioligand. [$^{111}$In]In-**13** and [$^{111}$In]In-**15** showed a longer blood circulation time and were mainly cleared via the kidneys, which could be explained by the hydrophilic nature of the $PEG_4$ linker located in their backbones [32]. Although [$^{111}$In]In-**12** and [$^{111}$In]In-**13** contain an extra $PEG_4$ linker between the lysine and TCO moiety to create more distance between the dye and binding domain, this seemed to have an effect on the clearance pathway rather than binding [22]. Our findings emphasize that the linker selection should be carefully evaluated as it can considerably impact the biological behavior of dual-modality probes.

High image contrast is required for clear tumor delineation in both a preoperative and intraoperative setting. We have shown that adjusting the imaging time point can positively impact image contrast, as delayed imaging benefits from increased clearance. Due to the natural affinity of cyanine dyes for human serum albumin [33], others have also reported on the need for delayed imaging after dye conjugation into the normally rapidly cleared peptides [34]. Twenty-four hours after injection, the dual-modality probe with the most favorable T/O was [$^{111}$In]In-**14**. Although the T/O for most background organs was more than sufficient to distinguish tumor tissue from normal tissue (i.e., >2) [9], uptake in the organs responsible for excretion was still high and would hinder the localization of tumor lesions in their immediate vicinity or downstream of the excretion route. However, it is encouraging that tumor uptake was maintained over time, because it suggests that imaging at an even later time point with further increased clearance might improve contrast in these regions.

Another important factor in achieving maximum image contrast with both imaging modalities is dose. A common challenge is to adapt the dose to match the sensitivity of both imaging techniques [35,36]. Surprisingly, the effect of administering increasing doses was observed best in the clearance pathway; liver uptake was more pronounced. Despite the fact that a surfactant was used during radiolabeling and injection preparation to prevent peptide aggregation and their subsequent accumulation in the liver, we suspect that at higher doses, the solubility limit of our probe was reached [37]. The concomitant decrease in renal clearance is most likely a result of this increased liver uptake. A higher liver uptake is less favorable when aiming for an image-guided surgery application in the abdominal cavity, hence the ideal dose of [$^{111}$In]In-**14** for our preclinical model was 0.75 nmol, as this led to a tumor-to-liver ratio of >2. The translation of our dual-modality probe requires additional studies to investigate whether, for example, higher concentrations of the surfactant can improve solubility.

All three tested doses were coupled to an equal amount of radioactivity, meaning that for higher doses the portion of unlabeled probe (i.e., containing only a fluorescent label) was increased. We observed that administering increasing doses resulted in a slight decrease in the radioactive signal measured in the tumor, indicative of receptor saturation. Incongruous with receptor saturation, tumor fluorescence was actually enhanced. Further analysis revealed strong and GRPR-nonspecific binding of [$^{111}$In]In-**14** to necrotic tumor cores. A possible explanation for this might be that dead cell binding is facilitated by sCy5, as this characteristic of cyanine-dyes has previously been reported (e.g., Xie et al., 2015 [38]; Stroet et al., 2021 [39]). The fact that an increase in the applied dose led to a further increase in the fluorescent tumor signal can be attributed to higher amounts of probe available to bind to dead cells, and to the abundance of cytoplasmic proteins. Since necrosis is a pathologic process and commonly observed in most solid tumors (e.g., breast and GIST tumors), this additional binding would only positively contribute to the differentiation of tumor tissue [40].





In the last part of the study, we provided implications for the clinical applicability of our dual-modality probe [$^{111}$In]In-**14**. The mimicked image-guided surgery demonstrated the ability to clearly visualize the tumor during all surgical steps and again underlined the target specificity of our probe, as NCI-H69 xenografts were not detected. Li et al. [41] also reported on the successful removal of tumor tissue by using a GRPR-targeting dual-modality probe for fluorescent guidance in their orthotopic brain tumor mouse model. Furthermore, we were able to establish the applicability of **14** for the detection and delineation of human prostate, breast and GIST tumors. Together, these findings indicate that our developed dual-modality probe would be a promising candidate for clinical translation. To develop a full picture of the translational potential of our dual-modality probe, additional studies investigating tumor retention over a longer period of time and up to the moment of surgery are needed.

## 5. Conclusions

In this study, we described the preclinical characterization of four dual-modality probes for preoperative nuclear imaging and intraoperative fluorescence imaging of GRPR-positive solid tumors. We demonstrated that the probes with a *p*ADA linker in their backbone presented the best tumor retention properties and that the addition of a $PEG_4$ linker negatively influenced the clearance rate. The image contrast was improved by delaying the imaging time point due to increased clearance, but the ideal time point with respect to renal clearance may not yet have been reached. The tumor-to-organ ratios of the most promising probe were also increased by reducing the injected dose to circumvent receptor saturation and reduce liver uptake. The binding of sCy5 to necrotic areas further enhanced the fluorescent signal. Finally, the ex vivo binding to various human cancer tissues and the ability to clearly visualize the tumor in a simulated surgical setting underline the potential for future clinical translation of our developed probe for image-guided surgery of GRPR-positive tumors.

**Supplementary Materials:** The following supporting information can be downloaded at: https: //www.mdpi.com/article/10.3390/cancers15072161/s1. Methods: Chemistry [43]; Figure S1: Uptake of [$^{111}$In]In-**12**-**15** and [$^{111}$In]In-NeoB (positive control) by GRPR-positive PC-3 cells (A) and GRPR-negative NCI-H69 cells (B) at 1 h after incubation with $10^{-9}$ M (20 MBq/nmol); Figure S2: Quantification of ex vivo fluorescence imaging of a selection of dissected organs and tissues at 4 h (A) and 24 h (B) post injection of [$^{111}$In]In-**12**-**15** (20 MBq/1 nmol); Figure S3: SPECT/CT images of PC-3 xenografted mice at 24 h post injection of 0.75, 1.25 or 1.75 nmol of [$^{111}$In]In-**14** (20 MBq per administered dose); Figure S4: Visualization of the radioactive signal in a well plate containing dead and alive PC-3 cells incubated with $10^{-9}$ M [$^{111}$In]In-**14** or [$^{111}$In]In-NeoB (control) (20 MBq/nmol); Table S1: Biodistribution of [$^{111}$In]In-**12**-**15** (20 MBq/1 nmol) in PC-3 and NCI-H69 xenografted balb/c nu/nu mice at 4 h post injection; Table S2: Biodistribution of [$^{111}$In]In-**12**-**15** (20 MBq/1 nmol) in PC-3 and NCI-H69 xenografted balb/c nu/nu mice at 24 h post injection; Table S3: Organ/tissue fluorescence after dissection of PC-3 and NCI-H69 xenografted balb/c nu/nu mice at 4 h post injection of [$^{111}$In]In-**12**-**15** (20 MBq/1 nmol); Table S4: Organ/tissue fluorescence after dissection of PC-3 and NCI-H69 xenografted balb/c nu/nu mice at 24 h post injection of [$^{111}$In]In-**12**-**15** (20 MBq/1 nmol); Table S5: Biodistribution of 0.75, 1.25 or 1.75 nmol [$^{111}$In]In-**14** (20 MBq per administered dose) in PC-3 xenografted balb/c nu/nu mice at 24 h post injection; Table S6: Organ/tissue fluorescence after dissection of PC-3 xenografted balb/c nu/nu mice at 24 h post injection of 0.75, 1.25 or 1.75 nmol [$^{111}$In]In-**14** (20 MBq per administered dose).

**Author Contributions:** Conceptualization, Y.S. and S.U.D.; Methodology, Y.S. and S.U.D.; Software, M.V.; Validation, M.V., M.H. and L.B.; Formal Analysis, M.V.; Investigation, M.V., M.H., L.B., C.M.A.R. and D.C.S.; Resources, S.U.D.; Data Curation, M.V., M.H. and L.B.; Writing—Original Draft Preparation, M.V.; Writing—Review and Editing, M.H., L.B., Y.S. and S.U.D.; Visualization, M.V.; Supervision, S.U.D.; Project Administration, S.U.D.; Funding Acquisition, S.U.D. All authors have read and agreed to the published version of the manuscript.

**Funding:** This research was funded by the Dutch Cancer Society (KWF; grant number 11671).

**Institutional Review Board Statement:** This study was conducted according to the guidelines of the Declaration of Helsinki, and approved by the Animal Welfare Committee of the Erasmus MC (license number: AVD101002017867, 28 September 2017).

**Informed Consent Statement:** Informed consent was obtained from all subjects involved in the study.

**Data Availability Statement:** The data presented in this study are available on request from the corresponding author.

**Acknowledgments:** This work was supported through the use of imaging equipment provided by the Applied Molecular Imaging Erasmus MC facility. We thank the Department of Pathology of the Erasmus MC for their support with histopathology.

**Conflicts of Interest:** The authors declare no conflicts of interest.

## References


1. Sung, H.; Ferlay, J.; Siegel, R.L.; Laversanne, M.; Soerjomataram, I.; Jemal, A.; Bray, F. Global Cancer Statistics 2020: GLOBOCAN Estimates of Incidence and Mortality Worldwide for 36 Cancers in 185 Countries. CA Cancer J. Clin. 2021, 71, 209–249.
2. Orosco, R.K.; Tapia, V.J.; Califano, J.A.; Clary, B.; Cohen, E.E.W.; Kane, C.; Lippman, S.M.; Messer, K.; Molinolo, A.; Murphy, J.D.; et al. Positive Surgical Margins in the 10 Most Common Solid Cancers. Sci. Rep. 2018, 8, 5686.
3. Zhang, L.; Wu, B.; Zha, Z.; Zhao, H.; Jiang, Y.; Yuan, J. Positive surgical margin is associated with biochemical recurrence risk following radical prostatectomy: A meta-analysis from high-quality retrospective cohort studies. World J. Surg. Oncol. 2018, 16, 124.
4. Osarogiagbon, R.U.; Ray, M.A.; Faris, N.R.; Smeltzer, M.P.; Fehnel, C.; Houston-Harris, C.; Signore, R.S.; McHugh, L.M.; Levy, P.; Wiggins, L.; et al. Prognostic Value of National Comprehensive Cancer Network Lung Cancer Resection Quality Criteria. Ann. Thorac. Surg. 2017, 103, 1557–1565.
5. Houssami, N.; Macaskill, P.; Luke Marinovich, M.; Morrow, M. The Association of Surgical Margins and Local Recurrence in Women with Early-Stage Invasive Breast Cancer Treated with Breast-Conserving Therapy: A Meta-Analysis. Ann. Surg. Oncol. 2014, 21, 717–730.
6. Mondal, S.B.; O'Brien, C.M.; Bishop, K.; Fields, R.C.; Margenthaler, J.A.; Achilefu, S. Repurposing Molecular Imaging and Sensing for Cancer Image-Guided Surgery. J. Nucl. Med. 2020, 61, 1113–1122.
7. Tanyi, J.L.; Randall, L.M.; Chambers, S.K.; Butler, K.A.; Winer, I.S.; Langstraat, C.L.; Han, E.S.; Vahrmeijer, A.L.; Chon, H.S.; Morgan, M.A.; et al. A Phase III Study of Pafolacianine Injection (OTL38) for Intraoperative Imaging of Folate Receptor-Positive Ovarian Cancer (Study 006). J. Clin. Oncol. 2023, 41, 276–284.
8. Van Oosterom, M.N.; Rietbergen, D.D.D.; Welling, M.M.; Van Der Poel, H.G.; Maurer, T.; Van Leeuwen, F.W.B. Recent advances in nuclear and hybrid detection modalities for image-guided surgery. Expert Rev. Med. Devices 2019, 16, 711–734.
9. van Leeuwen, F.W.B.; Schottelius, M.; Brouwer, O.R.; Vidal-Sicart, S.; Achilefu, S.; Klode, J.; Wester, H.J.; Buckle, T. Trending: Radioactive and Fluorescent Bimodal/Hybrid Tracers as Multiplexing Solutions for Surgical Guidance. J. Nucl. Med. 2020, 61, 13–19.
10. Baratto, L.; Duan, H.; Mäcke, H.; Iagaru, A. Imaging the Distribution of Gastrin-Releasing Peptide Receptors in Cancer. J. Nucl. Med. 2020, 61, 792–798.
11. Mansi, R.; Nock, B.A.; Dalm, S.U.; Busstra, M.B.; van Weerden, W.M.; Maina, T. Radiolabeled Bombesin Analogs. Cancers 2021, 13, 5766.
12. Chen, H.; Wan, S.; Zhu, F.; Wang, C.; Cui, S.; Du, C.; Ma, Y.; Gu, Y. A fast tumor-targeting near-infrared fluorescent probe based on bombesin analog for in vivo tumor imaging. Contrast Media Mol. Imaging 2014, 9, 122–134.
13. Pagoto, A.; Garello, F.; Marini, G.M.; Tripepi, M.; Arena, F.; Bardini, P.; Stefania, R.; Lanzardo, S.; Valbusa, G.; Porpiglia, F.; et al. Novel Gastrin-Releasing Peptide Receptor Targeted Near-Infrared Fluorescence Dye for Image-Guided Surgery of Prostate Cancer. Mol. Imaging Biol. 2020, 22, 85–93.
14. Xu, H.; Bandari, R.P.; Lee, L.; Li, R.; Yu, P.; Smith, C.J.; Ma, L. Design, Synthesis, and in Vitro and in Vivo Evaluation of High Affinity and Specificity Near-Infrared Fluorescent Bombesin Antagonists for Tumor Imaging. J. Med. Chem. 2018, 61, 7657–7670.
15. Cai, Q.-Y.; Yu, P.; Besch-Williford, C.; Smith, C.J.; Sieckman, G.L.; Hoffman, T.J.; Ma, L. Near-infrared fluorescence imaging of gastrin releasing peptide receptor targeting in prostate cancer lymph node metastases. Prostate 2013, 73, 842–854.
16. Dalm, S.U.; Bakker, I.L.; de Blois, E.; Doeswijk, G.N.; Konijnenberg, M.W.; Orlandi, F.; Barbato, D.; Tedesco, M.; Maina, T.; Nock, B.A.; et al. 68Ga/177Lu-NeoBOMB1, a Novel Radiolabeled GRPR Antagonist for Theranostic Use in Oncology. J. Nucl. Med. 2017, 58, 293–299.
17. Kaloudi, A.; Lymperis, E.; Giarika, A.; Dalm, S.; Orlandi, F.; Barbato, D.; Tedesco, M.; Maina, T.; de Jong, M.; Nock, B.A. NeoBOMB1, a GRPR-Antagonist for Breast Cancer Theragnostics: First Results of a Preclinical Study with [(67)Ga]NeoBOMB1 in T-47D Cells and Tumor-Bearing Mice. Molecules 2017, 22, 1950.

18. Handula, M.; Verhoeven, M.; Chen, K.-T.; Haeck, J.; de Jong, M.; Dalm, S.U.; Seimbille, Y. Towards Complete Tumor Resection: Novel Dual-Modality Probes for Improved Image-Guided Surgery of GRPR-Expressing Prostate Cancer. Pharmaceutics 2022, 14, 195.
19. de Blois, E.; Sze Chan, H.; Konijnenberg, M.; de Zanger, R.; Breeman, W.A.P. Effectiveness of Quenchers to Reduce Radiolysis of 111In- or 177Lu-Labelled Methionine-Containing Regulatory Peptides. Maintaining Radiochemical Purity as Measured by HPLC. Curr. Top. Med. Chem. 2012, 12, 2677–2685.
20. Hernot, S.; van Manen, L.; Debie, P.; Mieog, J.S.D.; Vahrmeijer, A.L. Latest developments in molecular tracers for fluorescence image-guided cancer surgery. Lancet Oncol. 2019, 20, e354–e367.
21. Baker, J.G.; Middleton, R.; Adams, L.; May, L.T.; Briddon, S.J.; Kellam, B.; Hill, S.J. Influence of fluorophore and linker composition on the pharmacology of fluorescent adenosine A1 receptor ligands. Br. J. Pharmacol. 2010, 159, 772–786.
22. Zhang, H.; Desai, P.; Koike, Y.; Houghton, J.; Carlin, S.; Tandon, N.; Touijer, K.; Weber, W.A. Dual-Modality Imaging of Prostate Cancer with a Fluorescent and Radiogallium-Labeled Gastrin-Releasing Peptide Receptor Antagonist. J. Nucl. Med. 2017, 58, 29–35.
23. Baranski, A.C.; Schäfer, M.; Bauder-Wüst, U.; Roscher, M.; Schmidt, J.; Stenau, E.; Simpfendörfer, T.; Teber, D.; Maier-Hein, L.; Hadaschik, B.; et al. PSMA-11-Derived Dual-Labeled PSMA Inhibitors for Preoperative PET Imaging and Precise Fluorescence- Guided Surgery of Prostate Cancer. J. Nucl. Med. 2018, 59, 639–645.
24. Maina, T.; Nock, B.A.; Kulkarni, H.; Singh, A.; Baum, R.P. Theranostic Prospects of Gastrin-Releasing Peptide Receptor- Radioantagonists in Oncology. PET Clin. 2017, 12, 297–309.
25. Ruigrok, E.A.M.; Verhoeven, M.; Konijnenberg, M.W.; de Blois, E.; de Ridder, C.M.A.; Stuurman, D.C.; Bertarione, L.; Rolfo, K.; de Jong, M.; Dalm, S.U. Safety of [177Lu]Lu-NeoB treatment: A preclinical study characterizing absorbed dose and acute, early, and late organ toxicity. Eur. J. Nucl. Med. Mol. Imaging 2022, 49, 4440–4451.
26. Hamann, F.M.; Brehm, R.; Pauli, J.; Grabolle, M.; Frank, W.; Kaiser, W.A.; Fischer, D.; Resch-Genger, U.; Hilger, I. Controlled Modulation of Serum Protein Binding and Biodistribution of Asymmetric Cyanine Dyes by Variation of the Number of Sulfonate Groups. Mol. Imaging 2011, 10, 258–269.
27. Chen, X.; Conti, P.S.; Moats, R.A. In vivo Near-Infrared Fluorescence Imaging of Integrin αvβ3 in Brain Tumor Xenografts. Cancer Res. 2004, 64, 8009–8014.
28. Bunschoten, A.; van Willigen, D.M.; Buckle, T.; van den Berg, N.S.; Welling, M.M.; Spa, S.J.; Wester, H.J.; van Leeuwen, F.W. Tailoring Fluorescent Dyes To Optimize a Hybrid RGD-Tracer. Bioconj. Chem. 2016, 27, 1253–1258.
29. Chen, Y.; Pullambhatla, M.; Banerjee, S.R.; Byun, Y.; Stathis, M.; Rojas, C.; Slusher, B.S.; Mease, R.C.; Pomper, M.G. Synthesis and Biological Evaluation of Low Molecular Weight Fluorescent Imaging Agents for the Prostate-Specific Membrane Antigen. Bioconj. Chem. 2012, 23, 2377–2385.
30. Buckle, T.; van Willigen, D.M.; Spa, S.J.; Hensbergen, A.W.; van der Wal, S.; de Korne, C.M.; Welling, M.M.; van der Poel, H.G.; Hardwick, J.C.H.; van Leeuwen, F.W.B. Tracers for Fluorescence-Guided Surgery: How Elongation of the Polymethine Chain in Cyanine Dyes Alters the Pharmacokinetics of a Dual-Modality c[RGDyK] Tracer. J. Nucl. Med. 2018, 59, 986–992.
31. Shrivastava, A.; Ding, H.; Kothandaraman, S.; Wang, S.H.; Gong, L.; Williams, M.; Milum, K.; Zhang, S.; Tweedle, M.F. A high-affinity near-infrared fluorescent probe to target bombesin receptors. Mol. Imaging Biol. 2014, 16, 661–669.
32. Veronese, F.M.; Pasut, G. PEGylation, successful approach to drug delivery. Drug Discov. Today 2005, 10, 1451–1458.
33. Berezin, M.Y.; Guo, K.; Akers, W.; Livingston, J.; Solomon, M.; Lee, H.; Liang, K.; Agee, A.; Achilefu, S. Rational Approach To Select Small Peptide Molecular Probes Labeled with Fluorescent Cyanine Dyes for in Vivo Optical Imaging. Biochemistry 2011, 50, 2691–2700.
34. Ghosh, S.C.; Hernandez Vargas, S.; Rodriguez, M.; Kossatz, S.; Voss, J.; Carmon, K.S.; Reiner, T.; Schonbrunn, A.; Azhdarinia, A. Synthesis of a Fluorescently Labeled (68)Ga-DOTA-TOC Analog for Somatostatin Receptor Targeting. ACS Med. Chem. Lett. 2017, 8, 720–725.

35. Stroet, M.C.M.; de Blois, E.; Stuurman, D.C.; de Ridder, C.M.A.; Haeck, J.; Seimbille, Y.; Mezzanotte, L.; de Jong, M.; Löwik, C.W.G.M.; Panth, K.M. In Vivo Evaluation of Indium-111–Labeled 800CW as a Necrosis-Avid Contrast Agent. Mol. Imaging Biol. 2020, 22, 1333–1341.
36. Kubeil, M.; Martínez, I.I.S.; Bachmann, M.; Kopka, K.; Tuck, K.L.; Stephan, H. Dual-Labelling Strategies for Nuclear and Fluorescence Molecular Imaging: Current Status and Future Perspectives. Pharmaceuticals 2022, 15, 432.
37. Lee, H.J.; McAuley, A.; Schilke, K.F.; McGuire, J. Molecular origins of surfactant-mediated stabilization of protein drugs. Adv. Drug Deliv. Rev. 2011, 63, 1160–1171.
38. Xie, B.; Stammes, M.A.; van Driel, P.B.A.A.; Cruz, L.J.; Knol-Blankevoort, V.T.; Löwik, M.A.M.; Mezzanotte, L.; Que, I.; Chan, A.; van den Wijngaard, J.P.H.M.; et al. Necrosis avid near infrared fluorescent cyanines for imaging cell death and their use to monitor therapeutic efficacy in mouse tumor models. Oncotarget 2015, 6, 39036–39049.
39. Stroet, M.C.M.; Dijkstra, B.M.; Dulfer, S.E.; Kruijff, S.; den Dunnen, W.F.A.; Kruyt, F.A.E.; Groen, R.J.M.; Seimbille, Y.; Panth, K.M.; Mezzanotte, L.; et al. Necrosis binding of Ac-Lys(0)(IRDye800CW)-Tyr(3)-octreotate: A consequence from cyanine-labeling of small molecules. EJNMMI Res. 2021, 11, 47.
40. Richards, C.H.; Mohammed, Z.; Qayyum, T.; Horgan, P.G.; McMillan, D.C. The prognostic value of histological tumor necrosis in solid organ malignant disease: A systematic review. Future Oncol. 2011, 7, 1223–1235.
41. Li, D.; Zhang, J.; Chi, C.; Xiao, X.; Wang, J.; Lang, L.; Ali, I.; Niu, G.; Zhang, L.; Tian, J.; et al. First-in-human study of PET and optical dual-modality image-guided surgery in glioblastoma using (68)Ga-IRDye800CW-BBN. Theranostics 2018, 8, 2508–2520.
42. Sasmal, R.; Das Saha, N.; Pahwa, M.; Rao, S.; Joshi, D.; Inamdar, M.S.; Sheeba, V.; Agasti, S.S. Synthetic Host–Guest Assembly in Cells and Tissues: Fast, Stable, and Selective Bioorthogonal Imaging via Molecular Recognition. Anal. Chem. 2018, 90, 11305–11314.

## Supplemental Information

### Methods

#### *Chemistry*

The four dual-modality NeoB analogs were synthesized following the Fmoc solid phase peptide synthesis strategy. The amino acids (4.0 equiv.) were coupled to the solid support using standard coupling agents, 2-(1*H*-benzotriazol-1-yl)-1,1,3,3-tetramethyluronium hexafluorophos-phate and Oxyma Pure (3.9 and 4.0 equiv., respectively), under basic conditions (pH ~9) for 1 h at RT. Using the same conditions, the linkers (Fmoc-NH-$PEG_4$-COOH or Fmoc-NH-*p*ADA-OH) (2.0 equiv.) and Fmoc- L-Lys(Boc)-OH (4.0 equiv.) were coupled for 2 h at RT and then the Fmoc protecting group was removed with a solution of 20% piperidine in dimethylformamide for 15 min at RT. The DOTA chelator (3.0 equiv.) was introduced using benzotriazole-1-yl-oxy-tris-pyrrolidino-phosphonium hexafluorophosphate (PyBOP; 3.0 equiv.) under basic conditions (pH ~9); coupling was performed for 2 h at RT. A cocktail of 1,1,1,3,3,3-hexafluoro-2-propanol/dichloromethane (20:80 V/V) was used to cleave the peptides from the solid support for 1 h at RT. Coupling of the 4-amino-2,6-dimethylheptane (2.5 equiv.) on the C-terminus was performed using PyBOP (2.5 equiv.) under basic conditions (pH ~9). A trifluoroacetic acid (TFA)/water/ triisopropyl silane cocktail (95:2.5:2.5 V/V/V) was then used to remove the side chain protecting groups for 1 h at RT. Due to the sensitivity of the TCO to acidic conditions, excess TFA was removed by C-18 Sep-Pak purification prior to coupling of TCO-NHS ester or TCO-$PEG_4$-NHS ester (3.0 equiv.) in water/acetonitrile (1:1 V/V). Finally, the tetrazinyl-fluorescent dye, Tz-sCy5 (1.1 equiv.), was conjugated to the TCO-functionalized peptides via the inverse electron- demand Diels-Alder reaction to obtain the final dual-modality probes **12**, **13**, **14** and **15** [1].

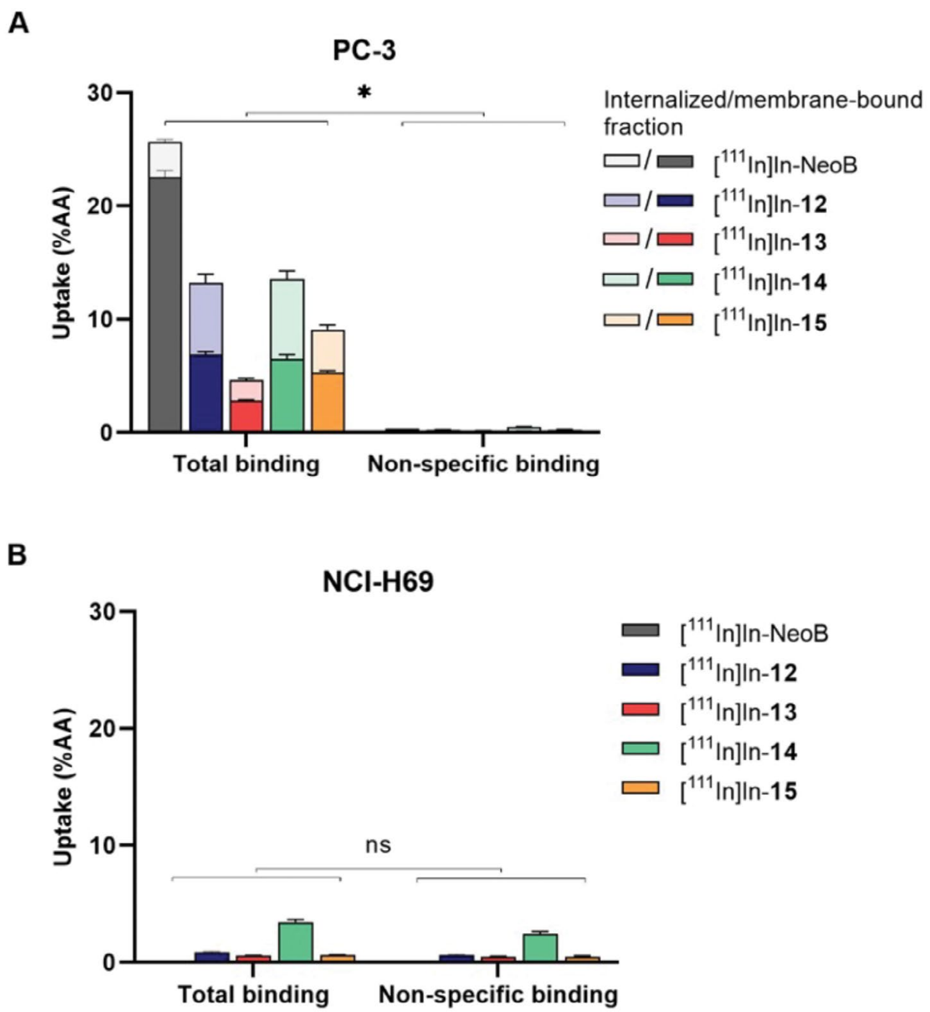


**Figure S1.** Uptake of [$^{111}$In]In-**12**-**15** and [$^{111}$In]In-NeoB (positive control) by GRPR-positive PC-3 cells (A) and GRPR-negative NCI-H69 cells (B) at 1 h after incubation with $10^{-9}$ M (20 MBq/nmol). The uptake by PC-3 cells is split into the internalized and membrane-bound fraction. Non-specific binding is defined as the uptake in the presence of a 1000x excess of unlabeled NeoB. Uptake values are expressed as percentage added activity (%AA). Results shown represent data from one independent experiment performed in triplicate (mean ± standard deviation). * = $p < 0.05$, ns = not significant

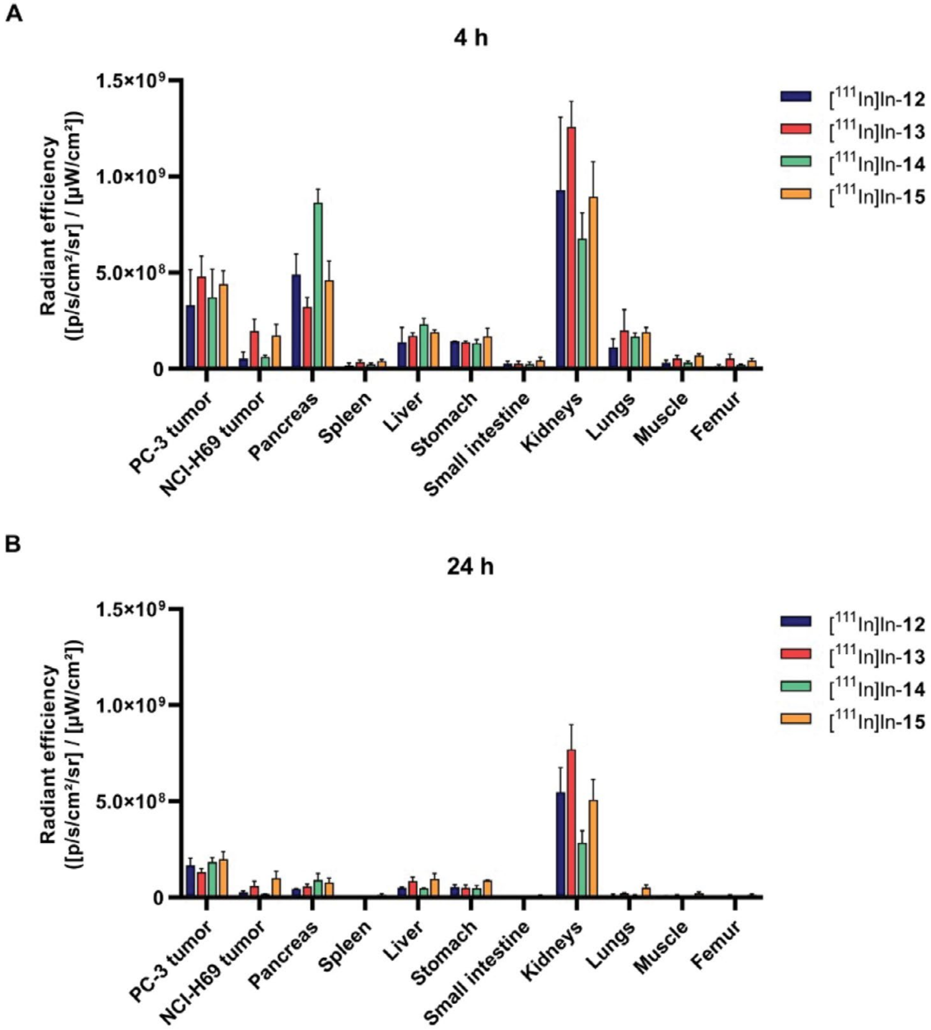


**Figure S2.** Quantification of *ex vivo* fluorescence imaging of a selection of dissected organs and tissues at 4 h (A) and 24 h (B) post injection of [$^{111}$In]In-**12-15 (**20 MBq/1 nmol). Data are presented as mean ± standard deviation ($n$ = 3/4).

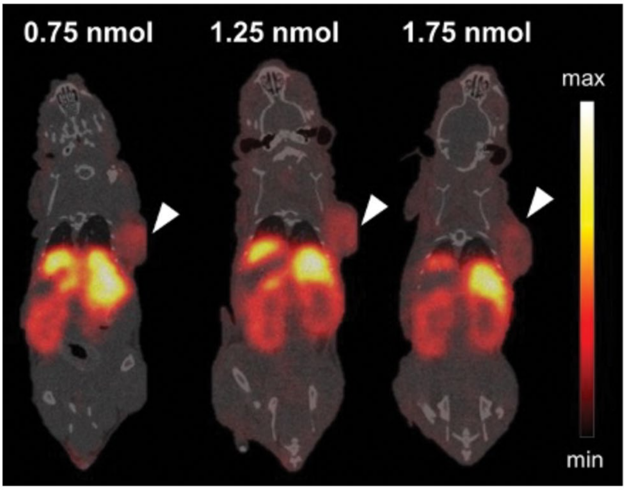


**Figure S3.** SPECT/CT images of PC-3 xenografted mice at 24 h post injection of 0.75, 1.25 or 1.75 nmol of [$^{111}$In]In-**14** (20 MBq/mass). SPECT/CT images represent an overlay of a CT slice and the corresponding SPECT slice on which the tumor cross-section is clearly visible. The arrow head points at the location of the tumor.

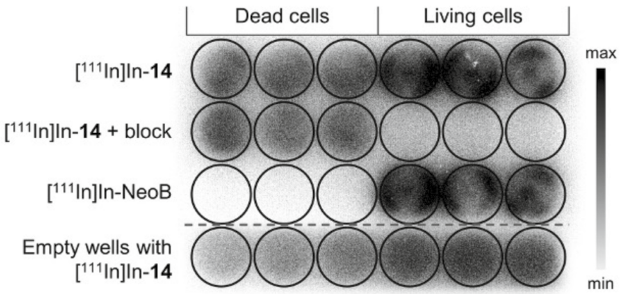


**Figure S4.** Visualization of the radioactive signal in a well-plate containing dead and alive PC-3 cells incubated with $10^{-9}$ M [$^{111}$In]In-**14** or [$^{111}$In]In-NeoB (control) (20 MBq/nmol). Blocking was performed by co-incubation with $10^{-6}$ M unlabeled NeoB. The wells below the red dotted line were empty and show the non-specific binding to plastic.

**Table S1.** Biodistribution of [$^{111}$In]In-**12-15** (20 MBq/1 nmol) in PC-3 and NCI-H69 xenografted balb/c nu/nu mice at 4 h post injection. Uptake values are expressed as percentage injected activity per gram of tissue (%IA/g) and represent the mean ± standard deviation.

| **Organ/tissue** | **[$^{111}$In]In-12 ($n$ = 3)** | **[$^{111}$In]In-13 ($n$ = 4)** | **[$^{111}$In]In-14 ($n$ = 4)** | **[$^{111}$In]In-15 ($n$ = 3)** |
|---|---|---|---|---|
| Blood | 2.26 ± 0.12 | 5.49 ± 1.27 | 2.68 ± 0.38 | 6.91 ± 0.98 |
| PC-3 tumor | 3.03 ± 1.08 | 3.16 ± 0.91 | 2.96 ± 0.78 | 3.31 ± 0.37 |
| NCI-H69 tumor | 0.68 ± 0.25 | 1.16 ± 0.56* | 0.84 ± 0.32 | 1.03 ± 0.61 |
| Prostate | 1.30 ± 0.98 | 2.00 ± 0.65 | 1.14 ± 0.34 | 1.15 ± 0.10 |
| Pancreas | 5.53 ± 0.21 | 2.25 ± 0.31 | 7.35 ± 0.75 | 3.28 ± 0.47 |
| Spleen | 1.59 ± 1.13 | 1.45 ± 0.42 | 2.34 ± 1.31 | 2.18 ± 0.74 |
| Liver | 8.55 ± 3.77 | 5.75 ± 1.64 | 10.69 ± 3.40 | 8.66 ± 0.13* |
| Stomach | 1.00 ± 0.26 | 1.03 ± 0.31 | 1.25 ± 0.29 | 1.47 ± 0.28 |
| Small intestine | 1.17 ± 0.32 | 0.76 ± 0.35 | 1.21 ± 0.40 | 1.79 ± 1.15 |
| Caecum | 0.81 ± 0.27 | 0.81 ± 0.23 | 1.03 ± 0.15 | 1.08 ± 0.05 |
| Colon | 0.76 ± 0.004* | 0.67 ± 0.11 | 1.31 ± 0.22 | 1.25 ± 0.14 |
| Adrenal glands | 1.22 ± 0.10 | 1.95 ± 0.60 | 1.73 ± 0.27 | 1.30 ± 0.85 |
| Kidneys | 13.04 ± 2.83 | 11.05 ± 3.27 | 8.11 ± 1.30 | 10.19 ± 3.68 |
| Lungs | 1.64 ± 0.68 | 1.65 ± 0.19* | 2.63 ± 0.85 | 2.55 ± 0.22 |
| Heart | 0.84 ± 0.14 | 1.93 ± 0.79 | 1.11 ± 0.20 | 1.89 ± 0.39 |
| Muscle | 0.33 ± 0.11 | 0.46 ± 0.15 | 0.38 ± 0.11 | 0.72 ± 0.29 |
| Femur | 0.46 ± 0.31 | 0.91 ± 0.48 | 0.58 ± 0.16 | 0.65 ± 0.07 |
| Tumor-to-organ ratio | | | | |
| PC-3 tumor-to-blood | 1.35 ± 0.53 | 0.58 ± 0.12 | 1.11 ± 0.29 | 0.42 ± 0.001* |
| PC-3 tumor-to-prostate | 2.84 ± 1.24 | 1.88 ± 0.07* | 2.79 ± 1.23 | 2.88 ± 0.16 |
| PC-3 tumor-to-liver | 0.36 ± 0.03 | 0.56 ± 0.09 | 0.28 ± 0.03 | 0.40 ± 0.02* |
| PC-3 tumor-to-kidneys | 0.23 ± 0.05 | 0.30 ± 0.07 | 0.36 ± 0.04 | 0.39 ± 0.003* |
| PC-3 tumor-to-muscle | 9.23 ± 2.05 | 7.00 ± 1.31 | 7.96 ± 0.40 | 4.92 ± 1.28 |

* Outlier excluded from dataset based on Grubbs' test ($n = n - 1$)

**Table S2.** Biodistribution of [$^{111}$In]In-**12-15** (20 MBq/1 nmol) in PC-3 and NCI-H69 xenografted balb/c nu/nu mice at 24 h post injection. Uptake values are expressed as percentage injected activity per gram of tissue (%IA/g) and represent the mean ± standard deviation.

| **Organ/tissue** | **[$^{111}$In]In-12 (*n* = 4)** | **[$^{111}$In]In-13 (*n* = 4)** | **[$^{111}$In]In-14 (*n* = 4)** | **[$^{111}$In]In-15 (*n* = 4)** |
|---|---|---|---|---|
| Blood | 0.16 ± 0.03 | 0.27 ± 0.04 | 0.28 ± 0.08 | 1.52 ± 0.13 |
| PC-3 tumor | 2.49 ± 0.83 | 1.17 ± 0.13 | 2.71 ± 0.72 | 1.97 ± 0.22 |
| NCI-H69 tumor | 0.47 ± 0.21 | 0.55 ± 0.10* | 0.47 ± 0.13 | 1.64 ± 1.08 |
| Prostate | 0.46 ± 0.07 | 0.69 ± 0.12 | 0.35 ± 0.23 | 1.24 ± 0.43 |
| Pancreas | 1.85 ± 0.38 | 0.42 ± 0.02 | 3.07 ± 0.53 | 0.79 ± 0.08 |
| Spleen | 1.10 ± 0.57 | 0.84 ± 0.13 | 2.06 ± 1.25 | 1.48 ± 0.39 |
| Liver | 5.70 ± 1.93 | 3.19 ± 0.16 | 8.02 ± 2.29 | 4.02 ± 0.65 |
| Stomach | 0.46 ± 0.17 | 0.24 ± 0.02 | 0.65 ± 0.08 | 0.44 ± 0.03 |
| Small intestine | 0.30 ± 0.13 | 0.19 ± 0.03 | 0.50 ± 0.08 | 0.37 ± 0.04 |
| Caecum | 0.41 ± 0.15 | 0.28 ± 0.03 | 0.58 ± 0.13 | 0.46 ± 0.04 |
| Colon | 0.50 ± 0.20 | 0.38 ± 0.06 | 0.61 ± 0.10 | 0.63 ± 0.08 |
| Adrenal glands | 0.61 ± 0.16 | 0.79 ± 0.10 | 0.90 ± 0.22 | 1.40 ± 0.14 |
| Kidneys | 12.14 ± 3.09 | 7.60 ± 0.62 | 7.74 ± 0.23 | 6.13 ± 0.47 |
| Lungs | 0.44 ± 0.19 | 0.39 ± 0.04* | 0.50 ± 0.06 | 0.91 ± 0.14 |
| Heart | 0.40 ± 0.15 | 0.42 ± 0.03 | 0.52 ± 0.09 | 0.87 ± 0.09 |
| Muscle | 0.16 ± 0.06 | 0.18 ± 0.02 | 0.21 ± 0.04 | 0.36 ± 0.08 |
| Femur | 0.22 ± 0.04* | 0.27 ± 0.06 | 0.33 ± 0.14 | 0.57 ± 0.14 |
| Tumor-to-organ ratio | | | | |
| PC-3 tumor-to-blood | 16.21 ± 5.02 | 4.37 ± 0.51 | 10.59 ± 3.91 | 1.31 ± 0.25 |
| PC-3 tumor-to-prostate | 5.34 ± 1.35 | 1.72 ± 0.26 | 5.84 ± 1.91* | 1.69 ± 0.39 |
| PC-3 tumor-to-liver | 0.44 ± 0.04 | 0.37 ± 0.04 | 0.35 ± 0.06 | 0.50 ± 0.06 |
| PC-3 tumor-to-kidneys | 0.20 ± 0.04 | 0.16 ± 0.03 | 0.35 ± 0.10 | 0.32 ± 0.03 |
| PC-3 tumor-to-muscle | 16.14 ± 2.05 | 6.48 ± 0.81 | 12.95 ± 2.36 | 5.88 ± 2.37 |

* Outlier excluded from dataset based on Grubbs' test (*n* = *n* - 1)

**Table S3.** Organ/tissue fluorescence after dissection of PC-3 and NCI-H69 xenografted balb/c nu/nu mice at 4 h post injection of [$^{111}$In]In-**12-15** (20 MBq/1 nmol). The signal is expressed as average radiant efficiency in $10^8$ p/sec/cm$^2$/sr per µW/cm$^2$.

| **Organ/tissue** | **[$^{111}$In]In-12 (*n* = 3)** | **[$^{111}$In]In-13 (*n* = 4)** | **[$^{111}$In]In-14 (*n* = 4)** | **[$^{111}$In]In-15 (*n* = 3)** |
|---|---|---|---|---|
| PC-3 tumor | 3.30 ± 1.86 | 4.80 ± 1.06 | 3.71 ± 1.47 | 4.40 ± 0.69 |
| Kidneys | 9.31 ± 3.81 | 12.59 ± 1.34 | 6.77 ± 1.34 | 8.97 ± 1.82 |
| Pancreas | 4.91 ± 1.06 | 3.21 ± 0.49 | 8.64 ± 0.69 | 4.60 ± 1.00 |
| Liver | 1.38 ± 0.76 | 1.72 ± 0.15 | 2.32 ± 0.31 | 1.91 ± 0.11 |
| NCI-H69 tumor | 0.54 ± 0.33 | 1.95 ± 0.63 | 0.62 ± 0.08 | 1.73 ± 0.58 |
| Femur | 0.15 ± 0.07 | 0.53 ± 0.22 | 0.22 ± 0.03 | 0.43 ± 0.10 |
| Muscle | 0.30 ± 0.15 | 0.53 ± 0.16 | 0.32 ± 0.08 | 0.69 ± 0.08 |
| Spleen | 0.19 ± 0.11 | 0.35 ± 0.01 | 0.25 ± 0.04 | 0.41 ± 0.08 |
| Small intestine | 0.72 ± 0.12 | 0.27 ± 0.12 | 0.26 ± 0.10 | 0.44 ± 0.16 |
| Lungs | 1.12 ± 0.43 | 1.99 ± 1.07 | 1.69 ± 0.16 | 1.90 ± 0.24 |
| Stomach | 1.44 ± 0.006* | 1.39 ± 0.006* | 1.33 ± 0.19 | 1.69 ± 0.41 |
| Tumor-to-organ ratio | | | | |
| PC-3 tumor-to-liver | 2.39 ± 0.19 | 2.78 ± 0.46 | 1.59 ± 0.55 | 2.30 ± 0.26 |
| PC-3 tumor-to-kidneys | 0.35 ± 0.07 | 0.38 ± 0.04 | 0.53 ± 0.12 | 0.49 ± 0.03 |
| PC-3 tumor-to-muscle | 10.87 ± 1.45 | 9.37 ± 1.66 | 11.48 ± 2.08 | 6.35 ± 0.31 |

* Outlier excluded from dataset based on Grubbs' test (*n* = *n* - 1)

**Table S4.** Organ/tissue fluorescence after dissection of PC-3 and NCI-H69 xenografted balb/c nu/nu mice at 24 h post injection of [$^{111}$In]In-**12-15** (20 MBq/1 nmol). The signal is expressed as average radiant efficiency in $10^8$ p/sec/cm$^2$/sr per µW/cm$^2$.

| Organ/tissue | [$^{111}$In]In-12 (*n* = 4) | [$^{111}$In]In-13 (*n* = 4) | [$^{111}$In]In-14 (*n* = 4) | [$^{111}$In]In-15 (*n* = 4) |
|---|---|---|---|---|
| PC-3 tumor | 1.65 ± 0.39 | 1.31 ± 0.18 | 1.83 ± 0.23 | 1.98 ± 0.41 |
| Kidneys | 5.47 ± 1.26 | 7.69 ± 1.30 | 2.83 ± 0.64 | 5.06 ± 1.07 |
| Pancreas | 0.45 ± 0.01* | 0.55 ± 0.14 | 0.89 ± 0.34 | 0.77 ± 0.24 |
| Liver | 0.49 ± 0.04* | 0.84 ± 0.22 | 0.47 ± 0.03* | 0.96 ± 0.28 |
| NCI-H69 tumor | 0.26 ± 0.06 | 0.58 ± 0.26 | 0.16 ± 0.02 | 1.00 ± 0.36 |
| Femur | 0.06 ± 0.007 | 0.11 ± 0.02 | 0.06 ± 0.003 | 0.13 ± 0.06 |
| Muscle | 0.07 ± 0.03 | 0.08 ± 0.05 | 0.04 ± 0.009 | 0.20 ± 0.09 |
| Spleen | 0.01 ± 0.01 | 0.05 ± 0.02 | 0.01 ± 0.01 | 0.13 ± 0.07 |
| Small intestine | 0.04 ± 0.04 | 0.02 ± 0.03 | 0.02 ± 0.02 | 0.08 ± 0.04 |
| Lungs | 0.12 ± 0.06 | 0.21 ± 0.04 | 0.09 ± 0.04 | 0.50 ± 0.14 |
| Stomach | 0.53 ± 0.13 | 0.49 ± 0.15 | 0.47 ± 0.15 | 0.88 ± 0.03 |
| *Tumor-to-organ ratio* | | | | |
| PC-3 tumor-to-liver | 3.01 ± 0.25* | 1.67 ± 0.56 | 4.00 ± 0.74* | 2.12 ± 0.24 |
| PC-3 tumor-to-kidneys | 0.30 ± 0.02 | 0.18 ± 0.05 | 0.67 ± 0.13 | 0.39 ± 0.05 |
| PC-3 tumor-to-muscle | 28.88 ± 13.75 | 12.56 ± 3.75 | 50.68 ± 9.55 | 12.47 ± 0.29* |

* Outlier excluded from dataset based on Grubbs' test (*n* = *n* - 1)

**Table S5.** Biodistribution of 0.75, 1.25 or 1.75 nmol [$^{111}$In]In-**14** (20 MBq/mass) in PC-3 xenografted balb/c nu/nu mice at 24 h post injection. Uptake values are expressed as percentage injected activity per gram of tissue (%IA/g) and represent the mean ± standard deviation.

| **Organ/tissue** | **0.75 nmol (*n* = 4)** | **1.25 nmol (*n* = 4)** | **1.75 nmol (*n* = 4)** |
|---|---|---|---|
| Blood | 0.27 ± 0.07 | 0.21 ± 0.05 | 0.19 ± 0.05 |
| PC-3 tumor | 2.74 ± 0.18 | 2.35 ± 0.40 | 2.09 ± 0.30 |
| Prostate | 0.55 ± 0.02* | 0.60 ± 0.10 | 0.48 ± 0.01* |
| Pancreas | 1.79 ± 0.15 | 1.15 ± 0.14 | 1.00 ± 0.15 |
| Spleen | 2.56 ± 1.12 | 3.68 ± 0.73 | 3.80 ± 0.06* |
| Liver | 0.45 ± 0.23* | 2.70 ± 1.89 | 5.50 ± 1.07 |
| Stomach | 0.60 ± 0.07 | 0.50 ± 0.09 | 0.39 ± 0.07 |
| Small intestine | 0.49 ± 0.12 | 0.39 ± 0.11 | 0.31 ± 0.05 |
| Caecum | 0.63 ± 0.12 | 0.47 ± 0.08 | 0.39 ± 0.05 |
| Colon | 0.79 ± 0.10 | 0.60 ± 0.08 | 0.45 ± 0.10 |
| Adrenal glands | 1.09 ± 0.39 | 1.03 ± 0.03* | 0.88 ± 0.06 |
| Kidneys | 8.90 ± 0.91 | 7.05 ± 1.40 | 5.55 ± 0.24* |
| Lungs | 0.73 ± 0.24 | 0.66 ± 0.18 | 0.56 ± 0.10 |
| Heart | 0.58 ± 0.08 | 0.51 ± 0.14 | 0.46 ± 0.08 |
| Muscle | 0.21 ± 0.05 | 0.18 ± 0.04 | 0.16 ± 0.03 |
| Femur | 0.51 ± 0.05 | 0.44 ± 0.08 | 0.39 ± 0.09 |
| Tumor-to-organ ratio | | | |
| Tumor-to-blood | 10.54 ± 2.54 | 11.27 ± 0.89 | 12.36 ± 0.31* |
| Tumor-to-prostate | 5.04 ± 0.20* | 3.94 ± 0.80 | 4.58 ± 0.36* |
| Tumor-to-liver | 8.01 ± 5.46* | 1.43 ± 1.14 | 0.39 ± 0.06 |
| Tumor-to-kidneys | 0.31 ± 0.05 | 0.33 ± 0.03 | 0.37 ± 0.07* |
| Tumor-to-muscle | 13.87 ± 3.90 | 13.36 ± 1.31 | 13.55 ± 3.45 |

* Outlier excluded from dataset based on Grubbs' test (*n* = *n* - 1)

**Table S6.** Organ/tissue fluorescence after dissection of PC-3 xenografted balb/c nu/nu mice at 24 h post injection of 0.75, 1.25 or 1.75 nmol [$^{111}$In]In-**14** (20 MBq/mass). The signal is expressed as average radiant efficiency in $10^8$ p/sec/cm$^2$/sr per µW/cm$^2$.

| **Organ/tissue** | **0.75 nmol (*n* = 4)** | **1.25 nmol (*n* = 4)** | **1.75 nmol (*n* = 4)** |
|---|---|---|---|
| PC-3 tumor | 7.30 ± 0.16* | 10.05 ± 0.90 | 12.10 ± 1.59 |
| Kidneys | 14.73 ± 1.47 | 2.48 ± 2.99 | 32.15 ± 3.79 |
| Pancreas | 2.81 ± 0.23 | 3.63 ± 0.40 | 4.15 ± 0.24 |
| Liver | 2.59 ± 0.06* | 3.79 ± 0.50 | 5.27 ± 0.07 |
| Lungs | 0.73 ± 0.20 | 1.01 ± 0.16 | 1.70 ± 0.46 |
| Stomach | 1.53 ± 0.13 | 1.62 ± 0.35 | 2.00 ± 0.26 |
| Muscle | 0.33 ±0.09 | 0.48 ± 0.13 | 0.63 ± 0.16 |
| Spleen | 0.27 ± 0.05 | 0.37 ± 0.07 | 0.58 ± 0.15 |
| Small intestine | 0.19 ± 0.04 | 0.27 ± 0.01* | 0.39 ± 0.04 |
| Femur | 0.34 ± 0.01* | 0.50 ± 0.07 | 0.64 ± 0.14 |
| Tumor-to-organ ratio | | | |
| PC-3 tumor-to-liver | 2.82 ± 0.13* | 2.77 ± 0.02* | 2.30 ± 0.32 |
| PC-3 tumor-to-kidneys | 0.52 ± 0.04* | 0.41 ± 0.03 | 0.38 ± 0.05 |
| PC-3 tumor-to-muscle | 22.94 ± 8.28* | 22.14 ± 5.79 | 20.38 ± 6.50 |

* Outlier excluded from dataset based on Grubbs' test (*n* = *n* - 1)

## References

1. Sasmal, R.; Das Saha, N.; Pahwa, M.; Rao, S.; Joshi, D.; Inamdar, M.S.; Sheeba, V.; Agasti, S.S. Synthetic Host–Guest Assembly in Cells and Tissues: Fast, Stable, and Selective Bioorthogonal Imaging via Molecular Recognition. Analytical Chemistry 2018, 90, 11305-11314.

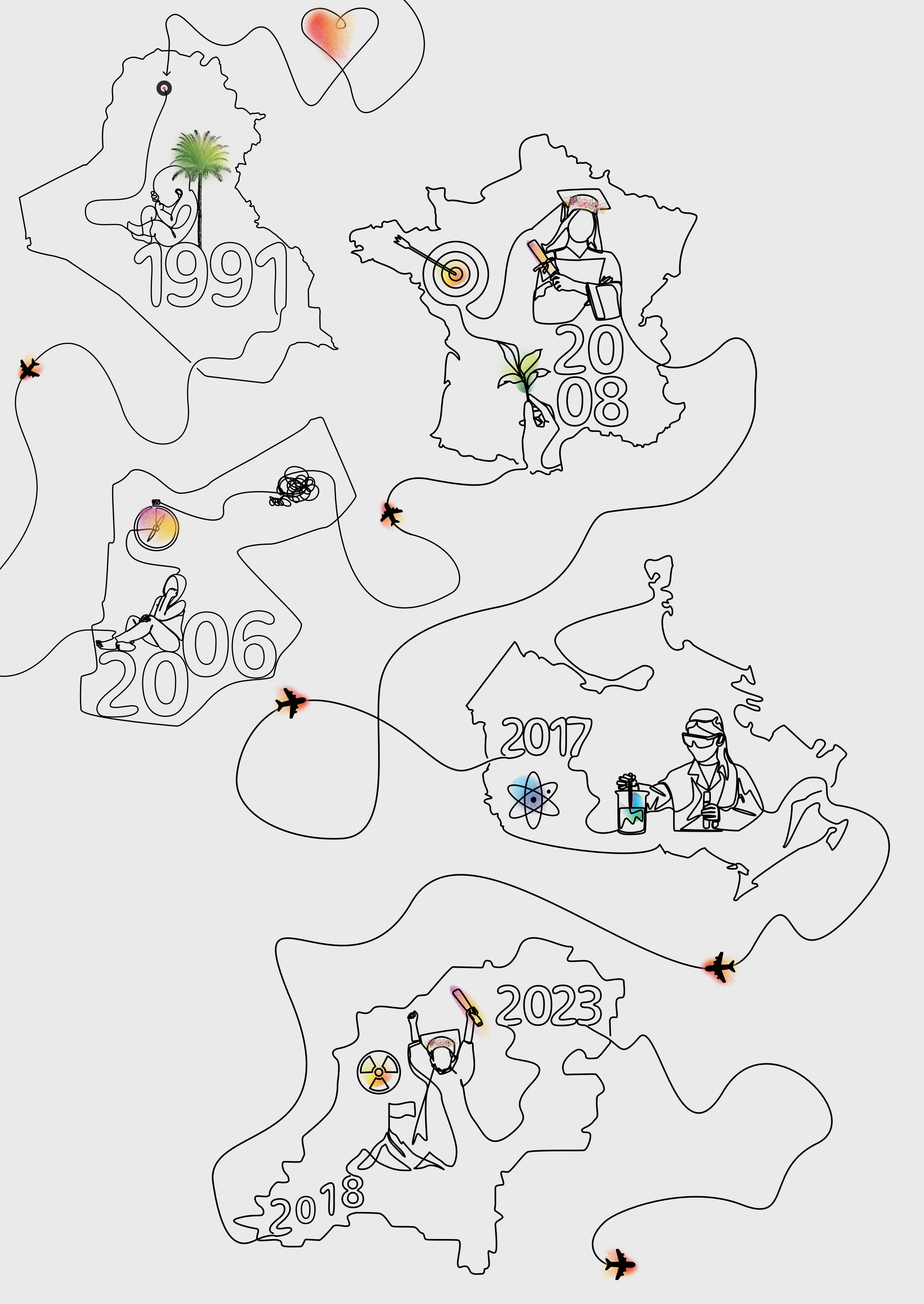
1991
2008
2006
2017
2023
2018

# CHAPTER 5

## Orthogonal Synthesis of a Versatile Building Block for Dual-Functionalization of Targeting Vectors

Maryana Handula[1], Dylan Chapeau[1] and Yann Seimbille[1,2]

[1] Department of Radiology and Nuclear Medicine, Erasmus MC Cancer Institute, Erasmus University Medical Center Rotterdam, 3015 GD Rotterdam, The Netherlands
[2] Life Sciences Division, TRIUMF, Vancouver, BC V6T 2A3, Canada

*Open Chemistry. 2023;21(1):20220361*

## Abstract

Dual-functionalization of targeting vectors, such as peptides and antibodies, is still synthetically challenging despite the increasing demand of such molecules serving multiple purposes (i.e., optical and nuclear imaging). Our strategy was to synthesize a versatile building block via the orthogonal incorporation of chemical entities (e.g., radionuclide chelator, fluorescent dye, cytotoxic drugs, click handle, albumin binder) in order to prepare various dual-functionalized biovectors. The functional groups were introduced on the building block using straightforward chemical reactions. Thus, an azidolysine and a biogenic lysine were installed into the building block to allow the coupling of the second functional group and the regioselective conjugation to the biovector via the strain-promoted azide alkyne cycloaddition, while the first functional group was inserted during the solid-phase peptide synthesis. To extend the applicability of the building block to large biomolecules, such as antibodies, a DBCO-maleimide linker was clicked to the azidolysine to present a maleimide group that could react with the exposed sulfhydryl groups of the cysteine residues. To exemplify the possibilities offered by the building block, we synthesized two dual-functionalized compounds containing a DOTA chelator and an albumin binder (**4a**) to extend the blood half-life of radiolabeled biovectors, or a click handle (**4b**) to enable late-stage click reaction. **4a** and **4b** were conjugated to a model cyclic peptide bearing a short thiolated linker at the *N*-terminal position, in a single step via the thiol-maleimide Michael addition. Both dual-functionalized peptides, **9a** and **9b**, were obtained rapidly in high chemical purity (> 95%), and labeled with [$^{111}$In]$InCl_3$. Both radiopeptides showed good stability in mouse serum and PBS buffer.

**Keywords:** orthogonal reaction, SPAAC, thiol-maleimide Michael addition, biovector

## 1. Introduction

In the past decade, peptides and antibodies have gained a lot of attention for targeted imaging and therapy of different types of cancers [1–3]. The low molecular weight of peptides confers multiple advantages compared to larger biomolecules, such as antibodies. For instance, peptides are cleared faster from the blood circulation, they present faster pharmacokinetics (PK) and they have a better penetration into the malignant tissue [4]. However, antibodies are known to exhibit a remarkable binding selectivity and affinity to the targeted antigens. Therefore, peptides and antibodies are getting more and more used for a panoply of applications for which chemical modifications of these biomolecules are required. Several functional groups have been recently considered to modify these biovectors, such as imaging probes (i.e., radiometal chelator, fluorescent dye) for non-invasive molecular imaging and fluorescence-guided surgery, cytotoxic drugs for small molecule- or antibody-drug conjugates, PK modifiers (i.e., albumin binder, cleavable linker) to improve their pharmacokinetics. The trend was initially to develop a mono-functionalized compound for each application. However, due to the rise of combined applications (i.e., multimodality imaging, targeted therapy and companion diagnostic) and cost-effectiveness, dual-functionalization of biomolecules is getting more and more popular.

The introduction of these functional groups into these biomolecules was usually achieved via amidation of lysine residues present in the peptide or protein sequence [5,6]. However, this approach is either synthetically challenging or lack regioselectivity. For peptide vectors, it is possible to select appropriate protecting groups during the solid-phase peptide synthesis (SPPS) to thwart these limitations. However, few functional groups, such as fluorescent cyanine dyes or *trans*-cyclooctene click handle, are too sensitive to bear the harsh conditions occurring during the synthesis (e.g., acidic and basic conditions) [7,8]. Therefore, alternative synthetic routes are required to functionalize these biovectors under friendly conditions. We recently described the synthesis of a multifunctional single-attachment-point (MSAP) to prepare dual fluorescent/nuclear labeled biovectors [9,10]. Herein, we report the applicability of a building block allowing dual-functionalization of biovectors. The synthetic approach was based on the chemoselective attachment of the functional groups using straightforward chemical reactions, such as the strain-promoted azide alkyne cycloaddition (SPAAC), the thiol-maleimide Michael addition or the inverse electron-demand Diels Alder (IEDDA) reaction. These reactions are known to be orthogonal, to occur under biologically friendly conditions, and the end-product is stable [11].

As a proof-of-concept, we synthesized two building blocks, **4a** and **4b**, functionalized with a 2,2′,2″,2‴-(1,4,7,10-tetraazacyclododecane-1,4,7,10-tetrayl) tetraacetic acid (DOTA) chelator for complexation of imaging and therapeutic radionuclides (e.g., indium-111, gallium-68, lutetium-177, actinium-225). Additionally, an azidolysine and a lysine were incorporated into the building block to provide two attachment points dedicated to the coupling of the second functional group and conjugation of the building block to the biovector. The side-chain of the lysine was used to attach an albumin-binding moiety (**4a**) or a *trans*-cyclooctene (**4b**), whereas a DBCO-maleimide linker was clicked to the azide group. The linker was inserted to increase the distance between the building block and the biovector, but also to provide a maleimide group that could react selectively with the cysteine residues present in antibodies. To demonstrate the versatility of our dual-functionalized building block, **4a** and **4b** were conjugated to a model cyclic peptide. The final compounds, **9a** and **9b**, were radiolabeled with [$^{111}$In]InCl$_3$, and their stability in PBS buffer and mouse serum was investigated.

## 2. Materials and methods

### *2.1 General information*

The chemicals and solvents were purchased from commercial suppliers and used without further purification. Fmoc-based solid-phase peptide synthesis (SPPS) was performed manually using manual reaction vessels (Chemglass, Vineland, United States). DOTA-NHS-ester was purchased from Macrocyclics (Plano, TX, USA) and [$^{111}$In]InCl$_3$ (370.0 MBq/mL in HCl, pH 1.5–1.9) was provided by Curium (Petten, The Netherlands). High-performance liquid chromatography (HPLC) and mass spectrometry (MS) were carried out on an Agilent 1260 Infinity II LC-MS system (Middelburg, The Netherlands). Instant thin-layer chromatography (iTLC) plates on silica gel impregnated glass fiber sheets were eluted with sodium citrate (0.1 M, pH 5). The plates were analyzed by a Brightspec bSCAN radio-chromatography scanner (Antwerp, Belgium) equipped with a sodium iodide detector. The radioactive samples used for the determination of LogD$_{7.4}$ were counted using a Perkin Elmer Wizard 2480 gamma counter (Waltham, MA, USA). Activity measurements were performed using the VDC-405 dose calibrator (Comecer, Joure, The Netherlands). Quality control of the products was performed using an analytical column (Poroshell 120, EC-C18, 2.7 µm, 3.0 × 100 mm) from Agilent with a gradient elution of acetonitrile (ACN) from 5% to 100% in $H_2O$, containing 0.1% formic acid (FA) at a flow rate of 0.5 mL/min over 8 min. Purification of compounds **3**, **4a** and **9a** was performed using a preparative Agilent 1290 Infinity II HPLC system and an Agilent 5 Prep C18 preparative column (50 × 21.2 mm, 5 µm) with a gradient elution of ACN (5% to 95% in $H_2O$ containing 0.1% FA for 8 min) at a flow rate of 10 mL/min over 10 min. Purification of compounds **8**, **4b** and **9b** was carried out using a semi-preparative Alliance HPLC system from Waters (Etten-Leur, The Netherlands). Purification of compound **8** was performed using a semi-preparative Phenomenex C-18 Luna® column (250.0 × 10.0 mm, 5 µm) with an isocratic elution of ACN (35% in $H_2O$ containing 0.1% trifluoroacetic acid (TFA) at a flow rate of 3 mL/

min over 30 min. Purification of compounds **4b** and **9b** was performed using the C18 Luna® semi-preparative column with a gradient elution of ACN (10% to 90% in $H_2O$, containing 0.01% TFA) at a flow rate of 3 mL/min over 30 min. Quality control of the radiolabeled compounds, as well as the stability studies, were carried out on a Waters Acquity Arc ultra-high performance liquid chromatography (UHPLC) system equipped with a diode array detector and a radio-detector from Canberra (Zelik, Belgium) using a Phenomenex C-18 Gemini® analytical column (250.0 × 4.6 mm, 5 µm) with a gradient elution of ACN (5% to 95% in $H_2O$, containing 0.1% TFA) at a flow rate of 1 mL/min over 30 min.

### *2.2 Chemistry*

*2,2',2''-(10-(2-(((S)-6-azido-1-(((S)-1,6-diamino-1-oxohexan-2-yl)amino)-1-oxohexan-2-yl) amino)-2-oxoethyl)-1,4,7,10-tetraazacyclododecane-1,4,7-triyl)triacetic acid (**2**).*

The synthesis started by loading Fmoc-Lys(Boc)-OH (0.5 mmol, 2 equiv.) onto the Rink Amide 4-methylbenzhydrylamine (MBHA) resin (370 mg, average loading capacity: 0.678 mmol/g) using solutions of 1-[bis(dimethylamino)methylene]-1H-1,2,3-triazolo[4,5-b] pyridinium 3-oxide hexafluorophosphate (HATU; 0.25 M, 2 mL, 2 equiv.) and *N*,*N*-diisopropylethylamine (DIPEA; 0.50 M, 2 mL, 4 equiv.) in DMF. The resin was shaken for 2 h at room temperature (rt). The beads were capped using a mixture of acetic anhydride (1.18 mL, 12.5 mmol, 50 equiv.) and 1 M DIPEA (2.19 mL, 12.5 mmol, 50 equiv.) for 30 min at rt. The *N*-terminal Fmoc protecting group was removed by treatment of the resin with a solution containing 20% piperidine in DMF (6 mL) for 13 min at rt. Fmoc-Lys($N_3$)-OH (198 mg, 0.5 mmol, 2 equiv.) was coupled following the protocol described above. After Fmoc removal, the peptidyl-resin was treated overnight with DOTA-NHS ester (382 mg, 0.5 mmol, 2 equiv.) and triethylamine ($Et_3N$; 315 µL, 2.2 mmol, 9 equiv.) in DMF (4 mL) to obtain **1**. Cleavage and removal of the Boc protecting group were carried out using a mixture of trifluoroacetic acid/triisopropylsilane/water (TFA/TIS/$H_2O$; 5 mL, v/v/v = 95:2.5:2.5). The beads were stirred for 2 h and washed twice with the cleavage cocktail. TFA was removed by air flow and the crude compound **2** was precipitated by addition of cold diethyl ether and collected by centrifugation. Compound **2** was obtained as a crude yellowish solid (294 mg, 12.8%). Analytical HPLC retention time: $t_R$ = 1.1 min. ESI-MS: m/z, calculated: 685.8 $C_{28}H_{51}N_{11}O_9$, Found: 686.3 $[M+H]^+$.

*2,2',2''-(10-(2-(((S)-1-(((S)-1,6-diamino-1-oxohexan-2-yl)amino)-6-(8-(3-(3-(2,5-dioxo-2,5-dihydro-1H-pyrrol-1-yl)propanamido)propanoyl)-8,9-dihydro-1H-dibenzo[b,f][1,2,3]triazolo[4,5-d]azocin-1-yl)-1-oxohexan-2-yl)amino)-2-oxoethyl)-1,4,7,10-tetraazacyclododecane-1,4,7-triyl)triacetic acid (**3**).*

**2** (74 mg, 0.107 mmol) and dibenzocyclooctyne-maleimide (DBCO-maleimide; 50 mg, 0.118 mmol, 1.1 equiv.) in MeOH (2 mL) were stirred for 30 min at 37 °C. Solvent was evaporated under vacuum and the crude residue was dissolved in a mixture of $H_2O$/ACN (2 mL, v/v = 1:1) for preparative HPLC purification. Compound **3** was obtained as a white solid (54 mg, 45%). Analytical HPLC retention time: $t_R$ = 3.5 min (Figure S1 A). Purity > 93%. ESI-MS: m/z, calculated: 1112.5 $C_{53}H_{72}N_{14}O_{13}$, Found: 557.4 $[M+2H]^{2+}$ (Figure S1 B).

*2,2',2''-(10-(2-(((S)-1-(((S)-1-amino-6-(4-(4-iodophenyl)butanamido)-1-oxohexan-2-yl) amino)-6-(8-(3-(3-(2,5-dioxo-2,5-dihydro-1H-pyrrol-1-yl)propanamido)propanoyl)-8,9-dihydro-1H-dibenzo[b,f][1,2,3]triazolo[4,5-d]azocin-1-yl)-1-oxohexan-2-yl)amino)-2-oxoethyl)-1,4,7,10-tetraazacyclododecane-1,4,7-triyl)triacetic acid (**4a**).*
2,5-Dioxopyrrolidin-1-yl 4-(4-iodophenyl)butanoate (AB-NHS ester) was synthesized as previously described [5]. **3** (20 mg, 0.018 mmol) was added to a solution of AB-NHS ester (10 mg, 0.027 mmol, 1.5 equiv.) and $Et_3N$ (5 µL, 0.036 mmol, 2 equiv.) in $H_2O$/ACN (2 mL, v/v = 1:1). The reaction mixture was stirred for 1 h at rt. Then, the product was purified by preparative HPLC to give **4a** as a white solid (12.5 mg, 50%). Analytical HPLC retention time: $t_R$ = 4.5 min (Figure S2 A). Purity > 97%. ESI-MS: m/z, calculated: 1384.5 $C_{63}H_{81}IN_{14}O_{14}$, Found: 1385.5 $[M+H]^+$ and 693.4 $[M+2H]^{2+}$ (Figure S3 A).

*2,2',2''-(10-(2-(((2S)-1-(((2S)-1-amino-6-(((((E)-cyclooct-4-en-1-yl)oxy)carbonyl)amino)-1-oxohexan-2-yl)amino)-6-(8-(3-(3-(2,5-dioxo-2,5-dihydro-1H-pyrrol-1-yl)propanamido) propanoyl)-8,9-dihydro-1H-dibenzo[b,f][1,2,3]triazolo[4,5-d]azocin-1-yl)-1-oxohexan-2-yl) amino)-2-oxoethyl)-1,4,7,10-tetraazacyclododecane-1,4,7-triyl)triacetic acid (**4b**).*
Treatment of **3** (20 mg, 0.018 mmol) with (*E*)-cyclooct-4-enyl-2,5-dioxo-1-pyrrolidinyl carbonate (TCO-NHS ester; 7.2 mg, 0.027 mmol, 1.5 equiv.) and $Et_3N$ (2.5 µL, 0.018 mmol, 1 equiv.) in $H_2O$/ACN (2 mL, v/v = 1:1) during 1 h at rt provided **4b** after semi-preparative HPLC purification. Compound **4b** was obtained as a white solid (6.5 mg, 29%). Analytical HPLC retention time: $t_R$ = 4.4 min (Figure S2 B). Purity > 98%. ESI-MS: m/z, calculated: 1264.6 $C_{62}H_{84}N_{14}O_{15}$, Found: 1265.6 $[M+H]^+$ (Figure S3 B).

*SH-$CH_2$-C(O)-Cpa-c[D-Cys-Aph(Hor)-D-Aph(Cbm)-Lys-Thr-Cys]-D-Tyr-$NH_2$ (**8**).*
Fmoc-Phe(4-Cl)-D-Cys(Acm)-Aph(Hor)-D-Aph(*t*Bu-Cbm-Lys(Boc)-Thr(*t*Bu)-Cys(Acm)-D-Tyr(*t*Bu) coupled to the resin (**5**) was obtained by sequential coupling of each amino acid for 1 h at rt in presence of a solution of HATU (0.25 M, 2 mL, 0.5 mmol, 2 equiv.) and DIPEA (0.5 M, 2 mL, 1 mmol, 4 equiv.) in DMF. Fmoc deprotection was accomplished by treatment of the resin with a 20% solution of piperidine in DMF (6 mL) for 13 min at rt. Amide formation and Fmoc deprotection were monitored by Kaiser and TNBS tests. Coupling and deprotection were repeated when the reaction was not complete. Peptide synthesis started by loading Fmoc-D-Tyr(*t*Bu)-OH (231 mg, 0.5 mmol, 2 equiv.) onto the Rink Amide MBHA resin (370 mg, average loading capacity: 0.678 mmol/g). The resin was shaken for 2 h at rt, then, it was capped using a mixture of acetic anhydride (1.18 mL, 12.5 mmol, 50 equiv.) and DIPEA (1 M, 2.19 mL, 12.5 mmol, 50 equiv.) for 1 h at rt. Subsequent Fmoc

deprotection and coupling with Fmoc-Cys(Acm)-OH (208 mg, 0.5 mmol, 2 equiv.), Fmoc-L-Thr(*t*Bu)-OH (199 mg, 0.5 mmol, 2 equiv.), Fmoc-L-Lys(Boc)-OH (235 mg, 0.5 mmol, 2 equiv.), Fmoc-D-Aph(*t*Bu-Cbm)-OH (252 mg, 0.5 mmol, 2 equiv.), Fmoc-Aph(Hor)-OH (272 mg, 0.5 mmol, 2 equiv.), Fmoc-D-Cys(Acm)-OH (208 mg, 0.5 mmol, 2 equiv.) and Fmoc-Phe(4-Cl)-OH (212 mg, 0.5 mmol, 2 equiv.) were achieved following the protocol described above. Cyclization of the peptide was accomplished using thallium(III) trifluoroacetate (273 mg, 0.5 mmol, 2 equiv.) in DMF (4 mL) for 1 h at rt to give **6**. After Fmoc deprotection, the resin was dried and divided in two fractions. The first fraction (~ 330 mg, 0.12 mmol) was coupled to 2,5-dioxopyrrolidin-1-yl-2-(tritylthio)acetate (108 mg, 0.25 mmol, 2 equiv.), prepared as previously reported [12] The reaction was performed in presence of DIPEA (500 µL, 0.25 mmol, 2 equiv.) and DMF (4 mL) for 3 h at rt. Cleavage and removal of the side-chain protecting groups was achieved using a solution of TFA/TIS/$H_2O$ (2 mL, v/v/v = 95:2.5:2.5) for 2 h at rt to give **8**. The resin was washed twice with the cleavage cocktail and all liquid phases were pooled. TFA was removed by air flow and the peptide was precipitated by addition of ice-cold diethyl ether and collected by centrifugation. A second treatment of the crude product with TFA/DCM (2 mL, v/v = 1:1) and triethylsilane (51 µL, 0.32 mmol, 2.5 equiv.) for 30 h at rt was carried out to complete the removal of the *t*Bu protecting groups. The solvents were evaporated under reduced pressure and the product was precipitated in ice-cold diethyl ether and collected by centrifugation. The residue was dissolved in $H_2O$/ACN (3 mL, v/v = 1:1) and purified by semi-preparative HPLC. Pure compound **8** was obtained as a white solid (32.6 mg, 9.5%). Analytical HPLC retention time: $t_R$ = 3.9 min (Figure S4 A). Purity > 95%. ESI-MS: m/z, calculated: 1375.4 $C_{60}H_{74}ClN_{15}O_{15}S_3$, Found: 1376.4 $[M+H]^+$ (Figure S4 B).

*2,2',2''-(10-(2-(((2S)-6-(8-(3-(3-(3-((2-(((2S)-1-(((4R,7S,10S,13S,16S,19R)-4-(((S)-1-amino-3-(4-hydroxyphenyl)-1-oxopropan-2-yl)carbamoyl)-10-(4-aminobutyl)-16-(4-(2,6-dioxohexahydropyrimidine-4-carboxamido)benzyl)-7-((S)-1-hydroxyethyl)-6,9,12,15,18-pentaoxo-13-(4-ureidobenzyl)-1,2-dithia-5,8,11,14,17-pentaazacycloicosan-19-yl)amino)-3-(4-chlorophenyl)-1-oxopropan-2-yl)amino)-2-oxoethyl)thio)-2,5-dioxopyrrolidin-1-yl)propanamido)propanoyl)-8,9-dihydro-1H-dibenzo[b,f][1,2,3]triazolo[4,5-d]azocin-1-yl)-1-(((S)-1-amino-6-(4-(4-iodophenyl)butanamido)-1-oxohexan-2-yl)amino)-1-oxohexan-2-yl)amino)-2-oxoethyl)-1,4,7,10-tetraazacyclododecane-1,4,7-triyl)triacetic acid (**9a**).*

To a solution of **4a** (12.5 mg, 0.009 mmol) in $H_2O$/ACN (2 mL, v/v = 1:1), was added **8** (13,7 mg, 0.010 mmol, 1.1 equiv.). The mixture was incubated at 37 °C and the reaction was monitored by LC/MS. Once the reaction was completed (~ 30 min), the crude mixture was purified by preparative HPLC to give compound **9a** as a white solid (18.8 mg, 76%). Analytical HPLC retention time: $t_R$ = 4.3 min (Figure S5 A). Purity > 96%. ESI-MS: m/z, calculated: 2759.9 $C_{123}H_{155}ClIN_{29}O_{29}S_3$, Found: 1381.7 $[M+2H]^{2+}$ (Figure S6 A).

*2,2',2''-(10-(2-(((2S)-6-(8-(3-(3-(3-((2-(((2S)-1-(((4R,7S,10S,13S,16S,19R)-4-(((S)-1-amino-3-(4-hydroxyphenyl)-1-oxopropan-2-yl)carbamoyl)-10-(4-aminobutyl)-16-(4-(2,6-dioxohexahydropyrimidine-4-carboxamido)benzyl)-7-((S)-1-hydroxyethyl)-6,9,12,15,18-pentaoxo-13-(4-ureidobenzyl)-1,2-dithia-5,8,11,14,17-pentaazacycloicosan-19-yl)amino)-3-(4-chlorophenyl)-1-oxopropan-2-yl)amino)-2-oxoethyl)thio)-2,5-dioxopyrrolidin-1-yl)propanamido)propanoyl)-8,9-dihydro-1H-dibenzo[b,f][1,2,3]triazolo[4,5-d]azocin-1-yl)-1-(((2S)-1-amino-6-(((((E)-cyclooct-4-en-1-yl)oxy)carbonyl)amino)-1-oxohexan-2-yl)amino)-1-oxohexan-2-yl)amino)-2-oxoethyl)-1,4,7,10-tetraazacyclododecane-1,4,7-triyl)triacetic acid (**9b**).*

Compound **4b** (6.5 mg, 0.005 mmol) reacted with **8** (8.5 mg, 0.006 mmol, 1.2 equiv.) in $H_2O$/ACN (2 mL, v/v = 1:1). The reaction mixture was incubated at 37 °C and was monitored by LC/MS. Once the reaction was completed (~ 2 h) the crude compound was purified by semi-preparative HPLC to give compound **9b** as a white solid (4.8 mg, 35%). Analytical HPLC retention time: $t_R$ = 4.2 min (Figure S5 B). Purity > 95%. ESI-MS: m/z, calculated: 2642.4 $C_{122}H_{158}ClN_{29}O_{30}S_3$, Found: 1322.2 $[M+2H]^{2+}$ (Figure S6 B).

### *2.3 Radiochemistry*

*Radiolabeling of compounds **9a** and **9b** with [$^{111}$In]In$Cl_3$.*

Compound **9a** or **9b** (1 nmol) was added to a mixture of [$^{111}$In]In$Cl_3$ (50 MBq), ascorbic acid/gentisic acid (10 µL, 50 mM), sodium acetate (2.5 M, 1 µL, pH 8) and water containing kolliphor (2.0 mg/mL, 58.6 µL). The labeling mixture (pH 4.5) was incubated at 90 °C for 20 min. Then, it was left to cool down for 5 min, and the radiochemical yield (RCY) was determined by iTLC on silica gel impregnated glass-fiber sheets. Diethylenetriaminepentaacetic acid (DTPA) (4 mM, 5 µL) was added to complex free indium-111. The radiochemical purity (RCP) of the $^{111}$In-labeled peptides was measured by radio-HPLC (Figure S7 A and B).

*Determination of the distribution coefficient (Log$D_{7.4}$) of [$^{111}$In]In-**9a** and [$^{111}$In]In-**9b**.*

The distribution coefficient of [$^{111}$In]In-**9a** and [$^{111}$In]In-**9b** was determined by the shake-flask method. The experiment was performed in triplicate for each compound. The radiolabeled compounds (~ 0.3 MBq) were added to a mixture of phosphate buffered saline (PBS)/n-octanol (1 mL, v/v = 1:1) in Eppendorf vials. The vials were vortexed vigorously and centrifuged at 10,000 rpm for 3 min. The organic phase was separated from the aqueous phase and poured into new vials. Samples from each phase (10 µL) were poured into glass tubes and measured with a gamma counter. The Log$D_{7.4}$ value was calculated using the following equation: $\mathrm{LogD}_{7.4} = \log_{10}$ ([counts in n-octanol phase]/[counts in PBS phase]).

*Stability studies in PBS and mouse serum.*

The $^{111}In$-labeled compounds (~ 0.3 MBq) were incubated in either PBS (250 µL) or mouse serum (125 µL) (Merck, Haarlerbergweg, The Netherlands) at 37 °C. Stability of the radiolabeled compounds was verified at 1 and 3 h post incubation. The proteins in mouse serum were precipitated by addition of an equal volume of ACN to the sample. The vial was vortexed and centrifuged at 10,000 rpm for 20 min. Stability studies in both media were monitored by radio-HPLC (Figure S8 and S9).

## 3. Results and discussion

Our synthetic approach aimed at the design of a building block allowing the incorporation of two different functional groups into the chemical structure of peptide-based biovector. The building block featured three different attachment points. A DOTA chelator was first introduced during SPPS since the chelator is not sensitive to the harsh reaction conditions experienced during the synthesis, such as the strong acidic conditions employed during the cleavage of the peptide from the solid support. The DOTA chelator was chosen due to its clinical relevance and its ability to complex a broad variety of radionuclides. However, other chelators (e.g., NOTA, DFO) could have been coupled to the building block [13]. Then, an azidolysine and a natural lysine residue were introduced into the building block to offer two additional attachment points. The presence of the two different attachment points warranted the orthogonal attachment of the building block to the biovector and the incorporation of the second functional group. The SPAAC click reaction was employed with the azidolysine due to its selectivity, favorable pharmacokinetics and orthogonality allowing the obtention of the desired compounds under friendly conditions [14]. The second functional group was introduced on the building block via an amide formation with the remaining lysine. Our synthetic route confirmed that the desired products could be obtained in liquid phase and allowed incorporation of sensitive functional groups at the last step of the synthesis.

Several investigations have demonstrated that incorporation of two different functional groups can be performed by the coupling onto lysine residues directly inserted into the amino acid sequence of a peptide [5,6,15]. However, the success of this approach is mainly depending on the presence of other lysine residues in the original peptide sequence. Moreover, regioselectivity of the introduction of the functional groups on the biovector is sparsely achieved, unless different protecting groups for the side-chain amino groups of the lysine residues are considered during the synthesis. However, this approach significantly complicates the synthetic pathway, and the deprotection conditions are not always compatible with the inserted functional groups (i.e., removal of an ivDde protecting group with hydrazine and groups containing a carbonyl function). Our chemical approach overcomes these limitations by allowing the orthogonal incorporation of the functional groups via straightforward chemical reactions, known to occur in smooth reaction conditions and high chemical yields. Furthermore, the regioselective attachment of the building block on the biovector enables to select a position at which the chemical modification has less influence on the biochemical properties of the parent peptide.

The orthogonality of the building block was confirmed by performing a SPAAC click reaction with a DBCO-maleimide linker prior to its conjugation to the biovector. We decided to add a linker to avoid the steric hindrance that could be caused by the bulky building block. The linker provides more space between the building block and the peptide, allowing better coupling efficiency and less effect on the binding properties of the peptide. However, addition of the linker would likely not be required with larger biovectors, such as antibodies and proteins. Furthermore, derivatization of the building block with a maleimide group enhance its utility, as it enables the conjugation of the building block to antibodies or antibody fragments. Indeed, those large biomolecules are usually functionalized with a chelator, a fluorescent dye, or a drug on a cysteine via the thiol-maleimide Michael addition. Therefore, the maleimide version of our building block could facilitate the dual-functionalization of these large and sensitive biovectors [16].

Compound **3** was a key intermediate in our synthetic approach due to its ability to be derivatized with broad variety of functional groups, such as fluorescent dyes (IRDye800CW, Cy5 derivatives), pharmacokinetic modifiers, and cytotoxic drugs. A large library of compounds could therefore be obtained by the conjugation of various chemical entities to the free lysine. As a proof-of-concept, we decided to functionalize **3** with either an albumin-binding moiety or a click handle. The 4-(*p*-iodophenyl)butanoic acid was selected as it has been widely applied to extend the blood circulation of radioligands (e.g., PSMA, folic acid, DOTA-TATE) by binding to albumin with a good affinity [17–20]. The *trans*-cyclooctene (TCO) group was chosen due to its high sensitivity towards acidic conditions, requiring flexibility in the synthesis of the building block and its incorporation into **3** at the last step of the synthesis [21]. TCO was incorporated into the building block to facilitate pretargeting applications [22]. Compound **4a** and **4b** were obtained by the SPAAC click reaction between the azido intermediate **2** and the DBCO-maleimide linker, followed by the conjugation of the activated succinimidyl AB-NHS and TCO-NHS esters (Scheme 1). This route provided **4a** and **4b** with 50 and 29% yield, respectively, after HPLC purification. The purity of **4a** and **4b** was determined by analytical HPLC and was found to be higher than 97 and 98%, respectively.

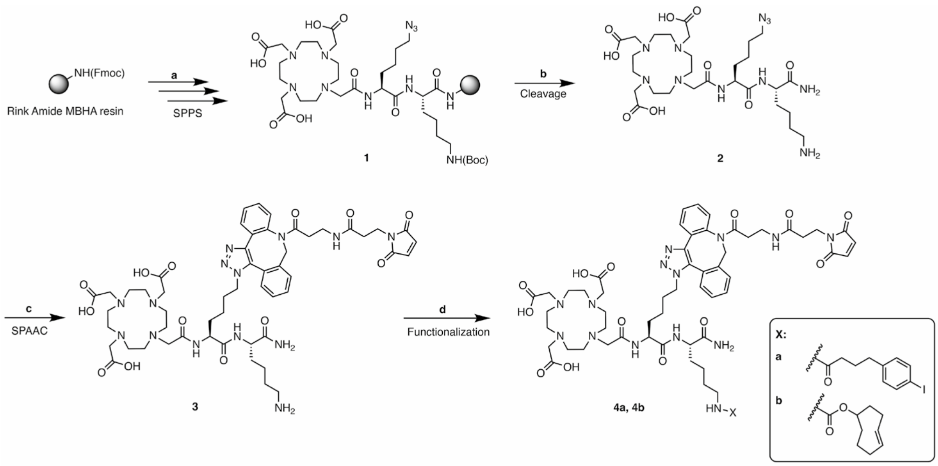

**Scheme 1:** Synthesis of the dual-functionalized building blocks (**4a** and **4b**). Reagents and conditions: (a) Fmoc-SPPS; (b) TFA/TIS/$H_2O$, 2 h, rt, 22%; (c) DBCO-maleimide, MeOH, 30 min, 37 °C, 45%; (d) AB-NHS ester or TCO-NHS ester, $Et_3N$, $H_2O$/ACN, 1 h, rt, 50% and 29%, respectively.

As mentioned above, the thiol group of the cysteine residues is commonly used to conjugate diverse functional groups to antibodies. Therefore, to mimic this situation, we attached a short thiolated linker at the *N*-terminal position of our model cyclic peptide JR11. We chose to demonstrate the application of our building block on a peptide since, like antibodies, peptides are constituted of amino acids but their chemistry is less challenging. Compound **8** was obtained by Fmoc-based SPPS on a Rink Amide MBHA resin, followed by cyclization of the peptide on resin by treatment with $Tl(TFA)_3$, Fmoc deprotection, conjugation of the succinimidyl ester of (tritylthio)acetic acid at the *N*-terminus, cleavage and deprotection of the side-chain protective groups [12]. **8** was obtained in 9.5% yield after HPLC purification with a purity higher than 95% (determined by analytical HPLC) (Scheme 2).

The final dual-functionalized compounds **9a** and **9b** were prepared by the conjugation of either **4a** or **4b** with **8** (Scheme 2). The thiol-maleimide Michael reaction was performed in a mixture of $H_2O$/ACN and the conversion of compound **8** into the desired compounds **9a** and **9b** was observed in only 30 min at 37 °C. During the reaction, we added a co-solvent, namely ACN, to improve the solubility of the peptides and the building block, but this reaction can typically be performed under biologically friendly conditions. **9a** and **9b** were obtained in 76 and 35% yield, respectively, after HPLC purification. The difference in chemical yields might be explained by the difference in the purification methods and the need to use less acidic solvent to purify **9b** in order to avoid its isomerization into the cis-isomer. It has been shown that *cis*-cyclooctene (CCO) is less reactive than TCO towards tetrazines during the IEDDA reaction [21]. **9a** and **9b** were characterized by mass spectrometry and their purity, determined by analytical HPLC, was higher than 96 and 95%, respectively.

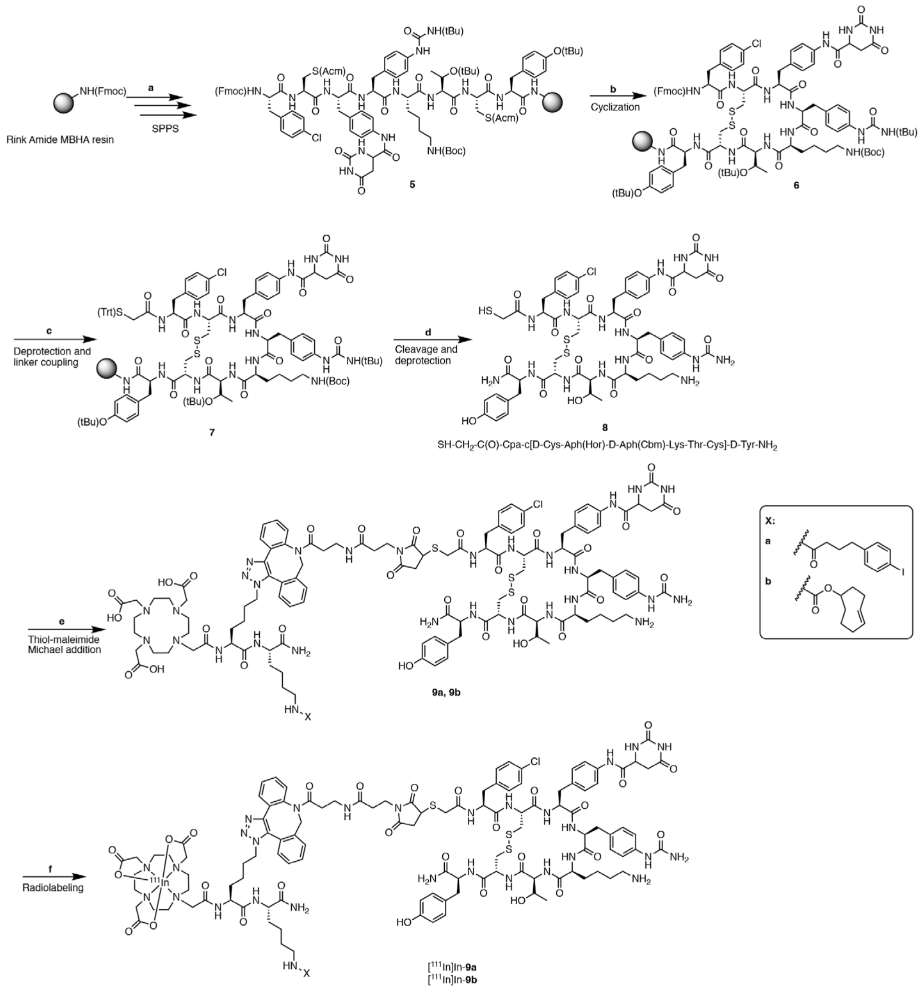


**Scheme 2:** Synthesis of compound **8**. Reagents and conditions: (a) Fmoc-SPPS; (b) $Tl(TFA)_3$, DMF, 1 h, rt; (c) (i) 20% piperidine in DMF, 13 min, rt, (ii) TrtS-$CH_2$-OSu, DIPEA, DMF, 3 h, rt; (d) (i) TFA/TIS/$H_2O$, 2 h, rt and (ii) TFA/DCM, 30 h, rt, 9.5%; (e) **4a** or **4b**, $H_2O$/ACN, 37 °C, 76% and 35%, respectively. (f) [$^{111}$In]$InCl_3$, **9a** or **9b**, gentisic/ascorbic acid, sodium acetate, 20 min, 90 °C, 96.3 and 96.1% respectively.




Subsequently, **9a** and **9b** were radiolabeled with [$^{111}$In]$InCl_3$ using gentisic and ascorbic acid. Both substances are quenchers, known to protect the radiolabeled peptides against radiolysis [23]. It has been reported that ascorbic acid reacts with the main radicals formed by gentisic acid, and reduces them into the original gentisic acid found in the initial dosage form [24]. Kolliphor, a well-known solubilizer and emulsifier, was added into the radiolabeling mixture in order to improve the solubility of the radiolabeled peptides and reduce their stickiness. Radiolabeling of both compounds with [$^{111}$In]$InCl_3$, using a molar activity of 50 MBq/nmol, was successful and comparable to what has been recently published with other DOTA-JR11 analogs [5]. It confirms that the chemical modifications did not hamper the efficiency of the complexation of $^{111}In^{3+}$ by the DOTA chelator. The RCY and RCP of both radiopeptides are presented in Table 1. [$^{111}$In]In-**9a** and [$^{111}$In]In-**9b** were obtained in 96.3 and 96.1% RCY and 94.9 and 86.0% RCP, respectively. Next, we determined the stability of both radiopeptides in PBS (pH 7.4) and mouse serum at 1 and 3 h after incubation at 37 °C. [$^{111}$In]In-**9a** and [$^{111}$In]In-**9b** exhibited good stability in mouse serum (> 92% intact radiopeptides at 3 h), demonstrating their inertness towards peptidase digestion. However, [$^{111}$In]In-**9a** showed a better stability in PBS compared to [$^{111}$In]In-**9b** (90.9% intact [$^{111}$In]In-**9a** vs. 75.1% intact [$^{111}$In]In-**9b** at 3 h). It might be explained by the presence of the carbamate bond between the *trans*-cyclooctene and the side chain of the lysine residue. Indeed, it has been previously reported that the carbamate linkage is sensitive to radiolysis [25].

**Table 1:** RCYs (n = 2), RCPs (n = 2), stability studies in PBS (n = 1) and mouse serum (n =1) and determination of the partition coefficient ($LogD_{7.4}$) (n = 3) of [$^{111}$In]In-**9a** and [$^{111}$In]In-**9b**.

| | | | Stability in PBS (%)* | | Stability in mouse serum (%)* | | |
|---|---|---|---|---|---|---|---|
| | **RCY (%)** | **RCP (%)** | **1 h** | **3 h** | **1 h** | **3 h** | **$LogD_{7.4}$** |
| [$^{111}$In]In-**9a** | 96.3 ± 0.7 | 94.9 ± 1.5 | 90.4 | 90.9 | 94.1 | 94.9 | -0.59 ± 0.05 |
| [$^{111}$In]In-**9b** | 96.1 ± 2.3 | 86.0 ± 3.3 | 76.3 | 75.1 | 93.7 | 92.5 | -0.66 ± 0.02 |

* Results are presented as percentage of intact radiopeptide after incubation at 37 °C.

The distribution coefficient was determined by the shake-flask method. Both radiopeptides displayed a $LogD_{7.4}$ value higher than the parent peptide DOTA-JR11 (-0.59 and -0.66 for [$^{111}$In]In-**9a** and [$^{111}$In]In-**9b** vs. -2.5 for [$^{177}$Lu]Lu-DOTA-JR11) [26]. Introduction of lipophilic chemical groups, such as DBCO, AB and TCO in the chemical structure of the DOTA-JR11 logically affected the hydrophilicity of the final molecules.

In the previous examples, a chelator, an albumin-binding moiety and a click handle were introduced into the dual-functionalized building block. However, presence of the azide and amine groups on the molecule confers full orthogonality to attach selectively various chemical entities. We showed that insertion of a maleimide into our building block offers the opportunity to functionalize other biovectors, such as antibodies, in a single step through the thiol-maleimide Michael reaction. The reaction proceeded quickly in biologically friendly conditions (aqueous medium and physiological temperature), allowing the radiolabeling of the building block in harsh reaction conditions (i.e., heating in acidic solution) before its conjugation to a fragile biomolecule [27].

## 4. Conclusion

In our study, we presented a versatile approach allowing the orthogonal incorporation of different functional groups (DOTA chelator, AB and TCO) into a building block that can be attached to biovectors in a single step via a SPAAC or thiol-maleimide Michael reaction. Our proof-of-concept was demonstrated by the preparation of two different dual-functionalized building blocks, **4a** and **4b**, which were coupled to the free sulfhydryl group of a cyclic peptide. Both final compounds, **9a** and **9b**, were obtained in very high chemical purities, and successfully radiolabeled with $[^{111}In]InCl_3$. We confirmed that the chemical remodeling of the peptides did not hamper the complexation of the radionuclide by the chelator, and high stability of the final radiopeptides was demonstrated in PBS and mouse serum. Consequently, this synthetic approach could be very valuable for the functionalization of radiolabeled biovectors.

**Acknowledgments**: we are grateful to the Dutch Cancer Society (KWF) for the financial support and the department of Radiology and Nuclear Medicine at the Erasmus MC for technical assistance.

**Research funding**: this research was funded by the Dutch Cancer Society (KWF), grant number 12259.

**Author contribution**: Conceptualization, Y.S.; methodology, M.H. and Y.S.; software, M.H.; validation, M.H.; formal analysis, M.H. and D.C.; investigation, M.H., D.C. and Y.S.; resources, Y.S.; data curation, M.H. and D.C.; writing—original draft preparation, M.H.; writing—review and editing, M.H., D.C. and Y.S.; visualization, Y.S.; supervision, Y.S.; project administration, Y.S.; funding acquisition, Y.S. All authors have read and agreed to the published version of the manuscript.

**Conflict of interest**: the authors do not declare any conflicts of interest.

**Ethical approval**: the conducted research is not related to either human or animal use.

**Data availability**: all data generated or analyzed during this study are included in this published article and its supplementary information file.

## References


1. Dalm SU, Bakker IL, De Blois E, Doeswijk GN, Konijnenberg MW, Orlandi F, et al. 68Ga/177Lu-NeoBOMB1, a novel radiolabeled GRPR antagonist for theranostic use in oncology. J Nucl Med 2017;58:293–299.
2. Sanli Y, Garg I, Kandathil A, Kendi T, Baladron Zanetti MJ, Kuyumcu S, et al. Neuroendocrine tumor diagnosis and management: 68 Ga-DOTATATE PET/CT. AJR 2018;211:267–277.
3. Kuil J, Velders AH, Van Leeuwen FWB. Multimodal tumor-targeting peptides functionalized with both a radio- and a fluorescent label. Bioconjug Chem 2010;21:1709–1719.
4. Bumbaca B, Li Z, Shah DK. Pharmacokinetics of protein and peptide conjugates. Drug Metab Pharmacokinet 2019;34:42–54.
5. Koustoulidou S, Handula M, de Ridder C, Stuurman D, Beekman S, de Jong M, et al. Synthesis and Evaluation of Two Long-Acting SSTR2 Antagonists for Radionuclide Therapy of Neuroendocrine Tumors. Pharmaceuticals 2022;15:1–15.
6. Handula M, Verhoeven M, Chen K, Haeck J, Jong M De, Dalm SU, et al. Towards Complete Tumor Resection : Novel Dual-Modality Probes for Improved Image-Guided Surgery of GRPR-Expressing Prostate Cancer. Pharmaceutics 2022;14:1–18.
7. Strekowski L, Mason CC, Lee H, Patonay G. Synhesis of a functionalized cyanine dye for covalent labeling of biomolecules with a pH-sensitive chromophore. Heterocycl Comm 2004;10:381–382.
8. Rossin R, Van Den Bosch SM, Ten Hoeve W, Carvelli M, Versteegen RM, Lub J, et al. Highly reactive trans-cyclooctene tags with improved stability for diels-alder chemistry in living systems. Bioconjug Chem 2013;24:1210–1217.
9. Chen KT, Nieuwenhuizen J, Handula M, Seimbille Y. A novel clickable MSAP agent for dual fluorescence/nuclear labeling of biovectors. Org Biomol Chem 2020;18:6134–6139.
10. Garanger E, Aikawa E, Reynolds F, Weissleder R, Josephson L. Simplified syntheses of complex multifunctional nanomaterials. ChemComm 2008;39:4792–4794.
11. Handula M, Chen KT, Seimbille Y. Iedda: An attractive bioorthogonal reaction for biomedical applications. Molecules 2021;26:1–20.
12. Chen X, Li L, Liu F, Liu B. Synthesis and biological evaluation of technetium-99m-labeled deoxyglucose derivatives as imaging agents for tumor. Bioorganic Med Chem Lett 2006;16:5503–5506.
13. Stasiuk GJ, Long NJ. The ubiquitous DOTA and its derivatives: The impact of 1,4,7,10-tetraazacyclododecane-1,4,7,10-tetraacetic acid on biomedical imaging. ChemComm 2013;49:2732–2746.
14. Deng Y, Shavandi A, Okoro OV, Nie L. Alginate modification via click chemistry for biomedical applications. Carbohydr Polym 2021;270:1–18.
15. Zhang H, Desai P, Koike Y, Houghton J, Carlin S, Tandon N, et al. Dual-modality imaging of prostate cancer with a fluorescent and radiogallium-labeled gastrin-releasing peptide receptor antagonist. J Nucl Med 2017;58:29–35.
16. Nair DP, Podgórski M, Chatani S, Gong T, Xi W, Fenoli CR, et al. The Thiol-Michael addition click reaction: A powerful and widely used tool in materials chemistry. Chem Mater 2014;26:724–744.
17. Müller C, Struthers H, Winiger C, Zhernosekov K, Schibli R. DOTA conjugate with an albumin-binding entity enables the first folic acid-targeted 177Lu-radionuclide tumor therapy in mice. J Nucl Med 2013;54:124–131.
18. Tiel S van, Tiel S van, Maina T, Nock B, Konijnenberg M, Blois E de, et al. Albutate-1, a Novel Long-Circulating Radiotracer Targeting the Somatostatin Receptor Subtype 2. J Nucl Med Radiat Sci 2021;2:1–9.
19. Rousseau E, Lau J, Zhang Z, Uribe CF, Kuo HT, Zhang C, et al. Effects of adding an albumin binder chain on [177Lu]Lu-DOTATATE. Nucl Med Biol 2018;66:10–17.
20. Kuo HT, Lin KS, Zhang Z, Uribe CF, Merkens H, Zhang C, et al. 177Lu-labeled albumin-binder-conjugated PSMA-targeting agents with extremely high tumor uptake and enhanced tumor-to-kidney absorbed dose ratio. J Nucl Med 2021;62:521–527.
21. La–Venia A, Dzijak R, Rampmaier R, Vrabel M. An Optimized Protocol for the Synthesis of Peptides Containing trans-Cyclooctene and Bicyclononyne Dienophiles as Useful Multifunctional Bioorthogonal Probes. Chem Eur J 2021;27:13632–13641.

22. Keinänen O, Fung K, Pourat J, Jallinoja V, Vivier D, Pillarsetty NVK, et al. Pretargeting of internalizing trastuzumab and cetuximab with a 18F-tetrazine tracer in xenograft models. EJNMMI Res 2017;7:1–12.
23. de Blois E, Sze Chan H, Konijnenberg M, de Zanger R, A.P. Breeman W. Effectiveness of Quenchers to Reduce Radiolysis of 111In- or 177Lu-Labelled Methionine-Containing Regulatory Peptides. Maintaining Radiochemical Purity as Measured by HPLC. Curr Top Med Chem 2013;12:2677–2685.
24. Larenkov A, Mitrofanov I, Pavlenko E, Rakhimov M. Radiolysis-Associated Decrease in Radiochemical Purity of 177Lu-Radiopharmaceuticals and Comparison of the Effectiveness of Selected Quenchers against This Process. Molecules 2023;28:1–26.
25. Wang WF, Schuchmann MM, Schuchmann HP, Knolle W, Von Sonntag J, Von Sonntag C. Radical cations in the OH-radical-induced oxidation of thiourea and tetramethylthiourea in aqueous solution. J Am Chem Soc 1999;121:238–245.
26. Rylova SN, Stoykow C, Del Pozzo L, Abiraj K, Tamma ML, Kiefer Y, et al. The somatostatin receptor 2 antagonist 64Cu-NODAGA-JR11 outperforms 64Cu-DOTA-TATE in a mouse xenograft model. PLoS One 2018;13:1–16.
27. Daniel RM, Cowan DA. Biomolecular stability and life at high temperatures. Cell Mol Life Sci 2000;57:250–264.

# Supplemental Information

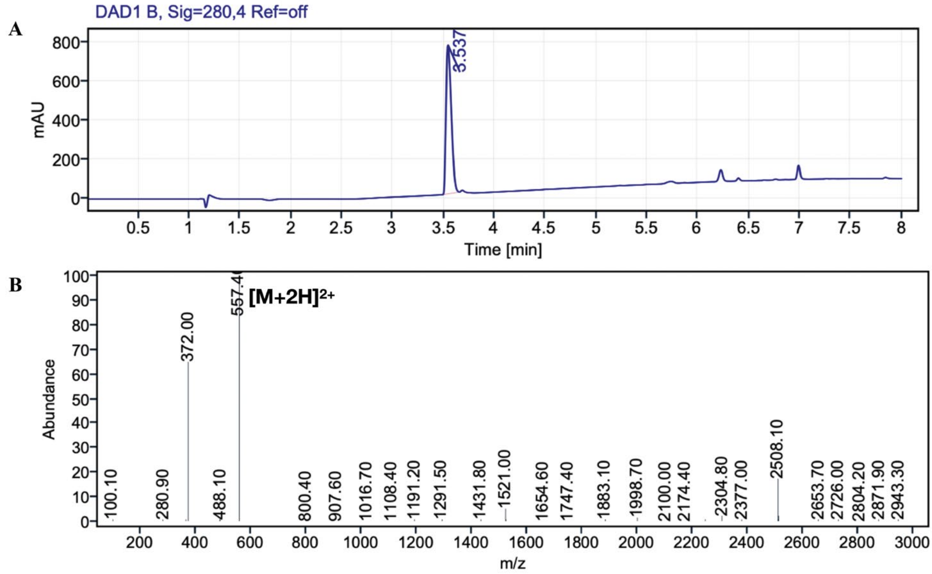


**Figure S1:** A) HPLC chromatogram and B) Mass spectrum of compound **3**.

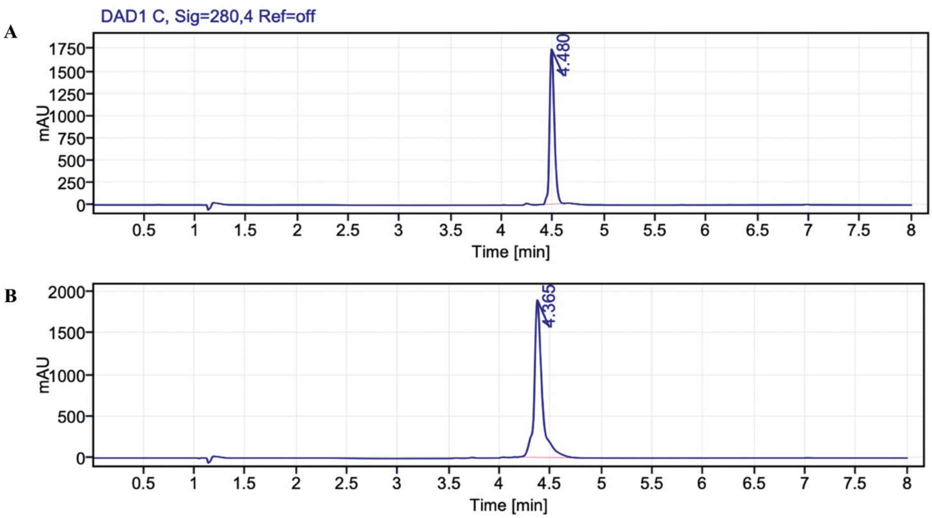


**Figure S2:** HPLC chromatograms of A) compound **4a** and B) compound **4b**.

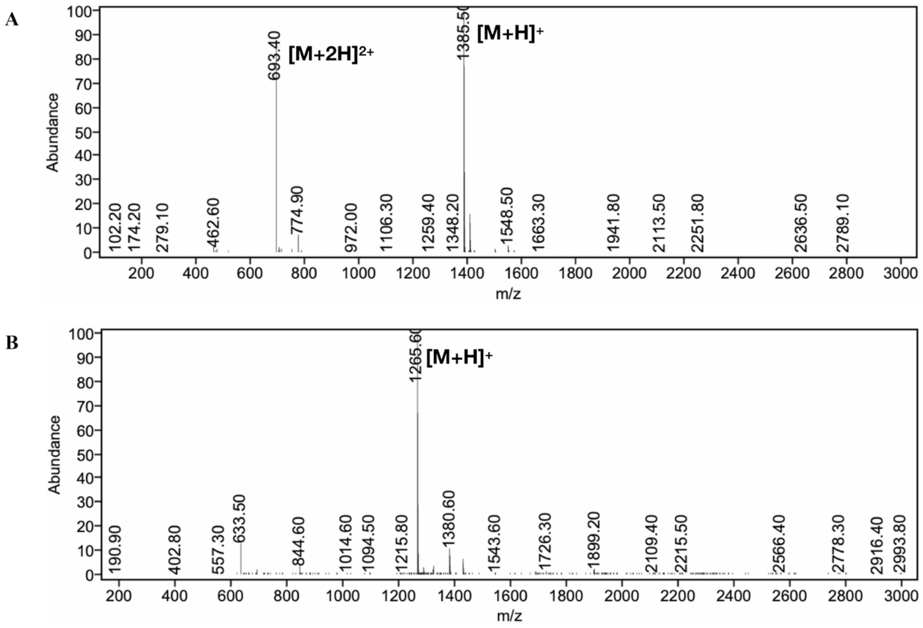


**Figure S3:** Mass spectra of A) compound **4a** and B) compound **4b**.

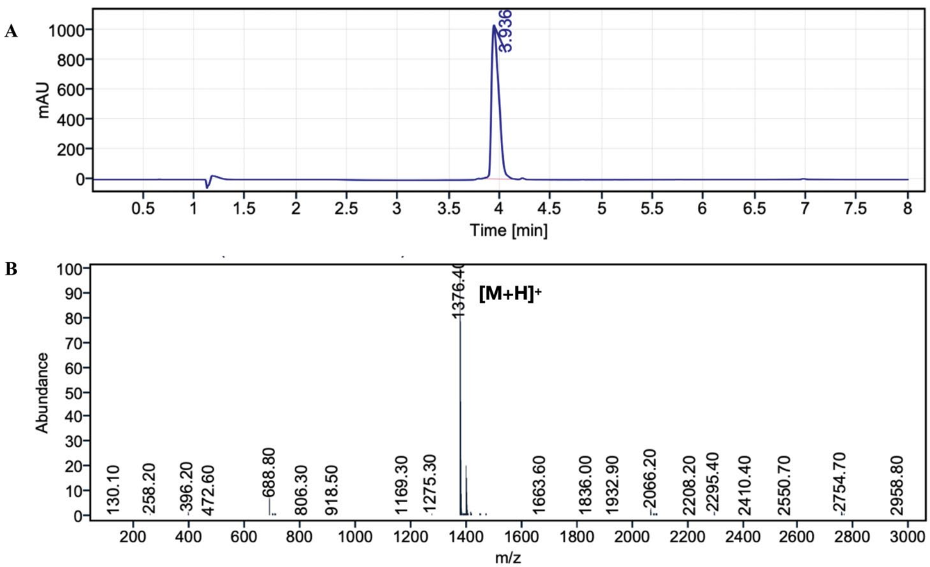


**Figure S4:** A) HPLC chromatogram and B) Mass spectrum of compound **8**.

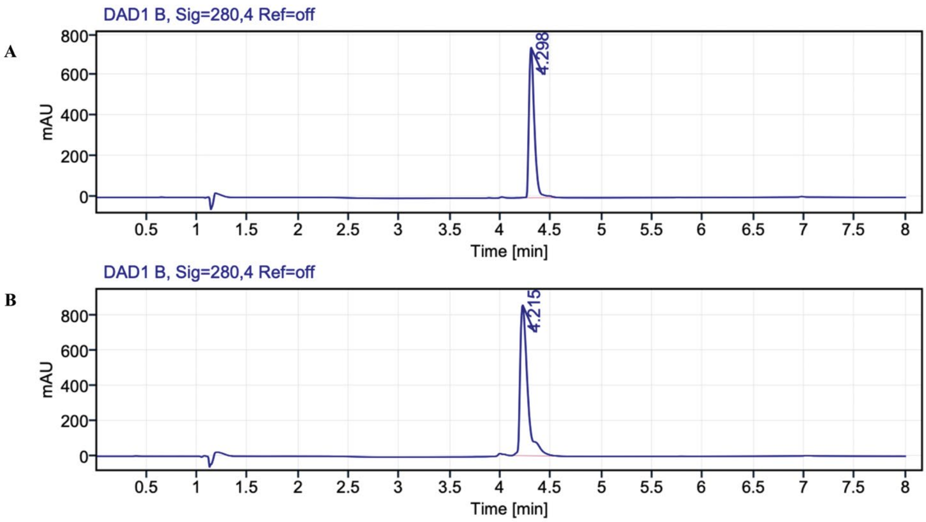


**Figure S5:** HPLC chromatograms of A) compound **9a** and B) compound **9b**.

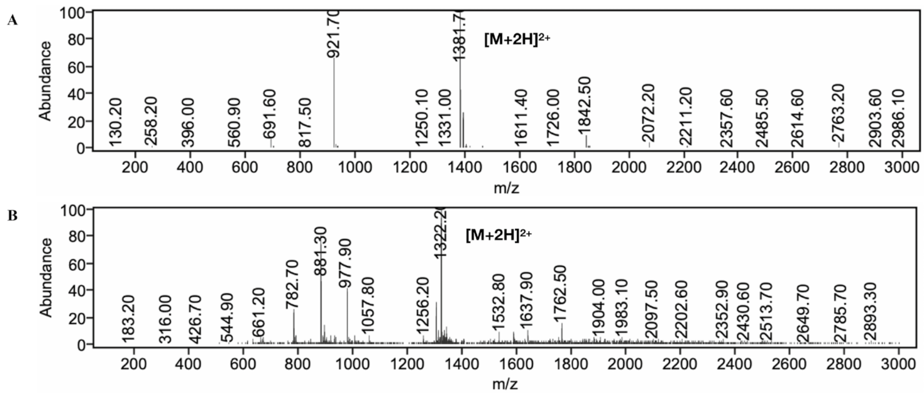


**Figure S6:** Mass spectra of A) compound **9a** and B) compound **9b**.

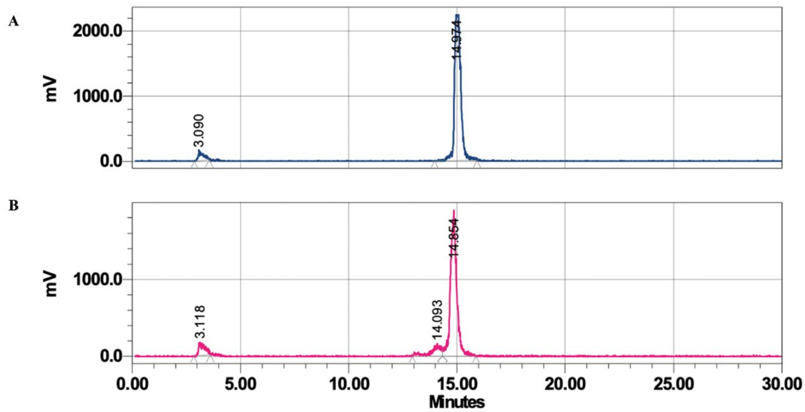


**Figure S7:** Radio-HPLC chromatograms of A) [$^{111}$In]In-**9a** and B) [$^{111}$In]In-**9b** in the labeling solution after incubation at 90 °C for 20 min.

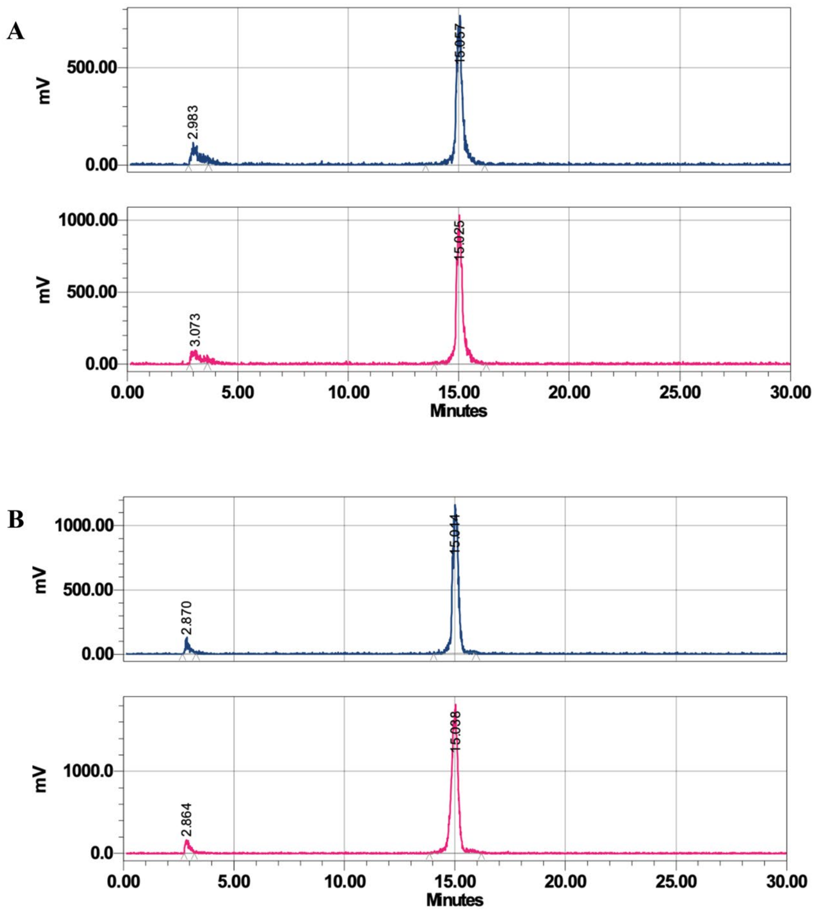


**Figure S8:** Radio-HPLC chromatograms of the stability studies performed for [$^{111}$In]In-**9a** at 1 h (blue) and 3 h (pink) post incubation at 37 °C of the radioligand in A) PBS and B) mouse serum.

A

B

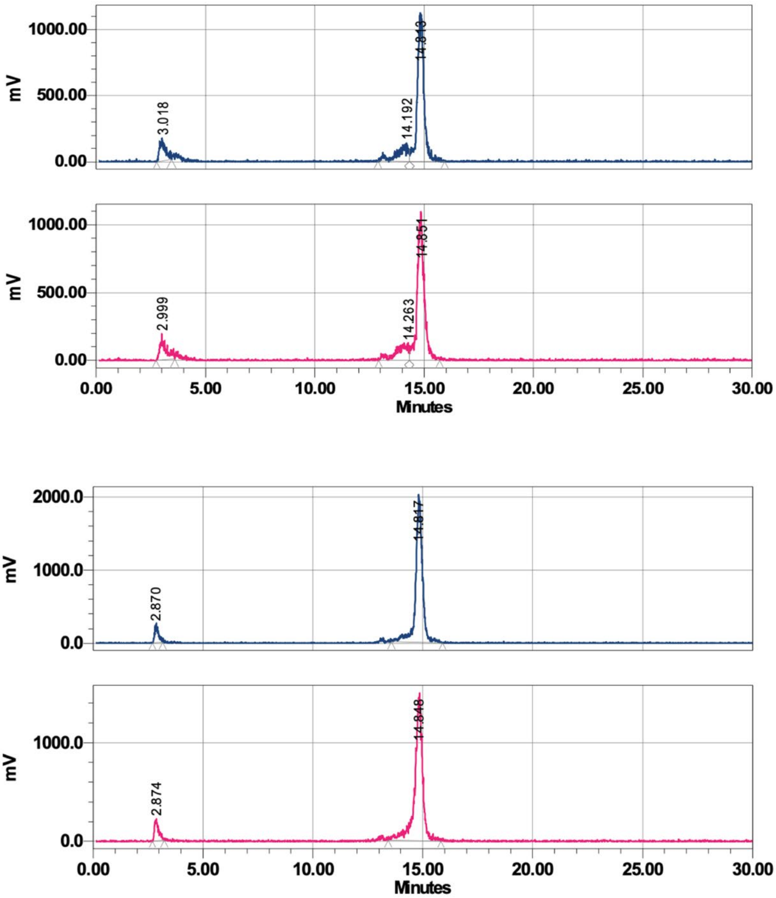


**Figure S9:** Radio-HPLC chromatograms of the stability studies performed for [$^{111}$In]In-**9b** at 1 h (blue) and 3 h (pink) post incubation at 37 °C of the radioligand in A) PBS and B) mouse serum.

# PART 2

## Improvement of The Treatment Efficacy of NETs

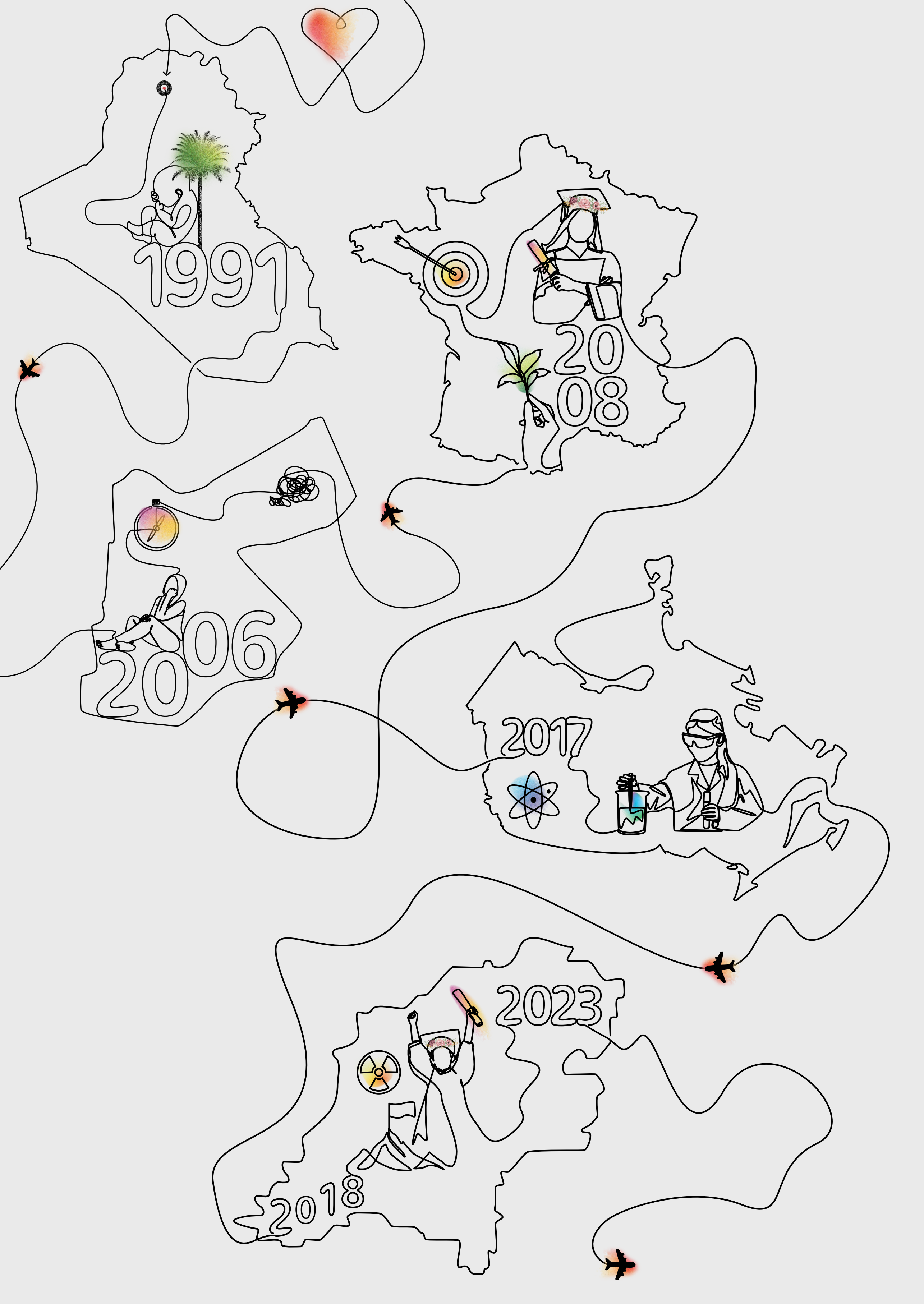
1991
2008
2006
2017
2023
2018

# CHAPTER 6

## Synthesis and Evaluation of Two Long-Acting SSTR2 Antagonists for Radionuclide Therapy of Neuroendocrine Tumors

Sofia Koustoulidou[1,†], Maryana Handula[1,†], Corrina de Ridder[1], Debra Stuurman[1], Savanne Beekman[1], Marion de Jong[1,‡], Julie Nonnekens[1,2] and Yann Seimbille[1,3]

[1] Department of Radiology and Nuclear Medicine, Erasmus MC Cancer Institute, Erasmus University Medical Center Rotterdam, 3015 GD Rotterdam, The Netherlands
[2] Department of Molecular Genetics, Erasmus MC Cancer Institute, Erasmus University Medical Center Rotterdam, 3015 GD Rotterdam, The Netherlands
[3] Life Sciences Division, TRIUMF, Vancouver, BC V6T 2A3, Canada

† These authors contributed equally to this work.
‡ The author recently passed away.

*Pharmaceuticals. 2022;15(9):1155*

**Abstract:** Somatostatin receptor subtype 2 (SSTR2) has become an essential target for radionuclide therapy of neuroendocrine tumors (NETs). JR11 was introduced as a promising antagonist peptide to target SSTR2. However, due to its rapid blood clearance, a better pharmacokinetic profile is necessary for more effective treatment. Therefore, two JR11 analogs (**8a** and **8b**), each carrying an albumin binding domain, were designed to prolong the blood residence time of JR11. Both compounds were labeled with lutetium-177 and evaluated via in vitro assays, followed by in vivo SPECT/CT imaging and ex vivo biodistribution studies. [$^{177}$Lu]Lu-**8a** and [$^{177}$Lu]Lu-**8b** were obtained with high radiochemical purity (>97%) and demonstrated excellent stability in PBS and mouse serum (>95%). [$^{177}$Lu]Lu-**8a** showed better affinity towards human albumin compared to [$^{177}$Lu]Lu-**8b**. Further, **8a** and **8b** exhibited binding affinities 30- and 48-fold lower, respectively, than that of the parent peptide JR11, along with high cell uptake and low internalization rate. SPECT/CT imaging verified high tumor accumulation for [$^{177}$Lu]Lu-**8a** and [$^{177}$Lu]Lu-JR11 at 4, 24, 48, and 72 h post-injection, but no tumor uptake was observed for [$^{177}$Lu]Lu-**8b**. Ex vivo biodistribution studies revealed high and increasing tumor uptake for [$^{177}$Lu]Lu-**8a.** However, its extended blood circulation led to an unfavorable biodistribution profile for radionuclide therapy.

**Keywords:** neuroendocrine tumors; somatostatin receptor subtype 2; JR11; albumin binder; radionuclide therapy

# 1. Introduction

Treatment of neuroendocrine tumors (NETs) largely depends on radioligands targeting somatostatin receptor type 2 (SSTR2). [$^{177}$Lu]Lu-DOTA-TATE (Lutathera®) is the leading radioligand with approval from both the Food and Drug Administration (FDA) and the European Medicines Agency (EMA) [1]. The NETTER-1 phase III study showed promising results, with a response rate of 18% for the [$^{177}$Lu]Lu-DOTA-TATE group [2]. However, novel developments are still necessary to achieve a better response. One such strategy is to enhance the radioligand delivery to increase the radiation dose to tumor cells.

Various studies have shown that SSTR2 antagonists, such as JR11, are more potent than SSTR2 agonists due to their ability to bind to more receptor binding sites. Therefore, several SSTR2 antagonist peptides have been labeled for diagnostic or therapeutic purposes [3–7]. However, the rapid blood clearance of such SSTR2 radioligands and the significant accumulation in non-target tissues pose a limit for higher tumor dose delivery and more efficient treatment [8]. In this context, binding of radioligands to serum protein can be an efficient method to improve the pharmacokinetic properties of these molecules [9]. Albumin binding domains (ABD) promise to increase the time-integral tumor uptake by prolonging blood circulation and reducing the uptake in healthy organs such as the kidneys [10]. Recently, Evans Blue (EB), a molecule known to bind to albumin, was conjugated to the agonist octreotate, and the resulting EB-TATE was labeled with the therapeutic radionuclide yttrium-90. [$^{90}$Y]Y-EB-TATE showed higher tumor uptake and improved tumor response in mice bearing SSTR2-positive tumors compared to [$^{177}$Lu]Lu-DOTA-TATE [11]. Other ABDs with different binding affinity for albumin have also been reported [12–14]. Of those, 4-(*p*-iodophenyl)butyryl and 4-(*p*-methoxyphenyl)butyryl were the most preferred albumin binding domains due to the aforementioned studies, in which enhanced tumor uptake and tumor-to-kidney dose ratio were observed. Thus, we report herein the synthesis of two JR11 derivatives containing one of these ABDs on the side chain of a lysine residue incorporated into the peptide sequence. Then, the in vitro characteristics of these long-acting SSTR2-antagonists (**8a** and **8b**) were evaluated. Both compounds were labeled with lutetium-177, and their in vivo distribution in tumor xenografts, overexpressing SSTR2 were investigated by SPECT/CT imaging and ex vivo biodistribution.

## 2. Results

### *2.1. Synthesis of the Long-Acting SSTR2 Antagonists*

The synthesis of the two long-acting JR11 analogs **8a** and **8b** was carried out following standard Fmoc-based SPPS protocols (Scheme 1). Coupling of the chelator was performed using PyBOP, as we previously observed faster reaction kinetics when using this coupling agent [15,16]. Cleavage of the peptides from the solid support resulted in the removal of most of the side chain protecting groups. However, a second treatment with neat TFA was required for the complete deprotection of the *tert*-butyl groups. Further, ivDde protection of the sidechain amino group of the lysine residue in position-3 allowed orthogonal coupling of the albumin binding domains on the additional lysine positioned between the cyclic peptide and the chelator. Conjugation of the ABDs to **6** was performed after their activation as NHS esters. The final products **8a** and **8b** were obtained at 9.9 and 8.7% yield, respectively, after deprotection of the ivDde protecting group of $Lys^3$ and purification by HPLC (Figures S1 and S2).

### *2.2. Radiolabeling with [$^{177}$Lu]LuCl$_3$*

Labeling of **8a** and **8b** with [$^{177}$Lu]LuCl$_3$ was performed in the presence of gentisic acid and ascorbic acid. Both additives are known scavengers to protect radiopharmaceuticals from radiolytic degradation [17]. Kolliphor, a non-ionic solubilizer and emulsifier used to improve the solubility of hydrophobic compounds, was added to the labeling reaction mixture to prevent stickiness of the peptides. The radiochemical yield (RCY) of both peptides and their radiochemical purity (RCP) are presented in Table 1. [$^{177}$Lu]Lu-**8a** and [$^{177}$Lu]Lu-**8b** were obtained in 97.7 and 98.2% RCP, respectively (Figure S3). Both tracers showed excellent stability in phosphate buffered saline (PBS) and mouse serum up to 24 h at 37 °C (Figures S4 and S5). The radioligands exhibited negative $LogD_{7.4}$ values, and [$^{177}$Lu]Lu-**8a** bound more efficiently to human albumin than did [$^{177}$Lu]Lu-**8b** (Table 1).

### *2.3. Competitive Binding Assay*

The $IC_{50}$ values of **8a** and **8b** were determined in a competitive binding assay using U2OS-SSTR2 cells and [$^{177}$Lu]Lu-JR11 as radioligand (Table 2 and Figure S6); **8a** and **8b** exhibited a binding affinity of 80 and 130 nM, respectively, which is 30- and 48-fold lower than the $IC_{50}$ value found for the parent peptide JR11. Considering that the binding affinities of **8a** and **8b** were still in the nanomolar range, we considered that they were suitable for further studies.

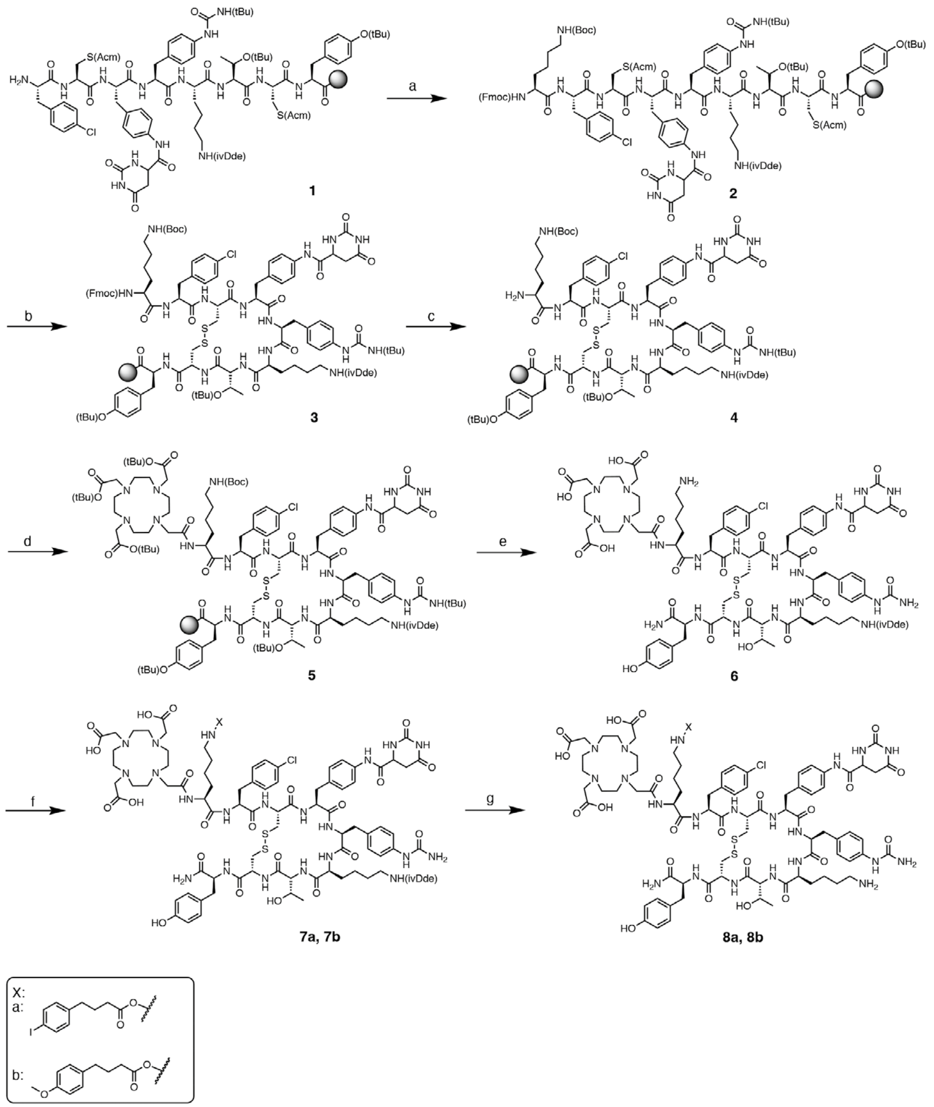

**Scheme 1.** Synthesis of compounds **8a** and **8b**: (**a**) Fmoc-L-Lys(Boc)-OH, HATU, DIPEA, DMF, 1 h, rt; (**b**) $Tl(TFA)_3$, DMF, 1 h, rt; (**c**) 20% piperidine in DMF; (**d**) DOTA-tris(*t*Bu) ester, PyBOP, DIPEA in DMF, 2 h, rt; (**e**) (i) TFA/$H_2O$/TIS, 2 h, rt and (ii) neat TFA, 8 h, rt, 29%; (**f**) 2,5-dioxopyrrolidin-1-yl 4-(4-iodophenyl)butanoate or 2,5-dioxopyrrolidin-1-yl 4-(*p*-methoxyphenyl)butanoate, $Et_3N$, 1 h, rt, 68% and 69% for compounds **7a** and **7b**, respectively; and (**g**) 2% hydrazine in DMF, 1 h, rt, 9.9% and 8.7% for compounds **8a** and **8b,** respectively.

**Table 1.** RCY, RCP, stability in PBS ($n$ = 1) and mouse serum ($n$ = 1), Log$D_{7.4}$ ($n$ = 3) and percentage of protein-bound fraction (n = 3) of [$^{177}$Lu]Lu-**8a** and [$^{177}$Lu]Lu-**8b**.

| | | | Stability in PBS (%) [a] | | | Stability in Mouse Serum (%) [a] | | | | |
|---|---|---|---|---|---|---|---|---|---|---|
| **Radioligand** | **RCY (%)** | **RCP (%)** | **1 h** | **4 h** | **24 h** | **1 h** | **4 h** | **24 h** | **Log $D_{7.4}$** | **Protein-Bound Fraction (%)** |
| [$^{177}$Lu]Lu-**8a** | 99.0 | 97.7 | 96.5 | 96.5 | 97.2 | 97.3 | 98.4 | 98.5 | −1.60 ± 0.03 | 89.5 ± 0.8 |
| [$^{177}$Lu]Lu-**8b** | 98.9 | 98.2 | 97.1 | 96.4 | 95.4 | 98.0 | 97.9 | 98.5 | −2.07 ± 0.02 | 56.3 ± 1.4 |
| [$^{177}$Lu]Lu-JR11 | 99.1 | 99.0 | | | | | | | −2.5 [18] | 33.6 ± 2.9 |

[a] Results are expressed as percentage (%) of intact radiolabeled ligand after incubation at 37 °C.

**Table 2.** In vitro competitive binding assays for compounds **8a** and **8b** in increasing concentrations (M) with [$^{177}$Lu]Lu-JR11 as radioligand.

| Ligand | $IC_{50}$ (nM) |
|---|---|
| **JR11** | 2.7 ± 0.26 |
| **8a** | 80 ± 0.43 |
| **8b** | 130 ± 0.30 |

### *2.4. Uptake and Internalization in U2OS-SSTR2 Cells and H69 Tumor Tissues*

Uptake of $^{177}$Lu-labeled **8a** and **8b** was observed in an in vitro assay using U2OS-SSTR2 cells (7.8 ± 0.05 and 3.1 ± 0.33% added dose, respectively (Figure 1A). Most radioactivity uptake was membrane-bound in both cases (5.8 ± 0.17 and 2.6 ± 0.38% added dose, respectively**)**, confirming the antagonist properties of the two compounds. However, compared to the [$^{177}$Lu]Lu-JR11 reference (total uptake 16.2 ± 3.0% added dose), this uptake was significantly lower, especially for [$^{177}$Lu]Lu-**8b**. A similar radioactive uptake pattern (930 ± 37 DLU/mm$^2$ for [$^{177}$Lu]Lu-JR11, 561 ± 18 DLU/mm$^2$ for [$^{177}$Lu]Lu-**8a**, and 280 ± 23 DLU/mm$^2$ for [$^{177}$Lu]Lu-**8b**) was observed when H69 human carcinoma tissues were incubated with the aforementioned compounds, as determined by autoradiography (Figure 1B).

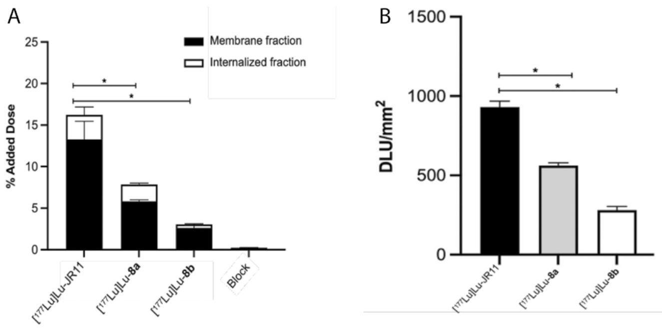


**Figure 1.** Uptake and internalization of compounds [$^{177}$Lu]Lu-**8a**, [$^{177}$Lu]Lu-**8b** and [$^{177}$Lu]Lu-JR11-in (**A**) U2OS-SSTR2 cells and (**B**) H69 tumor tissues expressing SSTR2. Quantification of the autoradiography images was performed and expressed as DLU/mm$^2$. *$P < 0.05$.

### *2.5. In Vivo Evaluation by SPECT/CT Imaging*

The biodistribution of lutetium-177-labeled **8a** and **8b** was first evaluated in vivo by single-photon emission computed tomography/computed tomography (SPECT/CT) imaging (Figure 2, Table 3). Mice bearing SSTR2-positive H69 xenografts were scanned at 4, 24, 48, and 72 h after intravenous (i.v.) injection of [$^{177}$Lu]Lu-**8a** or [$^{177}$Lu]Lu-**8b**. [$^{177}$Lu]Lu-JR11 was used as a positive control. The maximum intensity projections (MIP) depicted in Figure 2A showed high uptake of [$^{177}$Lu]Lu-**8a** in the tumor at 4, 24, 48, and 72 h post-injection (3.7 ± 0.9, 4.9 ± 0.5, 5.7 ± 0.6, and 4.9 ± 0.3% ID/mL, respectively) and substantial uptake in the heart. In contrast, [$^{177}$Lu]Lu-**8b** showed no tumor uptake, especially at later time points

(0.8 ± 0.1 and 0.6 ± 0.1% ID/mL at 48 and 72 h, respectively), and substantial accumulation in the kidneys (4.3 ± 0.3 and 3.1 ± 0.5% ID/mL at 48 and 72 h, respectively) (Figure 2B). Tumor uptake of the reference compound [$^{177}$Lu]Lu-JR11 could be observed until 24 h post-injection (3.3 ± 0.7% ID/mL). High kidney uptake was observed for all three compounds, probably as a result of urinary excretion. Based on the imaging data, we determined that [$^{177}$Lu]Lu-**8a** was suitable for further ex vivo biodistribution studies.

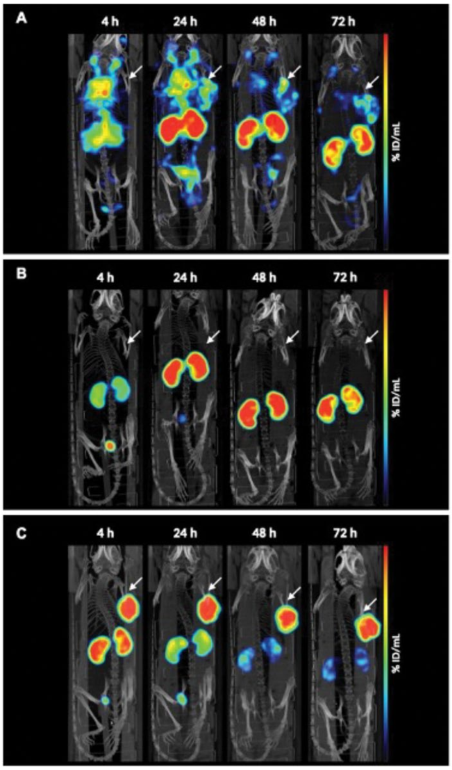


**Figure 2.** Representative MIP images of SPECT/CT scans of (**A**) [$^{177}$Lu]Lu-**8a**, (**B**) [$^{177}$Lu]Lu-**8b,** and (**C**) [$^{177}$Lu]Lu-JR11 at 4, 24, 48, and 72 h from H69 human xenograft-bearing mice (right shoulder; white arrows indicate tumors; n = 4). Color scale represents % ID/mL.

**Table 3.** SPECT quantification of xenograft tumor (T) and kidneys (K) per group at 4, 24, 48, and 72 h post-injection, represented in % ID/mL.

| Radioligand | | 4 h | 24 h | 48 h | 72 h |
|---|---|---|---|---|---|
| **[$^{177}$Lu]Lu-JR11** | T | 4.0 ± 0.6 | 3.3 ± 0.7 | 2.1 ± 0.5 | 1.8 ± 0.4 |
| | K | 3.7 ± 0.7 | 2.2 ± 0.3 | 1.2 ± 0.3 | 0.7 ± 0.1 |
| **[$^{177}$Lu]Lu-8a** | T | 3.7 ± 0.9 | 4.9 ± 0.5 | 5.7 ± 0.6 | 4.9 ± 0.3 |
| | K | 7.7 ± 0.9 | 10.1 ± 0.8 | 10.1 ± 0.3 | 8.9 ± 0.2 |
| **[$^{177}$Lu]Lu-8b** | T | 2.7 ± 0.2 | 1.0 ± 0.1 | 0.8 ± 0.1 | 0.6 ± 0.1 |
| | K | 14.8 ± 1.2 | 7.5 ± 0.4 | 4.3 ± 0.3 | 3.1 ± 0.5 |

### *2.6. Ex Vivo Biodistribution Analysis*

Next to the in vivo SPECT/CT imaging studies, ex vivo biodistribution was carried out after administration of [$^{177}$Lu]Lu-JR11 and [$^{177}$Lu]Lu-**8a** at the same time points (4, 24, 48, and 72 h). Compound **8b** was excluded due to the minimal tumor uptake observed earlier in the in vivo SPECT scans. An additional group of mice per compound received an excess of the corresponding non-radioactive compound (block group) to determine receptor specificity. At 4 h post-injection, the uptake of [$^{177}$Lu]Lu-**8a** in the blood was at 21.3 ± 1.1% ID/g and gradually decreased to 8.6 ± 0.5% ID/g at 72 h post-injection, reflecting the albumin-binding properties of the compound (Figure 3A and Table S1). Tumor uptake of [$^{177}$Lu]Lu-**8a** slightly increased over time (4.1 ± 0.5% ID/g at 4 h, 6.5 ± 0.2% ID/g at 24 h, 7.3 ± 0.4% ID/g at 48 h, and 7.3 ± 0.9% ID/g at 72 h). However, the kidneys showed high uptake at the early and late time points (9.6 ± 1.2% ID/g at 4 h and 21.6 ± 1.4% ID/g at 72 h), suggesting clearance of the compound through renal excretion. Shortly after injection, a substantial level of radioactivity was also found in the lungs, pancreas, skin, and spleen. Finally, only a slight reduction was observed in the tumor after injection of the blocking agent.

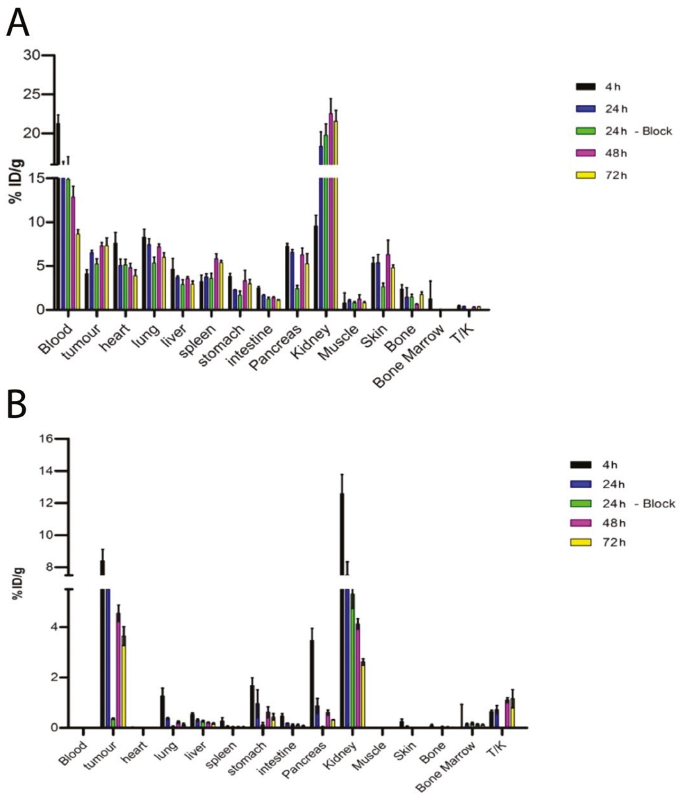


**Figure 3.** Ex vivo biodistribution analysis of (**A**) [$^{177}$Lu]Lu-**8a** (5 MBq/0.5 nmol) and (**B**) [$^{177}$Lu]Lu-JR11 (5 MBq/0.5 nmol) at 4, 24, 48, and 72 h post-injection (n = 4 mice/group). Data represented as percentage of injected dose per gram of tissue (% ID/g).

In contrast, the reference compound [$^{177}$Lu]Lu-JR11 showed high tumor uptake at 4 h post-injection (8.4 ± 0.5% ID/g, Figure 3B and Table S2) and even though the tumor uptake slightly decreased over time (6.1 ± 0.5% ID/g at 24 h, 4.6 ± 0.3% ID/g at 48 h, and 3.6 ± 0.4% ID/g at 72 h post-injection), the tumor-to-kidney ratio increased from 0.6 ± 0.05 at 4 h post-injection to 1.2 ± 0.3 at 72 h post-injection. Complete blocking of tumor uptake (Block group) at 24 h post-injection confirmed the specificity of the JR11 compound for the SSTR2 receptor.

## 3. Discussion

Somatostatin receptor subtype 2 (SSTR2) is present at a high incidence in neuroendocrine tumors (NETs) and therefore is an ideal target for imaging and therapy of this malignant disease. Somatostatin analogs have been widely used for the past decades and are considered a gold standard for NET treatment [19]. Among these drugs, radiolabeled somatostatin antagonists such as LM3, JR10, and JR11 have shown greater promise than agonists (e.g., DOTA-TATE and DOTA-TOC) [20]. However, preclinical and clinical studies have demonstrated that JR11 is cleared rapidly from the bloodstream, thus leading to high kidney uptake [7,21]. Therefore, our study aimed to develop two JR11 analogs carrying two different albumin binding domains to improve the pharmacokinetic profile of JR11.

The chemical structure of our new ligands (**8a** and **8b**) is directly based on the structure of the parent peptide JR11. The introduction of the albumin binding domains into the peptide sequence was established by the attachment of a lysine residue between the cyclic peptide and the DOTA chelator. This method has been previously employed to introduce fluorescent dye on the chemical structure of existing radioligands [22–24]. Here, we investigated the influence of two ABDs, namely 4-(*p*-iodophenyl)butyryl and 4-(*p*-methoxyphenyl)butyryl, on the in vivo behavior of JR11. These ABDs were selected due to the promising results reported in previous studies [12–14,25]. The 4-(*p*-iodophenyl) butyryl group has been widely used to improve the bioavailability of different radioligands, such as DOTA-TATE, PSMA-617, and folic acid. However, when conjugated to PSMA-617 ([$^{177}$Lu]Lu-HTK01169), Hsiou-Ting Kuo et al. noticed that not only was tumor uptake 8.3-fold higher for [$^{177}$Lu]Lu-HTK01169 in comparison to [$^{177}$Lu]Lu-PSMA-617, but also, the absorbed dose in the kidneys was 17.1-fold higher than that of the parent molecule [26]. Later, the same group reported a study comparing several albumin binding domains and concluded that 4-(*p*-methoxyphenyl)butyryl could be a potential candidate to improve blood circulation and reduce kidney radiotoxicity [13]. Radiolabeling of **8a** and **8b** with [$^{177}$Lu]$LuCl_3$ was successful, and both radiopeptides showed high RCYs and RCPs. They exhibited excellent inertness in PBS and mouse serum up to 24 h post-incubation, proving their stability towards radiolysis and peptidase digestion. When compared to JR11, the

$LogD_{7.4}$ values of our radiopeptides were slightly higher than the $LogD_{7.4}$ value of the parent peptide [18]. This is probably due to the lipophilic character of the two albumin binding domains. This observation is also confirmed by the data provided by Hsiou-Ting Kuo et al. [13]. Nevertheless, the $LogD_{7.4}$ values of [$^{177}$Lu]Lu-**8a** and [$^{177}$Lu]Lu-**8b** remained negative, suggesting that they are hydrophilic. [$^{177}$Lu]Lu-**8a** showed good binding to plasma proteins, as previously reported for other radioligands bearing the same ABD [27,28]. Furthermore, [$^{177}$Lu]Lu-**8a** showed stronger affinity towards human albumin in comparison to that of [$^{177}$Lu]Lu-**8b**, confirming that the interaction between the ABD and the plasma proteins is influenced by the lipophilicity of the substituted phenyl group [13]. Thus, two JR11 analogs were prepared and, as expected, **8a** interacted strongly with albumin, while **8b** exhibited a milder interaction with albumin. The parent peptide JR11 showed lower binding to plasma proteins in comparison to that of our long-acting analogs.

Competitive binding assays were performed to determine the $IC_{50}$ values of the newly synthesized compounds **8a** and **8b** for the SSTR2 receptor. The incorporation of the albumin binding moiety did affect the SSTR2 binding affinity of the two compounds, probably due to the sensitivity of the parent peptide JR11 to chemical modifications. Fani et al. noticed that different chelators affect the binding affinity of the peptide in vitro [7]. More specifically, exchanging the DOTA chelator with NODAGA ([$^{68}$Ga]Ga-NODAGA-JR11) significantly increased the affinity of the peptide toward the SSTR2 receptor. The authors speculated that in the case of the DOTA chelator, the geometry is hexacoordinate, and in solution, the chelator can act as a spacer, hence lowering the affinity. In vitro uptake of these compounds in cells and tumor sections expressing SSTR2 was lower than the uptake of JR11. The majority of the uptake was found in the membrane-bound fraction, confirming the compounds' antagonist properties.

SPECT/CT images revealed increased blood residence time of the compound [$^{177}$Lu]Lu-**8a** compared with [$^{177}$Lu]Lu-JR11. This suggests that the albumin binding affinity contributed to the different pharmacokinetic profiles. However, despite the higher tumor uptake, as observed by image analysis, accumulation in the kidneys was substantial, thus making it unsuitable for future therapeutic studies. In a different study, Rousseau et al. also observed the same pattern when comparing DOTA-TATE with an albumin binding moiety ([$^{177}$Lu]Lu-AspAB-DOTA-TATE) to the reference analog, highlighting that albumin binding moieties might negatively affect the pharmacokinetic profile of peptides [25]. In the clinic, the high kidney uptake can be reduced by perfusion of cationic amino acids, but bone marrow toxicity will remain a problem [29]. Unfortunately, and to our surprise, compound [$^{177}$Lu]Lu-**8b** showed no tumor uptake and rapid renal clearance despite earlier reports by Kuo et al. showing the opposite effect with PSMA ligands [13].

Ex vivo biodistribution analysis confirmed the uptake pattern observed during imaging. In addition, the introduction of a blocking group for both **8a** and JR11 showed non-specific tumor uptake for [$^{177}$Lu]Lu-**8a** compared to [$^{177}$Lu]Lu-JR11, for which a total blockade of SSTR2 receptor uptake was achieved. The high uptake of the compound in most organs could suggest that the plasma protein-binding prolongs the blood circulation substantially and interferes with the binding of **8a** to tumor cells, thus causing inefficient blockade. Müller and coworkers also used the 4-(*p*-iodophenyl)butyryl ABD conjugated to a folate radioligand, and they observed higher tumor uptake and a reduction in kidney accumulation [14]. However, the authors did not perform a blocking study, making it difficult to draw any conclusions on the specificity of their compound. On the other hand, van Tiel et al. did not observe total blockage of tumor uptake when they conjugated the same albumin binding domain onto Albutate-1 [12]. More specifically, the tumor uptake of [$^{177}$Lu]Lu-Albutate-1 was 24.42 ± 1.44% ID/g at 24 h post-injection, while the blocked group showed uptake of approximately 12% ID/g. From dosimetry calculations, the authors noticed a high radiation dose in several tissues, especially in bone marrow (total absorbed dose of 765 mGy/MBq), probably due to the prolonged circulation. Even though in this study bone marrow uptake was negligible due to the inadequate extraction of the sample during the ex vivo biodistribution, this could pose a limit for a better therapeutic index with compounds carrying albumin binding moieties.

In a more recent study, the 4-(*p*-iodophenyl)butyryl moiety was conjugated to the DOTA-$(PEG_{28})_2$-A20FMDV2 peptide labeled with [$^{177}$Lu]Lu and used for the imaging of αvβ6-positive tumors [30]. The authors noticed that even though blood uptake of the peptide was high at 1 h post-injection, it dropped rapidly by 48 h (0.04 ± 0.01% ID/g), while tumor uptake remained constant (4.06 ± 0.54% ID/g), rendering the tumor-to-blood ratio ideal for therapy. Kidney uptake was, however, responsible for the toxicity observed during these studies. Based on this, it is recommended to perform the blocking study at a later timepoint to allow for better clearance of the peptide from the blood.

Overall, the previously mentioned studies, together with our results, point out the need for different and better albumin binding moieties and further modifications to the peptide itself that will improve the binding affinity and the specificity of SSTR2-targeting antagonists towards the receptor.

## 4. Materials and Methods

### *4.1. General Information*

The chemicals and solvents mentioned in this manuscript were purchased from commercial suppliers and used without further purification. Fmoc-based solid-phase peptide synthesis (SPPS) of the peptide was performed manually using dedicated reaction vessels (Chemglass, Vineland, NJ, USA). DOTA-tris(*t*Bu)ester was purchased from Macrocyclics (Plano, TX, USA). Lutetium-177 (LuMark® Lutetium-177 chloride) was purchased from IDB Holland (Baarle-Nassau, The Netherlands). High-performance liquid chromatography (HPLC) and mass spectrometry (MS) were carried out on an LC/MS 1260 Infinity II system from Agilent (Middelburg, The Netherlands). Analyses were performed on an analytical column (Poroshell 120, EC-C18, 2.7 µm, 3.0 × 100 mm) from Agilent with a gradient elution of acetonitrile (ACN) (5% to 100% in $H_2O$, containing 0.1% formic acid) at a flow rate of 0.5 mL/min over 8 min. Nuclear magnetic resonance (NMR) spectra were recorded in deuterated dimethyl sulfoxide **(**DMSO-d6) and chloroform-d on a Bruker AVANCE 400 (Leiden, The Netherlands) or a Nanalysis 60 Pro (Calgary, AB, Canada) at ambient temperature. Chemical shifts are given as δ values in ppm, and coupling constants *J* are given in Hz. The splitting patterns are reported as s (singlet), d (doublet), t (triplet), q (quadruplet), qt (quintuplet), m (multiplet), and br (broad signal). Purification of AB2-NHS ester and compound **8b** was carried out on a preparative HPLC 1260 Infinity II system from Agilent (Middelburg, The Netherlands) using a preparative column (50 × 21.2 mm, 5 µm) from Agilent. AB2-NHS ester was purified using a gradient elution of ACN (10% to 95% in $H_2O$, containing 0.1% formic acid (FA)) at a flow rate of 10 mL/min over 10 min. Compound **8b** was purified via an isocratic elution of ACN (25% in $H_2O$) at a flow rate of 10 mL/min over 10 min. Purification of compound **8a** was performed on a semi-preparative HPLC e2695 Separation Module from Waters (Etten-Leur, The Netherlands) using a semi-preparative C18 Luna® column (250.0 × 10.0 mm, 5 µm) from Phenomenex (Torrance, CA, USA) with an isocratic elution of ACN (35% in $H_2O$) at a flowrate of 3 mL/min over 30 min. Instant thin-layer chromatography (iTLC-SG) plates on silica-gel-impregnated glass fiber sheets (Agilent; Folsom, CA, USA) were eluted with sodium citrate (0.1 M, pH 5). The plates were analyzed by a bSCAN radio-chromatography scanner from Brightspec (Antwerp, Belgium) equipped with a sodium iodide detector. The radioactive samples used to determine $LogD_{7.4}$ in in vitro assays and in vivo studies were counted using a Wizard 2480 gamma counter (Perkin Elmer; Waltham, MA, USA). Activity measurements were performed using a VDC-405 dose calibrator (Comecer; Joure, The Netherlands). Quality control of the radiolabeled compounds and analysis of their stability were carried out on an ultra-high performance liquid chromatography (UHPLC) Acquity Arc system from Waters (Etten-Leur, The Netherlands) equipped with a diode array detector, a radio-detector from Canberra (Zelik, Belgium), and an analytical C18 Gemini®

column (Phenomenex; 250.0 × 4.6 mm, 5 µm) eluted with a gradient of ACN (5 to 95% in $H_2O$, containing 0.1% trifluoroacetic acid (TFA)) at a flowrate of 1 mL/min over 30 min.

### *4.2. Chemistry*

4.2.1 Synthesis of DOTA-Lys-Phe(4-Cl)-c[D-Cys-Aph(Hor)-D-Aph(Cbm)-Lys(ivDde)-Thr-Cys]-D-Tyr-$NH_2$ (**6**)

The peptide sequence was synthesized using the standard $N^{\alpha}$-Fmoc solid-phase peptide synthesis (SPPS) strategy. Peptide synthesis started by loading Fmoc-D-Tyr(*t*Bu)-OH (0.5 mmol, 2 equiv.) onto the Rink amide MBHA resin (370 mg, average loading capacity: 0.678 mmol/g). The resin was stirred for 2 h at room temperature (rt). Then, the resin was capped using a mixture of acetic anhydride (50 equiv.) and DIPEA (50 equiv.) for 1 h at rt. Elongation of the peptidyl-resin was carried out in dimethylformamide (DMF) and in the presence of *N*-[(dimethylamino)-1*H*-1,2,3-triazolo-[4,5-*b*]pyridine-1-ylmethylen]-*N*-methylmethanaminium hexafluorophosphate *N*-oxide (HATU) and *N*,*N*-diisopropylethylamine (DIPEA). Fmoc deprotection was accomplished by treatment of the peptide with a 20% solution of piperidine in DMF. Subsequent couplings/Fmoc deprotections were performed with the following protected amino acids (2 equiv.): Fmoc-Cys(Acm)-OH, Fmoc-L-Thr(*t*Bu)-OH, Fmoc-L-Lys(ivDde)-OH, Fmoc-D-Aph(*t*Bu-Cbm)-OH, Fmoc-Aph(Hor)-OH, Fmoc-D-Cys(Acm)-OH, and Fmoc-Phe(4-Cl)-OH. Amide formation and Fmoc deprotection were monitored by Kaiser and TNBS tests. Double coupling and deprotection were performed when the reactions were not complete to obtain resin-bound Phe(4-Cl)-D-Cys(Acm)-Aph(Hor)-D-Aph(*t*Bu-Cbm)-Lys(ivDde)-Thr(*t*Bu)-Cys(Acm)-D-Tyr(*t*Bu) (**1**). Coupling of Fmoc-L-Lys(Boc)-OH (2 equiv.) to **1** according to the protocol described above provided **2**. Cyclization of the peptide was performed by treatment of **2** with thallium (III) trifluoroacetate ($Tl(TFA)_3$) (2 equiv.) in DMF for 1 h at rt. The cyclization reaction was monitored by LC/MS after cleavage of a small sample of peptide from the solid support. Upon Fmoc deprotection, compound **5** was obtained by coupling of DOTA-tris (*t*Bu) ester (3 equiv.) to **4** using benzotriazole-1-yl-oxy-tris-pyrrolidino-phosphonium hexafluorophosphate (PyBOP) (3 equiv.) and DIPEA (6 equiv.) in DMF for 2 h at rt. Finally, cleavage and removal of the sidechain protecting groups were performed by reacting **5** with a solution of trifluoroacetic acid/triisopropylsilane/water **(**TFA/TIS/$H_2O$) (2 mL, v:v:v = 95:2.5:2.5) for 2 h at rt. The resin was washed twice with the cleavage cocktail, and after evaporation of the solvent, the peptide was treated with neat TFA to completely remove the *tert*-butyl groups. Solvent was evaporated with gentle airflow, and the product was precipitated in cold diethyl ether and collected by centrifugation to obtain **6** as a yellowish solid (46.3, 29%). Analytical HPLC retention time of **6 was**: $t_R$ = 4.08 min; ESI-MS: *m*/*z*, calculated: 2021.9, found: 1012.7 $[M + 2H]^{2+}$.

4.2.2 Synthesis of 2,5-dioxopyrrolidin-1-yl 4-(4-iodophenyl)butanoate (AB1-NHS ester)

The 4-(*p*-iodophenyl)butanoic acid (500 mg, 1.7 mmol) and *N*-hydroxysuccinimide (NHS) (198 mg, 1.7 mmol, 1 equiv.) were dissolved in anhydrous tetrahydrofuran (THF) (10 mL) under nitrogen atmosphere. *N*,*N′*-Dicyclohexylcarbodiimide (DCC) (354 mg, 1.7 mmol, 1 equiv.) was dissolved in anhydrous THF (4 mL) under nitrogen atmosphere and added dropwise to the reaction mixture. The reaction mixture was stirred for 1 h at 0 °C and left to react overnight at rt. The white precipitate was removed by filtration, and the solvent was evaporated under vacuum. The crude compound was purified by flash chromatography (hexane/ethyl acetate 4:1 → 1:1) to yield AB1-NHS ester as white crystals (492 mg, 75%). Analytical HPLC retention time of AB1-NHS ester was: $t_R$ = 6.0 min; purity > 90%; 1H NMR (400 MHz, DMSO-d6): δ 7.65 (d, *J* = 7.8 Hz, 2H), 7.05 (d, *J* = 7.9 Hz, 2H), 2.82 (s, 4H), 2.64 (dt, *J* = 12.0, 7.6 Hz, 4H), 1.94–1.84 (m, 2H).

4.2.3 Synthesis of 2,5-dioxopyrrolidin-1-yl 4-(*p*-methoxyphenyl)butanoate (AB2-NHS ester)

AB2-NHS ester was obtained by reacting 4-(4-methoxyphenyl)butanoic acid (500 mg, 2.6 mmol) with NHS (296 mg, 2.6 mmol, 1 equiv.) and DCC (530 mg, 2.6 mmol, 1 equiv.) following the protocol described above for AB1-NHS ester. The crude compound was purified by prep-HPLC, and AB2-NHS ester was obtained as a white solid (564 mg, 75%). Analytical HPLC retention time of AB2-NHS ester was: $t_R$ = 5.5 min; purity > 95%; 1H NMR (60 MHz, Chloroform-d) δ 7.23–6.71 (m, 4H), 3.79 (s, 3H), 2.83 (s, 4H), 2.59 (t, *J* = 6.3 Hz, 4H), 2.29–1.81 (m, 2H).

4.2.4 Synthesis of DOTA-Lys(4-(*p*-iodophenyl)butyryl)-Phe(4-Cl)-c[D-Cys-Aph(Hor)-D-Aph(Cbm)-Lys(ivDde)-Thr-Cys]-D-Tyr-$NH_2$ (**7a**)

Compound **7a** was obtained by adding AB1-NHS ester and triethylamine ($Et_3N$) to peptide **6** (57 mg, 28 µmol) dissolved in 1 mL of a mixture of $H_2O$/ACN (v:v = 1:1). $Et_3N$ (39 µL, 0.28 mmol, 10 equiv.) was added to reach pH 9, followed by the addition of AB1-NHS ester (16.4 mg, 42 µmol, 1.5 equiv.). The reaction mixture was stirred at rt, and progress of the reaction was monitored by LC/MS. Solvent was evaporated under reduced pressure, and the crude product **7a** was obtained as a yellowish solid (82 mg, 68%). Analytical HPLC retention time of **7a** was: $t_R$ = 15.7 min; ESI-MS: m/z, calculated: 2293.8, found: 1148.8 $[M + 2H]^{2+}$.

4.2.5 Synthesis of DOTA-Lys(4-(*p*-methoxyphenyl)butyryl)-Phe(4-Cl)-c[D-Cys-Aph(Hor)-D-Aph(Cbm)-Lys(ivDde)-Thr-Cys]-D-Tyr-$NH_2$ (**7b**)

Compound **7b** was obtained by following the protocol described above for **7a** and starting from **6** (28.9 mg, 14 µmol) and AB2-NHS ester (6.24 mg, 21 µmol, 1.5 equiv.). Crude product **7b** was obtained as a yellowish solid (36.2 mg, 69%). Analytical HPLC retention time of **7b** was: $t_R$ = 4.55 min. ESI-MS: *m*/*z*, calculated: 2197.9, found: 1100.6 $[M + 2H]^{2+}$.

4.2.6 Synthesis of DOTA-Lys(4-(*p*-iodophenyl)butyryl)-Phe(4-Cl)-c[D-Cys-Aph(Hor)-D-Aph(Cbm)-Lys-Thr-Cys]-D-Tyr-$NH_2$ (**8a**) and DOTA-Lys(4-(*p*-methoxyphenyl)butyryl)-Phe(4-Cl)-c[D-Cys-Aph(Hor)-D-Aph(Cbm)-Lys-Thr-Cys]-D-Tyr-$NH_2$ (**8b**)

The ivDde deprotection was performed by treatment of **7a** and **7b** with a solution of 2% hydrazine in DMF. The reaction mixture was stirred for 1 h at rt. Progress of the reaction was analyzed by LC/MS. Then, the reaction mixture was diluted in $H_2O$/ACN (v:v = 1:1) and purified by semi-preparative HPLC for compound **8a** and preparative HPLC for compound **8b**. Compound **8a** was obtained as a white solid (13 mg, 9.9%) Analytical HPLC retention time of **8a** was: $t_R$ = 4.0 min; purity > 96% (Figure S1A); ESI-MS: *m/z*, calculated: 2087.7, found: 1045.5 $[M + 2H]^{2+}$ and 697.2 $[M + 3H]^{3+}$ (Figure S2A). Compound **8b** was obtained as a white solid (7.1 mg, 8.7%) Analytical HPLC retention time of **8b** was: $t_R$ = 3.8 min; purity > 94% (Figure S1B); ESI-MS: *m/z*, calculated: 1991.8, found: 997.6 $[M + 2H]^{2+}$ and 665.3 $[M + 3H]^{3+}$ (Figure S2B).

### ***4.3. Radiochemistry***

4.3.1 Lutetium-177 radiolabeling of **8a** and **8b**

$[^{177}Lu]LuCl_3$ was obtained as a 0.05 M hydrochloric acid (HCl) aqueous solution. A total of 100 MBq was added to **8a** or **8b** (1 nmol), ascorbic/gentisic acids (10 µL, 50 mM), sodium acetate (1 µL, 2.5 M), and kolliphor in $H_2O$ (2.0 mg/mL, 60.8 µL). The mixture was incubated for 20 min at 90 °C and then left to cool down for 5 min. The radiolabeling yield was determined by instant thin-layer chromatography on silica-gel-impregnated glass fiber sheets eluted using a solution of sodium citrate (0.1 M, pH 5). Diethylenetriaminepentaacetic acid (DTPA, 5 µL, 4 mM) was added to complex free Lu-177. The radiochemical purity of $[^{177}Lu]$Lu-**8a** and $[^{177}Lu]$Lu-**8b** was determined by radio-HPLC (Figure S3).




4.3.2 Determination of lipophilicity

The distribution coefficient ($LogD_{7.4}$) of the $^{177}$Lu-labeled peptides was determined by the shake-flask method. For each radioligand, the experiment was performed in triplicate. The radiolabeled compound (~1.5 MBq) was added to a solution of phosphate buffered saline (PBS)/n-octanol (1 mL, v:v = 1:1) in eppendorf vials. The vials were vortexed vigorously and centrifuged at 10,000 rpm for 3 min. The n-octanol phase was separated from the aqueous phase, poured into new vials, and centrifuged for 15 min. Samples from each phase (10 µL) were measured using a gamma counter. The $LogD_{7.4}$ value was calculated using the following equation: $LogD_{7.4}$ = ([counts in the n-octanol phase]/[counts in the PBS phase]).

4.3.3 Stability studies in PBS and mouse serum

The $^{177}$Lu-labeled compounds (~3 MBq) were incubated in PBS (300 µL) at 37 °C. The stability of the radiolabeled peptides was verified by radio-HPLC at 1, 4, and 24 h. The stability in serum was determined by incubating the radiolabeled compounds (~3 MBq) into 150 µL of mouse serum (Merck; Haarlerbergweg, The Netherlands) at 37 °C. At 1, 4, and 24 h post-incubation, the proteins were precipitated by adding an aliquot of 35 µL of the mixture to an equal volume of ACN. The vial was vortexed and centrifuged for 20 min. stability was monitored by radio-HPLC (Figures S4 and S5).

#### 4.3.4 Albumin binding properties

Compounds **8a**, **8b**, and JR11 were radiolabeled with lutetium-177 at a molar activity of 50 MBq/nmol. Radiopeptides (~1 MBq) were incubated in either PBS (500 µL) or human albumin/PBS (500 µL, v:v = 1:4) for 1 h at 37 °C. Three aliquots of 10 µL were counted in a gamma counter to determine the amount of activity in the loading solution. The mixtures were loaded onto Centrifree Ultrafiltration devices (Centrifree Ultrafiltration device with Ultracel PL membrane, 30 KDa, Merck, Haarlerbergweg, The Netherlands) preconditioned with 700 µL of kolliphor in PBS (0.06 mg/mL). The Centrifree Ultrafiltration devices were centrifuged at 7000 rpm for 30 min. Three aliquots of 10 µL from each mixture were counted in a gamma counter, and the protein-bound fraction was calculated based on the radioactivity measured in the filtrate relative to the corresponding loading solution.

### *4.4. In Vitro Assays*

#### 4.4.1 Cell lines and culture

Human osteosarcoma cells (U2OS) stably expressing the SSTR2 receptor were used in all in vitro cell assays [21]. Cells were cultured in Dulbecco's modified Eagle's medium (DMEM) from Gibco (Paisley, UK) supplemented with 2 mM L-glutamine, 10% fetal bovine serum (FBS), 50 units/mL penicillin, and 50 µg/mL streptomycin (Sigma Aldrich; Haarlerbergweg, The Netherlands) and maintained at 37 °C and in a 5% $CO_2$ humidified chamber. Passages were performed weekly using trypsin/EDTA (0.05%/0.02% *w*/*v*).

#### 4.4.2 Competitive binding assay

Competitive binding experiments against [$^{177}$Lu]Lu-JR11 were performed with **8a** and **8b** in U2OS-SSTR2 cells. Cells were seeded in a 24-well plate 24 h in advance ($2 \times 10^5$ cells/well). On the day of the experiment, medium was removed, and the cells were washed once with PBS (Gibco). Then, solutions containing unlabeled compound **8a** or **8b** in increasing concentrations ($10^{-12}$ to $10^{-5}$ M) in internalization medium (DMEM media, 20 mM HEPES, 1% BSA, pH 7.4) were added, followed by the addition of [$^{177}$Lu]Lu-JR11 ($10^{-9}$ M). For each concentration, experiments were performed in triplicate. Cells were incubated at 37 °C for 90 min. After incubation, medium was removed, and cells were washed once with PBS and lysed with 0.5 M sodium hydroxide (NaOH) for 10 min at rt. The lysate was transferred to counting tubes, and measurement was performed using the $\gamma$-counter.

4.4.3 Uptake and internalization assay

Cells were seeded in 6-well plates 48 h before the experiment ($2 \times 10^5$ cells/well). The following day, adhered cells were incubated with $10^{-9}$ M of [$^{177}$Lu]Lu-JR11, [$^{177}$Lu]Lu-**8a**, or [$^{177}$Lu]Lu-**8b** in 1 mL of culture medium for 2 h at 37 °C. After incubation, medium was removed, and cells were washed twice with PBS. The membrane-bound fraction was collected by incubating cells with an acid buffer (50 mM glycine, 100 mM sodium chloride (NaCl), pH 2.8) for 10 min at rt. Cells were lysed using 0.5 M NaOH for 10 min at rt to acquire the internalized fraction. Both fractions were counted in a $\gamma$-counter, and data were expressed as percentage of added dose.

4.4.4 Uptake and autoradiography of H69 tumor sections

Subcutaneous fresh frozen H69 tumor tissues were cut at 10 µm thickness and immediately mounted on Starfrost glass slides (Thermo Scientific; Bleiswijk, The Netherlands). Tissue sections were incubated with washing buffer (167 mM Tris-HCl, 5 mM $MgCl_2$) containing 0.25% BSA for 10 min at rt to prevent nonspecific binding. Then, each section was incubated with $10^{-9}$ M of [$^{177}$Lu]Lu-JR11, [$^{177}$Lu]Lu-**8a** or [$^{177}$Lu]Lu-**8b** diluted in incubation buffer (washing buffer containing 1% BSA) for 90 min at rt. Each slide was drained off and washed with PBS. Finally, the slides were exposed to super-resolution phosphor screens for 48 h and imaged with the Cyclone system (PerkinElmer; Waltham, MA, USA). Images were analyzed and quantified using the Optiquant software Version 5 (PerkinElmer; Waltham, MA, USA).

### ***4.5. In Vivo Studies***

All animal experiments were approved by the Animal Welfare Committee of the Erasmus MC, and all procedures were conducted according to accepted guidelines. Mice were subcutaneously inoculated with $5 \times 10^6$ SSTR2-positive H69 human small cell lung carcinoma cells in Matrigel, and tumors were left to grow for 3-4 weeks to an average volume of approximately 300 mm$^3$. When the tumors reached the desired volume, each animal was injected intravenously (i.v.) through the tail vein with 100 µL of 20 MBq/0.5 nmol [$^{177}$Lu]Lu-JR11, [$^{177}$Lu]Lu-**8a**, or [$^{177}$Lu]Lu-**8b** diluted in PBS containing Kolliphor® HS 15 (0.06 mg/mL) for SPECT/CT imaging, and with 5 MBq/0.5 nmol for ex vivo biodistribution studies (n = 4 mice/group).

4.5.1 SPECT/CT imaging

The small-animal VECTor$^5$/CT (MILAbs B. V.; Utrecht, The Netherlands) was used for all imaging studies. Image acquisition was performed at 4, 24, 48, and 72 h post-injection using the high-energy general-purpose mouse collimator (HE-GP-M, 0.8 mm pinhole size) in list mode. Corresponding CT scans were acquired in total-body and normal mode (50 kV, 0.21 mA, 75 ms) for anatomical reference and attenuation correction.

All SPECT images were reconstructed using the similarity-regulated ordered-subsets expectation maximization (SROSEM) algorithm (MILAbs Rec 11.00 software, MILAbs, Utrecht, The Netherlands) with 5 iterations, 128 subsets, and a voxel size of 0,4 $mm^3$. Image processing and analyses of the reconstructed data were performed using the PMOD image analysis software version 3.10 (PMOD Technologies; Zurich, Switzerland) to calculate the percentage of injected dose per mL (% ID/mL). To allow quantification of the SPECT data, calibration factors were derived from [$^{177}$Lu]Lu phantoms.

### 4.5.2 Ex vivo biodistribution

For the ex vivo biodistribution studies, animals were euthanized at selected time points (4, 24, 48, and 72 h) after injection. Specific tissues and tumors were excised, and their radioactivity uptake was determined. The following organs were collected from each animal: blood, tumor, heart, lung, liver, spleen, stomach, intestine, pancreas, kidney, muscle, skin, bone, and bone marrow. To confirm receptor specificity, mice were co-injected with [$^{177}$Lu]Lu-JR11 or [$^{177}$Lu]Lu-**8a** and a 50-molar excess of their respective unlabeled compound (JR11 or **8a**), after which uptake in organs and tumor was determined at 24 h post-injection. All tissues were weighed and counted in a *γ*-counter, and data were reported as percentage injected dose per gram of tissue (% ID/g).

### 4.5.3 Statistical Analysis

Statistical analysis and nonlinear regression were performed using GraphPad Prism 9 (GraphPad software, San Diego, CA, USA), and a Mann–Whitney test was used to compare medians between groups. Data were reported as mean ± SEM (standard error of mean) for at least three independent replicates.

## 5. Conclusions

Our manuscript reported a successful synthesis of two long-acting JR11 analogs for improved radionuclide therapy of NETs. Radiolabeling of both analogs with lutetium-177 was achieved with very high RCYs and RCPs. Both radiopeptides showed excellent stability in PBS and mouse serum, conserved their hydrophilic behavior, and exhibited good binding to human albumin. Compounds **8a** and **8b** showed good binding affinity towards SSTR2, high cell uptake, and low internalization rate. [$^{177}$Lu]Lu-**8a** demonstrated extended residence in the blood, higher kidney uptake, and nonspecific tumor accumulation compared to [$^{177}$Lu]Lu-JR11. Unfortunately, [$^{177}$Lu]Lu-**8b** did not show any tumor uptake despite the high potential of the 4-(*p*-methoxyphenyl)butyryl ABD. Although insertion of a 4-(*p*-iodophenyl)butyryl ABD into JR11 improved its blood circulation, as expected, we also noticed high uptake in non-target organs with [$^{177}$Lu]Lu-**8a**. Therefore, further optimization is required to combine an ABD and JR11 to obtain a long-acting

SSTR2 antagonist with an adequate biodistribution and pharmacokinetic profile for safe and efficient radionuclide therapy of neuroendocrine tumors.

**Supplementary Materials:** The following supporting information can be downloaded at: https:// www.mdpi.com/article/10.3390/ph15091155/s1, Figure S1: HPLC chromatograms of (A) compound **8a** and (B) compound **8b**; Figure S2: Mass spectra of (A) compound **8a** and (B) compound **8b**; Figure S3: Radio-HPLC chromatograms of (A) [$^{177}$Lu]Lu-**8a** and (B) [$^{177}$Lu]Lu-**8b**; Figure S4: Radio-HPLC chromatograms of the stability studies performed for [$^{177}$Lu]Lu-**8a** at 1, 4, and 24 h post-incubation at 37 °C of the radioligand in (A) PBS and (B) mouse serum; Figure S5: Radio-HPLC chromatograms of the stability studies performed for [$^{177}$Lu]Lu-**8b** at 1, 4, and 24 h post incubation at 37 °C of the radioligand in (A) PBS and (B) mouse serum; Figure S6: $IC_{50}$ curves of the in vitro competitive binding assays for compounds **8a** and **8b** in increasing concentrations (M) with [$^{177}$Lu]Lu-JR11 as radioligand; Table S1: Ex vivo biodistribution analysis of [$^{177}$Lu]Lu-**8a** (5 MBq/0.5 nmol) at 4, 24, 48, and 72 h post-injection (n = 4 mice/group). Data are represented as percentage of injected dose per gram of tissue (% ID/g); Table S2: Ex vivo biodistribution analysis of [$^{177}$Lu]Lu-JR11 (5 MBq/0.5 nmol) at 4, 24, 48, and 72 h post-injection (n = 4 mice/group). Data are represented as percentage of injected dose per gram of tissue (% ID/g).

**Author Contributions:** Conceptualization, Y.S., J.N., and M.d.J.; methodology, Y.S.; software, S.K. and M.H.; validation, S.K. and M.H.; formal analysis, S.K., M.H., C.d.R., D.S., and S.B.; investigation, Y.S.; resources, Y.S., J.N., and M.d.J.; data curation, S.K. and M.H.; writing—original draft preparation, S.K. and M.H.; writing—review and editing, S.K., M.H., C.d.R., D.S., S.B., J.N., and Y.S.; visualization, Y.S.; supervision, J.N. and Y.S.; project administration, Y.S.; funding acquisition, Y.S. All authors have read and agreed to the published version of the manuscript.



**Funding:** This research was funded by the Dutch Cancer Society (KWF), grant number 12259.



**Institutional Review Board Statement:** The study was conducted according to the guidelines of the Declaration of Helsinki and approved by the Animal Welfare Committee of the Erasmus MC and was conducted in agreement with institutional guidelines (license number: AVD101002017867, 28 September 2017).

**Informed Consent Statement:** Not applicable.

**Data Availability Statement:** Data is contained within the article and supplementary material.

**Acknowledgments:** The authors are grateful to the Dutch Cancer Society (KWF) for the financial support (grant 12259/2019-1) and the department of Radiology and Nuclear Medicine at the Erasmus MC for technical assistance. All Imaging experiments were conducted at the Applied Molecular Imaging Erasmus MC core facility (AMIE).

**Conflicts of Interest:** The authors declare no conflict of interest.

## References


1. Hennrich, U.; Kopka, K. Lutathera®: The first FDA-and EMA-approved radiopharmaceutical for peptide receptor radionuclide therapy. Pharmaceuticals 2019, 12, 114.
2. Strosberg, J.; El-Haddad, G.; Wolin, E.; Hendifar, A.; Yao, J.; Chasen, B.; Mittra, E.; Kunz, P.L.; Kulke, M.H.; Jacene, H.; et al. Phase 3 Trial of 177 Lu-Dotatate for Midgut Neuroendocrine Tumors. N. Engl. J. Med. 2017, 376, 125–135.
3. Fani, M.; Nicolas, G.P.; Wild, D. Somatostatin receptor antagonists for imaging and therapy. J. Nucl. Med. 2017, 58, 61S–66S.
4. Nicolas, G.P.; Schreiter, N.; Kaul, F.; Uiters, J.; Bouterfa, H.; Kaufmann, J.; Erlanger, T.E.; Cathomas, R.; Christ, E.; Fani, M.; et al. Sensitivity comparison of 68 Ga-OPS202 and 68 Ga-DOTATOC PET/CT in patients with gastroenteropancreatic neuroendocrine tumors: A prospective phase II imaging study. J. Nucl. Med. 2018, 59, 915–921.
5. Cescato, R.; Waser, B.; Fani, M.; Reubi, J.C. Evaluation of 177Lu-DOTA-sst 2 antagonist versus 177Lu-DOTA-sst 2 agonist binding in human cancers in vitro. J. Nucl. Med. 2011, 52, 1886–1890.
6. Wild, D.; Fani, M.; Behe, M.; Brink, I.; Rivier, J.E.F.; Reubi, J.C.; Maecke, H.R.; Weber, W.A. First clinical evidence that imaging with somatostatin receptor antagonists is feasible. J. Nucl. Med. 2011, 52, 1412–1417.
7. Fani, M.; Braun, F.; Waser, B.; Beetschen, K.; Cescato, R.; Erchegyi, J.; Rivier, J.E.; Weber, W.A.; Maecke, H.R.; Reubi, J.C. Unexpected sensitivity of sst 2 antagonists to N-terminal radiometal modifications. J. Nucl. Med. 2012, 53, 1481–1489.
8. Nicolas, G.P.; Mansi, R.; McDougall, L.; Kaufmann, J.; Bouterfa, H.; Wild, D.; Fani, M. Biodistribution, pharmacokinetics, and dosimetry of 177Lu-,90Y-, and 111In-labeled somatostatin receptor antagonist OPS201 in comparison to the agonist 177Lu-DOTATATE: The mass effect. J. Nucl. Med. 2017, 58, 1435–1441.
9. Lau, J.; Rousseau, E.; Kwon, D.; Lin, K.S.; Bénard, F.; Chen, X. Insight into the development of PET radiopharmaceuticals for oncology. Cancers 2020, 12, 1312.
10. Brandt, F.; Ullrich, M.; Laube, M.; Kopka, K.; Bachmann, M.; Löser, R.; Pietzsch, J.; Pietzsch, H.-J.; van den Hoff, J.; Wodtke, R. “Clickable” Albumin Binders for Modulating the Tumor Uptake of Targeted Radiopharmaceuticals. J. Med. Chem. 2022, 65, 710–733.
11. Tian, R.; Jacobson, O.; Niu, G.; Kiesewetter, D.O.; Wang, Z.; Zhu, G.; Ma, Y.; Liu, G.; Chen, X. Evans blue attachment enhances somatostatin receptor subtype-2 imaging and radiotherapy. Theranostics 2018, 8, 735–745.
12. van Tiel, S.; Maina, T.; Nock, B.; Konijnenberg, M.; de Blois, E.; Seimbille, Y.; Bernsen, M.; de Jong, M. Albutate-1, a Novel Long-Circulating Radiotracer Targeting the Somatostatin Receptor Subtype 2. J. Nucl. Med. Radiat. Sci. 2021, 2, 1–9.
13. Kuo, H.T.; Lin, K.S.; Zhang, Z.; Uribe, C.F.; Merkens, H.; Zhang, C.; Benard, F. 177Lu-labeled albumin-binder-conjugated PSMA-targeting agents with extremely high tumor uptake and enhanced tumor-to-kidney absorbed dose ratio. J. Nucl. Med. 2021, 62, 521–527.
14. Müller, C.; Struthers, H.; Winiger, C.; Zhernosekov, K.; Schibli, R. DOTA conjugate with an albumin-binding entity enables the first folic acid-targeted 177Lu-radionuclide tumor therapy in mice. J. Nucl. Med. 2013, 54, 124–131.
15. Arujõe, M.; Ploom, A.; Mastitski, A.; Järv, J. Comparison of various coupling reagents in solid-phase aza-peptide synthesis. Tetrahedron Lett. 2017, 58, 3421–3425.
16. Santini, C.; Kuil, J.; Bunschoten, A.; Pool, S.; De Blois, E.; Ridwan, Y.; Essers, J.; Bernsen, M.R.; Van Leeuwen, F.W.B.; De Jong, M. Evaluation of a fluorescent and radiolabeled hybrid somatostatin analog in vitro and in mice bearing H69 neuroendocrine xenografts. J. Nucl. Med. 2016, 57, 1289–1295.
17. de Blois, E.; Chan, H.S.; de Zanger, R.; Konijnenberg, M.; Breeman, W.A.P. Application of single-vial ready-for-use formulation of 111In- or 177Lu-labelled somatostatin analogs. Appl. Radiat. Isot. 2014, 85, 28–33.
18. Rylova, S.N.; Stoykow, C.; Del Pozzo, L.; Abiraj, K.; Tamma, M.L.; Kiefer, Y.; Fani, M.; Maecke, H.R. The somatostatin receptor 2 antagonist 64Cu-NODAGA-JR11 outperforms 64Cu-DOTA-TATE in a mouse xenograft model. PLoS ONE 2018, 13, e0195802.

19. Smit Duijzentkunst, D.A.; Kwekkeboom, D.J.; Bodei, L. Somatostatin receptor 2-targeting compounds. J. Nucl. Med. 2017, 58, 54S–60S.
20. Ginj, M.; Zhang, H.; Waser, B.; Cescato, R.; Wild, D.; Wang, X.; Erchegyi, J.; Rivier, J.; Mäcke, H.R.; Reubi, J.C. Radiolabeled somatostatin receptor antagonists are preferable to agonists for in vivo peptide receptor targeting of tumors. Proc. Natl. Acad. Sci. USA 2006, 103, 16436–16441.
21. Dalm, S.U.; Nonnekens, J.; Doeswijk, G.N.; De Blois, E.; Van Gent, D.C.; Konijnenberg, M.W.; De Jong, M. Comparison of the therapeutic response to treatment with a 177Lu-labeled somatostatin receptor agonist and antagonist in preclinical models. J. Nucl. Med. 2016, 57, 260–265.
22. Zhang, H.; Desai, P.; Koike, Y.; Houghton, J.; Carlin, S.; Tandon, N.; Touijer, K.; Weber, W.A. Dual-modality imaging of prostate cancer with a fluorescent and radiogallium-labeled gastrin-releasing peptide receptor antagonist. J. Nucl. Med. 2017, 58, 29–35.
23. Li, D.; Zhang, J.; Chi, C.; Xiao, X.; Wang, J.; Lang, L.; Ali, I.; Niu, G.; Zhang, L.; Tian, J.; et al. First-in-human study of PET and optical dual-modality image-guided surgery in glioblastoma using 68Ga-IRDye800CW-BBN. Theranostics 2018, 8, 2508–2520.
24. Handula, M.; Verhoeven, M.; Chen, K.; Haeck, J.; De Jong, M.; Dalm, S.U.; Seimbille, Y. Towards Complete Tumor Resection: Novel Dual-Modality Probes for Improved Image-Guided Surgery of GRPR-Expressing Prostate Cancer. Pharmaceutics 2022, 14, 195.
25. Rousseau, E.; Lau, J.; Zhang, Z.; Uribe, C.F.; Kuo, H.T.; Zhang, C.; Zeisler, J.; Colpo, N.; Lin, K.S.; Bénard, F. Effects of adding an albumin binder chain on [177Lu]Lu-DOTATATE. Nucl. Med. Biol. 2018, 66, 10–17.
26. Kuo, H.T.; Merkens, H.; Zhang, Z.; Uribe, C.F.; Lau, J.; Zhang, C.; Colpo, N.; Lin, K.S.; Bénard, F. Enhancing Treatment Efficacy of 177Lu-PSMA-617 with the Conjugation of an Albumin-Binding Motif: Preclinical Dosimetry and Endoradiotherapy Studies. Mol. Pharm. 2018, 15, 5183–5191.
27. Umbricht, C.A.; Benešová, M.; Schibli, R.; Müller, C. Preclinical Development of Novel PSMA-Targeting Radioligands: Modulation of Albumin-Binding Properties to Improve Prostate Cancer Therapy. Mol. Pharm. 2018, 15, 2297–2306.
28. Benešová, M.; Umbricht, C.A.; Schibli, R.; Müller, C. Albumin-Binding PSMA Ligands: Optimization of the Tissue Distribution Profile. Mol. Pharm. 2018, 15, 934–946.
29. Chigoho, D.M.; Bridoux, J.; Hernot, S. Reducing the renal retention of low- to moderate-molecular-weight radiopharmaceuticals. Curr. Opin. Chem. Biol. 2021, 63, 219–228.
30. Huynh, T.T.; Sreekumar, S.; Mpoy, C.; Rogers, B.E. Therapeutic Efficacy of177Lu-Labeled A20FMDV2 Peptides Targeting αvβ6. Pharmaceuticals 2022, 15, 229.

## Supplemental Information

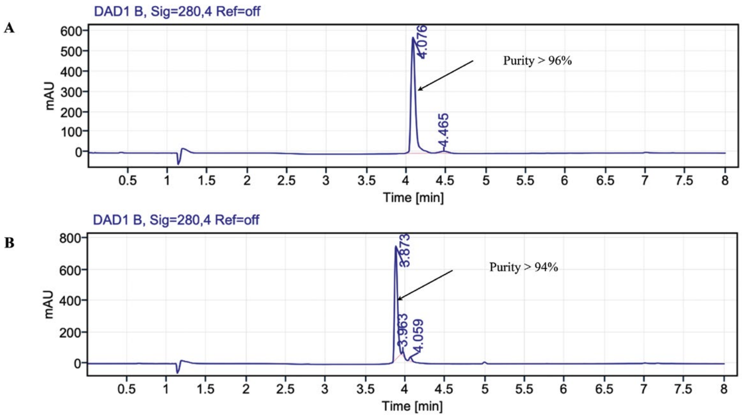


**Figure S1.** HPLC chromatograms of A) compound **8a** and B) compound **8b**.

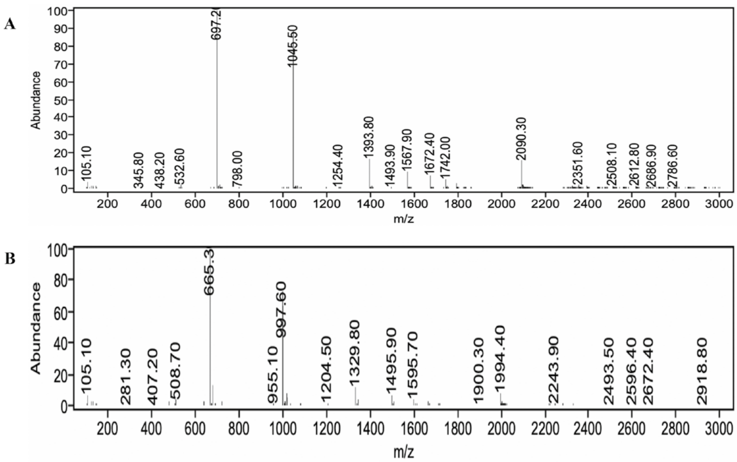


**Figure S2.** Mass spectra of A) compound **8a** and B) compound **8b**.

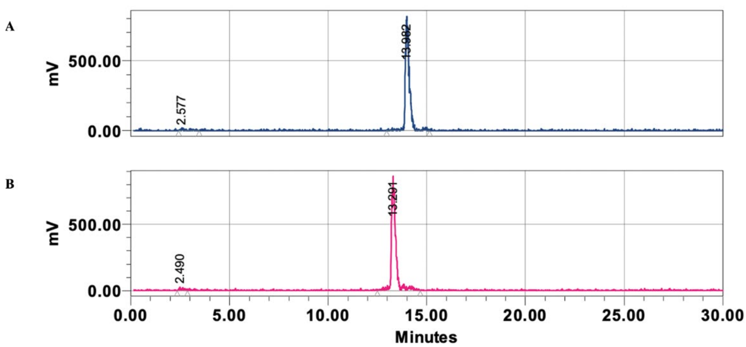


**Figure S3.** Radio-HPLC chromatograms of A) [$^{177}$Lu]Lu-**8a** and B) [$^{177}$Lu]Lu-**8b**.

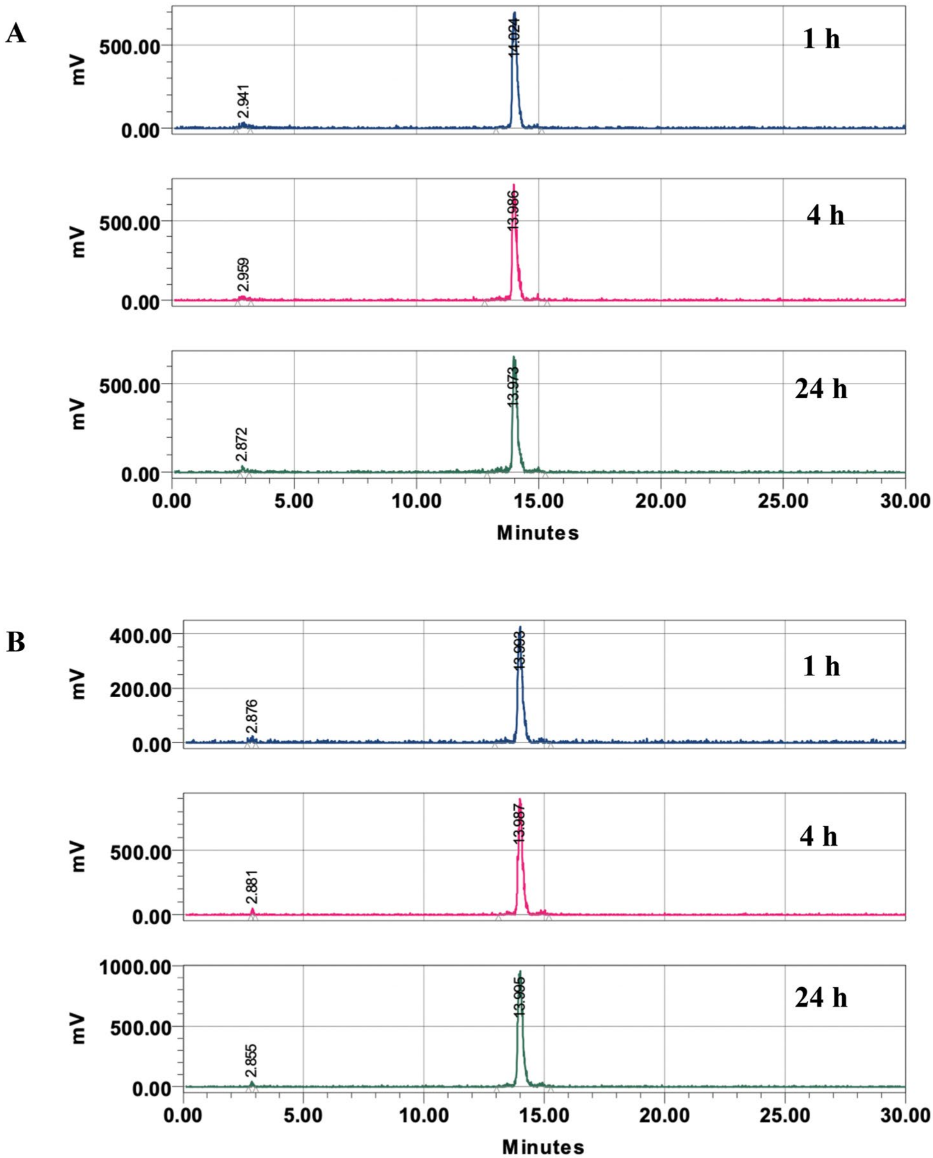


**Figure S4.** Radio-HPLC chromatograms of the stability studies performed for [$^{177}$Lu]Lu-**8a** at 1 h, 4 h and 24 h post incubation at 37 °C of the radioligand in A) PBS and B) mouse serum.

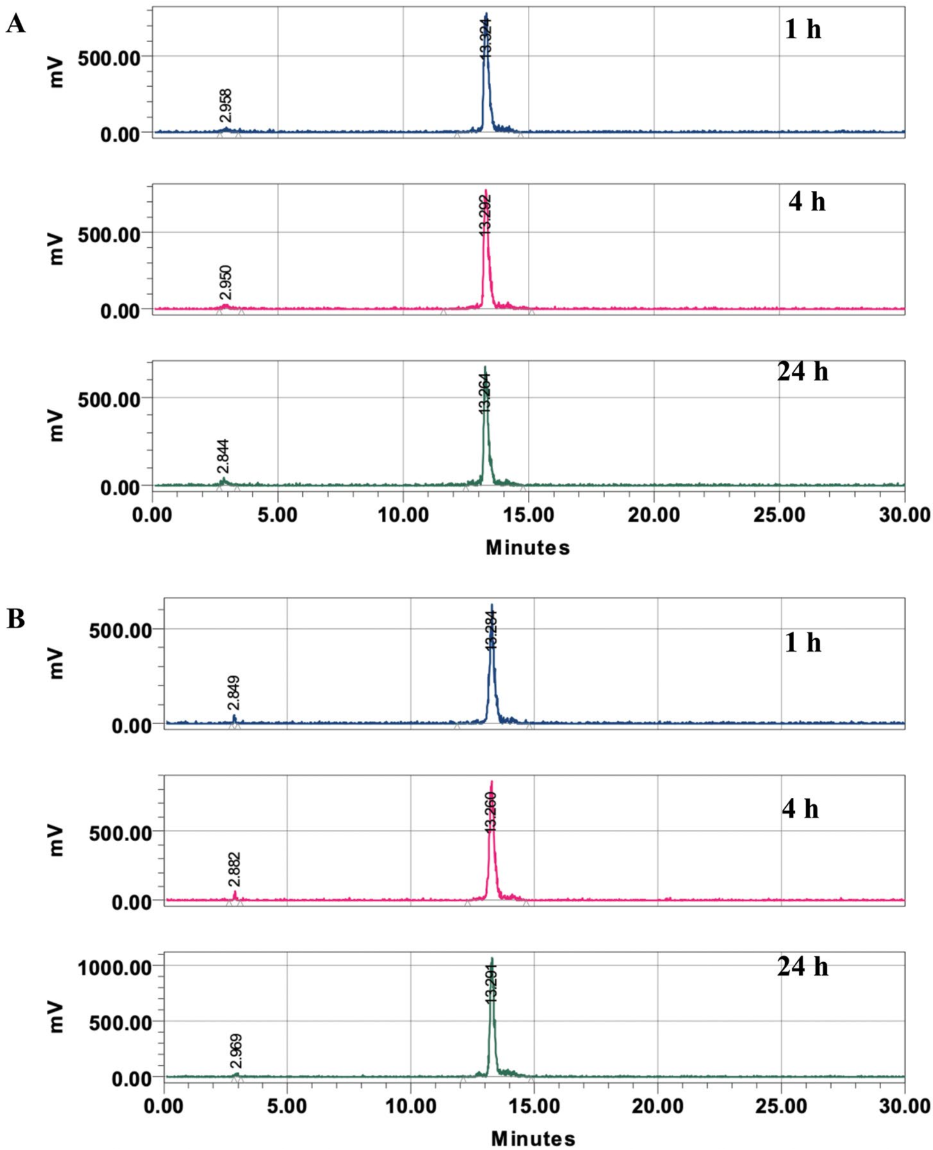




**Figure S5.** Radio-HPLC chromatograms of the stability studies performed for [$^{177}$Lu]Lu-**8b** at 1 h, 4 h and 24 h post incubation at 37 °C of the radioligand in A) PBS and B) mouse serum.

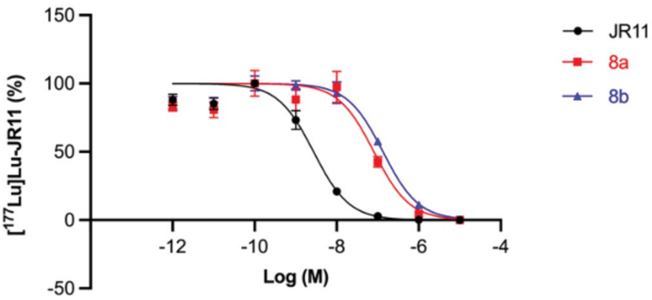


**Figure S6.** $IC_{50}$ curves of the *in vitro* competition binding assay for compounds **8a** and **8b** in increasing concentrations (M) while [$^{177}$Lu]Lu-JR11 was used as radioligand.

**Table S1.** *Ex vivo* biodistribution analysis of [$^{177}$Lu]Lu-**8a** (5 MBq/0.5 nmol) at 4, 24, 48 and 72 h post-injection (n = 4 mice/group). Data is represented as percentage of injected dose per gram of tissue (% ID/g).

| Organ | 4 h | 24 h | 24 h - Block | 48 h | 72 h |
|---|---|---|---|---|---|
| **Blood** | 21.3 ± 1.1 | 18.1 ± 4.2 | 14.9 ± 2.1 | 12.9 ± 1.2 | 8.6 ± 0.5 |
| **Tumor** | 4.1 ± 0.5 | 6.5 ± 0.2 | 5.2 ± 0.6 | 7.3 ± 0.4 | 7.3 ± 0.9 |
| **Heart** | 7.6 ± 1.2 | 5.1 ± 0.7 | 5.1 ± 0.6 | 4.8 ± 0.5 | 3.9 ± 0.7 |
| **Lung** | 9.9 ± 2.9 | 7.5 ± 0.6 | 5.4 ± 0.6 | 7.2 ± 0.3 | 6.0 ± 0.5 |
| **Liver** | 4.6 ± 1.2 | 3.7 ± 0.2 | 2.9 ± 0.5 | 3.6 ± 0.2 | 2.9 ± 0.3 |
| **Spleen** | 3.2 ± 0.7 | 3.8 ± 0.4 | 3.6 ± 0.6 | 5.8 ± 0.6 | 5.4 ± 0.2 |
| **Stomach** | 3.8 ± 0.4 | 3.1 ± 1.4 | 1.7 ± 0.4 | 3.3 ± 1.2 | 3.0 ± 0.5 |
| **Intestine** | 2.5 ± 0.2 | 1.7 ± 0.1 | 1.3 ± 0.2 | 1.4 ± 0.1 | 1.1 ± 0.0 |
| **Pancreas** | 7.2 ± 0.3 | 6.6 ± 0.3 | 2.4 ± 0.4 | 6.3 ± 0.7 | 5.3 ± 1.2 |
| **Kidneys** | 9.6 ± 1.2 | 18.4 ± 1.9 | 19.7 ± 1.4 | 22.6 ± 1.9 | 21.6 ± 1.4 |
| **Muscle** | 0.8 ± 1.1 | 1.1 ± 0.1 | 0.8 ± 0.1 | 1.2 ± 0.5 | 0.8 ± 0.1 |
| **Skin** | 5.9 ± 1.1 | 5.4 ± 0.9 | 3.2 ± 1.2 | 6.3 ± 1.6 | 4.8 ± 0.3 |
| **Bone** | 1.3 ± 1.8 | 1.5 ± 1.1 | 1.5 ± 0.3 | 0.9 ± 0.4 | 1.2 ± 1.0 |
| **Bone Marrow** | 1.2 ± 2.0 | -0.2 ± 0.1 | -0.8 ± 1.7 | -0.3 ± 0.1 | -0.1 ± 0.1 |

**Table S2.** *Ex vivo* biodistribution analysis of [$^{177}$Lu]Lu-JR11 (5 MBq/0.5 nmol) at 4, 24, 48 and 72 h post-injection (n = 4 mice/group). Data is represented as percentage of injected dose per gram of tissue (% ID/g).

| Organ | 4 h | 24 h | 24 h - Block | 48 h | 72 h |
|---|---|---|---|---|---|
| **Blood** | -0.1 ± 0.0 | -0.1 ± 0.1 | -0.1 ± 0.1 | 0.0 ± 0.0 | -0.1 ± 0.0 |
| **Tumor** | 8.4 ± 0.5 | 6.1 ± 0.5 | 0.4 ± 0.0 | 4.6 ± 0.3 | 3.6 ± 0.4 |
| **Heart** | 0.0 ± 0.0 | 0.0 ± 0.0 | 0.0 ± 0.0 | 0.0 ± 0.0 | -0.1 ± 0.0 |
| **Lung** | 1.3 ± 0.3 | 0.4 ± 0.0 | 0.1 ± 0.0 | 0.2 ± 0.0 | 0.1 ± 0.0 |
| **Liver** | 0.5 ± 0.0 | 0.3 ± 0.0 | 0.3 ± 0.0 | 0.2 ± 0.0 | 0.2 ± 0.0 |
| **Spleen** | 0.3 ± 0.1 | 0.1 ± 0.0 | 0.0 ± 0.0 | 0.0 ± 0.0 | 0.0 ± 0.0 |
| **Stomach** | 1.7 ± 0.3 | 1.5 ± 1.2 | 0.1 ± 0.1 | 0.6 ± 0.2 | 0.4 ± 0.1 |
| **Intestine** | 0.5 ± 0.1 | 0.2 ± 0.0 | 0.1 ± 0.0 | 0.1 ± 0.0 | 0.1 ± 0.0 |
| **Pancreas** | 3.5 ± 0.4 | 0.9 ± 0.3 | 0.1 ± 0.0 | 0.6 ± 0.1 | 0.3 ± 0.0 |
| **Kidneys** | 12.6 ± 1.2 | 8.6 ± 2.3 | 5.9 ± 1.2 | 4.1 ± 0.2 | 3.4 ± 1.4 |
| **Muscle** | -0.1 ± 0.0 | -0.1 ± 0.0 | -0.1 ± 0.0 | -0.1 ± 0.0 | -0.1 ± 0.0 |
| **Skin** | 0.3 ± 0.1 | 0.0 ± 0.1 | -0.1 ± 0.1 | -0.2 ± 0.1 | -0.4 ± 0.2 |
| **Bone** | 0.1 ± 0.0 | -0.6 ± 0.4 | -0.4 ± 0.5 | -0.2 ± 0.2 | -0.1 ± 0.1 |
| **Bone Marrow** | 1.1 ± 2.0 | 0.1 ± 0.0 | 0.2 ± 0.0 | 0.1 ± 0.0 | 0.1 ± 0.0 |

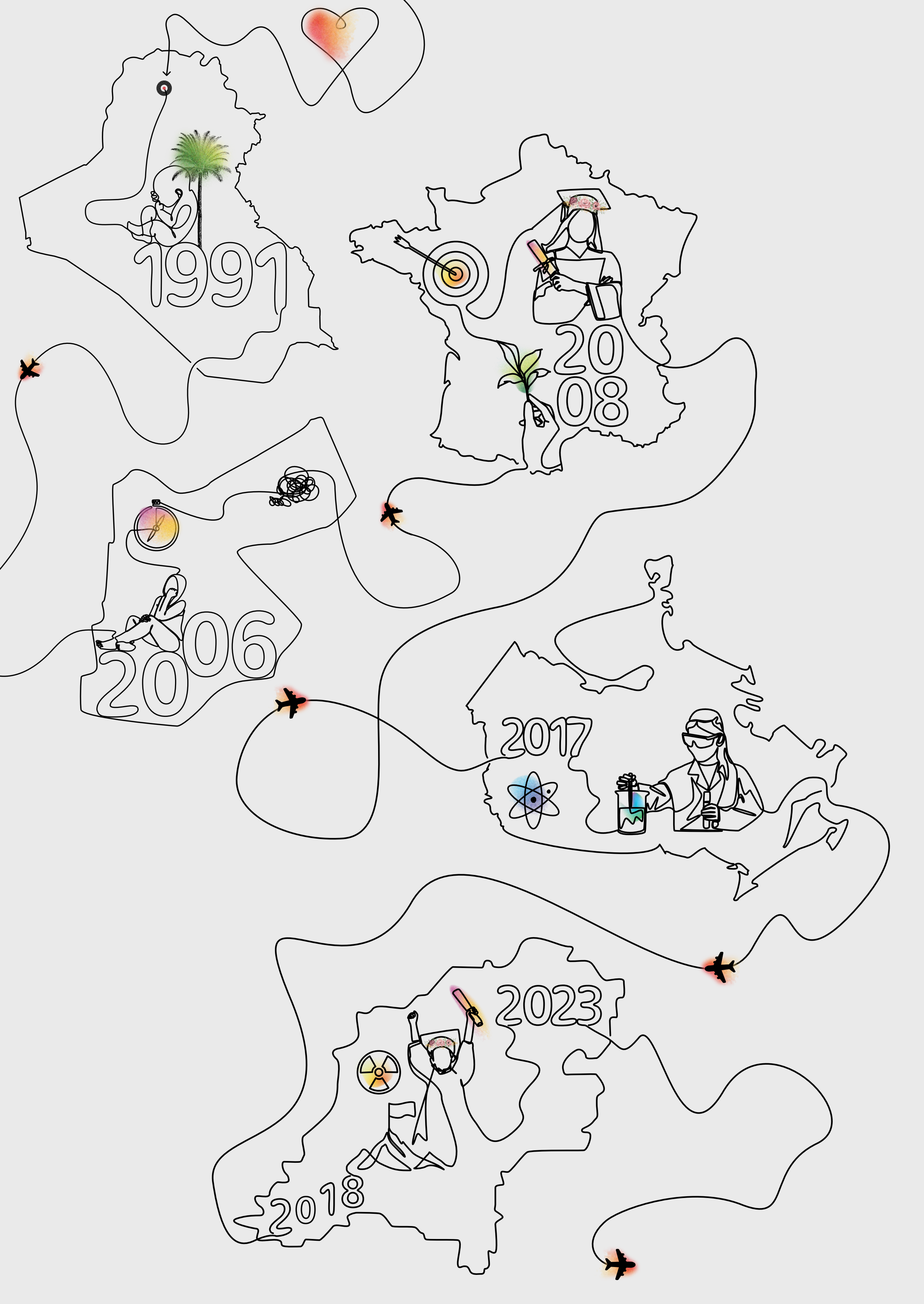
1991
2008
2006
2017
2023
2018

# CHAPTER 7

## First Preclinical Evaluation of $[^{225}Ac]$Ac-DOTA-JR11 and Comparison With $[^{177}Lu]$Lu-DOTA-JR11, Alpha Versus Beta Radionuclide Therapy of NETs

Maryana Handula[1]. Savanne Beekman[1]. Mark Konijnenberg[1]. Debra Stuurman[1,2]. Corrina de Ridder[1,2]. Frank Bruchertseifer[3]. Alfred Morgenstern[3]. Antonia Denkova[4]. Erik de Blois[1]. Yann Seimbille[1,5]

[1] Department of Radiology and Nuclear Medicine, Erasmus MC Cancer Institute, Erasmus University Medical Center, 3015 GD Rotterdam, The Netherlands
[2] Department of Experimental Urology, Erasmus University Medical Center, 3015 GD Rotterdam, The Netherlands
[3] European Commission, Join Research Centre, 76344 Karlsruhe, Germany
[4] Applied Radiation and Isotopes, Department of Radiation Science and Technology, Faculty of Applied Sciences, Delft University of Technology, Delft, the Netherlands
[5] Life Sciences Division, TRIUMF, Vancouver, BC V6T 2A3, Canada

*EJNMMI Radiopharmacy and Chemistry. 2023;8(13):1-16*

## Abstract

**Background:** The [$^{177}$Lu]Lu-DOTA-TATE mediated peptide receptor radionuclide therapy (PRRT) of neuroendocrine tumors (NETs) can sometimes lead to treatment resistance and disease recurrence. An interesting alternative could be the somatostatin antagonist, [$^{177}$Lu]Lu-DOTA-JR11, that demonstrated better biodistribution profile and higher tumor uptake than [$^{177}$Lu]Lu-DOTA-TATE. Furthermore, treatment with alpha emitters showed improvement of the therapeutic index of PRRT due to the high LET offered by the alpha particles compared to beta emitters. Therefore, [$^{225}$Ac]Ac-DOTA-JR11 can be a potential candidate to improve the treatment of NETs. DOTA-JR11 was radiolabeled with [$^{225}$Ac]Ac($NO_3$)$_3$ and [$^{177}$Lu]Lu$Cl_3$. Stability studies were performed in phosphate buffered saline (PBS) and mouse serum. In vitro competitive binding assay was carried out in U2OS-SSTR2+ cells for $^{nat}$La-DOTA-JR11, $^{nat}$Lu-DOTA-JR11 and DOTA-JR11. Ex vivo biodistribution studies were performed in mice inoculated with H69 cells at 4, 24, 48 and 72 h after injection of [$^{225}$Ac]Ac-DOTA-JR11. A blocking group was included to verify uptake specificity. Dosimetry of selected organs was determined using the OLINDA phantom and MIRD S-values for [$^{225}$Ac]Ac-DOTA-JR11 and [$^{177}$Lu]Lu-DOTA-JR11.

**Results:** [$^{225}$Ac]Ac-DOTA-JR11 was successfully prepared and obtained in high radiochemical yield (RCY; 95%) and radiochemical purity (RCP; 94%). [$^{225}$Ac]Ac-DOTA-JR11 showed reasonably good stability in PBS (77% intact radiopeptide at 24 h after incubation) and in mouse serum (~81% intact radiopeptide 24 h after incubation). [$^{177}$Lu]Lu-DOTA-JR11 demonstrated excellent stability in both media (> 93%) up to 24 h post incubation. Competitive binding assay revealed that complexation of DOTA-JR11 with $^{nat}$La and $^{nat}$Lu did not affect its binding affinity to SSTR2. Similar biodistribution profiles were observed for both radiopeptides, however, higher uptake was noticed in the kidneys, liver and bone for [$^{225}$Ac]Ac-DOTA-JR11 than [$^{177}$Lu]Lu-DOTA-JR11.

**Conclusion:** [$^{225}$Ac]Ac-DOTA-JR11 showed a higher absorbed dose in the kidneys compared to [$^{177}$Lu]Lu-DOTA-JR11, which may limit further studies with this radiopeptide. However, several strategies can be explored to reduce nephrotoxicity and offer opportunities for future clinical investigations with [$^{225}$Ac]Ac-DOTA-JR11.

**Keywords**. SSTR2, DOTA-JR11, actinium-225, lutetium-177, Radionuclide Therapy

## Background

Neuroendocrine tumors (NETs) are an indolent and well-differentiated type of neuroendocrine neoplasms (NENs) [1,2]. Most commonly appearing in the gastroenteropancreatic (GEP) system, those malignancies are remaining rare (worldwide, 35 out of 100,000 people are diagnosed yearly) [3,4]. NETs are known to express 5 subtypes of somatostatin receptor (SSTR 1-5) [5]. However, the high expression of SSTR2 by NETs makes it an ideal target for imaging and therapy [6–9]. SSTR2-mediated peptide receptor radionuclide therapy (PRRT) has been widely employed for the treatment of NETs. Many studies using either somatostatin agonists (e.g., DOTA-TATE and DOTA-TOC) or antagonists (e.g., DOTA-JR11 and DOTA-LM3) were reported [10–12]. [$^{177}$Lu]Lu-DOTA-TATE (Lutathera®) was recently approved by the Food and Drug Administration (FDA) as the first radiopharmaceutical for the treatment of GEP-NETs. PRRT of NETs using [$^{177}$Lu]Lu-DOTA-TATE showed positive outcomes by increasing the overall survival and improving the quality of life of the patients [13,14]. However, treatment resistance of NETs indicates that PRRT became less effective due to upregulated DNA damage repair [15,16].

Several studies reported that DOTA-JR11 exhibited lower binding affinity to SSTR2 compared to DOTA-TATE [17–19]. However, preclinical and clinical studies revealed a higher tumor uptake with the antagonist, due to its ability to bind to more binding sites on the receptor than the agonist [20,21]. Nevertheless, Reidy-Lagunes et al. reported an increased hematologic toxicity with [$^{177}$Lu]Lu-DOTA-JR11 in comparison to [$^{177}$Lu]Lu-DOTA-TATE [22]. Nevertheless, it was found that DOTA-JR11 is a promising SSTR2-antagonist for targeted radionuclide therapy of NETs. Recently, targeted alpha therapy (TAT) demonstrated to be more effective than the standard PRRT, due to the high linear energy transfer (LET) offered by the alpha particles compared to beta emitters (80 – 100 vs. 0.1 – 1.0 keV/µm, respectively) [23–25]. In fact, it was confirmed that alpha particles can induce more DNA damage compared to beta emitters, hence leading to more cell death [26,27]. Furthermore, unlike PRRT where hypoxia can lead to treatment resistance, the use of alpha radiation does not require the presence of oxygen to create effective DNA damage. Thus, several alpha particles-emitters were introduced as good candidates for TAT (e.g., bismuth-213, lead-212). However, actinium-225 has gained a lot of attention due to its long half-life ($t_{1/2}$ = 9.92 days) and interesting decay chain offering 4 alpha particles [28,29].

Thus, we report herein optimized radiolabeling conditions using various quenchers (e.g., gentisic/ascorbic acids, ethanol and L-melatonin) to reduce or prevent radiolysis. Due to the high LET of alpha particles, different studies reported the instability of biomolecules to alpha radiation. Therefore, we evaluated the stability of [$^{225}$Ac]Ac-DOTA-JR11 towards radiolysis in PBS buffer and enzymatic degradation in mouse serum. Chemical modifications performed at the *N*-terminal of DOTA-JR11 were previously reported to affect the binding affinity of the peptide to SSTR2. Therefore, we evaluated the influence of metal complexation with different nuclides on SSTR2 binding affinity. Furthermore, preclinical evaluation of [$^{225}$Ac]Ac-DOTA-JR11 in tumor bearing mice was carried out. The pharmacokinetic and biodistribution profiles of [$^{225}$Ac]Ac-DOTA-JR11 were compared to the previously published data for [$^{177}$Lu]Lu-DOTA-JR11. Besides, we performed dosimetry studies to compare the therapeutic efficacy of [$^{225}$Ac]Ac-DOTA-JR11 and [$^{177}$Lu]Lu-DOTA-JR11. Murine dosimetry calculations were performed using the OLINDA phantom and MIRD S-values.

## Materials and methods

### *General information*

The chemicals and solvents were purchased from commercial suppliers and used without further purification. Lanthanum (III) chloride hydrate (99.9%) and lutetium (III) chloride (99.9%) were purchased from Sigma Aldrich (Amsterdam, The Netherlands) and abcr (Karlsruhe, Germany), respectively. Lutetium-177 (non-carrier added, [$^{177}$Lu]$LuCl_3$) with a specific activity of 4081 GBq/mg, was purchased from ITM (München, Germany). Actinium-225, with a specific activity of 2150 GBq/mg, was provided by the Joint Research Centre (JRC, Karlsruhe, Germany). [$^{111}$In]$InCl_3$ (370.0 MBq/mL in HCl, pH 1.5–1.9) was provided by Curium (Petten, The Netherlands). High-performance liquid chromatography (HPLC) and mass spectrometry (MS) were carried out on a LC/MS 1260 Infinity II system from Agilent (Middelburg, The Netherlands). Analyses were performed on an analytical column (Poroshell 120, EC-C18, 2.7 µm, 3.0 × 100 mm) from Agilent with a gradient elution of acetonitrile (ACN) (5% to 100% in $H_2O$, containing 0.1% formic acid) at a flow rate of 0.5 mL/min over 8 min. Purification of the complexed DOTA-JR11 peptides was carried out on a preparative HPLC 1290 Infinity II system from Agilent using a preparative Agilent 5 Prep C18 column (50 × 21.2 mm, 5 µm). Both compounds were purified using a gradient elution of ACN (10% to 95% in $H_2O$, containing 0.1% formic acid) at a flow rate of 10 mL/min over 10 min. Instant thin-layer chromatography on silica-gel-impregnated glass fiber iTLC-SG sheets (Agilent; Folsom, CA, USA) were eluted with sodium citrate (0.1 M, pH 5). The radioactive samples used to determine the radiochemical yield (RCY), radiochemical purity (RCP) and in vivo studies were counted using a Wizard 2480 gamma counter (Perkin Elmer; Waltham, MA, USA). Quality control of [$^{225}$Ac]Ac-DOTA-JR11 and analysis of its stability were carried out on a HPLC Alliance system from Waters (Etten-Leur, The Netherlands) equipped with a diode array detector, a Canberra Osprey multichannel analyzer (Zelik, Belgium), and an analytical C18 Symmetry® column (Waters; 250.0 × 4.6 mm, 5 µm) eluted with a gradient of methanol (0 to 100% in $H_2O$, containing 0.1%

trifluoroacetic acid) at a flowrate of 1 mL/min over 25 min. HPLC fractions (1 fraction/30 seconds) were collected using an automated fraction collector III from Waters (Etten-Leur, The Netherlands). Determination of the radioactivity in the fractions was performed using a Wizard 2480 gamma counter. The detector (thallium activated sodium iodide crystal) was calibrated for francium-221 energy window (186 – 226 keV) and each fraction was counted for 1 min [30]. Determination of the injected activity of [$^{225}$Ac]Ac-DOTA-JR11 for biodistribution studies was performed using High Purity Germanium (HPGe) detector from Miron Technologies Canberra (Olen, Belgium). Quality control of [$^{177}$Lu]Lu-DOTA-JR11 and analysis of its stability were carried out on an ultra-high performance liquid chromatography (UHPLC) Acquity Arc system from Waters equipped with a diode array detector, a Canberra Osprey multichannel analyzer, and an analytical C18 Gemini® column (250.0 × 4.6 mm, 5 µm) from Phenomenex (Torrance, CA, USA) eluted with a gradient of ACN (5 to 95% in $H_2O$, containing 0.1% trifluoroacetic acid) at a flowrate of 1 mL/min over 30 min.

***Chemistry***

Complexation of DOTA-JR11 with natural lanthanum and lutetium

DOTA-JR11 was synthesized as previously described [31,32]. $^{nat}$La and $^{nat}$Lu complexes were prepared using an excess (15 equiv.) of $^{nat}LaCl_3$ and $^{nat}LuCl_3$ in sodium acetate buffer (100 mM, pH 6) and DOTA-JR11 (2.36 µmol). The mixtures were incubated at 45 °C for 1 h. The complexed peptides were separated from the free metal ions by preparative-HPLC purification. $^{nat}$La-DOTA-JR11 was obtained as a white solid (3.0 mg, 70%). Analytical HPLC retention time of $^{nat}$La-DOTA-JR11: $t_R$ = 3.61 min (Fig. S1A), purity > 97%; ESI-MS: *m*/*z*, calculated: 1825.16, found: 913.50 $[M + 2H]^{2+}$ (Fig. S1B). $^{nat}$Lu-DOTA-JR11 was obtained as a white solid (3.0 mg, 68%). Analytical HPLC retention time of $^{nat}$Lu-DOTA-JR11: $t_R$ = 3.52 min (Fig. S1C), purity > 97%; ESI-MS: *m*/*z*, calculated: 1861.22, found: 931.50 $[M + 2H]^{2+}$ (Fig. S1D).

***Radiochemistry***

Actinium-225 radiolabeling of DOTA-JR11

[$^{225}$Ac]$Ac(NO_3)_3$ was obtained as a powder, and dissolved in 0.1 M hydrochloride acid (HCl) before use. DOTA-JR11 (10 nmol) was labeled at a molar activity of 50 kBq/nmol in a solution containing gentisic/ascorbic acids (10 µL, 50 mM), sodium acetate (1 µL, 2.5 M, pH 8), DOTA-JR11, ethanol (10 µL), MilliQ water (90.5 µL) supplemented with kolliphor® HS 15 (2.0 mg/mL), and [$^{225}$Ac]$Ac(NO_3)_3$ (2.16 µL, 500 kBq) (condition 1, Table 1). The radiolabeling mixture was incubated at 90 °C for 20 min. Diethylenetriaminepentaacetic acid (DTPA, 5 µL, 4 mM) was added after labeling to complex the free actinium-225. The radiochemical yield (RCY) was determined by instant thin-layer chromatography (iTLC). The iTLC strip was cut into pieces, which were counted in the gamma counter. To determine the radiochemical purity, 100 µL of [$^{225}$Ac]Ac-DOTA-JR11 (10 kBq) diluted in water containing Kolliphor® HS 15 (2.0 mg/mL) were injected into HPLC. Fractions were collected and counted in the gamma counter. The data collected from the iTLC strip or the HPLC fractions were presented as francium-221 counts per centimeter or fraction, respectively.

[$^{225}$Ac]Ac-DOTA-JR11 was prepared following two other radiolabeling conditions (conditions 2 and 3) at a molar activity of 100 kBq/nmol (Table 1). Radiolabeling of DOTA-JR11 was carried out in TRIS buffer containing the peptide (75 µL, 0.1 M, pH 9), $H_2O$ (10 µL), ascorbate buffer (50 µL, 1.0 M, pH 5.8) and [$^{225}$Ac]Ac($NO_3$)$_3$ dissolved in 0.1 M HCl. Radiolabeling was performed without (condition 2) or with (condition 3) L-melatonin (10 µL, 0.5 M). The labeling mixture (pH ~ 6) was heated at 90 °C for 20 min. The radiochemical yield and purity were determined by iTLC (Fig. S3) and radio-HPLC, respectively.

**Table 1:** Summary of the radiolabeling conditions.

| | Condition 1 | Condition 2 | Condition 3 |
|---|---|---|---|
| MilliQ water | | 10 µL | 10 µL |
| MilliQ water containing Kolliphor® HS 15 (2.0 mg/mL) | 90.5 µL | | |
| TRIS buffer containing the peptide (0.1 M, pH 9) | | 75 µL | 75 µL |
| Ascorbate buffer (1.0 M, pH 5.8) | | 50 µL | 50 µL |
| L-melatonin (0.5 M) | | | 10 µL |
| Gentisic/ascorbic acids (50 mM) | 10 µL | | |
| Sodium acetate (2.5 M, pH 8) | 1 µL | | |
| Ethanol | 10 µL | | |
| Molar activity | 50 kBq/nmol | 100 kBq/nmol | 100 kBq/nmol |
| DTPA (4 mM) | 5 µL | 5 µL | 5 µL |





Lutetium-177 and indium-111 radiolabeling of DOTA-JR11

[$^{177}$Lu]Lu$Cl_3$ was obtained as a 0.05 M hydrochloric acid aqueous solution. A total activity of 50 MBq of either [$^{177}$Lu]Lu$Cl_3$ or [$^{111}$In]In$Cl_3$ was added to DOTA-JR11 (1 nmol), gentisic/ascorbic acids (10 µL, 50 mM), sodium acetate (1 µL, 2.5 M, pH 8), and kolliphor® HS 15 in $H_2O$ (2.0 mg/mL, 60.8 µL) [33]. The mixture was incubated for 20 min at 90 °C and then left to cool down for 5 min. The RCY was determined by iTLC eluted with a solution of sodium citrate buffer (0.1 M, pH 5). DTPA (5 µL, 4 mM) was added to complex free lutetium-177 or indium-111. The RCP of [$^{177}$Lu]Lu-DOTA-JR11 was determined by radio-HPLC (Fig. S4).

Stability studies in PBS and mouse serum of [$^{225}$Ac]Ac-DOTA-JR11 and [$^{177}$Lu]Lu-DOTA-JR11

[$^{225}$Ac]Ac-DOTA-JR11 and [$^{177}$Lu]Lu-DOTA-JR11 (50 kBq and 1.2 MBq, respectively) were incubated in phosphate buffered saline (PBS; 500 and 200 µL, respectively) and mouse serum (Merck; Haarlerbergweg, The Netherlands) (250 and 100 µL, respectively) at 37

°C. The stability of [$^{225}$Ac]Ac-DOTA-JR11 was verified in PBS and mouse serum at 22 h, 24 h and 27 h after incubation at 37 °C for condition 1, 2 and 3, respectively. The stability of [$^{177}$Lu]Lu-DOTA-JR11 was monitored in PBS and mouse serum at 2 and 24 h post incubation. In mouse serum, the proteins were precipitated by adding an aliquot of the radiotracer to an equal volume of acetonitrile. The vial was vortexed vigorously and centrifuged for 20 min at 10,000 rpm. Stability studies were monitored by radio-HPLC (Fig. S5 and S6).

***In vitro evaluation of $^{nat}$La-DOTA-JR11 and $^{nat}$Lu-DOTA-JR11***

Cell line and culture

Human osteosarcoma cells (U2OS) transfected with SSTR2 receptor were used for the cell-based competitive binding assays. Cells were cultured in Dulbecco's modified Eagle's medium (DMEM) from Gibco (Paisley, UK) supplemented with 2 mM L-glutamine, 10% fetal bovine serum (FBS), 50 units/mL penicillin, and 50 µg/mL streptomycin (Sigma Aldrich; Haarlerbergweg, The Netherlands) and maintained at 37 °C and in a 5% $CO_2$ humidified chamber. Passages were performed weekly using trypsin/ethylenediaminetetraacetic acid (trypsin/EDTA) (0.05%/0.02% *w/v*).

Competition binding assay

Competitive binding experiments against [$^{111}$In]In-DOTA-JR11 were performed with DOTA-JR11, $^{nat}$La-DOTA-JR11 and $^{nat}$Lu-DOTA-JR11 in U2OS.SSTR2 cells [34]. Cells were seeded in a 24-well plate 24 h in advance (2 × $10^5$ cells/well). On the day of the experiment, medium was removed, and the cells were washed once with PBS (Gibco). Then, solutions containing unlabeled compound DOTA-JR11, $^{nat}$La-DOTA-JR11 or $^{nat}$Lu-DOTA-JR11 in increasing concentrations ($10^{-12}$ to $10^{-5}$ M) in internalization medium (DMEM media, 20 mM HEPES, 1% BSA, pH 7.4) were added, followed by the addition of [$^{111}$In]In-DOTA-JR11 ($10^{-9}$ M). Experiments were performed in triplicate for each concentration. Cells were incubated at 37 °C for 90 min. After incubation, medium was removed, and cells were washed twice with PBS and lysed with 1.0 M sodium hydroxide (NaOH) for 15 min at rt. The lysate was transferred to counting tubes, and measurement was performed using the gamma counter. $IC_{50}$ values were determined by non-linear regression plot analysis using Graphpad Prism v5 (GraphPad software, San Diego, CA, USA). Data were reported as percentage binding of [$^{111}$In]In-DOTA-JR11.

***Ex vivo studies***

Ex vivo biodistribution of [$^{225}$Ac]Ac-DOTA-JR11

All animal experiments were approved by the animal welfare body of the Erasmus Medical Center, and were performed according to accepted guidelines. BALB/cAnN Rj-Nude mice were inoculated subcutaneously with 5 × $10^6$ SSTR2-positive H69 cells (human small-cell lung carcinoma) in Matrigel (Corning, NY, USA). The tumors were left to grow for approximatively two weeks until reaching an average volume of 300 $mm^3$. Then, the animals were intravenously (i.v.) injected through the tail vein with 100 µL of [$^{225}$Ac]Ac-DOTA-JR11 (23.4 ± 1.5 kBq/0.5 nmol) diluted in PBS containing Kolliphor® HS 15 (0.06 mg/ mL) ($n$ = 3 mice/group). Ex vivo biodistribution studies were performed at 4, 24, 48 and 72 h post injection (p.i.). The radioactivity uptake of the following organs was determined: blood, tumor, heart, lungs, liver, spleen, stomach, intestines, pancreas, kidneys, muscle, skin and bone. To confirm uptake specificity of [$^{225}$Ac]Ac-DOTA-JR11, a group of mice were co-injected with [$^{225}$Ac]Ac-DOTA-JR11 and a 50-fold excess of unlabeled DOTA-JR11 24 h prior the organs were harvested. The weight of the tissues was measured and the activity present in each organ and tumor was counted in the gamma counter 24 h later. The results were reported as percentage of injected activity per gram of tissue (% IA/g).

### Ex vivo biodistribution of [$^{177}$Lu]Lu-DOTA-JR11

The ex vivo biodistribution data of [$^{177}$Lu]Lu-DOTA-JR11 were previously published by our group [35]. Briefly, BALB/cAnN Rj-Nude mice (4 mice/group) inoculated with SSTR2-positive H69 cells were injected intravenously, through the tail vein, with 100 µL of [$^{177}$Lu]Lu-DOTA-JR11 (5 MBq/0.5 nmol). Ex vivo biodistribution studies were performed at 4, 24, 48 and 72 h p.i. Uptake specificity of [$^{177}$Lu]Lu-DOTA-JR11 was confirmed by co-injection of the radiopeptide with a 50-fold excess of unlabeled DOTA-JR11. The harvested organs of interest were counted in a gamma counter and data were reported as % IA/g (Table. S2).

### Digital autoradiography of tumor and kidney slices

Tumor and kidneys were harvested from one mouse 24 h after administration of 23.4 ± 1.5 kBq/0.5 nmol of [$^{225}$Ac]Ac-DOTA-JR11. The tissues were directly stored in KP-CryoCompound a frozen tissues medium from Klinipath (Olen, Belgium). After being embedded in optimal cutting temperature, the tissues were cut into 10 µm sections using Cryostar NX70 from Thermo Fisher scientific (Eindhoven, The Netherlands). Digital autoradiography images were obtained using BeaQuant from Ai4r (Nantes, France). Image acquisition and image analysis were performed using Beavacq and Beamage, respectively, provided by Ai4r (Nantes, France).

### Statistical analysis

All statistical analysis and nonlinear regression were performed using GraphPad Prism 9.3.1 (San Diego, CA, USA). Outliners were evaluated with the Grubbs' test and removed from the data set. Significant differences were determined using an unpaired $t$-test. Data were reported as mean ± SEM (standard error of mean) for three independent replicates.

### *Dosimetry studies*

The absorbed dose was calculated according to the MIRD-scheme [MIRD pamphlet 21]. Single-exponential curves were fitted to the biodistribution data and decision on inclusion of a residual activity was based on the Aikake Information Criterion using Graphpad Prism. The resulting time-activity curves (TAC) were folded with the actinium-225 decay function and integrated over time to determine the time-integrated activity concentration coefficient $[\tilde{a}(r_s)]$ for each source organ $r_s$. The daughters of actinium-225 were assumed to be in equilibrium with actinium-225 activity and the same time-integrated activity concentrations $[\tilde{a}(r_s)]$ were applied for each daughter except polonium-213 and thallium-209, which were corrected for their decay branching ratio of 0.9786 and 0.0214, respectively. Absorbed dose coefficients $d(r_t)$ to target organ $r_t$ were calculated by the MIRD equation:

$$d(r_t) = \sum_{r_s} [\tilde{a}(r_s)]\, m(r_s) \times S_{RBE}(r_t \leftarrow r_s)$$

using the radiation RBE weighted S-values for actinium-225 and its progeny and the source organ masses $m(r_s)$ for the 25 g mouse phantom from the Olinda dosimetry software (Version 2.1, Hermes software) [36]. The default RBE of 5 was used for α-radiation and RBE=1 for all other radiations. The absorbed dose to the tumor was determined by taking the S-value for a 0.15 $cm^3$ water sphere from IDAC-dose (version 2.1), again with RBE=5 for α-radiation and RBE=1 for all other. The cross-doses from other source organs to the tumor were calculated by adding the cross doses in the testes to the self-dose of the tumor, as both testes and tumor are superficial on the mouse body.

The dosimetry calculations for $[^{177}Lu]$Lu-DOTA-JR11 were performed in the same manner, except that for lutetium-177, RBE=1. The biodistribution data of $[^{177}Lu]$Lu-DOTA-JR11 was also fitted with single-exponential curves and the resulting time-integrated activity concentration coefficients used to calculate the absorbed doses inside 25 g Olinda mouse phantom. Tumor dosimetry was based on the spheres S-values for actinium-225 with daughters taken from the IDAC code [36].

## Results

Synthesis of $^{nat}La$-DOTA-JR11 and $^{nat}Lu$-DOTA-JR11

Complexation of DOTA-JR11 with $^{nat}LaCl_3$ and $^{nat}LuCl_3$ was successfully performed using sodium acetate buffer. The complexes, $^{nat}La$-DOTA-JR11 and $^{nat}Lu$-DOTA-JR11 were obtained in high chemical purity (> 97%) and yields of 70 and 68%, respectively.

Radiolabeling and stability studies of [$^{225}$Ac]Ac-DOTA-JR11 and [$^{177}$Lu]Lu-DOTA-JR11

Labeling of DOTA-JR11 was successfully performed with [$^{225}$Ac]Ac($NO_3$)$_3$ and [$^{177}$Lu]Lu$Cl_3$ using a mixture of gentisic/ascorbic acids and ethanol as radiolysis quenchers [37]. Kolliphor® HS 15 was employed during the labeling to reduce the stickiness encountered with the radiolabeled peptides [35]. The use of L-melatonin in condition 3 did not only improve the RCP of [$^{225}$Ac]Ac-DOTA-JR11 compared to condition 2, but also improved its stability towards radiolysis (81.0% vs. 56.6%, respectively) [38]. [$^{225}$Ac]Ac-DOTA-JR11 from condition 1 and [$^{177}$Lu]Lu-DOTA-JR11 were both obtained with a RCP of > 92% (Table 2 and 3). [$^{177}$Lu]Lu-DOTA-JR11 showed a better stability in PBS and mouse serum compared to the $^{225}$Ac-labeled analog. Considering our stability data, DOTA-JR11 was radiolabeled with [$^{225}$Ac]Ac($NO_3$)$_3$ following condition 1 for the in vivo studies.

**Table 2:** RCYs, RCPs and stability studies in PBS and mouse serum of [$^{225}$Ac]Ac-DOTA-JR11 prepared following different radiochemical conditions: 1, 2 (without L-melatonin) and 3 (with L-melatonin).

| | RCY (%)* | RCP (%)* | PBS (%)† | Mouse serum (%)† |
|---|---|---|---|---|
| **Condition 1** | 95.1 ± 0.3 | 92.5 ± 3.8 | 76.9 [a] | 80.9 [a] |
| **Condition 2** | 86.9 ± 13.2 | 76.5 ± 14.7 | 56.6 [b] | 81.4 [b] |
| **Condition 3** | 98.4 ± 0.5 | 83.3 ± 7.5 | 81.0 [c] | 81.0 [c] |

* RCYs and RCPs are presented as percentage of radiolabeled peptide (n = 4, 3 and 4 for conditions 1, 2 and 3 respectively).

† Results are expressed as percentage (%) of intact radiolabeled peptide after incubation at 37 °C (n = 1).

[a] Stability studies performed at 22 h.

[b] Stability studies performed at 24 h.

[c] Stability studies performed at 27 h.

**Table 3:** RCY, RCP and stability studies of [$^{177}$Lu]Lu-DOTA-JR11 in PBS and mouse serum.

| | | | PBS (%)* | | Mouse serum (%)* | |
|---|---|---|---|---|---|---|
| | RCY (%) | RCP (%) | 2 h | 24 h | 2 h | 24 h |
| **[$^{177}$Lu]Lu-DOTA-JR11** | 99.0 | 96.6 | 96.5 | 96.8 | 94.5 | 93.7 |

* Results are expressed as percentage (%) of intact radiolabeled peptide after incubation at 37 °C (n = 1).



Competition binding assay

The competitive binding assay was carried out in U2OS-SSTR2+ cells and [$^{111}$In]In-DOTA-JR11 was used as radioligand. The obtained $IC_{50}$ curves are reported in figure 1. DOTA-JR11, $^{nat}$La-DOTA-JR11 and $^{nat}$Lu-DOTA-JR11 exhibited $IC_{50}$ values of 4.69 ± 0.03, 4.71 ± 0.04 and 3.88 ± 0.05 nM, respectively.

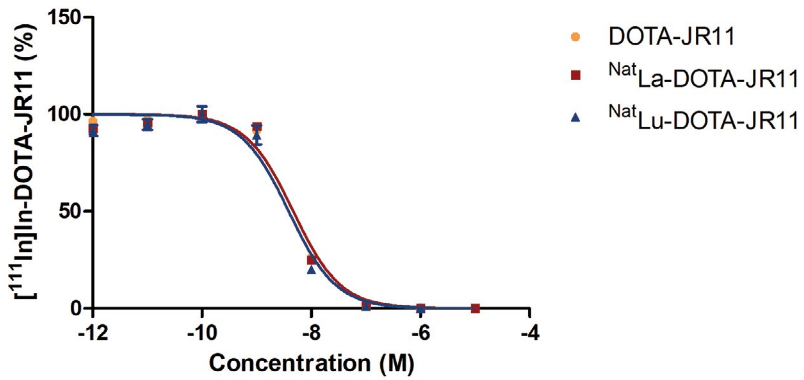


**Figure 1:** $IC_{50}$ curves of $^{nat}$La-DOTA-JR11, $^{nat}$Lu-DOTA-JR11 and DOTA-JR11.

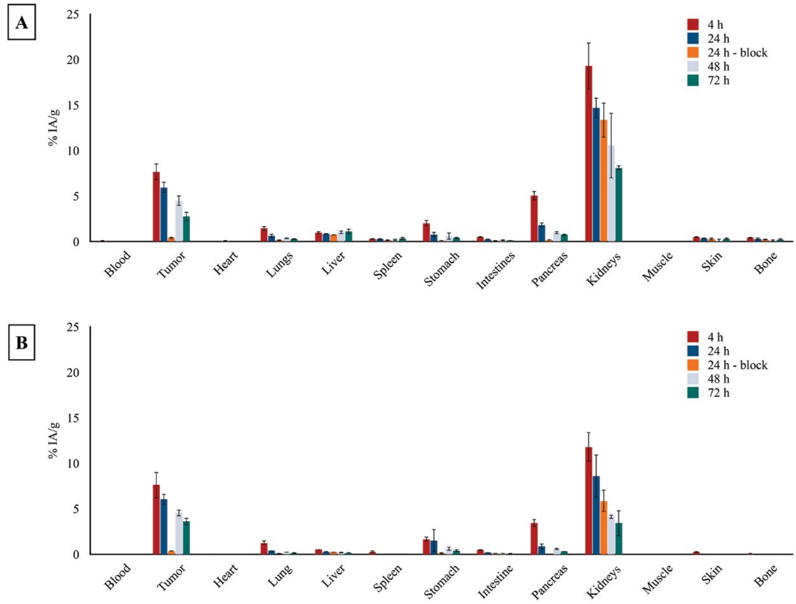


**Figure 2:** Ex-vivo biodistribution of A) [$^{225}$Ac]Ac-DOTA-JR11 and B) [$^{177}$Lu]Lu-DOTA-JR11 at 4, 24, 48 and 72 h post-injection (n = 3 mice/group). Data are presented as the percentage of injected activity per gram of tissue (% IA/g).





Ex vivo biodistribution of [$^{225}$Ac]Ac-DOTA-JR11

Each mouse was injected with 23.4 ± 1.5 kBq/0.5 nmol of radiolabeled peptide and ex vivo biodistribution studies were performed at 4, 24, 48 and 72 h p.i. of [$^{225}$Ac]Ac-DOTA-JR11. A high tumor uptake (7.7 ± 0.9% IA/g) was observed at 4 h p.i. (Fig. 2 and Table S1), but the radiopeptide was slowly cleared from the tumor to reach an uptake of 2.8 ± 0.5% IA/g at 72 h p.i.. The blocking group confirmed the specific uptake of [$^{225}$Ac]Ac-DOTA-JR11 at 24 h p.i. (0.4 ± 0.1% IA/g compared to 6.0 ± 0.6% IA/g for the non-block group). Furthermore, we noticed a high kidney uptake of [$^{225}$Ac]Ac-DOTA-JR11 at 4 h p.i. (19.3 ± 2.6% IA/g), which decreased overtime (8.1 ± 0.3% IA/g at 72 h p.i.). The clearance of [$^{225}$Ac]Ac-DOTA-JR11 from the tumor and the elimination from the kidneys resulted in low and steady tumor-to-kidney ratio (0.4 and 0.3 at 4 and 72 h p.i., respectively).

### Digital autoradiography

Tumor and kidneys of one mouse were excised 24 h after administration of [$^{225}$Ac]Ac-DOTA-JR11, sliced and imaged by autoradiography. The images revealed a homogeneous tumor uptake (Fig. 3A). However, heterogenous uptake of [$^{225}$Ac]Ac-DOTA-JR11 was observed in the kidneys (Fig. 3B). In fact, higher uptake was found in the renal cortex compared to the medulla. This finding suggests that the renal distribution of [$^{225}$Ac]Ac-DOTA-JR11 is similar to previously reported somatostatin analogs [39].

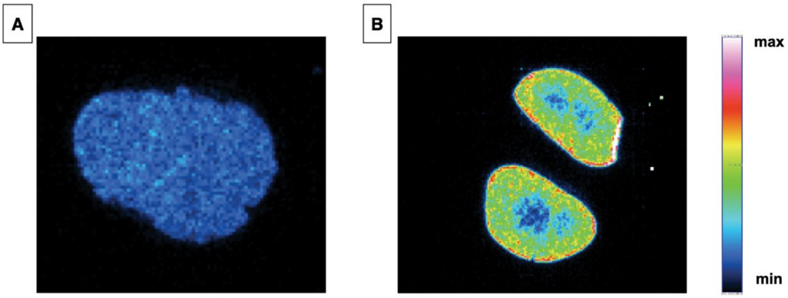


**Figure 3:** Autoradiography acquisition of A) a tumor slice and B) left and right kidneys slice. Tissues were harvested from a mouse 24 h after injection of 23.4 ± 1.5 kBq/0.5 nmol of [$^{225}$Ac]Ac-DOTA-JR11.

### Dosimetry studies

The TACs were fitted with single-exponential functions to the biodistribution data with $R^2 > 0.8$, except for liver and bone. The uptake in the liver was considered to be trapped and the TAC was modelled by a horizontal line. The clearance from the tumor proceeded with biological half-lives of 50 h (95% CI: 40 - 65 h) and 62 h (45 - 93 h) for actinium-225 and lutetium-177, respectively (Fig. 4A). Kidney clearance proceeded with a biological half-life of 48 h (34 - 75 h) for [$^{225}$Ac]Ac-DOTA-JR11, which is 40% (but not significantly) longer than the 34 h (25 - 49 h) for [$^{177}$Lu]Lu-DOTA-JR11 (Fig. 4B). Absorbed doses for the organs of interest are presented in table 4.

Time-activity curves for the organs of interest are presented for [$^{225}$Ac]Ac-DOTA-JR11 and [$^{177}$Lu]Lu-DOTA-JR11 in Figures S8 and S9 respectively.

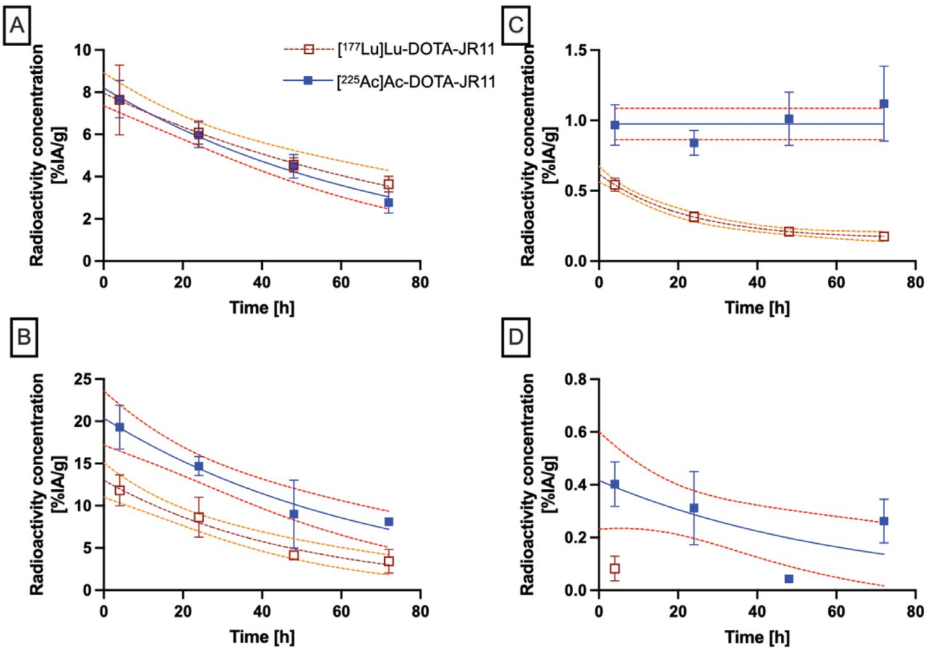


**Figure 4:** Comparison of A) tumor, B) kidneys, C) liver and D) bone TAC of [$^{225}$Ac]Ac-DOTA-JR11 (blue curves) and [$^{177}$Lu]Lu-DOTA-JR11 (brown curves). Single-exponential curve fits are shown with 95% confidence intervals.

**Table 4:** Absorbed dose per administered activity for [$^{225}$Ac]Ac-DOTA-JR11 and [$^{177}$Lu]Lu-DOTA-JR11. The alpha-contribution to the absorbed dose by [$^{225}$Ac]Ac-DOTA-JR11 were weighted with an RBE=5. The last row indicates the tumor/kidney absorbed dose ratio.

| Target organ ($r_t$) | $d(r_t)$ [mGy/kBq [$^{225}$Ac]Ac-DOTA-JR11] | $d(r_t)$ [mGy/MBq [$^{177}$Lu]Lu-DOTA-JR11] |
|---|---|---|
| Intestines | 40.3 | 23.4 |
| Stomach Wall | 137.2 | 48.8 |
| Heart | 11.2 | 1.9 |
| Kidneys | 952.6 | 406.9 |
| Liver | 271.4 | 38.5 |
| Lungs | 37.2 | 37.7 |
| Pancreas | 284.4 | 120.8 |
| Skeleton | 0.1 | 2.8 |
| Spleen | 76.4 | 8.4 |
| Total Body | 44.0 | 12.6 |
| Tumor (150 mg) | 328.5 | 464.4 |
| T/K ratio[a] | 0.35 | 1.14 |

[a] Tumor-to-kidney ratio

## Discussion

Our study aimed to explore the efficacy of TAT in treating NETs using the $^{225}$Ac-labeled somatostatin antagonist DOTA-JR11. The current gold standard method for PRRT using [$^{177}$Lu]Lu-DOTA-TATE is insufficient due to resistance and recurring disease, and therefore requires improvement [15,16]. Alpha particles have a greater ability to induce DNA damage and result in higher cell death compared to beta emitters, making TAT a promising alternative. However, DOTA-JR11 is known to be very sensitive to N-terminus modifications [20]. Therefore, we first investigated the effect of the complexation with different nuclides on the affinity of the peptide to SSTR2. $^{nat}LaCl_3$ was considered as a surrogate for actinium-225 to complex DOTA-JR11 due to identical chemical properties to lanthanide and more specifically $La^{3+}$ [40]. Competitive binding assay revealed that the complexes, $^{nat}$La-DOTA-JR11 and $^{nat}$Lu-DOTA-JR11, exhibited similar binding affinity for SSTR2 compared to the parent peptide DOTA-JR11. These data suggest that complexation of DOTA-JR11 with $La^{3+}$ and $Lu^{3+}$ does not affect the binding affinity of the peptide to SSTR2, which is in agreement with findings previously reported by Fani et al. [20,41]. Radiolabeling with [$^{225}$Ac]$Ac(NO_3)_3$ is often challenging due to the important degradation of the radiolabeled product caused by the alpha particles. However, we established optimized radiolabeling conditions to obtain [$^{225}$Ac]Ac-DOTA-JR11 in high RCP (condition 1). Lower radiochemical purity and more degradation were observed using condition 2. The use of L-melatonin, as radiolysis quencher (condition 3), was an interesting option to stabilize [$^{225}$Ac]Ac-DOTA-JR11. However, the concentration used during radiolabeling would cause adverse effects during the in vivo preclinical evaluation [42,43]. Stability studies in PBS and mouse serum revealed that [$^{225}$Ac]Ac-DOTA-JR11 was more sensitive to degradation compared to [$^{177}$Lu]Lu-DOTA-JR11. This is probably due to the higher sensitivity of biomolecules to alpha radiation than beta particles [44,45].

Ex vivo analyses showed that the biodistribution profile of [$^{225}$Ac]Ac-DOTA-JR11 is similar to the biodistribution we previously reported for [$^{177}$Lu]Lu-DOTA-JR11 [35]. No statistical difference of tumor uptake could be found between both radiolabeled DOTA-JR11, showing that complexation with lutetium-177 or actinium-225 did not affect tumor uptake in vivo. [$^{225}$Ac]Ac-DOTA-JR11 was completely cleared from the blood circulation 4 h after injection. Uptake in stomach and pancreas was observed, which can be explained by the natural expression of SSTR2 in these organs [46,47]. The specificity of [$^{225}$Ac]Ac-DOTA-JR11 towards SSTR2 was confirmed using the blocking group performed at 24 h after injection, this finding follows the data reported for [$^{177}$Lu]Lu-DOTA-JR11 [35]. However, significantly higher kidneys, liver and bone uptake were found for [$^{225}$Ac]Ac-DOTA-JR11 than [$^{177}$Lu]Lu-DOTA-JR11, it might be due to the slight instability of the $^{225}$Ac-labeled peptide towards radiolysis compared to [$^{177}$Lu]Lu-DOTA-JR11. In fact, it was reported that free actinium-225 or complexed actinium-225 with aminopolycarboxylate chelators distributes mainly to the liver, femur and kidneys [48,49]. In previous research studies reported by Schwartz and coworkers, it was demonstrated that bismuth-213 generated from the decay of actinium-225 in vivo can accumulate in the kidneys [50]. However, in our current research, the measurement of the organs resulted from the ex vivo biodistribution studies were based on the detection of francium-221 (mother radionuclide of bismuth-213), therefore, the higher kidneys uptake cannot result from an extended retention of bismuth-213.

Considering the tumor/kidney ratio of 0.35 for [$^{225}$Ac]Ac-DOTA-JR11, this seems to prohibit its use as therapeutic agent. However, the absorbed doses were all calculated based on homogeneous uptake in the organs and this can lead to an overestimation of the actual absorbed dose to the glomeruli. In a mouse phantom it was calculated that with actinium-225 located in the proximal tubule the dose to the glomeruli was 57% lower than the mean dose to the kidneys assuming homogenous distribution [51]. In the larger human kidneys this effect is more pronounced and can lead to 81% reduction in absorbed dose to the nephron/glomeruli. Comparable differences were observed between heterogeneous and homogeneous [$^{177}$Lu]Lu-DOTA-TATE absorbed dose distributions [52].

Increased uptake in the femur might lead to higher absorbed doses to the bone marrow, although this is not apparent in the present study. Larger animal models would be needed to determine the bone uptake in further detail, as for instance differentiation between bone and bone marrow. Previous pre-clinical investigations on [$^{177}$Lu]Lu-DOTA-JR11 did not lead to large concerns on its potential hematologic toxicity, whereas the phase 1 clinical trial with [$^{177}$Lu]Lu-DOTA-JR11 was stopped because of severe grade 4 hematologic toxicity. When the skeletal uptake is in the bone structure and not in the bone marrow, the alpha-particles from actinium-225 might be creating less hematopoietic damage than lutetium-177, due to its shorter range. Furthermore, the dosimetry calculations showed that the liver and the pancreas had a 7- and 2-fold higher absorbed dose for [$^{225}$Ac]Ac-DOTA-JR11 compared to [$^{177}$Lu]Lu-DOTA-JR11, respectively. Based on the results obtained in the current study and the dosimetry calculations, there is a clear need for a better prediction model of bone marrow toxicity in the clinical as in the pre-clinical setting.

The use of [$^{225}$Ac]Ac-DOTA-JR11 in clinical trials may lead to radiotoxicity to non-targeted organs, more specifically to the kidneys. However, several studies showed that kidneys uptake can be reduced using multiple strategies, such as the administration of amino acid cocktails and gelofusine [53,54]. Furthermore, introduction of a linker cleaved by the renal brush border enzymes and the pretargeting approach proved their potential in limiting the nephrotoxicity [55,56]. Those strategies might reduce the kidneys uptake up to 45 – 50% offering an opportunity to consider further studies with [$^{225}$Ac]Ac-DOTA-JR11 for TAT of NETs.

## Conclusion

In the current study, we have reported a successful and optimized radiolabeling of DOTA-JR11 with [$^{225}$Ac]Ac($NO_3$)$_3$ for TAT of NETs. The radiolabeled peptide was obtained in high RCY and RCP. [$^{177}$Lu]Lu-DOTA-JR11 showed better stability in PBS and mouse serum compared to [$^{225}$Ac]Ac-DOTA-JR11. Complexation of DOTA-JR11 with either $^{nat}$La or $^{nat}$Lu did not affect binding affinity to SSTR2. Both radiolabeled peptides showed similar biodistribution profile in vivo. However, due to potential radiotoxicity of the alpha particles in non-targeted organs (e.g., kidneys and bone marrow), further optimization of the pharmacokinetics of [$^{225}$Ac]Ac-DOTA-JR11 are needed for safe and efficient TAT of NETs.

## Supplementary Information

The online version contains supplementary material.

## Acknowledgements

We would like to thank Sofia Koustoulidou, Ho Sze Chan, Lilian van den Brink, Marjolein Verhoeven, Ilva Klomp, Erika Murce, Dylan Chapeau and Eline Hooijman for their assistance. We are grateful to the Dutch Cancer Society (KWF) for the financial support (grant 12259/2019-1) and the department of Radiology and Nuclear Medicine at the Erasmus MC for technical assistance.

## Funding

The project was financed by the Dutch Cancer Society (KWF), grant number 12259.

## Author contributions

Conceptualization, Y.S.; methodology, Y.S.; software, M.H. S.B. and M.K.; validation, M.H. S.B. and M.K.; formal analysis, M.H., C.d.R., D.S., and S.B.; investigation, A.D., E.d.B., and Y.S.; resources, F.B., A.M. and Y.S.; data curation, M.H.; writing—original draft preparation, M.H.; writing—review and editing, M.H., S.B., M.K., D.S., C.d.R., F.B., A.M., A.D., E.d.B., and Y.S.; visualization, Y.S.; supervision, Y.S.; project administration, Y.S.; funding acquisition, Y.S. All authors have read and agreed to the published version of the manuscript.

## Availability of data and materials

All data generated and analysed during this study are included in this published article. Supporting information is provided containing additional data. Additional information are available from the corresponding author upon reasonable request.

## References


1. Rizen EN, Phan AT. Neuroendocrine Tumors: a Relevant Clinical Update. Curr Oncol Rep 2022;24:703–714.
2. Das S, Dasari A. Epidemiology, Incidence, and Prevalence of Neuroendocrine Neoplasms: Are There Global Differences? Curr Oncol Rep 2021;23:1–7.
3. Öberg K, Castellano D. Current knowledge on diagnosis and staging of neuroendocrine tumors. Cancer and Metastasis Reviews 2011;30:3–7.
4. Singh S, Granberg D, Wolin E, Warner R, Sissons M, Kolarova T, et al. Patient-reported burden of a neuroendocrine tumor (NET) diagnosis: Results from the first global survey of patients with NETs. J Glob Oncol 2017;3:43–53.
5. Mizutani G, Nakanishi Y, Watanabe N, Honma T, Obana Y, Seki T, et al. Expression of somatostatin receptor (SSTR) subtypes (SSTR-1, 2A, 3, 4 and 5) in neuroendocrine tumors using real-time RT-PCR method and immunohistochemistry. Acta Histochem Cytochem 2012;45:167–176.
6. Elf AK, Johanson V, Marin I, Bergström A, Nilsson O, Svensson J, et al. Evaluation of sstr2 expression in si-nets and relation to overall survival after prrt. Cancers (Basel) 2021;13:2035.
7. Tafreshi NK, Pandya DN, Tichacek CJ, Budzevich MM, Wang Z, Reff JN, et al. Preclinical evaluation of [225Ac]Ac-DOTA-TATE for treatment of lung neuroendocrine neoplasms. Eur J Nucl Med Mol Imaging 2021;48:3408–3421.
8. Rufini V, Lorusso M, Inzani F, Pasciuto T, Triumbari EKA, Grillo LR, et al. Correlation of somatostatin receptor PET/CT imaging features and immunohistochemistry in neuroendocrine tumors of the lung: a retrospective observational study. Eur J Nucl Med Mol Imaging 2022;49:4182–4193.
9. Fonti R, Panico M, Pellegrino S, Pulcrano A, Vastarella LA, Hakkak A, et al. Heterogeneity of SSTR2 expression assessed by 68 Ga-DOTATOC PET/CT using coefficient of variation in patients with neuroendocrine tumors. Journal of Nuclear Medicine 2022;63:1509–1514.
10. Zhu W, Cheng Y, Jia R, Zhao H, Bai C, Xu J, et al. A prospective, randomized, double-blind study to evaluate the safety, biodistribution, and dosimetry of 68Ga-NODAGA-LM3 and 68Ga-DOTA-LM3 in patients with well-differentiated neuroendocrine tumors. Journal of Nuclear Medicine 2021;62:1398–1405.
11. Albrecht J, Exner S, Grötzinger C, Prasad S, Konietschke F, Beindorff N, et al. Multimodal Imaging of 2-Cycle PRRT with 177Lu-DOTA-JR11 and 177Lu-DOTATOC in an Orthotopic Neuroendocrine Xenograft Tumor Mouse Model. J Nucl Med 2021;62:393–398.
12. Thakur S, Daley B, Millo C, Cochran C, Jacobson O, Lu H, et al. 177Lu-DOTA-EB-TATE, a Radiolabeled analogue of somatostatin receptor Type 2, for the imaging and treatment of thyroid cancer. Clinical Cancer Research 2021;27:1399–1409.
13. Strosberg J, Wolin E, Chasen B, Kulke M, Bushnell D, Caplin M, et al. Health-Related Quality of Life in Patients With Progressive Midgut Neuroendocrine Tumors Treated With 177 Lu-Dotatate in the Phase III NETTER-1 Trial. Journal of Clinical Oncology 2018;36:2578–84.
14. Ianniello A, Sansovini M, Severi S, Nicolini S, Grana CM, Massri K, et al. Peptide receptor radionuclide therapy with 177Lu-DOTATATE in advanced bronchial carcinoids: prognostic role of thyroid transcription factor 1 and 18F-FDG PET. Eur J Nucl Med Mol Imaging 2016;43:1040–6.
15. Katona BW, Roccaro GA, Soulen MC, Yang YX, Bennett BJ, Riff BP, et al. Efficacy of Peptide Receptor Radionuclide Therapy in a United States-Based Cohort of Metastatic Neuroendocrine Tumor Patients: Single-Institution Retrospective Analysis. Pancreas 2017;46:1121–6.
16. Mariniello A, Bodei L, Tinelli C, Baio SM, Gilardi L, Colandrea M, et al. Long-term results of PRRT in advanced bronchopulmonary carcinoid. Eur J Nucl Med Mol Imaging 2016;43:441–452.
17. Hou G, Zhang Y, Liu Y, Wang P, Xia W, Xing X, et al. Head-to-Head Comparison of 68Ga-DOTA-TATE and 68Ga-DOTA-JR11 PET/CT in Patients With Tumor-Induced Osteomalacia: A Prospective Study. Front Oncol 2022;12:1–6.
18. Zhu W, Cheng Y, Wang X, Yao S, Bai C, Zhao H, et al. Head-to-head comparison of 68Ga-DOTA-JR11 and 68Ga-DOTATATE PET/CT in patients with metastatic, well-differentiated neuroendocrine tumors: A prospective study. J Nucl Med 2020;61:897–903.

19. Fani M, Nicolas GP, Wild D. Somatostatin receptor antagonists for imaging and therapy. J Nucl Med 2017;58:61S–66S.
20. Fani M, Braun F, Waser B, Beetschen K, Cescato R, Erchegyi J, et al. Unexpected sensitivity of sst 2 antagonists to N-terminal radiometal modifications. J Nucl Med 2012;53:1481–1489.
21. Wild D, Fani M, Fischer R, Pozzo L Del, Kaul F, Krebs S, et al. Comparison of somatostatin receptor agonist and antagonist for peptide receptor radionuclide therapy: A pilot study. J Nucl Med 2014;55:1248–1252.
22. Reidy-Lagunes D, Pandit-Taskar N, O'Donoghue JA, Krebs S, Staton KD, Lyashchenko SK, et al. Phase I Trial of Well-Differentiated Neuroendocrine Tumors (NETs) with Radiolabeled Somatostatin Antagonist 177Lu-Satoreotide Tetraxetan. Clin Cancer Res 2019;25:6939–6947.
23. Müller C, Van Der Meulen NP, Benešová M, Schibli R. Therapeutic radiometals beyond 177Lu and 90Y: Production and application of promising α-particle, β--particle, and auger electron emitters. Journal of Nuclear Medicine 2017;58:91S-96S.
24. Navalkissoor S, Grossman A. Targeted Alpha Particle Therapy for Neuroendocrine Tumours: The Next Generation of Peptide Receptor Radionuclide Therapy. Neuroendocrinology 2019;108:256–264.
25. Brechbiel MW. Targeted α-therapy: Past, present, future? Dalton Transactions 2007:4918–28.
26. Feijtel D, de Jong M, Nonnekens J. Peptide Receptor Radionuclide Therapy: Looking Back, Looking Forward. Curr Top Med Chem 2020;20:2959–2969.
27. Miederer M, Henriksen G, Alke A, Mossbrugger I, Quintanilla-Martinez L, Senekowitsch-Schmidtke R, et al. Preclinical evaluation of the α-particle generator nuclide 225Ac for somatostatin receptor radiotherapy of neuroendocrine tumors. Clinical Cancer Research 2008;14:3555–3561.
28. Tafreshi NK, Doligalski ML, Tichacek CJ, Pandya DN, Budzevich MM, El-Haddad G, et al. Development of targeted alpha particle therapy for solid tumors. Molecules 2019;24:1–48.
29. Parker C, Lewington V, Shore N, Kratochwil C, Levy M, Lindén O, et al. Targeted Alpha Therapy, an Emerging Class of Cancer Agents: A Review. JAMA Oncol 2018;4:1765–1772.
30. Hooijman EL, Chalashkan Y, Ling SW, Kahyargil FF, Segbers M, Bruchertseifer F, et al. Development of [225ac] ac-psma-i&t for targeted alpha therapy according to gmp guidelines for treatment of mcrpc. Pharmaceutics 2021;13:1–15.
31. Fani M, Del Pozzo L, Abiraj K, Mansi R, Tamma ML, Cescato R, et al. PET of somatostatin receptor-positive tumors using64Cu- and 68Ga-somatostatin antagonists: The chelate makes the difference. J Nucl Med 2011;52:1110–8.
32. Cescato R, Erchegyi J, Waser B, Piccand V, Maecke HR, Rivier JE, et al. Design and in vitro characterization of highly sst2-selective somatostatin antagonists suitable for radiotargeting. J Nucl Med 2008;51:4030–4037.
33. de Blois E, Chan HS, de Zanger R, Konijnenberg M, Breeman WAP. Application of single-vial ready-for-use formulation of 111In- or 177Lu-labelled somatostatin analogs. Applied Radiation and Isotopes 2014;85:28–33.
34. Dalm SU, de Jong M. Comparing the use of radiolabeled SSTR agonists and an SSTR antagonist in breast cancer: does the model choice influence the outcome? EJNMMI Radiopharm Chem 2017;2:1–4.
35. Koustoulidou S, Handula M, de Ridder C, Stuurman D, Beekman S, de Jong M, et al. Synthesis and Evaluation of Two Long-Acting SSTR2 Antagonists for Radionuclide Therapy of Neuroendocrine Tumors. Pharmaceuticals 2022;15:1–15.
36. Andersson M, Johansson L, Eckerman K, Mattsson S. IDAC-Dose 2.1, an internal dosimetry program for diagnostic nuclear medicine based on the ICRP adult reference voxel phantoms. EJNMMI Res 2017;7:1–10.
37. de Blois E, Chan HS, de Zanger R, Konijnenberg M, Breeman WAP. Application of single-vial ready-for-use formulation of 111In- or 177Lu-labelled somatostatin analogs. Applied Radiation and Isotopes 2014;85:28–33.
38. de Blois E, Sze Chan H, Konijnenberg M, de Zanger R, A.P. Breeman W. Effectiveness of Quenchers to Reduce Radiolysis of 111In- or 177Lu-Labelled Methionine-Containing Regulatory Peptides. Maintaining Radiochemical Purity as Measured by HPLC. Curr Top Med Chem 2013;12:2677–2685.
39. Melis M, Krenning EP, Bernard BF, Barone R, Visser TJ, De Jong M. Localisation and mechanism of renal retention of radiolabelled somatostatin analogues. Eur J Nucl Med Mol Imaging 2005;32:1136–1143.
40. Thiele NA, Wilson JJ. Actinium-225 for targeted α therapy: Coordination chemistry and current chelation approaches. Cancer Biother Radiopharm 2018;33:336–348.
41. Elkins G. Somatostatin analogues: From Research to Clinical Practice. vol. 70. 2015.

42. Kennaway DJ, Voultsios A, Varcoe TJ, Moyer RW. Melatonin in mice: Rhythms, response to light, adrenergic stimulation, and metabolism. Am J Physiol Regul Integr Comp Physiol 2002;282:358–365.
43. Kennaway DJ. Melatonin research in mice: a review. Chronobiol Int 2019;36:1167–1183.
44. Pouget JP, Constanzo J. Revisiting the Radiobiology of Targeted Alpha Therapy. Front Med 2021;8:1–11.
45. Desouky O, Ding N, Zhou G. Targeted and non-targeted effects of ionizing radiation. J Radiat Res Appl Sci 2015;8:247–254.
46. Kailey B, van de Bunt M, Cheley S, Johnson PR, MacDonald PE, Gloyn AL, et al. SSTR2 is the functionally dominant somatostatin receptor in human pancreatic β- and α-cells. Am J Physiol Endocrinol Metab 2012;303:1107–16.
47. Watanabe H, Fujishima F, Komoto I, Imamura M, Hijioka S, Hara K, et al. Somatostatin Receptor 2 Expression Profiles and Their Correlation with the Efficacy of Somatostatin Analogues in Gastrointestinal Neuroendocrine Tumors. Cancers (Basel) 2022;14:1–15.
48. Davis IA, Glowienka KA, Boll RA, Deal KA, Brechbiel MW, Stabin M, et al. Comparison of 225actinium chelates: Tissue distribution and radiotoxicity. Nucl Med Biol 1999;26:581–589.
49. Yoshimoto M, Yoshii Y, Matsumoto H, Shinada M, Takahashi M, Igarashi C, et al. Evaluation of aminopolycarboxylate chelators for whole-body clearance of free225ac: A feasibility study to reduce unexpected radiation exposure during targeted alpha therapy. Pharmaceutics 2021;13:1–15.
50. Schwartz J, Jaggi JS, O'donoghue JA, Ruan S, McDevitt M, Larson SM, et al. Renal uptake of bismuth-213 and its contribution to kidney radiation dose following administration of actinium-225-labeled antibody. Phys Med Biol 2011;56:721–33.
51. Hobbs RF, Song H, Huso DL, H Sundel M, Sgouros G. A nephron-based model of the kidneys for macro-to-micro α-particle dosimetry. Phys Med Biol 2012;57:4403–4424.
52. Konijnenberg M, Melis M, Valkema R, Krenning E, De Jong M. Radiation dose distribution in human kidneys by octreotides in peptide receptor radionuclide therapy. Journal of Nuclear Medicine 2007;48:134–142.
53. Van Eerd JEM, Vegt E, Wetzels JFM, Russel FGM, Masereeuw R, Corstens FHM, et al. Gelatin-based plasma expander effectively reduces renal uptake of 111In-octreotide in mice and rats. Journal of Nuclear Medicine 2006;47:528–533.
54. Geenen L, Nonnekens J, Konijnenberg M, Baatout S, De Jong M, Aerts A. Overcoming nephrotoxicity in peptide receptor radionuclide therapy using [177Lu]Lu-DOTA-TATE for the treatment of neuroendocrine tumours. Nucl Med Biol 2021;102:1–11.
55. Arano Y. Renal brush border strategy: A developing procedure to reduce renal radioactivity levels of radiolabeled polypeptides. Nucl Med Biol 2021;92:149–155.
56. Chigoho DM, Bridoux J, Hernot S. Reducing the renal retention of low- to moderate-molecular-weight radiopharmaceuticals. Curr Opin Chem Biol 2021;63:219–228.

## Supplemental Information

***Table of Contents***

# 1. Chemistry

### *1.1. Complexation of DOTA-JR11 with natural lanthanum and lutetium*

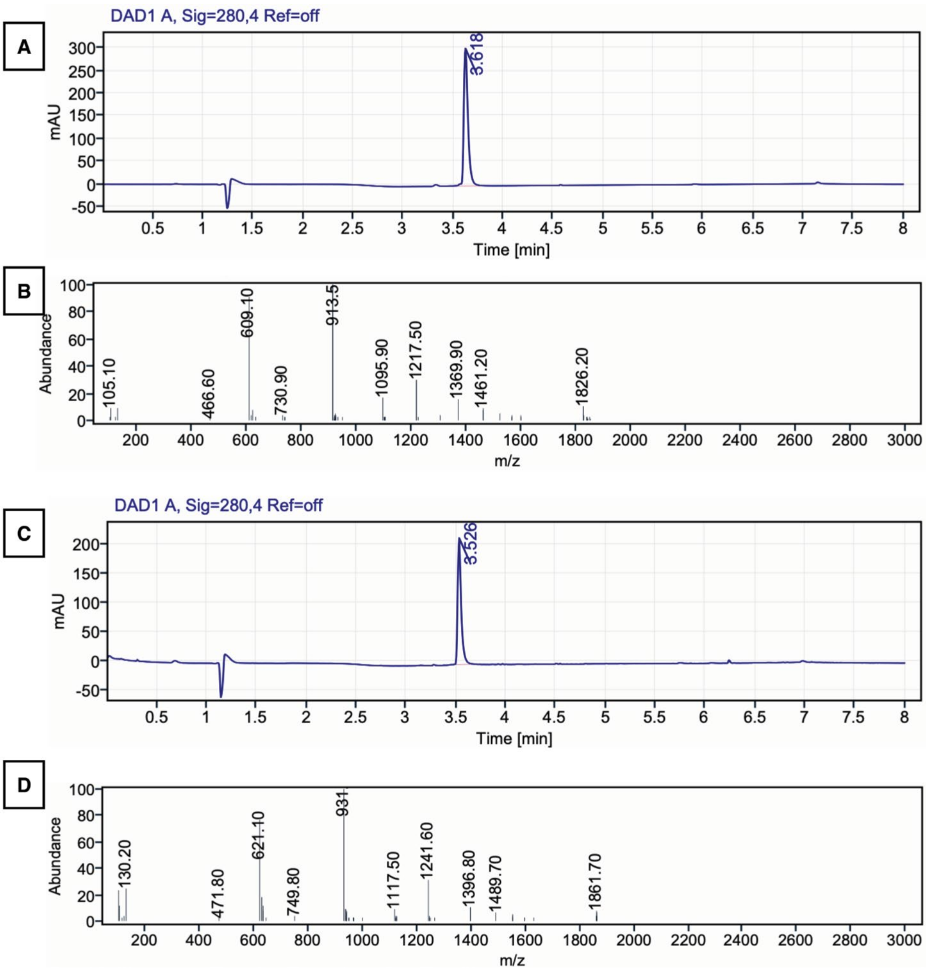


**Figure S1:** A) and C) HPLC chromatograms and B) and D) mass spectra of $^{nat}$La-DOTA-JR11 and $^{nat}$Lu-DOTA-JR11 respectively.

# 2. Radiochemistry

The quality control of all samples containing [$^{225}$Ac]Ac-DOTA-JR11 was based on the measurement of francium-221 in the gamma counter, due to its gamma emission at 218 KeV. Francium-221 is the first daughter radionuclide of actinium-225. Samples were counted at least 30 minutes after collection to ensure that an equilibrium between actinium-225 and francium-221 was achieved (Fig. S2).

$$A_2(t) = \frac{\lambda_2}{\lambda_2 - \lambda_1} A_1(0)\left(e^{-\lambda_1 t} - e^{-\lambda_2 t}\right) + A_2(0)e^{-\lambda_2 t}$$

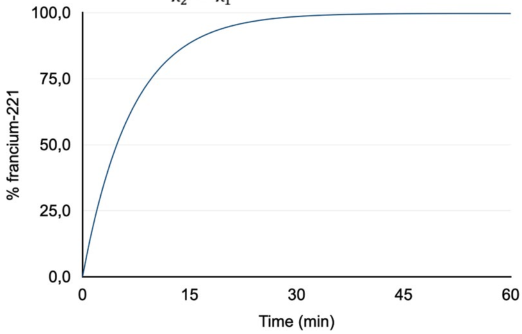


**Figure S2:** Percentage ingrowth of francium-221 based on the decay of actinium-225 overtime. The curve was calculated based on the mathematical equation shown above.

### *2.1. Actinium-225 radiolabeling of DOTA-JR11*

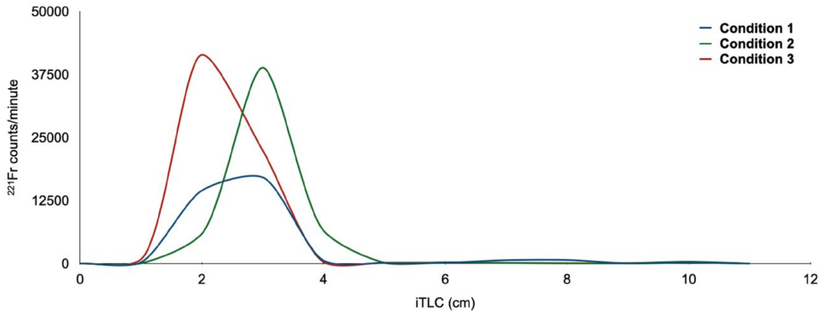


**Figure S3:** iTLC chromatograms of DOTA-JR11 radiolabeled with [$^{225}$Ac]Ac($NO_3$)$_3$ following conditions 1, 2 and 3.

### *2.2. Lutetium-177 radiolabeling of DOTA-JR11*

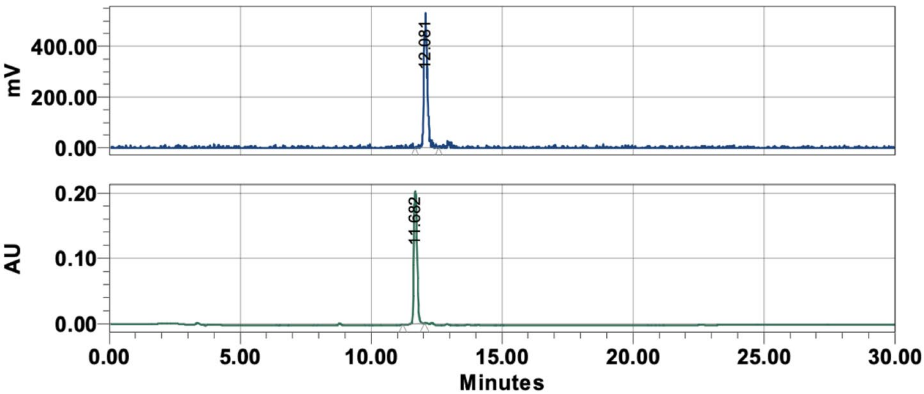


**Figure S4:** Radio-HPLC chromatogram (blue) and HPLC chromatogram (green) of [$^{177}$Lu]Lu-DOTA-JR11 and $^{nat}$Lu-DOTA-JR11 respectively. [$^{177}$Lu]Lu-DOTA-JR11 was 'spiked' with $^{nat}$Lu-DOTA-JR11, the co-elution of the radioactive and the non-radioactive peaks confirms the presence of identical chemical complexes.

### *2.3. Stability studies in PBS and mouse serum of [$^{225}$Ac]Ac-DOTA-JR11 and [$^{177}$Lu]Lu-DOTA-JR11*

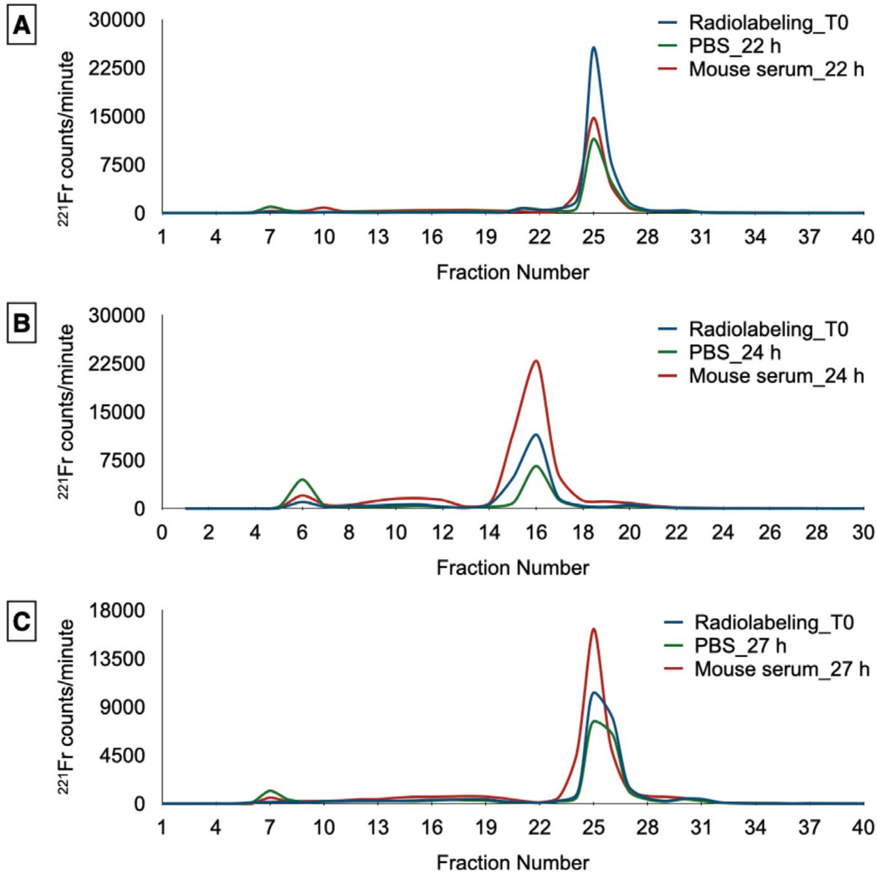


**Figure S5:** Radio-HPLC chromatograms of the stability studies performed for [$^{225}$Ac]Ac-DOTA-JR11 following A) condition 1, B) condition 2 and C) condition 3 in PBS and mouse serum. The fractions of the radiolabeling and stability studies obtained for condition 2 were collected manually.

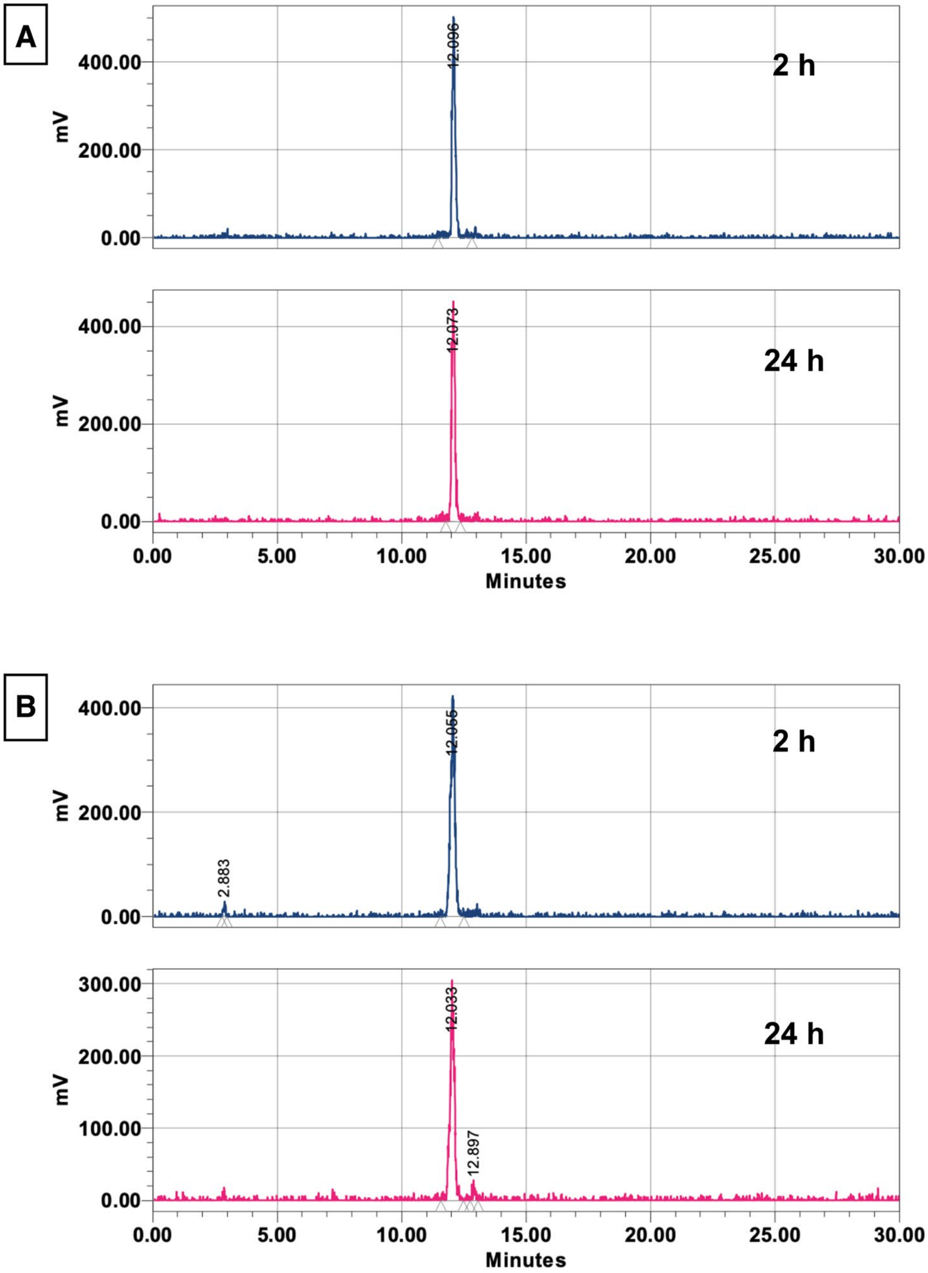


**Figure S6:** Radio-HPLC chromatograms of the stability studies performed for [$^{177}$Lu]Lu-DOTA-JR11 in A) PBS and B) mouse serum at 2 and 24 h post incubation at 37 °C.

## 3. Ex vivo studies

### *3.1. Ex vivo biodistribution of [$^{225}$Ac]Ac-DOTA-JR11*

**Table S1:** Ex-vivo biodistribution of [$^{225}$Ac]Ac-DOTA-JR11 (23.4 ± 1.5 kBq/0.5 nmol) at 4, 24, 48 and 72 h post-injection (n = 3 mice/group). Data are presented as the percentage of injected activity per gram of tissue (% IA/g).

| Organ | 4 h | 24 h | 24 h - Block | 48 h | 72 h |
|---|---|---|---|---|---|
| Blood | 0.1 ± 0.0 | 0.0 ± 0.0 | 0.0 ± 0.0 | 0.0 ± 0.0 | 0.0 ± 0.0 |
| Tumor | 7.7 ± 0.9 | 6.0 ± 0.6 | 0.4 ± 0.1 | 4.5 ± 0.6 | 2.8 ± 0.5 |
| Heart | 0.0 ± 0.1 | 0.1 ± 0.0 | 0.1 ± 0.0 | 0.0 ± 0.1 | 0.0 ± 0.0 |
| Lungs | 1.4 ± 0.3 | 0.7 ± 0.2 | 0.2 ± 0.1 | 0.4 ± 0.0 | 0.3 ± 0.1 |
| Liver | 1.0 ± 0.1 | 0.8 ± 0.1 | 0.8 ± 0.0 | 1.0 ± 0.2 | 1.1 ± 0.3 |
| Spleen | 0.3 ± 0.1 | 0.3 ± 0.1 | 0.2 ± 0.1 | 0.2 ± 0.1 | 0.4 ± 0.2 |
| Stomach | 2.0 ± 0.3 | 0.8 ± 0.3 | 0.1 ± 0.0 | 0.6 ± 0.4 | 0.4 ± 0.1 |
| Intestines | 0.5 ± 0.1 | 0.2 ± 0.0 | 0.1 ± 0.0 | 0.2 ± 0.0 | 0.1 ± 0.0 |
| Pancreas | 5.1 ± 0.5 | 1.8 ± 0.3 | 0.2 ± 0.0 | 1.0 ± 0.1 | 0.8 ± 0.1 |
| Kidneys | 19.3 ± 2.6 | 14.7 ± 1.1 | 13.4 ± 1.9 | 10.6 ± 3.6 | 8.1 ± 0.3 |
| Muscle | 0.0 ± 0.0 | 0.0 ± 0.0 | 0.1 ± 0.1 | 0.0 ± 0.0 | 0.1 ± 0.1 |
| Skin | 0.5 ± 0.1 | 0.4 ± 0.1 | 0.3 ± 0.2 | 0.1 ± 0.2 | 0.3 ± 0.1 |
| Bone | 0.4 ± 0.1 | 0.3 ± 0.1 | 0.2 ± 0.1 | 0.1 ± 0.1 | 0.3 ± 0.1 |
| T/K Ratio[a] | 0.4 ± 0.0 | 0.4 ± 0.0 | | 0.4 ± 0.1 | 0.3 ± 0.1 |

[a] Tumor-to-kidney ratio

Statistical analysis was performed to compare tumor, kidneys, liver and bone uptake for [$^{225}$Ac]Ac-DOTA-JR11 and [$^{177}$Lu]Lu-DOTA-JR11. The results revealed no significant difference of tumor uptake between both radiopeptides (Fig. S7A). Even though kidneys uptake constantly decreased overtime, the results showed that significantly higher uptake was noticed for [$^{225}$Ac]Ac-DOTA-JR11 compared to [$^{177}$Lu]Lu-DOTA-JR11 (19.3 ± 2.6 % IA/g and 12.6 ± 1.6 % IA/g at 4 h, 8.1 ± 0.3 % IA/g and 3.4 ± 1.4 % IA/g at 72 h, respectively) (Fig. S7B). However, a different tendency was found in the liver uptake. Although the liver uptake decreased overtime for [$^{177}$Lu]Lu-DOTA-JR11 (0.5 ± 0.0 % IA/g at 4 h and 0.2 ± 0.0 % IA/g at 72 h p.i.), it remained steady for [$^{225}$Ac]Ac-DOTA-JR11 (1.0 ± 0.1 % IA/g at 4 h and 1.1 ± 0.3 % IA/g at 72 h p.i.) (Fig. S7C). Significantly higher bone uptake was found for [$^{225}$Ac]Ac-DOTA-JR11 compared to [$^{177}$Lu]Lu-DOTA-JR11 (0.4 ± 0.1 % IA/g and 0.1 ± 0.0 % IA/g at 4 h, 0.3 ± 0.1 % IA/g and 0.0 ± 0.4 % IA/g at 24 h, respectively) (Fig. S7D).

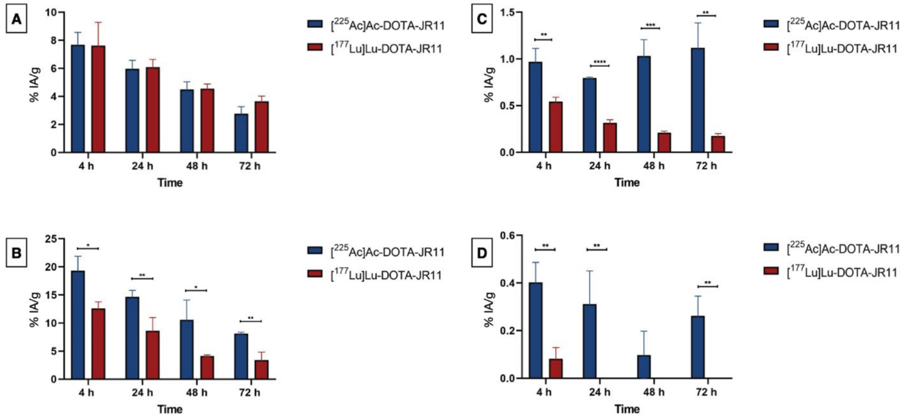


**Figure S7:** Comparison of A) tumor, B) kidneys, C) liver and D) bone uptake of [$^{225}$Ac]Ac-DOTA-JR11 and [$^{177}$Lu]Lu-DOTA-JR11 at 4, 24, 48 and 72 h p.i. Data is represented as % IA/g. * $p < 0.05$. ** $p < 0.01$. *** $p < 0.0005$. **** $p < 0.0001$. Absence of * means no significant difference found.

### *3.2. Ex vivo biodistribution of [$^{177}$Lu]Lu-DOTA-JR11*

**Table S2:** Ex-vivo biodistribution analysis of [$^{177}$Lu]Lu-DOTA-JR11 (5 MBq/0.5 nmol) at 4, 24, 48 and 72 h post-injection (n = 4 mice/group). Data is represented as percentage of injected activity per gram of tissue (% IA/g).

| Organ | 4 h | 24 h | 24 h - Block | 48 h | 72 h |
|---|---|---|---|---|---|
| Blood | -0.1 ± 0.0 | -0.1 ± 0.1 | -0.1 ± 0.1 | 0.0 ± 0.0 | -0.1 ± 0.0 |
| Tumor | 8.4 ± 0.5 | 6.1 ± 0.5 | 0.4 ± 0.0 | 4.6 ± 0.3 | 3.6 ± 0.4 |
| Heart | 0.0 ± 0.0 | 0.0 ± 0.0 | 0.0 ± 0.0 | 0.0 ± 0.0 | -0.1 ± 0.0 |
| Lung | 1.3 ± 0.3 | 0.4 ± 0.0 | 0.1 ± 0.0 | 0.2 ± 0.0 | 0.1 ± 0.0 |
| Liver | 0.5 ± 0.0 | 0.3 ± 0.0 | 0.3 ± 0.0 | 0.2 ± 0.0 | 0.2 ± 0.0 |
| Spleen | 0.3 ± 0.1 | 0.1 ± 0.0 | 0.0 ± 0.0 | 0.0 ± 0.0 | 0.0 ± 0.0 |
| Stomach | 1.7 ± 0.3 | 1.5 ± 1.2 | 0.1 ± 0.1 | 0.6 ± 0.2 | 0.4 ± 0.1 |
| Intestine | 0.5 ± 0.1 | 0.2 ± 0.0 | 0.1 ± 0.0 | 0.1 ± 0.0 | 0.1 ± 0.0 |
| Pancreas | 3.5 ± 0.4 | 0.9 ± 0.3 | 0.1 ± 0.0 | 0.6 ± 0.1 | 0.3 ± 0.0 |
| Kidneys | 12.6 ± 1.2 | 8.6 ± 2.3 | 5.9 ± 1.2 | 4.1 ± 0.2 | 3.4 ± 1.4 |
| Muscle | -0.1 ± 0.0 | -0.1 ± 0.0 | -0.1 ± 0.0 | -0.1 ± 0.0 | -0.1 ± 0.0 |
| Skin | 0.3 ± 0.1 | 0.0 ± 0.1 | -0.1 ± 0.1 | -0.2 ± 0.1 | -0.4 ± 0.2 |
| Bone | 0.1 ± 0.0 | -0.6 ± 0.4 | -0.4 ± 0.5 | -0.2 ± 0.2 | -0.1 ± 0.1 |
| T/K ratio[a] | 0.7 ± 0.0 | 0.7 ± 0.02 | | 1.1 ± 0.1 | 1.2 ± 0.4 |

[a] Tumor-to-kidney ratio

# 4. Dosimetry studies

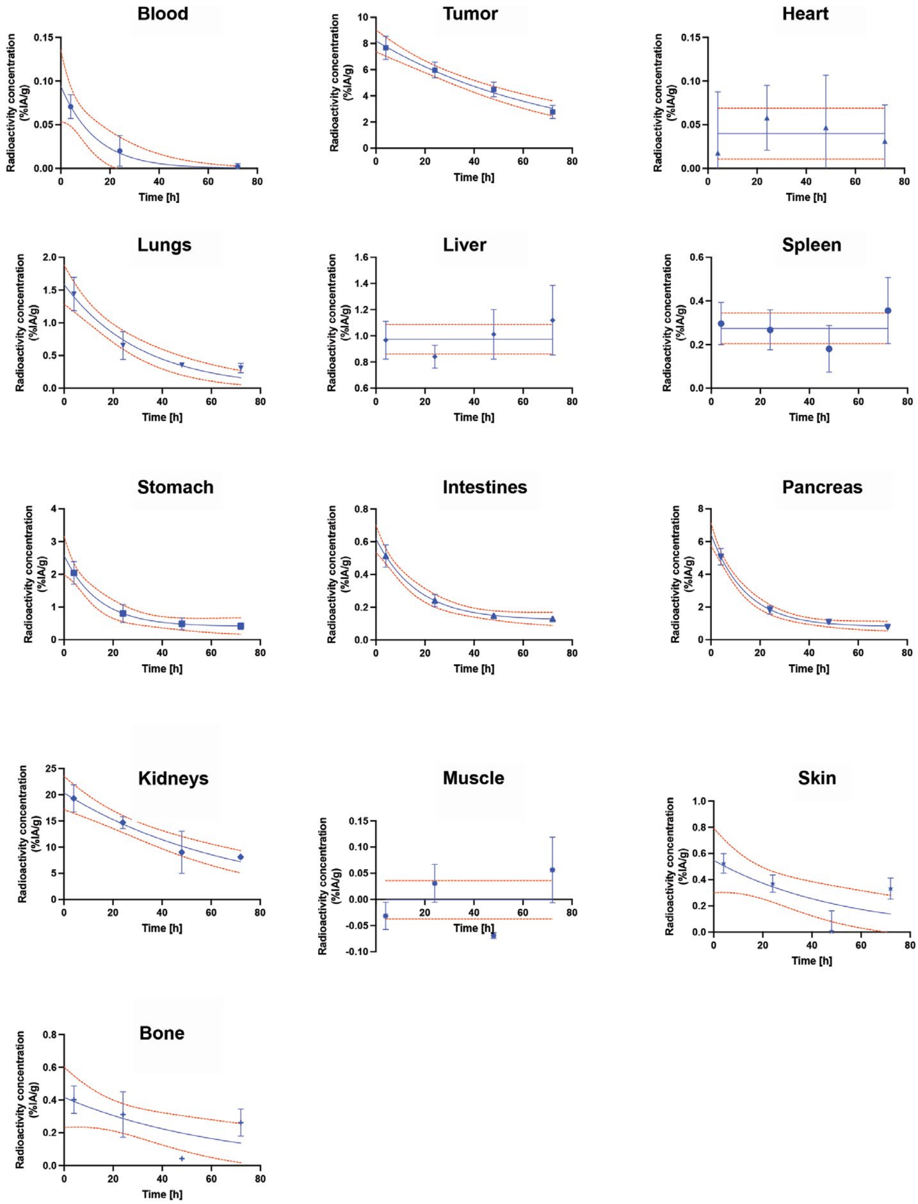


**Figure S8:** Time-activity curves of the organs and tissues of interest from mice injected with [$^{225}$Ac]Ac-DOTA-JR11. Single-exponential curve fits are shown with 95% confidence intervals.

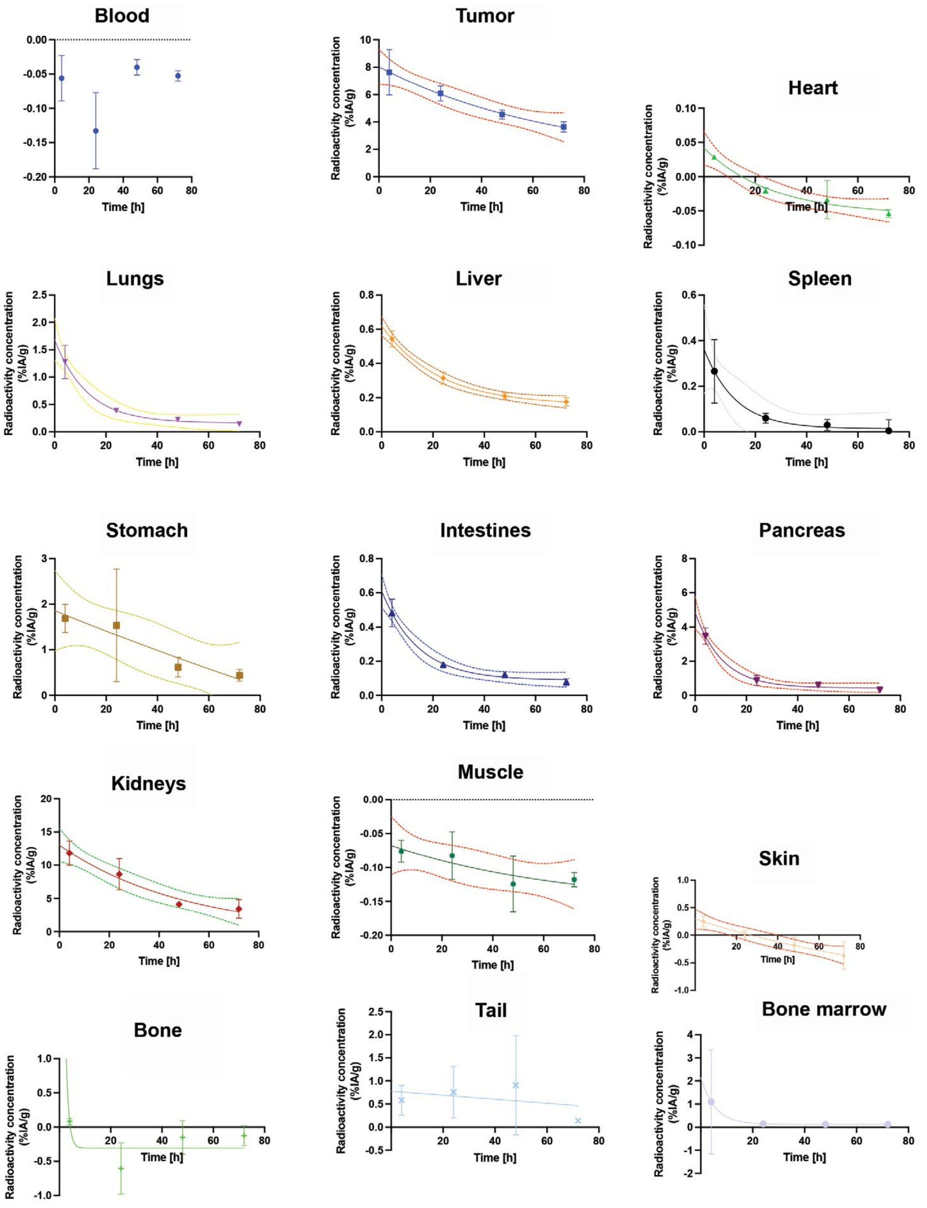


**Figure S9:** Time-activity curves of the organs and tissues of interest from mice injected with [$^{177}$Lu]Lu-DOTA-JR11. Single-exponential curve fits are shown with 95% confidence intervals.

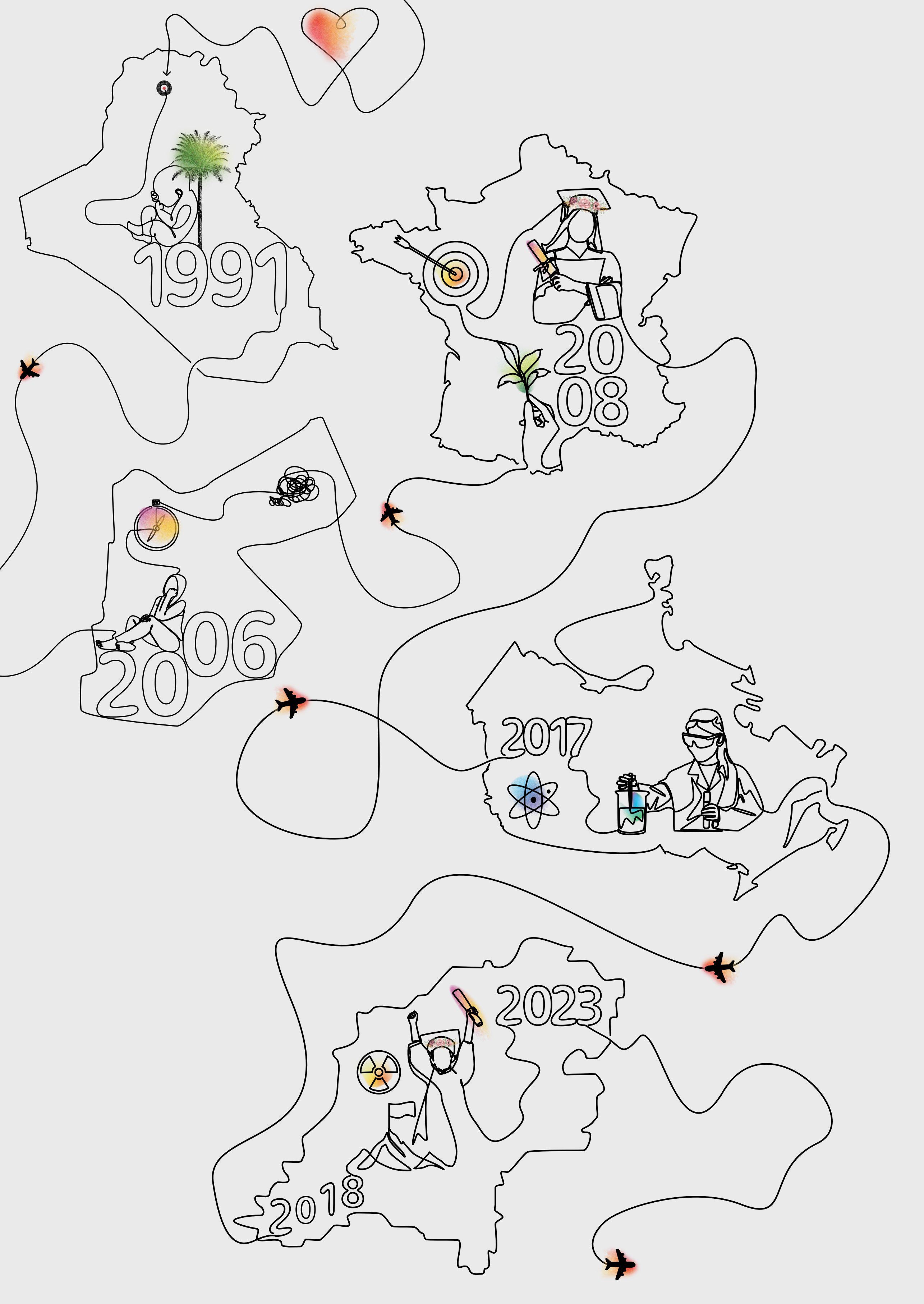
1991
2008
2006
2017
2023
2018

# CHAPTER 8

## Summary, Conclusion, General Discussion and Future Perspectives

## Summary and conclusion

Targeted radionuclide imaging and therapy became a primordial tool for diagnosis and treatment of multiple types of cancer [1,2]. This approach demonstrated its potential to achieve positive outcomes using peptide agonist and antagonist analogs [3–5]. Furthermore, the availability of a large spectrum of radioisotopes offers the opportunity to radiolabel these biovectors with diverse diagnostic (e.g., indium-111, gallium-68 …) and therapeutic (e.g., lutetium-177, yttrium-90 …) radionuclides. Hence, offering the opportunity to find the best combination of radiopharmaceuticals for a personalized and more efficient nuclear medicine.

Within this thesis, we explored diverse strategies to improve the diagnosis and treatment of PCa and NETs by targeting GRPR and SSTR2, respectively. The incidence rate and the severity of those cancer types motivated us to emphasize on strategies that can have an impact on the management of PCa and NET patients. For all our studies, we chose to work with GRPR and SSTR2 antagonists. In fact, many investigations reported the greater performance of peptide antagonists over agonists [6–9]. It was reported that antagonists can offer a higher tumor accumulation, and thus lead to an improved tumor-to-background ratio.

In this thesis, we focused our attention on applying new chemical and radiochemical strategies to our biovectors. One of the most promising approaches described in the literature is the application of bioorthogonal reactions. In the past decade, bioorthogonal reactions were applied to pretargeting, drug-to-release and labeling strategies. These reactions played an important role in this thesis and most chapters involved multiple click reactions. Therefore, in **Chapter 2**, a review explored the potential of the most relevant bioorthogonal and click reactions (e.g., CuAAC and SPAAC), with a special focus on IEDDA due to its fully bioorthogonal characteristics. Recently, the IEDDA reaction was instrumental for the regioselective labeling of antibodies with short lived radioisotopes using the pretaregting strategy [10,11]. Lewis and Zeglis demonstrated the positive outcomes of pretargeting by comparing this approach to the conventional direct targeting [12,13]. Additionally, those reactions could help to overcome the limitations of the existing therapeutic agents, by enabling the release of the drug at the disease site (e.g., drug-to-release).




In **Chapter 3**, we used the IEDDA click reaction to perform regioselective dual-labeling. In fact, the TCO moiety coupled to the NeoB analogs reacted with the Tz conjugated to the sCy5 fluorescent dye resulting in the generation of four dual-labeled probes (**12** – **15**) for image-guided surgery of PCa. Indeed, due to the high recurrence rates (20 – 40%) of PCa after prostatectomy, we aimed to help the surgeon to remove more precisely the cancer tissue. Our four dual-labeled probes were successfully synthesized, characterized and evaluated in vitro and in vivo. A high RCY (> 90%) was achieved when the probes were radiolabeled with indium-111. Despite the introduction of hydrophobic prosthetic groups (e.g., TCO), the four NeoB analogs conserved their hydrophilicity ($LogD_{4.7}$ < -1.5). The binding affinity of the four dual-labeled probes was 9.2 – 24.7-fold lower than the binding affinity of the parent peptide NeoB (44.1 – 118.7 nM compared to 4.8 nM respectively). The four probes showed excellent stability in mouse serum (> 94% intact radiolabeled peptides) up to 4 h post incubation at 37 °C. However, sensitivity to radiolysis was observed in PBS (e.g., 33.7% intact [$^{111}$In]In-**14** at 4 h post incubation at 37 °C). Two NeoB analogs ([$^{111}$In]In-**12** and [$^{111}$In]In-**15**) were tested in vivo. The obtained data showed that the pharmacokinetic profile of the two probes was modified compared to NeoB. Thus, longer blood circulation was observed resulting in higher uptake in the excretory organs (liver and kidneys), this is probably due to the modified lipophilicity and global charge of the radiopharmaceuticals. The high liver uptake can be also attributed to the large size of the molecules. However, high radioactive and fluorescent tumor accumulation was reported 2 h post injection for both dual-labeled probes. In **Chapter 4**, further studies were conducted to better evaluate the four dual-labeled probes.

In **Chapter 4**, we further investigated the utility of our four dual-labeled probes. In vitro cell binding assay showed that the four dual-labeled probes had lower uptake into the GRPR-positive PC3 cells compared to the parent peptides NeoB. Besides, lower membrane bound fraction of [$^{111}$In]In-**12**-**15** was observed than [$^{111}$In]In-NeoB (47.7 – 61.0% compared to 88.0%, respectively). Specificity of [$^{111}$In]In-**12**-**15** to GRPR was confirmed by a blocking group. Ex vivo biodistribution studies revealed similar patterns for the radioactive and fluorescent signals. Nearly identical tumor uptake was observed for the four dual-labeled probes at 4 h post injection. [$^{111}$In]In-**13** and [$^{111}$In]In-**15** showed extended blood circulation compared to [$^{111}$In]In-**12** and [$^{111}$In]In-**14** (5.49 and 6.91% IA/g compared to 2.26 and 2.68% IA/g at 4 h p.i., respectively). However, [$^{111}$In]In-**12** and [$^{111}$In]In-**14** exhibited better tumor retention compared to [$^{111}$In]In-**13** and [$^{111}$In]In-**15** (2.49 and 2.71% IA/g compared to 1.17 and 1.97% IA/g at 24 h p.i., respectively). High uptake was observed in the excretory organs (liver and kidneys) for all dual-labeled probes, however, [$^{111}$In]In-**14** showed the lowest renal accumulation. Dose optimization studies of [$^{111}$In]In-**14** revealed lower tumor uptake with increased injected dose (2.74% IA/g for 0.75 nmol; 2.35% IA/g for 1.25 nmol and 2.09% IA/g for 1.75 nmol). However, kidneys uptake also decreased when the dose injected increased, while liver and spleen uptake increased. The tumor was accurately localized using SPECT/CT imaging and could be precisely removed through the fluorescence guidance after administration of [$^{111}$In]In-**14**. As a result, the investigations performed in this chapter demonstrated the translational applicability of [$^{111}$In]In-**14** for image-guided resection of GRPR-positive tumors.

In **Chapter 5**, we introduced a new building block strategy based on the development of a multi-functionalized MSAP agent. The diversity of the attachment points available on the MSAP agent allowed orthogonal coupling of different functional groups. Thus, it enabled the incorporation of multiple prosthetic groups into the chemical structure of a biomolecule based on a single step reaction. To confirm the orthogonality of our newly synthesized MSAP agent, we customized it with a DOTA chelator and an AB or a TCO. Furthermore, we selectively introduced a maleimide group allowing the conjugation of the MSAP agent onto large biomolecules, such as antibodies, antibody fragments and nanobodies. In fact, the maleimide of the MSAP agent can be coupled to the sulfhydryl group of the cysteine present on those molecules through the thiol-maleimide Michael addition. As a proof-of-concept, a thiolated JR11 derivative was used to prepare two DOTA-JR11 analogs carrying an albumin-binding moiety (**9a**) or a TCO group (**9b**). Both compounds were obtained in high chemical purity (> 95%) and yields (76% and 35% for compounds **9a** and **9b**, respectively). Both peptides were successfully radiolabeled with indium-111 and obtained in very high RCYs (> 96%) and RCPs (> 94% and > 86% for [$^{111}$In]In-**9a** and [$^{111}$In]In-**9b**, respectively). **9a** and **9b** exhibited higher Log$D_{7.4}$ values compared to DOTA-JR11, probably due to the chemical modifications performed and the presence of groups known to be lipophilic (e.g., the albumin binder and TCO). They showed good stability towards peptidase digestion 3 h after incubation at 37 °C in mouse serum (> 92% intact radiopeptides). However, [$^{111}$In]In-**9a** showed a better stability towards radiolysis compared to [$^{111}$In]In-**9b** (90.9% vs. 75.1% intact radiopeptides at 3 h after incubation at 37 °C). This approach facilitates the obtention of multi-functionalized biovectors. Many functional groups can be introduced regioselectively, and the MSAP agent can be coupled to a large variety of biomolecules offering the possibility to generate a large library of compounds in a single step synthesis.




**Chapter 6** consisted in the evaluation of two DOTA-JR11 analogs carrying albumin binding moieties. The pharmacokinetic profile of DOTA-JR11 needs to be improved due to the fast clearance of the radiopeptide upon injection, leading to a suboptimal tumor uptake. Albumin binders were introduced in the literature as potential tools to increase the blood half-life of drugs [14–16]. Thus, two DOTA-JR11 analogs containing the 4-(4-iodophenyl) butanoate or the 4-(*p*-methoxyphenyl)butanoate (**8a** and **8b**, respectively) were synthesized and evaluated in vitro and in vivo. Peptides **8a** and **8b** were obtained in 9.9 and 8.7% chemical yield, respectively. They were successfully radiolabeled with lutetium-177 and obtained in high RCYs (> 98%) and RCPs (> 97%). The lipophilicity of the newly synthesized peptides was slightly affected due to the chemical modifications performed (-1.60, -2.07 for [$^{177}$Lu]Lu-**8a** and [$^{177}$Lu]Lu-**8b** vs. -2.5 for [$^{177}$Lu]Lu-DOTA-JR11). [$^{177}$Lu]Lu-**8a** showed better binding to human albumin compared to [$^{177}$Lu]Lu-**8b** confirming data reported in previous studies [17]. Both radiopeptides showed excellent inertness towards radiolysis (> 95% intact radiopeptides) and peptidase digestion (> 97% intact radiopeptides) up to 24 h after incubation in PBS and mouse serum, respectively. Both compounds showed a binding affinity 30 – 48-fold lower than the binding affinity of the parent peptide DOTA-JR11. [$^{177}$Lu]Lu-**8a** and [$^{177}$Lu]Lu-**8b** showed a good uptake in U2OS.SSTR2 cells (7.8 and 3.1% AD, respectively), but lower than the uptake of [$^{177}$Lu]Lu-DOTA-JR11 (16.2% AD). The internalization studies confirmed that both radiopeptides conserved their antagonistic properties. SPECT/CT imaging revealed that the introduction of the albumin binding moiety in compound **8a** remarkably improved its blood circulation and led to an increase in the tumor uptake. However, no tumor uptake was observed for [$^{177}$Lu]Lu-**8b**. Ex vivo biodistribution studies performed for [$^{177}$Lu]Lu-**8a** and [$^{177}$Lu]Lu-DOTA-JR11 confirmed the imaging data. Blocking studies showed that more non-specific tumor uptake was observed for [$^{177}$Lu]Lu-**8a** than [$^{177}$Lu]Lu-DOTA-JR11. Furthermore, higher kidney uptake was noticed for [$^{177}$Lu]Lu-**8a** compared to [$^{177}$Lu]Lu-DOTA-JR11 (21.6 and 3.4% ID/g at 72 h after injection, respectively). In conclusion, the introduction of an albumin binder to improve the pharmacokinetic profile of a biomolecule does not always lead to positive outcomes. There is no 'universal' albumin binder that can offer ideal outputs for all biomolecules; therefore, the 'optimal' albumin binder has to be identified for each bioconjugate separately.

In **Chapter 7**, we explored the potential of TAT for the treatment of NETs. Treatment resistance and disease recurrence are observed after PRRT of NETs, therefore, there is a need to improve the therapeutic index of [$^{177}$Lu]Lu-DOTA-TATE. TAT might offer a better alternative than conventional targeted radionuclide therapy due to the high LET of alpha particles compared to beta emitters. Thus, we studied the possibility of using [$^{225}$Ac]Ac-DOTA-JR11 for TAT of NETs. Furthermore, a side-by-side comparison was performed with [$^{177}$Lu]Lu-DOTA-JR11. DOTA-JR11 was successfully radiolabeled with [$^{225}$Ac]Ac($NO_3$)$_3$ and obtained in high RCY and RCP (94.9 and 93.6%, respectively). [$^{225}$Ac]Ac-DOTA-JR11 was slightly more sensitive to radiolysis compared to [$^{177}$Lu]Lu-DOTA-JR11 (76.9 and 96.8% intact radiolabeled peptides at 22 and 24 h, respectively). Additionally, modest degradation of [$^{225}$Ac]Ac-DOTA-JR11 was observed in mouse serum compared to [$^{177}$Lu]Lu-DOTA-JR11 (80.9 and 93.7% intact radiolabeled peptides at 22 and 24 h, respectively). Competitive binding assay showed that $^{nat}$La-DOTA-JR11 and $^{nat}$Lu-DOTA-JR11 exhibited similar $IC_{50}$ values than the non-complexed DOTA-JR11 (4.71, 3.88 and 4.69 nM, respectively). These findings suggested that the complexation of DOTA-JR11 with actinium-225 and lutetium-177 did not affect the affinity of DOTA-JR11 to SSTR2. In vivo studies showed that [$^{225}$Ac]Ac-DOTA-JR11 presented similar biodistribution profile to [$^{177}$Lu]

Lu-DOTA-JR11. Although identical tumor uptake was reported for both radiopeptides, significantly higher kidneys, liver and bone uptake was observed for [$^{225}$Ac]Ac-DOTA-JR11 than [$^{177}$Lu]Lu-DOTA-JR11. Dosimetry studies showed that the low tumor/kidney ratio (0.35) limits the possibility of using [$^{225}$Ac]Ac-DOTA-JR11 for TAT of NETs. Further improvements need to be performed to reduce the absorbed dose to the kidneys and lower nephrotoxicity due to alpha particles.

This thesis aimed at exploring different strategies to improve imaging and treatment of PCa and NETs. Through the different chapters, we showed that a variety of NeoB and DOTA-JR11 analogs were successfully synthesized and characterized. Radiolabeling with different radioisotopes (e.g., indium-111, lutetium-177 and actinium-225) for SPECT imaging and targeted radionuclide therapy were successfully achieved using optimized conditions. The impact of the chemical modifications on the biochemical properties of the corresponding peptide vectors was characterized in vitro. Finally, our labeled peptide analogs were evaluated in vivo in diverse preclinical models to determine their pharmacokinetics and biodistribution profiles.

## General discussion

***The click reactions as a potent tool in chemical synthesis***

We showed through the different chapters presented in this thesis (**Chapters 2**, **3, 4** and **5**) the important role that click reactions can play in synthetic approaches. The high chemoselectivity of these reactions, their fast kinetics, the stability of the generated products and their occurrence under friendly conditions constitute an asset to overcome the limitations encountered during conventional synthesis strategies [18]. Thus, the orthogonality of the click reactions eased the functionalization of biomolecules via the development of MSAP agents and the obtention of a library of compounds based on a single step synthesis [19]. Furthermore, the bioorthogonal properties of these chemical reactions (i.e., IEDDA) offered the possibility to introduce new research lines aiming to overcome the drawbacks of the existing techniques. For instance, the pretargeting strategy was introduced as a very promising approach to overcome the limitations of direct targeting. Several investigations showed the positive outcomes achieved with the pretargeting approach in optimizing radionuclide therapy using antibodies [20,21]. Besides, the IEDDA reaction was applied to the "click-to-release" approach aiming at specifically deliver a drug to the tumor cells while sparing the surrounding healthy tissues [22]. On the other hand, several studies reported challenges related to the use of such approaches. In fact, the click moieties were reported to be sensitive to acidic and basic conditions encountered during the synthesis. Furthermore, higher reactivity of the tetrazine results in lower stability and vis versa. Besides, the optimal timing should be identified between the injection of the first and the second click moiety. Administration of the second click moiety should be performed when ideal tumor accumulation and washout from untargeted organs is achieved for the first click moiety. This might require the injection of masking or clearing agent prior to the administration of the second click moiety. Hence, leading to more logistic optimizations. Furthermore, it is not clear yet whether both molecules should be injected using the same dose, thus the reaction occurring at a 1:1 molar ratio, or if different ratios should be studied to obtain the best output.

***Dual-modality labeled probes for image-guided surgery of PCa***

It is often crucial to avoid tumor-positive margins during surgical resection in order to reduce the risk of tumor recurrence. Image-guided surgery, a surgical procedure relying on the injection of a fluorescent tracer, was introduced as a new technique for the removal of solid tumors (e.g., breast, prostate, kidney and lung cancers) with high accuracy [23,24]. Dual-modality imaging probes, designed to accumulate in the malignant tissue, were recently developed to harness the benefits of both the preoperative localization of the malignant lesions via PET imaging and the intraoperative surgical guidance by optical imaging. Indeed, fluorescence imaging offers real-time visualization of the tumors and delineation of the resection margins during surgery [25–28]. Thus, dual-modality labeled compounds offer multiple advantages compared to mono-modality labeled probes. This strategy allows the synthesis of one molecule carrying two different functional groups providing two information. Consequently, this leads to limit the costs related to the preparation and validation of the probe. Furthermore, one injection of the probe radiolabeled with a PET radionuclide is sufficient to provide accurate information about the localization of the tumor and the possibility for the patient to benefit from fluorescence-guided surgery. Besides, the fluorescent dye of the same probe helps to precisely remove the cancer tissue during surgery. Additionally, a dual-labeled probe obeys to one pharmacokinetic profile, which might not be the case if two mono-labeled compounds are used. One the other hand, dual-labeled probes are usually large molecules, meaning that their pharmacokinetic profile might be modified compared to the parent compound. The chemical modifications (e.g., fluorescent dye) can modify the hydrophilicity of the dual-labeled probe and consequently lead to undesired uptake in non-targeted organs (e.g., liver). Furthermore, addition of charges, modification of the hydrophilicity and the size of the final molecule can modify the excretion route of the radiopharmaceutical.

Even though, the combination of radioactive imaging and fluorescent imaging showed its potential in different studies, there is a need to find the optimal injected dose based on the sensitivity of the scanner and the level of expression of the molecular target. In fact, due to the high sensitivity of nuclear imaging, few picomoles are enough to achieve high resolution images. However, in optical imaging, higher concentrations of the fluorescent dye have to be administered to achieve high tumor-to-background contrast. Furthermore, the quality of the signal provided by the fluorescent dye is related to its emission wavelength and its quantum yield, therefore, the best fluorescent dye has to be selected.





***Albumin binders for improved radionuclide therapy of NETs***

The fast excretion of the radioligands upon administration, the high kidney accumulation and the partial response observed during targeted radionuclide therapy encouraged scientists to improve the pharmacokinetic profile of the bioconjugates. Hence, the insertion of albumin binding moieties into the chemical structure of diverse biomolecules was confirmed to elongate their blood retention and increase the tumor uptake [17,29]. The aim of this strategy is to improve the bioavailability of the radioligands to increase their tumor accumulation and ideally reduce the radiotoxicity to non-targeted organs (e.g., kidneys and bone marrow). Although several studies reported the benefit of this strategy to increase the dose delivered to the tumor and limit nephrotoxicity, others reported the disadvantages of an extended blood circulation [15,16]. In fact, the increased blood half-life of the radioligand can lead to an increased renal uptake due to the excretory pathway. Furthermore, extended blood circulation can cause toxicity to the bone marrow, known to be highly sensitive to radiation, thus limiting the therapeutic index of the radiopharmaceutical. In the study presented in this thesis, we have shown that the extended blood residence of our radioligand bearing an albumin binder caused undesired radioactive accumulation in healthy organs (e.g., kidneys, liver, spleen, heart, ...).

The rapid excretion of a peptide from the blood circulation leads to suboptimal tumor accumulation, therefore albumin binding moieties might be used. The introduction of an albumin binder helps to extend the blood residence of a radiopharmaceutical. However, the unbound radiopharmaceutical should be cleared from the blood circulation and must not accumulate in the non-targeted organs (e.g., bone marrow, kidneys, liver, ...) causing undesired radiotoxicity to healthy tissues. Therefore, ideal albumin binder should be identified to provide the most optimal pharmacokinetic profile to a radiopharmaceutical.

***TAT as a powerful tool for improved treatment of NETs***

The higher radiotoxicity of alpha particles compared to beta particles induces more DNA double-strand breaks. This leads to a more efficient cell death, and consequently to an enhanced treatment efficacy. This property offered by the alpha particles (e.g., actinium-225, bismuth-213, lead-212) was applied in different preclinical and clinical studies [30–34]. In the literature, several investigations using [$^{225}$Ac]Ac-PSMA and [$^{225}$Ac]Ac-DOTA-TATE showed that better treatment efficiency was achieved using TAT compared to the standard radionuclide therapy [30,35]. However, the high radiotoxicity of the alpha particles can constitute the limiting point of this approach in clinical settings. In fact, several preclinical and clinical studies demonstrated the radiotoxicity effects of $^{225}$Ac-labeled ligands to non-targeted organs, such as the bone marrow and the salivary glands [31,36,37]. Additionally, the recoil effect and the distribution of the daughter radionuclides after being released from the chelate needs to be clarified. There is a controversy about the fate of the daughter radionuclides: are they directly eliminated or do they distribute through the body causing undesired radiotoxicity to non-targeted organs? Therefore, several studies reported the advantages of using internalizing biovectors to thwart the recoil effect.

Actinium-225 has the advantage of a relatively long half-life ($t_{1/2}$ = 9.9 days) suitable for efficient TAT compared to other alpha particles such as bismuth-213 ($t_{1/2}$ = 45.6 min). It is the parent radionuclide of multiple alpha particles generated in vivo and this property makes it particularly cytotoxic. The high cytotoxicity of actinium-225 plays an important role in improving the therapeutic index of TAT. The radioisotope has the advantage to be complexed by the DOTA chelator, approved for its clinical relevance. On the other hand, actinium-225 has the disadvantage of generating multiple alpha particles in vivo, that can cause undesired toxicity to healthy tissues. Furthermore, due to the high cytotoxicity of the radionuclide, limited number of therapeutic cycles can be considered, which is limiting the efficacy of $^{225}$Ac-mediated TAT. Besides, its clinical application should be implemented by well-trained personnel and should follow validated protocols for radiolabeling and quality control.

Although TAT was presented as a promising alternative to the standard targeted radionuclide therapy, further research and optimization have to be conducted in order to determine the potential side effects and radiotoxicity.

## Future perspectives

Multiple strategies were recently developed to overcome the disadvantages encountered in various existing techniques for imaging and therapy of different types of cancer. The ideal technique adapted to all types of cancer might not have been found yet, however, our research was aiming to find optimized methods that offer limited drawbacks for diagnosis and treatment of cancers.

The dual-modality imaging strategy presented in this thesis demonstrated the real potential of using dual imaging modalities compared to a mono imaging modality in image-guided surgery of PCa. Additionally, our studies showed that optimized parameters (scanning time, injected dose and tumor/organ ratios) have to be identified for an optimal outcome. This strategy can be applied for image-guided surgery of various types of solid tumors. However, developing a new dual-modality imaging probe require extensive efforts to obtain optimized parameters (e.g., physicochemical properties, binding affinity, pharmacokinetics, tumor specificity, ...) that can lead to an ideal outcome.

For the treatment of other cancer tissues, based on our findings and other studies reported in the literature and for future investigations, we think that the most optimized strategy for a successful therapy study, would be the application of the pretargeting approach. This strategy, separating the biovector from the radionuclide offers safer therapy. In fact, the administration of an unlabeled biovector would allow its accumulation mainly at the tumor site (due to difference in washout between the tumor and the non-targeted organs). Next, based on a bioorthogonal reaction, accumulation of the radionuclide will be specifically occurring at the tumor site. However, if the pretargeting approach is based on peptides, known to be rapidly cleared from the blood circulation, it is important to improve their bioavailability to maximize the tumor uptake. Therefore, the peptide carrying a TCO can be customized with an albumin binding moiety to improve its blood residence and thus increase the accumulation at the tumor site. As the biovector does not carry any radionuclide at this stage, its prolonged blood residence will not present significant undesirable side effects. An adapted albumin binder has to be selected in order to achieve an optimized blood residence and tumor accumulation. Higher tumor uptake of the unlabeled biovector would lead to an optimized bioorthogonal reaction in vivo and consequently, help to achieve higher doses to the cancer tissue. It is very important to mention that the pretargeting approach must be applied using antagonists. In fact, the bioorthogonal reaction between the peptide and the small molecule carrying the radionuclide is easier if the peptide is present at the membrane side and not internalized inside the cancer cell. The click reaction must be fully bioorthogonal (e.g., IEDDA). Besides, the small molecule carrying the radionuclide should not show uptake in non-targeted organs and must be rapidly cleared upon administration. For therapy studies, in order to achieve the best therapeutic index, a toxic radionuclide can be chosen (e.g., actinium-225) thus, offering the possibility to induce selective radiotoxicity mainly to the cancer cells.

In Chapter 6 of this thesis, we observed that the binding affinity of the DOTA-JR11 analogs was affected due to the chemical modifications at the N-terminal of the peptides. This observation is in agreement with what was previously reported [38]. Therefore, a potential alternative would be to introduce the chemical modifications (e.g., TCO, albumin binder, fluorescent dye, …) at the C-terminal position. Thus, the binding affinity of the peptide to SSTR2 might be conserved. We are currently working on optimizing the pharmacokinetic profile of DOTA-JR11 analogs by introducing different albumin binding moieties at the C-terminal of the peptides. Dansylglycine and palmitic acid were introduced to have good binding properties to human albumin. Therefore, we synthesized DOTA-JR11 analogs carrying the albumin binders at the C-terminal of the peptides. Furthermore, different studies reported in the literatures showed the optimized pharmacokinetic profile obtained with palmitic acid carrying a free acid group and introduced to the biovector through two $PEG_2$ linkers and a glutamic acid. Therefore, synthesis and evaluation of the new peptides are underway.

## References


1. Jadvar H. Targeted radionuclide therapy: An evolution toward precision cancer treatment. AJR 2017;209:277–288.
2. Ersahin D, Doddamane I, Cheng D. Targeted radionuclide therapy. Cancers 2011;3:3838–3855.
3. Das S, Al-Toubah T, El-Haddad G, Strosberg J. 177Lu-DOTATATE for the treatment of gastroenteropancreatic neuroendocrine tumors. Expert Rev Gastroenterol Hepatol 2019;13:1023–1031.
4. Ruigrok EAM, Verhoeven M, Konijnenberg MW, de Blois E, de Ridder CMA, Stuurman DC, et al. Safety of [177Lu]Lu-NeoB treatment: a preclinical study characterizing absorbed dose and acute, early, and late organ toxicity. EJNMMI 2022;49:4440–4451.
5. Dalm SU, Nonnekens J, Doeswijk GN, De Blois E, Van Gent DiC, Konijnenberg MW, et al. Comparison of the therapeutic response to treatment with a 177Lu-labeled somatostatin receptor agonist and antagonist in preclinical models. J Nucl Med 2016;57:260–265.
6. Liu Z, Yang C, Zeng X, Ke C, Tian J, Wang Z, et al. Effectiveness of GnRH Antagonists and Agonists in Patients with Hormone-Sensitive Prostate Cancer: A Retrospective Study. Appl Bionics Biomech 2022;2022:1–5.
7. Nock BA, Kaloudi A, Lymperis E, Giarika A, Kulkarni HR, Klette I, et al. Theranostic perspectives in prostate cancer with the gastrin-releasing peptide receptor antagonist NeoBOMB1: Preclinical and first clinical results. J Nucl Med 2017;58:75–80.
8. Rylova SN, Stoykow C, Del Pozzo L, Abiraj K, Tamma ML, Kiefer Y, et al. The somatostatin receptor 2 antagonist 64Cu-NODAGA-JR11 outperforms 64Cu-DOTA-TATE in a mouse xenograft model. PLoS One 2018;13:1–16.
9. Zhu W, Cheng Y, Wang X, Yao S, Bai C, Zhao H, et al. Head-to-head comparison of 68Ga-DOTA-JR11 and 68Ga-DOTATATE PET/CT in patients with metastatic, well-differentiated neuroendocrine tumors: A prospective study. J Nucl Med 2020;61:897–903.
10. Rondon A, Degoul F. Antibody Pretargeting Based on Bioorthogonal Click Chemistry for Cancer Imaging and Targeted Radionuclide Therapy. Bioconjug Chem 2020;31:159–173.
11. Bailly C, Bodet-Milin C, Rousseau C, Faivre-Chauvet A, Kraeber-Bodéré F, Barbet J. Pretargeting for imaging and therapy in oncological nuclear medicine. EJNMMI Radiopharm Chem 2017;2:1–14.
12. Houghton JL, Zeglis BM, Abdel-Atti D, Sawada R, Scholz WW, Lewis JS. Pretargeted immuno-PET of pancreatic cancer: Overcoming circulating antigen and internalized antibody to reduce radiation doses. J Nucl Med 2016;57:453–459.
13. Meyer JP, Houghton JL, Kozlowski P, Abdel-Atti D, Reiner T, Pillarsetty NVK, et al. 18F-Based Pretargeted PET Imaging Based on Bioorthogonal Diels-Alder Click Chemistry. Bioconjug Chem 2016;27:298–301.
14. Müller C, Struthers H, Winiger C, Zhernosekov K, Schibli R. DOTA conjugate with an albumin-binding entity enables the first folic acid-targeted 177Lu-radionuclide tumor therapy in mice. J Nucl Med 2013;54:124–131.
15. Rousseau E, Lau J, Zhang Z, Uribe CF, Kuo HT, Zhang C, et al. Effects of adding an albumin binder chain on [177Lu]Lu-DOTATATE. Nucl Med Biol 2018;66:10–17.
16. Tiel S van, Tiel S van, Maina T, Nock B, Konijnenberg M, Blois E de, et al. Albutate-1, a Novel Long-Circulating Radiotracer Targeting the Somatostatin Receptor Subtype 2. J Nucl Med Radiat Sci 2021;2:1–9.
17. Kuo HT, Lin KS, Zhang Z, Uribe CF, Merkens H, Zhang C, et al. 177Lu-labeled albumin-binder-conjugated PSMA-targeting agents with extremely high tumor uptake and enhanced tumor-to-kidney absorbed dose ratio. J Nucl Med 2021;62:521–527.
18. Handula M, Chen KT, Seimbille Y. Iedda: An attractive bioorthogonal reaction for biomedical applications. Molecules 2021;26:1–20.
19. Chen KT, Nieuwenhuizen J, Handula M, Seimbille Y. A novel clickable MSAP agent for dual fluorescence/nuclear labeling of biovectors. Org Biomol Chem 2020;18:6134–6139.
20. Keinänen O, Brennan JM, Membreno R, Fung K, Gangangari K, Dayts EJ, et al. Dual Radionuclide Theranostic Pretargeting. Mol Pharm 2019;16:4416–21.
21. Membreno R, Cook BE, Fung K, Lewis JS, Zeglis BM. Click-Mediated Pretargeted Radioimmunotherapy of Colorectal Carcinoma. Mol Pharm 2018;15:1729–34.

22. Rossin R, Versteegen RM, Wu J, Khasanov A, Wessels HJ, Steenbergen EJ, et al. Chemically triggered drug release from an antibody-drug conjugate leads to potent antitumour activity in mice. Nat Commun 2018;9:1–11.
23. Tringale KR, Pang J, Nguyen QT. Image-guided surgery in cancer: A strategy to reduce incidence of positive surgical margins. Wiley Interdiscip Rev Syst Biol Med 2018;10:1–18.
24. Wojtynek NE, Mohs AM. Image-guided tumor surgery: The emerging role of nanotechnology. Wiley Interdiscip Rev Nanomed Nanobiotechnol 2020;12:1–45.
25. Hernandez Vargas S, Lin C, Tran Cao HS, Ikoma N, AghaAmiri S, Ghosh SC, et al. Receptor-Targeted Fluorescence-Guided Surgery With Low Molecular Weight Agents. Front Oncol 2021;11:1–15.
26. Goto M, Ryoo I, Naffouje S, Mander S, Christov K, Wang J, et al. Image-guided surgery with a new tumour-targeting probe improves the identification of positive margins. EBioMedicine 2022;76:103850.
27. Li D, Zhang J, Chi C, Xiao X, Wang J, Lang L, et al. First-in-human study of PET and optical dual-modality image-guided surgery in glioblastoma using 68Ga-IRDye800CW-BBN. Theranostics 2018;8:2508–2520.
28. Zhang H, Desai P, Koike Y, Houghton J, Carlin S, Tandon N, et al. Dual-modality imaging of prostate cancer with a fluorescent and radiogallium-labeled gastrin-releasing peptide receptor antagonist. J Nucl Med 2017;58:29–35.
29. Xu M, Zhang P, Ding J, Chen J, Huo L, Liu Z. Albumin Binder–Conjugated Fibroblast Activation Protein Inhibitor Radiopharmaceuticals for Cancer Therapy. J Nucl Med 2022;63:952–958.
30. Zacherl MJ, Gildehaus FJ, Mittlmeier L, Böning G, Gosewisch A, Wenter V, et al. First Clinical Results for PSMA-Targeted α-Therapy Using 225Ac-PSMA-I&T in Advanced-mCRPC Patients. J Nucl Med 2021;62:669–674.
31. Dhiantravan N, Hofman MS, Ravi Kumar AS. Actinium-225 Prostate-specific Membrane Antigen Theranostics: Will α Beat β? Eur Urol 2021;79:351–352.
32. Lawal IO, Morgenstern A, Vorster M, Knoesen O, Mahapane J, Hlongwa KN, et al. Hematologic toxicity profile and efficacy of [225Ac]Ac-PSMA-617 α-radioligand therapy of patients with extensive skeletal metastases of castration-resistant prostate cancer. EJNMMI 2022;49:3581–3592.
33. Paden KA, NT G, Raju N, Stanley F. 225Ac-Macropatate: A Novel Alpha Particle Peptide Receptor Radionuclide Therapy for Neuroendocrine Tumors. J Nucl Med 2022:1–25.
34. Kratochwil C, dos Santos J, Lehnert W, Bruchertseifer F, Morgenstern A, Haberkorn U, et al. Development and dosimetry of Pb-203/Pb-212 labeled PSMA ligands – Bringing “the Lead” into PSMA-Targeting Alpha Therapy? EJNMMI 2019;58:1081–1091.
35. Ballal S, Yadav MP, Bal C, Sahoo RK, Tripathi M. Broadening horizons with 225Ac-DOTATATE targeted alpha therapy for gastroenteropancreatic neuroendocrine tumour patients stable or refractory to 177Lu-DOTATATE PRRT: first clinical experience on the efficacy and safety. EJNMMI 2020;47:934–946.
36. Pelletier K, Côté G, Fallah-Rad N, John R, Kitchlu A. CKD After 225Ac-PSMA617 Therapy in Patients With Metastatic Prostate Cancer. Kidney Int Rep 2021;6:853–856.
37. Scheinberg DA, McDevitt MR. Actinium-225 in targeted alpha-particle therapeutic applications. Curr Radiopharm 2011;4:306–320.
38. Fani M, Braun F, Waser B, Beetschen K, Cescato R, Erchegyi J, et al. Unexpected sensitivity of sst 2 antagonists to N-terminal radiometal modifications. J Nucl Med 2012;53:1481–1489.

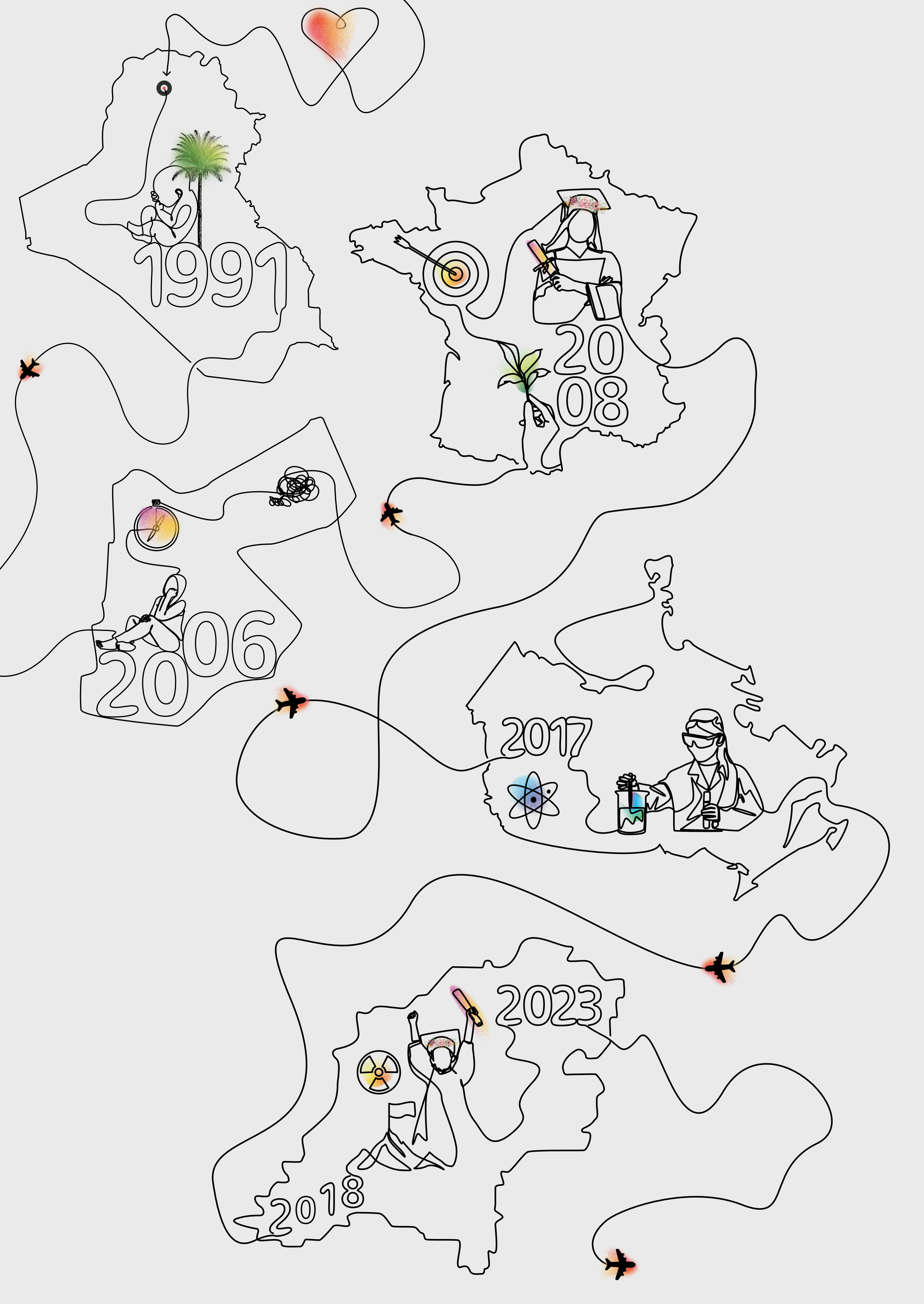

1991
2008
2006
2017
2023
2018

# APPENDIX

# A

Nederlandse Samenvatting

Curriculum Vitae

List of Publications

Oral and Poster Presentations

PhD Portfolio

Acknowledgments

# Nederlandse Samenvatting

Gerichte beeldvorming en therapie met radionucliden werd een primordiaal hulpmiddel voor de diagnose en behandeling van meerdere soorten kanker [1,2]. Deze aanpak demonstreerde het potentieel om positieve resultaten te bereiken met behulp van peptide-agonisten en antagonist-analogen [3–5]. Bovendien biedt de beschikbaarheid van een groot spectrum aan radio-isotopen de mogelijkheid om deze bio-vectoren radioactief te labelen met diverse diagnostische (vb. indium-111, gallium-68 ...) en therapeutische (vb. lutetium-177, yittrium-90 ...) radionucliden. Dit biedt de mogelijkheid om de beste radiofarmaca te vinden voor een gepersonaliseerde en efficiëntere nucleaire geneeskunde.

Binnen dit proefschrift zijn verschillende strategieën onderzocht om de diagnose en behandeling van prostaatcarcinoom (PCa) en neuroendocrine tumoren (NET's) te verbeteren door ons respectievelijk op GRPR en SSTR2 te richten. De incidentie en de ernst van die soorten kanker motiveerden ons om de nadruk te leggen op strategieën die van invloed kunnen zijn op de behandeling van PCa- en NET-patiënten. Binnen ons onderzoek hebben wij ons er op gericht met GRPR- en SSTR2-antagonisten te werken. In veel onderzoeken is de betere prestatie van peptide-antagonisten dan voor agonisten gerapporteerd [6–9]. Het is beschreven dat antagonisten een hogere tumoraccumulatie kunnen bieden en dus kunnen leiden tot een verbeterde tumor-tot-achtergrondverhouding.

In dit proefschrift hebben wij onze aandacht gericht op het toepassen van nieuwe chemische en radiochemische strategieën voor onze bio-vectoren. Een van de meest veelbelovende benaderingen beschreven in de literatuur, is de toepassing van bio-orthogonale reacties. In het afgelopen decennium werden bio-orthogonale reacties toegepast op pretargeting-, drug-to-release- en labelingstrategieën. Deze reacties speelden een belangrijke rol in dit proefschrift en de meeste hoofdstukken gaan over meerdere klikreacties. Daarom is in **Hoofdstuk 2** een overzichtsstudie uitgevoerd waarin het potentieel van de meest relevante bio-orthogonale en klikreacties (bijv. CuAAC en SPAAC) is onderzocht, met speciale aandacht voor IEDDA vanwege de volledig bio-orthogonale kenmerken ervan. Onlangs speelde de IEDDA-reactie een belangrijke rol bij de regio-selectieve labeling van antilichamen met kortlevende radio-isotopen met behulp van de pretaregting-strategie [10,11]. Lewis en Zeglis demonstreerden de positieve resultaten van pretargeting door deze aanpak te vergelijken met de conventionele directe targeting [12,13]. Bovendien zouden die reacties kunnen helpen om de beperkingen van de bestaande therapeutische middelen te overwinnen, door de afgifte van het geneesmiddel op de plaats van de ziekte, mogelijk te maken (bijv. drug-to-release).

In **hoofdstuk 3** hebben we de IEDDA-klikreactie gebruikt om regioselectieve dual-labeling uit te voeren. In feite reageerde de TCO-groep gekoppeld aan de NeoB-analogen met de Tz geconjugeerd aan de sCy5-fluorescente kleurstof, wat resulteerde in de generatie van vier dubbel gelabelde probe (**12** - **15**) voor beeldgeleide chirurgie van PCa. Vanwege de hoge recidiefpercentages (20 - 40%) van PCa na een prostatectomie, wilden wij de chirurg ondersteunen om het kankerweefsel nauwkeuriger te kunnen verwijderen. Onze vier dubbel gelabelde probes werden met succes in vitro en in vivo gesynthetiseerd, gekarakteriseerd en geëvalueerd. Een hoge RCY (> 90%) werd bereikt wanneer de probes radioactief werden gemerkt met Indium-111. Ondanks de introductie van hydrofobe prothetische groepen (bijv. TCO), behielden de vier NeoB-analogen hun hydrofiliciteit ($LogD_{4.7}$ < -1.5). De bindingsaffiniteit van de vier dubbel gelabelde probes was 9,2 – 24,7 maal lager dan de bindingsaffiniteit van het oorspronkelijke peptide NeoB (respectievelijk 44,1 – 118,7 nM vergeleken met 4,8 nM). De vier probes vertoonden uitstekende stabiliteit in muizenserum (> 94% intacte radioactief gemerkte peptiden) tot 4 uur na incubatie bij 37 °C. Gevoeligheid voor radiolyse werd echter waargenomen in PBS (bijv. 33,7% intact [$^{111}$In]In-**14**, 4 uur na incubatie bij 37 °C). Twee NeoB-analogen ([$^{111}$In]In-**12** en [$^{111}$In]In-**15**) werden in vivo getest. De verkregen gegevens toonden aan dat het farmacokinetische profiel van de twee probes gewijzigd was in vergelijking met NeoB. Er werd dus een langere bloedcirculatie waargenomen, resulterend in een hogere opname in de uitscheidingsorganen (lever en nieren), dit is waarschijnlijk te wijten aan de gewijzigde lipofiliciteit en netto lading van het radiofarmacacon. De hoge leveropname kan ook worden toegeschreven aan de grote omvang van de moleculen. Echter, hoge radioactieve en fluorescerende tumoraccumulatie werd 2 uur na injectie gemeld voor beide dubbel gelabelde probes. In **Hoofdstuk 4** zijn verdere studies uitgevoerd om de vier dubbel gelabelde probes beter te kunnen evalueren.

In **Hoofdstuk 4** hebben we het nut van onze vier dubbel gelabelde probes verder onderzocht. In vitro celbindingsassays toonden aan dat de vier dubbel gelabelde probes een lagere opname hadden in de GRPR-positieve PC3-cellen in vergelijking met het moederpeptide NeoB. Bovendien werd een lagere membraangebonden fractie van [$^{111}$In]In-**12**-**15** waargenomen dan [$^{111}$In]In-NeoB (respectievelijk 47,7 – 61,0% vergeleken met 88,0%). De specificiteit van [$^{111}$In]In-**12**-**15** voor GRPR werd bevestigd door een blokkerende groep. Ex vivo biodistributie studies onthulden vergelijkbare patronen voor de radioactieve en fluorescerende signalen. Bijna identieke tumoropname werd waargenomen voor de vier dubbel gelabelde sondes 4 uur na injectie. [$^{111}$In]In-**13** en [$^{111}$In]In-**15** vertoonden een verlengde bloedcirculatie vergeleken met [$^{111}$In]In-**12** en [$^{111}$In]In-**14** (5,49 en 6,91% IA/g vergeleken met 2,26 en 2,68% IA/g bij 4 h p.i., respectievelijk). [$^{111}$In]In-**12** en [$^{111}$In]In-**14** vertoonden echter een betere tumorretentie vergeleken met [$^{111}$In]In-**13** en [$^{111}$In]In-**15** (2,49 en 2,71% IA/g vergeleken met 1,17 en 1,97% IA/ g bij respectievelijk

24 uur p.i.). Hoge opname werd waargenomen in de uitscheidingsorganen (lever en nieren) voor alle dubbel gelabelde probes, maar [$^{111}$In]In-**14** vertoonde de laagste renale accumulatie. Dosisoptimalisatiestudies van [$^{111}$In]In-**14** onthulden een lagere tumoropname met een verhoogde geïnjecteerde dosis (2,74% IA/g voor 0,75 nmol; 2,35% IA/g voor 1,25 nmol en 2,09% IA/g voor 1,75 nmol). De opname door de nieren nam echter ook af wanneer de geïnjecteerde dosis toenam, terwijl de opname door de lever en de milt toenam. De tumor werd nauwkeurig gelokaliseerd met behulp van SPECT/CT-beeldvorming en kon nauwkeurig worden verwijderd door de fluorescentiegeleiding na toediening van [$^{111}$In]In-**14**. Als gevolg hiervan hebben de onderzoeken die in dit hoofdstuk zijn uitgevoerd de translationele toepasbaarheid aangetoond van [$^{111}$In]In-**14** voor beeldgeleide resectie van GRPR-positieve tumoren.

In **hoofdstuk 5** hebben wij een nieuwe bouwsteenstrategie gebaseerd op de ontwikkeling van een multifunctionele MSAP-agent geintroduceerd. De diversiteit van de beschikbare bevestigingspunten op de MSAP-agent maakte orthogonale koppeling van verschillende functionele groepen mogelijk. Het maakte dus de opname mogelijk van meerdere prothetische groepen in de chemische structuur van een biomolecuul op basis van een één-staps-reactie. Om de orthogonaliteit van onze nieuw gesynthetiseerde MSAP-agent te bevestigen, hebben we deze aangepast met een DOTA-chelator en een AB of TCO. Verder hebben wij selectief een maleïmidegroep geïntroduceerd die de conjugatie van het MSAP-agens aan grote biomoleculen mogelijk maakt, zoals antilichamen, antilichaamfragmenten en nanobodies. In feite kan het maleïmide van het MSAP-middel worden gekoppeld aan de sulfhydrylgroep van het cysteïne dat op die moleculen aanwezig is door de thiol-maleïmide Michael-additie. Als proof-of-concept werd een gethioleerd JR11-derivaat gebruikt om twee DOTA-JR11-analogen te bereiden die een albuminebindende groep (**9a**) of een TCO-groep (**9b**) droegen. Beide verbindingen werden verkregen met een hoge chemische zuiverheid (> 95%) en opbrengsten (respectievelijk 76% en 35% voor verbindingen **9a** en **9b**). Beide peptiden werden met succes radioactief gemerkt met indium-111 en verkregen in zeer hoge RCY's (> 96%) en RCP's (> 94% en> 86% voor respectievelijk [$^{111}$In]In-**9a** en [$^{111}$In]In-**9b**). 9a en 9b vertoonden hogere $LogD_{7.4}$-waarden in vergelijking met DOTA-JR11, waarschijnlijk als gevolg van de uitgevoerde chemische modificaties en de aanwezigheid van groepen waarvan bekend is dat ze lipofiel zijn (bijv. de albuminebinder en TCO). Ze vertoonden een goede stabiliteit ten opzichte van peptidasedigestie 3 uur na incubatie bij 37 °C in muizenserum (> 92% intacte radiopeptiden). [$^{111}$In]In-**9a** vertoonde echter een betere stabiliteit ten opzichte van radiolyse in vergelijking met [$^{111}$In]In-**9b** (90,9% vs. 75,1% intacte radiopeptiden 3 uur na incubatie bij 37 °C). Deze benadering vergemakkelijkt het verkrijgen van multifunctionele bio-vectoren. Veel functionele groepen kunnen regioselectief worden geïntroduceerd en het MSAP-middel kan worden gekoppeld aan een grote verscheidenheid aan biomoleculen, wat de mogelijkheid biedt om een grote bibliotheek van verbindingen te genereren in een enkele stapsgewijze synthese.

**Hoofdstuk 6** bestond uit de evaluatie van twee DOTA-JR11-analogen die albuminebindende delen dragen. Het farmacokinetisch profiel van DOTA-JR11 moet worden verbeterd vanwege de snelle klaring van het radiopeptide na injectie, wat leidt tot een suboptimale tumoropname. Albuminebinders werden in de literatuur geïntroduceerd als mogelijke middelen om de bloedhalfwaardetijd van geneesmiddelen te verhogen [14–16]. Aldus werden twee DOTA-JR11-analogen die het 4-(4-joodfenyl)butanoaat of het 4-(p-methoxyfenyl)butanoaat (respectievelijk **8a** en **8b**) bevatten, gesynthetiseerd en in vitro en in vivo geëvalueerd. Peptiden **8a** en **8b** werden verkregen met een chemische opbrengst van respectievelijk 9,9 en 8,7%. Ze werden met succes radioactief gelabeld met lutetium-177 en verkregen in hoge RCY's (> 98%) en RCP's (> 97%). De lipofiliciteit van de nieuw gesynthetiseerde peptiden werd enigszins beïnvloed door de uitgevoerde chemische modificaties (-1,60, -2,07 voor [$^{177}$Lu]Lu-**8a** en [$^{177}$Lu]Lu-**8b** vs. -2,5 voor [$^{177}$Lu]Lu-DOTA-JR11). [$^{177}$Lu]Lu-**8a** vertoonde een betere binding aan humaan albumine in vergelijking met [$^{177}$Lu]Lu-**8b**, wat gegevens bevestigt die in eerdere studies gerapporteerd zijn [17]. Beide radiopeptiden vertoonden een uitstekende inertheid ten opzichte van radiolyse (> 95% intacte radiopeptiden) en peptidase digestie (> 97% intacte radiopeptiden) tot 24 uur na incubatie in respectievelijk PBS en muizenserum. Beide verbindingen vertoonden een bindingsaffiniteit die 30 tot 48 maal lager was dan de bindingsaffiniteit van het oorspronkelijke peptide DOTA-JR11. [$^{177}$Lu]Lu-**8a** en [$^{177}$Lu]Lu-**8b** vertoonden een goede opname in U2OS.SSTR2-cellen (respectievelijk 7,8 en 3,1% AD), maar lager dan de opname van [$^{177}$Lu]Lu-DOTA-JR11 (16,2% AD). De internalisatiestudies bevestigden dat beide radiopeptiden hun antagonistische eigenschappen behouden. SPECT/CT-beeldvorming onthulde dat de introductie van de albumine-bindende groep in verbinding **8a** de bloedcirculatie opmerkelijk verbeterde en leidde tot een toename van de tumoropname. Er werd echter geen tumoropname waargenomen voor [$^{177}$Lu]Lu-**8b**. Ex vivo biodistributiestudies uitgevoerd voor [$^{177}$Lu]Lu-**8a** en [$^{177}$Lu]Lu-DOTA-JR11 bevestigden de beeldvormingsgegevens. Studies met een blokkerende groep toonden aan dat er meer niet-specifieke tumoropname werd waargenomen voor [$^{177}$Lu]Lu-**8a** dan voor [$^{177}$Lu]Lu-DOTA-JR11. Bovendien werd een hogere nieropname waargenomen voor [$^{177}$Lu]Lu-**8a** in vergelijking met [$^{177}$Lu]Lu-DOTA-JR11 (respectievelijk 21,6 en 3,4% ID/g 72 uur na injectie). Concluderend leidt de introductie van een albuminebindmiddel om het farmacokinetisch profiel van een biomolecuul te verbeteren niet altijd tot positieve resultaten. Er is geen 'universeel' albuminebindmiddel dat ideale output kan bieden voor alle biomoleculen; daarom moet voor elk bioconjugaat afzonderlijk de 'optimale' albuminebinder worden geïdentificeerd.

In **hoofdstuk 7** is het potentieel van TAT voor de behandeling van NET's onderzocht. Behandelingsresistentie en terugkeer van de ziekte worden waargenomen na PRRT van NET's, daarom is er behoefte aan verbetering van de therapeutische index van [$^{177}$Lu]Lu-DOTA-TATE. TAT zou een beter alternatief kunnen bieden dan conventionele gerichte radionuclidetherapie vanwege de hoge LET van alfadeeltjes in vergelijking met bètastralers. Daarom hebben we de mogelijkheid bestudeerd om [$^{225}$Ac]Ac-DOTA-JR11 te gebruiken voor TAT van NET's. Verder werd een side-by-side vergelijking uitgevoerd met [$^{177}$Lu]Lu-DOTA-JR11. DOTA-JR11 werd met succes radioactief gelabeled met [$^{225}$Ac]Ac$(NO_3)_3$ en verkregen in hoge RCY en RCP (respectievelijk 94,9 en 93,6%). [$^{225}$Ac]Ac-DOTA-JR11 was iets gevoeliger voor radiolyse in vergelijking met [$^{177}$Lu]Lu-DOTA-JR11 (respectievelijk 76,9 en 96,8% intacte radioactief gemerkte peptiden na 22 en 24 uur). Bovendien werd een gedeeltelijke afbraak van [$^{225}$Ac]Ac-DOTA-JR11 waargenomen in muizenserum in vergelijking met [$^{177}$Lu]Lu-DOTA-JR11 (respectievelijk 80,9 en 93,7% intacte radioactief gemerkte peptiden na 22 en 24 uur). Competitieve bindingsassay toonde aan dat $^{nat}$La-DOTA-JR11 en $^{nat}$Lu-DOTA-JR11 vergelijkbare $IC_{50}$-waarden vertoonden als de niet-gecomplexeerde DOTA-JR11 (respectievelijk 4,71, 3,88 en 4,69 nM). Deze bevindingen suggereerden dat de complexering van DOTA-JR11 met actinium-225 en lutetium-177 geen invloed had op de affiniteit van DOTA-JR11 met SSTR2. In vivo studies toonden aan dat [$^{225}$Ac]Ac-DOTA-JR11 een vergelijkbaar biodistributieprofiel vertoonde als [$^{177}$Lu]Lu-DOTA-JR11. Hoewel identieke tumoropname werd gerapporteerd voor beide radiopeptiden, werd significant hogere nier-, lever- en botopname waargenomen voor [$^{225}$Ac]Ac-DOTA-JR11 dan [$^{177}$Lu]Lu-DOTA-JR11. Dosimetriestudies toonden aan dat de lage tumor/nierverhouding (0,35) de mogelijkheid beperkt om [$^{225}$Ac]Ac-DOTA-JR11 voor TAT van NET's te gebruiken. Er zijn verdere verbeteringen nodig om de door de nieren geabsorbeerde dosis te verminderen en de nefrotoxiciteit als gevolg van alfadeeltjes te verminderen.

Dit proefschrift is gericht op het verkennen van verschillende strategieën om de beeldvorming en behandeling van PCa en NET's te verbeteren. Door middel van de verschillende hoofdstukken hebben we laten zien dat een verscheidenheid aan NeoB- en DOTA-JR11-analogen met succes werd gesynthetiseerd en gekarakteriseerd. Radiolabeling met verschillende radio-isotopen (bijv. indium-111, lutetium-177 en actinium-225) voor SPECT-beeldvorming en gerichte radionuclidetherapie werden met succes bereikt onder geoptimaliseerde omstandigheden. De impact van de chemische modificaties op de biochemische eigenschappen van de overeenkomstige peptidevectoren werd in vitro gekarakteriseerd. Ten slotte werden onze gelabelde peptide-analogen in vivo geëvalueerd in diverse preklinische modellen om hun farmacokinetiek en biodistributieprofielen te bepalen.

## Referenties


1. Jadvar H. Targeted radionuclide therapy: An evolution toward precision cancer treatment. AJR 2017;209:277–288.
2. Ersahin D, Doddamane I, Cheng D. Targeted radionuclide therapy. Cancers 2011;3:3838–3855.
3. Das S, Al-Toubah T, El-Haddad G, Strosberg J. 177Lu-DOTATATE for the treatment of gastroenteropancreatic neuroendocrine tumors. Expert Rev Gastroenterol Hepatol 2019;13:1023–1031.
4. Ruigrok EAM, Verhoeven M, Konijnenberg MW, de Blois E, de Ridder CMA, Stuurman DC, et al. Safety of [177Lu]Lu-NeoB treatment: a preclinical study characterizing absorbed dose and acute, early, and late organ toxicity. EJNMMI 2022;49:4440–4451.
5. Dalm SU, Nonnekens J, Doeswijk GN, De Blois E, Van Gent DiC, Konijnenberg MW, et al. Comparison of the therapeutic response to treatment with a 177Lu-labeled somatostatin receptor agonist and antagonist in preclinical models. J Nucl Med 2016;57:260–265.
6. Liu Z, Yang C, Zeng X, Ke C, Tian J, Wang Z, et al. Effectiveness of GnRH Antagonists and Agonists in Patients with Hormone-Sensitive Prostate Cancer: A Retrospective Study. Appl Bionics Biomech 2022;2022:1–5.
7. Nock BA, Kaloudi A, Lymperis E, Giarika A, Kulkarni HR, Klette I, et al. Theranostic perspectives in prostate cancer with the gastrin-releasing peptide receptor antagonist NeoBOMB1: Preclinical and first clinical results. J Nucl Med 2017;58:75–80.
8. Rylova SN, Stoykow C, Del Pozzo L, Abiraj K, Tamma ML, Kiefer Y, et al. The somatostatin receptor 2 antagonist 64Cu-NODAGA-JR11 outperforms 64Cu-DOTA-TATE in a mouse xenograft model. PLoS One 2018;13:1–16.
9. Zhu W, Cheng Y, Wang X, Yao S, Bai C, Zhao H, et al. Head-to-head comparison of 68Ga-DOTA-JR11 and 68Ga-DOTATATE PET/CT in patients with metastatic, well-differentiated neuroendocrine tumors: A prospective study. J Nucl Med 2020;61:897–903.
10. Rondon A, Degoul F. Antibody Pretargeting Based on Bioorthogonal Click Chemistry for Cancer Imaging and Targeted Radionuclide Therapy. Bioconjug Chem 2020;31:159–173.
11. Bailly C, Bodet-Milin C, Rousseau C, Faivre-Chauvet A, Kraeber-Bodéré F, Barbet J. Pretargeting for imaging and therapy in oncological nuclear medicine. EJNMMI Radiopharm Chem 2017;2:1–14.
12. Houghton JL, Zeglis BM, Abdel-Atti D, Sawada R, Scholz WW, Lewis JS. Pretargeted immuno-PET of pancreatic cancer: Overcoming circulating antigen and internalized antibody to reduce radiation doses. J Nucl Med 2016;57:453–459.
13. Meyer JP, Houghton JL, Kozlowski P, Abdel-Atti D, Reiner T, Pillarsetty NVK, et al. 18F-Based Pretargeted PET Imaging Based on Bioorthogonal Diels-Alder Click Chemistry. Bioconjug Chem 2016;27:298–301.
14. Müller C, Struthers H, Winiger C, Zhernosekov K, Schibli R. DOTA conjugate with an albumin-binding entity enables the first folic acid-targeted 177Lu-radionuclide tumor therapy in mice. J Nucl Med 2013;54:124–131.
15. Rousseau E, Lau J, Zhang Z, Uribe CF, Kuo HT, Zhang C, et al. Effects of adding an albumin binder chain on [177Lu]Lu-DOTATATE. Nucl Med Biol 2018;66:10–17.
16. Tiel S van, Tiel S van, Maina T, Nock B, Konijnenberg M, Blois E de, et al. Albutate-1, a Novel Long-Circulating Radiotracer Targeting the Somatostatin Receptor Subtype 2. J Nucl Med Radiat Sci 2021;2:1–9.
17. Kuo HT, Lin KS, Zhang Z, Uribe CF, Merkens H, Zhang C, et al. 177Lu-labeled albumin-binder-conjugated PSMA-targeting agents with extremely high tumor uptake and enhanced tumor-to-kidney absorbed dose ratio. J Nucl Med 2021;62:521–527.

# Curriculum Vitae

Maryana Handula was born the $12^{th}$ of May 1991 in Nineveh, Iraq. After the difficult times that her country experienced in the beginning of the 2000s, she first moved to Jordan with her family in 2006, where she spent 2 years. Then, she moved to France in 2008, where she demonstrated incredible enthusiasm in learning French in a very short time which allowed her to complete her secondary school education at the Lycée Blanche de Castille, Nantes, France in 2010. Then, she integrated the medical school with the dream of becoming a pharmacist, but life led her to integrate the science and technology college at the University of Nantes, where she studied analytical chemistry. She completed her education at the same university from which she obtained her Bachelor's degree in 2015 and her Master's degree in 2018.

During her Bachelor's and Master's studies, she had the opportunity to do her internships in valuable laboratories. As such, she integrated the research and development team at Arronax in 2015 and 2016 in Nantes, France; where she discovered the field of nuclear medicine for the first time under the supervision of Dr. Sandrine Huclier and Dr. Cyrille Alliot. During her two internships, she worked on the characterization of new chelators suitable for the radiolabeling of scandium-44. Those internships allowed her to come across this domain more in details and improved her curiosity in discovering other aspects of the field of nuclear medicine. Therefore, with the precious help of Dr. Sandrine Huclier, she had the chance to integrate the life science division of the largest cyclotron in the world, TRIUMF, in Vancouver, Canada in 2017. In this wonderful team, she performed her first year Master's internship and worked under the supervision of Dr. Valery Radchenko on the radiolabeling of new chelators with scandium-44.

After having completed her internship at TRIUMF, she joined Dr. Yann Seimbille's laboratory in 2018 at the Department of Radiology and nuclear medicine at the Erasmus Medical Center, Rotterdam, The Netherlands. During this internship, she worked on the development of NeoB analogs suitable for pretagrgeting applications and dual-modality imaging probes based on nuclear and optical imaging. After having obtained her Master's degree, she was hired by Dr. Seimbille as a research analyst to continue working on the same project. However, very quickly, she felt that she needed bigger challenges and therefore, she decided to follow her PhD studies under the supervision of Prof. Dr. Frederik Verburg, Dr. Antonia Denkova and Dr. Yann Seimbille.

# List of Publications

**Scientific publications relevant to this thesis**

**M. Handula**, S. Beekman, M. Konijnenberg, D. Stuurman, C. de Ridder, F. Bruchertseifer, A. Morgenstern, A. Denkova, E. de Blois and Y. Seimbille. First preclinical evaluation of [$^{225}$Ac]Ac-DOTA-JR11 and comparison with [$^{177}$Lu]Lu-DOTA-JR11, alpha versus beta radionuclide therapy of NETs. Accepted for publication in EJNMMI Radiopharmacy and Chemistry in June 2023.

S. Koustoulidou*, **M. Handula***, C. de Ridder, D. Struuman, S. Beekman, J. Nonnekens, M. de Jong and Y. Seimbille. Synthesis, characterization, and evaluation of long-acting SSTR2 antagonists for improved radionuclide therapy of neuroendocrine tumors. Pharmaceuticals, 2022, **15**, 1-15.
* Equal contribution

**M. Handula**, D. Chapeau and Y. Seimbille. Orthogonal synthesis of a versatile building block for dual-functionalization of targeting vectors. Accepted for publication in the journal of Open Chemistry in June 2023.

M. Verhoeven, **M. Handula**, L. van den Brink, C. de Ridder, D. Stuurman, Y. Seimbille and S. Dalm. Pre- and intraoperative visualization of GRPR-expressing solid tumors: preclinical profiling of novel dual-modality probes for nuclear and fluorescence imaging. Cancers, 2023, **15**, 1-17.

**M. Handula***, M. Verhoeven*, K.T Chen, J. Haeck, M. de Jong, S. Dalm and Y. Seimbille. Towards complete tumor resection: novel dual-modality probes for improved image-guided surgery of GRPR-expressing prostate cancer. Pharmaceutics, 2022, **14**, 1-18.
* Equal contribution

**M. Handula**, K.T Chen and Y. Seimbille. IEDDA: An attractive bioorthogonal reaction for biomedical applications. Molecules, 2021, **26**, 1-20.



**Manuscripts in Preparation**

M. Verhoeven*, **M. Handula***, L. van den brink, K. T. Chen, Y. Seimbille and S. Dalm. A peptide-based pretargeting approach with TCO-functionalized NeoB conjugates for theranostics of GRPR-positive cancers.
* Equal contribution

**M. Handula***, S. Koustoulidou*, M. de Jong, J. Nonnekens and Y. Seimbille. Proof-of-concept of a pretargeting strategy based on IEDDA bioorthogonal reaction mediated by an SSTR2 antagonist for the diagnosis and treatment of NETs.
* Equal contribution

N. Gaspar*, **M. Handula***, M. C. Stroet, K. Marella-Panth, J. Haeck, T. Kirkland, M. Hall, L. Encell, S. Dalm, M. de Jong, C. Lowik, Y. Seimbille and L. Mezzanotte. A novel reporter gene technology allowing simultaneous optical and radionuclide imaging of cells.
* Equal contribution

**Other publications**

K.T Chen, J. Nieuwenhuizen, **M. Handula** and Y. Seimbille. A novel clickable MSAP agent for dual-fluorescence/nuclear labeling of biovectors. Organic & biomolecular chemistry, 2020, **18**, 6134-6139.

E. Murce, S. Beekman, E. Spaan, **M. Handula**, D. Stuurman, C. de Ridder and Y. Seimbille. Preclinical evaluation of a PSMA-targeting homodimer with an optimized linker for imaging of prostate cancer. Molecules, 2023, **28**, 1-20.

E. Murce, S. Ahenkorah, S. Beekman, **M. Handula**, C. de Ridder, D. Stuurman, F. Cleeren and Y. Seimbille. Radiochemical and biological evaluation of 3p-C-NETA-ePSMA-16, a promising PSMA-targeting agent for radiotheranostics. Submitted to Pharmaceuticals in May 2023.

E. Murce, E. Spaan, S. Beekman, L. van den Brink, **M. Handula**, D. Stuurman, C. de Ridder, S. Dalm and Y. Seimbille. Synthesis and evaluation of ePSMA-DM1: a new theranostic small-molecule drug conjugate (T-SMDC) for prostate cancer. Submitted to Pharmaceuticals in June 2023.

D. Chapeau, S. Koustoulidou, **M. Handula**, S. Beekman, C. de Ridder, D. Stuurman, E. de Blois, M. de Jong, M. Konijnenberg and Y. Seimbille. [$^{212}$Pb]Pb-eSOMA-01: a Promising Radioligand for Targeted Alpha Therapy of Neuroendocrine Tumors. Submitted to Pharmaceuticals in June 2023.

# Oral and Poster Presentations

**POSTER PRESENTATION | INTERNATIONAL SYMPOSIUM OF RADIOPHARMACEUTICAL SCIENCES (ISRS)**

M. Handula, S. Beekman, A. Denkova and Yann Seimbille. Development of C-terminal modified long-acting DOTA-JR11 analogs for optimized treatment of NETs.
May 2023, Hawaii, USA.

**ORAL PRESENTATION | EUROPEAN ASSOCIATION OF NUCLEAR MEDICINE (EANM)**

M. Handula, E. de Blois, J. Nonnekens, A. Denkova and Yann Seimbille. Radiolabeling and preclinical evaluation of [$^{225}$Ac]Ac-DOTA-JR11 for targeted alpha therapy of neuroendocrine tumors. October 2022, Barcelona, Spain.

**POSTER PRESENTATION | INTERNATIONAL SYMPOSIUM OF RADIOPHARMACEUTICAL SCIENCES (ISRS)**

S. Koustoulidou, M. Handula, J. Nonnekens, M. de Jong and Y. Seimbille. Albumin binders: a potential strategy for enhanced treatment of NETs using SSTR2 antagonists. May 2022, Nantes, France.

**POSTER PRESENTATION | INTERNATIONAL SYMPOSIUM OF RADIOPHARMACEUTICAL SCIENCES (ISRS)**

M. Handula, E. de Blois, A. Denkova and Y. Seimbille. Actinium-225 labeling of DOTATATE and JR11 for the treatment of SSTR2-positive tumors. May 2022, Nantes, France.

**ORAL PRESENTATION | EUROPEAN MOLECULAR IMAGING MEETING (EMIM)**

M. Verhoeven, M. Handula, L. van den Brink, C. de Ridder, D. Stuurman, Y. Seimbille and S. Dalm. Preclinical Evaluation of Four Dual-modality Probes for Image-guided Surgery of GRPR-positive Cancer. March 2022, Thessaloniki, Greece.

**ORAL PRESENTATION | EUROPEAN ASSOCIATION OF NUCLEAR MEDICINE (EANM)**

S. Koustoulidou, M. Handula, J. Nonnekens, M. de Jong and Y. Seimbille. Proof-of-concept of a pretargeting strategy mediated by SSTR2 antagonists for the therapy of neuroendocrine tumors. October 2021.

**POSTER PRESENTATION | EUROPEAN MOLECULAR IMAGING MEETING (EMIM)**

M. Handula, S. Koustoulidou, J. Nonnekens, M. de Jong and Y. Seimbille. Investigation on long-acting SSTR2 antagonists to improve radionuclide therapy of NETs. August 2021, Göttingen, Germany. *Poster award in the session of Imaging Cancer Therapy I.*

**POSTER PRESENTATION | INTERNATIONAL SYMPOSIUM OF RADIOPHARMACEUTICAL SCIENCES (ISRS)**

M. Handula, M. Verhoeven, K.T Chen, J. Haeck, I. Klomp, L. de Bruin, M. de Jong, S. Dalm and Y. Seimbille. Development of versatile dual-modality imaging probes based on a GRPR antagonist for preoperative imaging and image guided surgery of prostate cancer. May 2021.

**ORAL PRESENTATION | EUROPEAN ASSOCIATION OF NUCLEAR MEDICINE (EANM)**

M. Verhoeven, M. Handula, K.T Chen, M. de Jong, Y. Seimbille and S. Dalm. First pretargeting approach for peptide receptor radionuclide therapy of GRPR-positive prostate cancer. October 2020.

# PhD Portfolio

| | |
|---|---|
| **PhD candidate** | Maryana Handula |
| **Erasmus Mc department** | Radiology and nuclear medicine |
| **Promoter** | Prof.dr. F.A. Verburg |
| **Co-promoters** | Dr. Y. Seimbille and Dr.ir. A.G. Denkova |

| **Courses and training** | **Year** | **ECTS** |
|---|---|---|
| PhD day | 2022 | 0.30 |
| CPO-course: Patient Oriented Research | 2022 | 0.30 |
| The career development, CV and LinkedIn workshops | 2021 | 0.15 |
| Course on laboratory animal science | 2021 | 3.00 |
| PhD introduction session | 2021 | 0.20 |
| Personal leadership and communication | 2021 | 1.00 |
| Biomedical research techniques | 2020 | 1.50 |
| Biomedical English writing | 2020 | 2.00 |
| The power point tricks you didn’t know | 2020 | 0.30 |
| The word advances: create large documents the right way | 2020 | 0.30 |
| Basic and translational oncology | 2020 | 2.00 |
| Research integrity | 2020 | 0.30 |
| **Total** | | **11.35** |

| **General meetings** | **Year** | **ECTS** |
|---|---|---|
| Weekly meeting with the PI | 2018 - 2023 | 4.00 |
| RPC group meeting | 2020 - 2023 | 1.50 |
| Joint Research meeting | 2018 - 2023 | 3.00 |
| Alpha project meeting | 2021 - 2022 | 0.50 |
| KWF project meeting | 2020 - 2022 | 2.00 |
| Pretargeting meeting | 2018 - 2021 | 2.00 |
| **Total** | | **12.50** |





| **Workshops and International conferences** | **Year** | **ECTS** |
|---|---|---|
| EANM, Annual congress 2022, Barcelona, Spain | 2022 | 1.50 |
| iSRS Annual congress 2022, Nantes, France | 2022 | 1.50 |
| EMIM Annual congress 2021, Göttingen, Germany | 2021 | 1.25 |
| eSRS Annual congress, 2021, online | 2021 | 1.5 |
| NKRV workshops | 2019 - 2023 | 1.9 |
| **Total** | | **7.65** |

| Teaching and other activities | Year | ECTS |
|---|---|---|
| Supervision of students | 2020 - 2023 | 6.30 |
| Organization of the Lab Day Out | 2021 | 0.50 |
| Organization of the BBQ day_RPC group | 2020 | 0.50 |
| Cancer institute research day | 2020 | 0.50 |
| Imaging Research on The Move | 2018 | 0.25 |
| **Total** | | **8.05** |

| | | |
|---|---|---|
| **Total** | | **39.55** |

# Thank you

# Acknowledgments

I cannot believe that the time to write those few lines has FINALLY come!

First of all, I would like to thank Prof.dr. Frederik Verburg. Dear Erik, thank you very much for everything. I always felt that you believed in me and this was a great honor. Thank you for all the time you dedicated for our meetings. Thank you for the support, advice and encouragements. Thank you for having supervised me in this very special period of my life.

Dear Antonia, thank you for having received me in Delft to perform my first actinium-225 experiments. It was a pleasure being in your facility. Thank you for all the corrections, modifications and comments on the abstracts and manuscript, it only made them more valuable. Finally, thank you for being my co-promoter and your supervision, help and advice meant a lot to me.

Yann, I do not know how can I start. The first thing I remember was the day I met you for the first time at TRIUMF. I was so happy that I could communicate in French with someone else in this country at the other side of the world. But then, you became my supervisor, not only for my master's but also for the coming years of my PhD. PhD? I always said that I do not want to do a PhD, that I was not able to handle the pressure for so many years. But you always believed in me and you did not give up trying to push me to accept. Finally, I accepted and I think that this was one of the best decisions I made. There are no words that can describe how thankful I am for having you as my main supervisor for more than five years. You taught me to be patient, work hard, always focus on the final goal and the most important is that you transmitted me your passion for research. We disagreed on so many points, but we always found a solution for every issue. I really thank you for having listened to me, for having appreciated my ideas concerning my research, for the correction of my manuscripts (even though this could take months), abstracts, presentations, and for all the times you were proud of me. Thank you for having given me the chance to be part of your group. Thank you for the trust you had in me and that you continue having.

KT, I cannot finish my PhD without telling you how much I appreciated being daily supervised by a great researcher as you. I cannot forget who was with me in the lab checking my experiments step by step every day. Thank you for having taught me the peptide synthesis and for having solved all my research issues. I was always scared when something was going wrong but you were always there to tell me that this was 'OK'. I am still sad that you left us because you were an asset in the group. At the same time, I am jealous that your new students have a talented supervisor as you.

Erik, thank you very much for all the help and guidance you provided regarding the radiochemistry part of my research. Thank you for the support and the advice you gave me during the past years. You are a great expert in radiochemistry and I learned a lot from you. It was a pleasure sharing the office together for few years and a pleasure working with you in the group.

I would like to thank the AMIE Core facility for their presence and assistance with the different in vivo studies.

I am grateful to all the people that I have met during the past five years. To every person that contributed from near and far in the good achievement of this journey. Ho Sze, thank you so much for the time you spent helping me understanding the results I obtained for the actinium-225 study. Giorgia, thank you for having been there whenever I had a question.

A special thank you goes to all the colleagues with whom I collaborated in different projects. Marjolein, Lilian and Simone, it was a nice experience working with you. Laura, many thanks for the great collaboration we had together. Natasa, I could not ask for a better collaborator, thank you for having been always kind, flexible and a great supporter.

Julie, I really appreciated our collaboration and I would like to thank you for all the time you dedicated listening to me. I am grateful for your advice. Thank you for having helped me to stand up whenever I was down.

Corrina and Debra, thank you very much for all the help provided during the in vivo studies. I am so grateful for having such skilled and talented technicians who assisted me in my experiments. Thank you for having been flexible and always available to answer my questions.

Thanks to all the RadioPharmaceutical Chemistry group for all the help, support and the fun moments we have shared together. A special thank you goes to Savanne, for having taken care of all the in vitro experiments, I really appreciate your professionalism and all the assistance you provided for the different projects. Hanyue, thank you for having listened to me when I needed it, you have always been present and always took the initiative to ask if everything was going well. Eline, many thanks for the help provided for the actinium-225 study and of course all the Dutch translations.

I cannot forget all the good and nice moments spent with the students that integrated the lab for few months, especially, Angelos, Kevin, Lucas, and Naomi. I shared such nice time with each one of you in the lab discussing about all type of subjects. Jordy, thank you for the time you spent in the lab collecting hundreds of tubes during the actinium-225 experiments.

Erika and Dylan, the two people with whom I shared so many things. Happy, sad, disappointments and so many other feelings. Thank you for every moment we have spent together, going to the lab in the weekends during Covid-19, taking care of the in vivo studies on Saturday and Sunday, the coffee breaks, the picnics in the parcs, the lunches and the fun moments we had together at iSRS in Nantes. Erika, I cannot forget all the fun we had taking the tea together during the lockdown. Being neighbors helped me a lot to overcome the difficult times we had. So, thank you for your support. Dylan, thank you for being nice, kind and very helpful when needed. I wish both of you a very good luck for the last step of your PhD and I believe that the best is yet to come.

Priciana and Carolline, the two people with whom I have spent so much time complaining about every single day of my life as a PhD student. You were always there to listen and I really appreciate your patience with me. Priciana, thank you for all the secrets we have exchanged and the advice you have given me. Thank you for all our conversations about food, movies, series, fashion and traveling. Carolline, you are such a great person with so much potential, thank you for all the moments we have spent together. Thank you for having organized so many events because you care so much about others, please stay as you are. I wish both of you the best of luck for your PhD and it will be a great pleasure for me supporting you till the end of your trajectory.

Sofia, my friend, I was so lucky for having collaborated and worked with such a skilled biologist as you. I appreciate all the work we have done, all the data we have generated, and the papers we published together. Your presence, help and support were so valuable. You have taught me so many things, on imaging, in vitro and in vivo studies, writing and presenting. You shared with me the most difficult moments of my PhD life and you were always present to listen and advise me. But we also shared so many nice and fun moments. Thank you for having been there whenever I needed it.

Özlem, my little paranymph, thank you for everything you have done for me. Thank you for the lunches we had together in the weekends and for all the conversations we had in the lab. Thank you for your endless positivity, and kindness. I appreciate all the time you have spent organizing this event and I do not know how to thank you for that.

Carlijn, sissi, I would have never expected to meet someone like you when arriving to EMC. I met a friend and a sister from another mother. Thank you for all your help since I have arrived to The Netherlands, you were my family here. Thank you for always having believed in me. Thank you so much for all your support.

To my parents, brother and sister, obtaining my doctorate would not have been possible without you believing in every single step that I have made in my life. I am thankful to have you as a great support and hope that you are proud of what I have accomplished.

To the person that supported and believed in me the most. I am so grateful to have you in my life, your presence was always enough to help me to overcome whatever difficulty I was experiencing. You always did all your best to make me feel better whenever you saw me down and about to give up. You always knew how to help and support me. Thank you for everything.

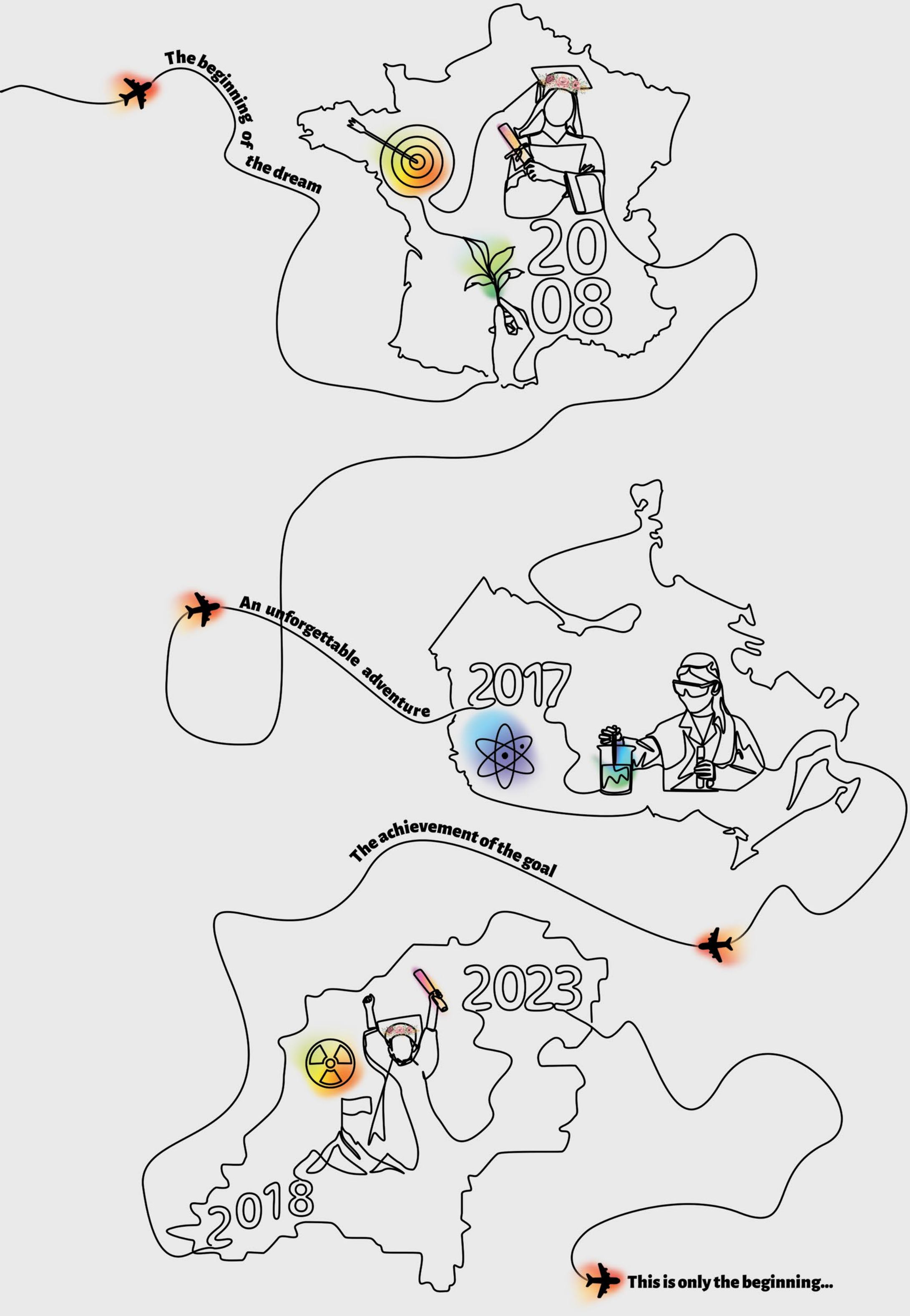
The beginning of the dream
2008
An unforgettable adventure
2017
The achievement of the goal
2023
2018
This is only the beginning...